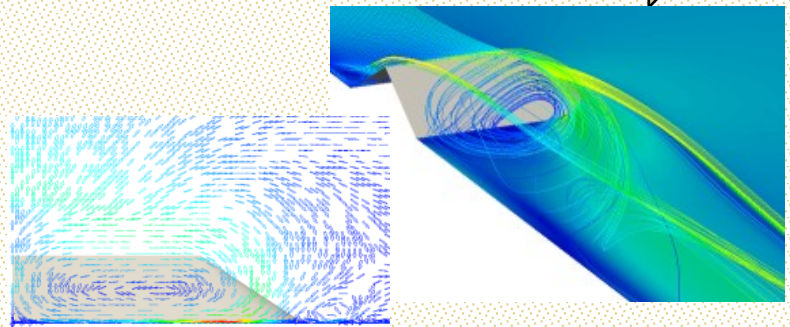


EROSION TEST: FREE-SURFACE EVOLUTION



Raquel Almeida de Azevedo Faria

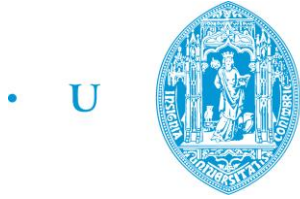
NUMERICAL AND EXPERIMENTAL STUDY OF GRANULAR PILES WHEN SUBJECTED TO WIND EROSION

Doctoral Thesis in Mechanical Engineering, branch of Industrial Aerodynamics and Wind Engineering, supervised by Professor Almerindo Domingues Ferreira and Professor Antonio Carlos Mendes de Sousa, submitted to the Department of Mechanical Engineering, Faculty of Sciences and Technology of the University of Coimbra

April, 2018



UNIVERSIDADE DE COIMBRA



• U • C •

FCTUC FACULDADE DE CIÊNCIAS
E TECNOLOGIA
UNIVERSIDADE DE COIMBRA

NUMERICAL AND EXPERIMENTAL STUDY OF GRANULAR PILES WHEN SUBJECTED TO WIND EROSION

by

Raquel Almeida de Azevedo Faria

Dissertation submitted to the Department of Mechanical Engineering in
partial fulfilment to the requirements for degree of

Doctor of Philosophy in Mechanical Engineering

by the

FACULTY OF SCIENCES AND TECHNOLOGY
UNIVERSITY OF COIMBRA

Thesis supervisors:

Almerindo Domingues Ferreira, Assistant Professor

Department of Mechanical Engineering of the University of Coimbra, Portugal

Antonio Carlos Mendes de Sousa, Professor Emeritus

Department of Mechanical Engineering of the University of New Brunswick, Canada

Coimbra, April 2018

*I can't change the direction of the wind, but I can adjust my sails to always reach
my destination*

Jimmy Dean

AGRADECIMENTOS

Este espaço é dedicado àqueles que deram a sua contribuição para que esta tese fosse realizada. Peço desde já desculpa àqueles que tenha omitido. A todos eles deixo aqui o meu agradecimento sincero.

Em primeiro lugar agradeço ao Doutor Almerindo Ferreira pela forma como orientou o meu trabalho. De enfatizar a utilidade das suas recomendações e a forma como sempre me motivaram. Estou grata por ambas, e também pela liberdade de ação que foi decisiva para que este trabalho contribuísse para o meu desenvolvimento pessoal e me apontasse um caminho a seguir na minha carreira académica. E mais importante, nas alturas mais difíceis, quando por várias vezes cheguei a duvidar se conseguiria avançar com este trabalho para a frente, ter-me sempre apoiado, não ter desistido de mim, tendo sempre uma palavra amiga e de motivação.

Um agradecimento muito especial também ao Professor Antonio Sousa, pelo seu apoio, conselhos valiosos, disponibilidade inquestionável e uma das principais fontes de inspiração e motivação para a realização deste trabalho.

Fica também aqui uma nota de apreço a todos os colegas do DEM/ISEC que me apoiaram durante toda esta fase, tendo eles muitas vezes ficado sobrecarregados de trabalho. Em especial ao Doutor Pedro Ferreira, ao Engenheiro Paulo Amaro e aos responsáveis dos laboratórios de Mecânica Aplicada, Biomecânica e de Fabrico Assistido por Computador, nomeadamente, Doutor Luís Roseiro e Doutor Fernando Simões, pela contribuição que deram na construção de dispositivo utilizado para a construção da pilha oblonga tridimensional.

Deixo também uma palavra de agradecimento aos professores do DEM / FCTUC, pela forma como lecionaram a parte curricular no curso de Doutoramento em Engenharia Mecânica, pelos ensinamentos e conselhos transmitidos, os quais foram bastante úteis para a realização do meu trabalho e redação da presente tese.

Agradecer ainda à ADAI por me ter acolhido como membro da sua equipa de investigação e permitir que realizasse nas suas instalações a parte experimental do presente trabalho, sendo esta crucial para alcançar os objetivos a que me proponho.

Por fim, um especial e sentido obrigado à minha família e em especial ao meu namorado João Pereira, por, ao longo deste período, me terem apoiado e “aturado” nos momentos mais difíceis, em que, por vezes, e por serem as pessoas mais próximas, descarreguei neles as minhas frustrações e inseguranças.

Mais uma vez agradeço a todos, e espero que continuem a ser o meu apoio e suporte ao longo da minha carreira académica e de investigação.

ABSTRACT

The transport of soil particles by wind is of enormous relevance in a wide range of events from those related to agriculture (e.g., seed transport) to the formation and modification of the landscape. A classic example is sand dunes, which can be formed, moved, or entirely eroded due to aeolian processes. Still, aeolian transport of particles may cause serious damage in transportation, communications and severe environmental problems, such as the degradation of air quality due to dispersion of pollutants from stockpiles.

The wind exposure will lead to the particles movement through several mechanisms, such as, suspension, creeping, saltation, and saltation bombardment. Consequently, the free surface will change over time due to entrainment and deposition phenomena.

The main objective of this study is assessing the airflow characteristics over and around granular material complex three-dimensional piles when subjected to the wind erosion and its influence in the behavior of the free surface, as well as, in the sand emission rate.

A literature review was made over the main subjects of interest to the present work, from the basics, such as granular material and aeolian transport mechanisms, to the key magnitudes involved in the wind erosion phenomena. Studies performed to calculate the dust emission from stockpiles are presented and reviewed along with the widely applied methodology from United States Environmental Protection Agency (USEPA). This methodology estimates the emission of particles from stockpiles only during specific erosion events, such as bursts, when in reality emissions occur in many other occasions. The present work offers the possibility of conducting the determination of emissions from stockpiles along time; this approach makes viable to follow the time-dependent evolution of the free surface enhancing in this way the accuracy of the predictions. Therefore, studies that are related to free surface progress are also reviewed.

The present work has a significant experimental component, and the thesis describes in considerable detail the experimental apparatus and procedures, including wind tunnel, granular material, tested pile configurations and performed tests – in particular, erosion and shear stress (with *Irwin* probes) measurements.

In addition, the use of Computational Fluid Dynamics (CFD) plays an important role in the present study; therefore, for completeness, key concepts related to CFD are included in this thesis along with a brief survey of studies that employ CFD methodology to evaluate aeolian erosion.

The present CFD studies were conducted by using an open source CFD code – OpenFOAM (OF). The motivation for the selection of OF, as the CFD tool, is related to its wide acceptance in the scientific community; moreover, its application to the prediction and study of wind erosion is

an original contribution to this field of research. Full description of the numerical model and its implementation are given along with the methodology used in the model validation.

Two different pile configurations were studied - a two-dimensional triangular pile and a three-dimensional oblong pile. The increasing geometrical complexity of the piles allowed gaining gradual experience with the procedures and methodologies involved. The experimental and numerical studies for these cases and their results are analyzed and discussed.

In what concerns the oblong piles, the numerical results are correlated with the registered free surface deformation of the piles and compared against other study available in the literature, in which oil film visualization tests were conducted and a different CFD tool was used.

Considering that the model validation is partly performed against experimental results, particular attention was given to their accuracy. For the triangular piles, the comparison is primarily against the wall shear stress results obtained using the *Irwin* probes, which were built and calibrated for this work. The study of these probes was extensive and it led to an innovative and significant contribution to this field of research, which justifies an integrated, but autonomous Part B of this thesis.

Due to the versatility of experimental apparatus built to assist the calibration of the *Irwin* probes, a more in-depth study was also carried out on the flow through rectangular ducts with a constant and variable cross-section.

Finally, the main findings resulting from the present work are summed up and some recommendations for future work are given.

Keywords: Computational Fluid Dynamics (CFD), OpenFOAM, Wind tunnel, Aeolian erosion, Emission rate, Shear Stress, Oblong piles, Triangular piles, Rectangular Duct, *Irwin* probes, *Preston* tube

RESUMO

O transporte de partículas do solo pelo vento é de enorme relevância numa ampla gama de eventos, desde os relacionados com a agricultura (por exemplo, o transporte de sementes) até a formação e modificação da paisagem. Um exemplo clássico são as dunas de areia, que se podem formar, mover ou erodir totalmente devido a processos eólicos. Por outro lado, o transporte de partículas pode provocar sérios danos no sector dos transportes, comunicações e graves problemas ambientais, como a degradação da qualidade do ar devido à dispersão de poluentes provenientes de pilhas de armazenamento.

A exposição ao vento pode levar ao movimento das partículas através de vários mecanismos, tais como, suspensão, arrastamento, saltação e bombardeamento das partículas em saltação. Consequentemente, a superfície livre irá mudar ao longo do tempo devido aos fenómenos de arrastamento e deposição.

O objetivo principal deste estudo é investigar as características do fluxo de ar sobre e ao redor de pilhas tridimensionais (3D) complexas de material granular quando sujeitas à erosão do vento e avaliar a sua influência no comportamento da superfície livre, bem como na taxa de emissão.

Uma revisão bibliográfica foi feita sobre os principais temas de interesse para o presente trabalho, desde o básico, como material granular e mecanismos de transporte eólicos, até às grandezas chave envolvidas nos fenómenos de erosão do vento. Estudos realizados para calcular a emissão de poeira de pilhas de armazenamento são apresentados e revistos juntamente com a metodologia, amplamente aplicada, da Agência de Proteção Ambiental dos Estados Unidos (United States Environmental Protection Agency - USEPA). Esta metodologia estima as emissões de partículas a partir de pilhas de armazenamento apenas durante eventos de erosão específicos, tais como rajadas, quando as emissões na realidade ocorrem em muitas outras ocasiões. O presente trabalho oferece a possibilidade de realizar a determinação de emissões de pilhas de armazenamento ao longo do tempo; esta abordagem torna viável seguir a evolução dependente do tempo da superfície livre, aumentando assim a precisão das previsões. Portanto, estudos relacionados com a evolução da superfície livre são também revistos.

O presente trabalho tem uma componente experimental significativa, e a tese descreve em considerável detalhe a montagem experimental e os procedimentos, incluindo o túnel de vento, o material granular, as configurações de pilhas testadas e os testes executados – em particular, testes de erosão e de medição da tensão de atrito com sondas *Irwin*.

Adicionalmente, o uso da Dinâmica de Fluidos Computacional (em inglês: Computational Fluid Dynamics — CFD) desempenha um papel importante no presente estudo, assim sendo, para completar, conceitos chave relacionados a CFD estão incluídos nesta tese, juntamente com

uma breve pesquisa de estudos que empregam a metodologia CFD para avaliar a erosão eólica. Os presentes estudos CFD foram realizados usando um software CFD de código aberto - OpenFOAM (OF). A motivação para a seleção do OF, como ferramenta CFD, está relacionada com a sua ampla aceitação na comunidade científica; e além disso, a sua aplicação na previsão e estudo da erosão eólica é uma contribuição original para este campo de pesquisa. A descrição completa do modelo numérico e da sua implementação são dadas juntamente com a metodologia utilizada na validação do modelo.

Foram estudadas duas configurações de pilha diferentes - uma pilha triangular bidimensional (2D) e uma pilha tridimensional (3D) oblonga. A crescente complexidade geométrica das pilhas permitiu ganhar experiência de forma gradual com os procedimentos e metodologias envolvidos no estudo. Os estudos experimentais e numéricos para estes casos, bem como os seus resultados, são analisados e discutidos

No que diz respeito às pilhas oblongas, os resultados numéricos são correlacionados com a deformação de superfície livre das pilhas e comparados com outro estudo disponível na literatura, no qual foram realizados testes de visualização de filmes de óleo e utilizada uma ferramenta CFD diferente.

Considerando que a validação do modelo é parcialmente realizada através da comparação com dados experimentais; especial atenção foi dada à sua precisão. Para as pilhas triangulares, a comparação é feita, principalmente, com resultados da tensão de atrito da parede medidos através das sondas *Irwin*, as quais foram construídas e calibradas para este trabalho. O estudo efetuado com estas sondas foi extenso e contribuiu de forma inovadora e significativa para esta área de pesquisa, o que justifica uma Parte B integrada, mas autónoma desta tese.

Devido à versatilidade da montagem experimental construída para auxiliar a calibração das sondas *Irwin*, um estudo mais aprofundado foi também realizado sobre escoamentos em condutas retangulares com seção transversal constante e variável.

Finalmente, as principais conclusões que resultam do presente trabalho são resumidas e sugerem-se algumas recomendações para o trabalho futuro.

Palavras chave: Dinâmica de Fluidos Computacional, OpenFOAM, Túnel de vento, Erosão eólica, Taxa de emissão, Tensão de atrito, Pilhas Oblongas, Pilhas Triangulares, Conduta Retangular, sondas de *Irwin*, tubo de *Preston*

CONTENTS

INTRODUCTION	1
MOTIVATION	2
RESEARCH FRAMEWORK	4
MAIN GOALS	5
MAIN CONTRIBUTIONS	6
THESIS OUTLINE	7
PART A. - NUMERICAL AND EXPERIMENTAL STUDY OF GRANULAR PILES WHEN SUBJECTED TO WIND EROSION	11
CHAPTER A1. INTRODUCTION	13
A1.1. INTRODUCTORY CONCEPTS.....	14
A1.1.1. Granular material.....	14
A1.1.2. Aeolian transport mechanisms	15
A1.1.3. Wind erosion.....	16
A1.1.3.1. Friction velocity (u^*)	17
A1.1.3.2. Horizontal and vertical flux	19
A1.2. CFD PACKAGE	23
A1.3. STATE OF THE ART	23
CHAPTER A2. EXPERIMENTAL SETUP	31
A2.1. WIND TUNNEL.....	32
A2.1.1. Tunnel description	32
A2.1.2. Similarity criteria.....	34
A2.2. SAND	34
A2.3. STUDIED CONFIGURATIONS	35
A2.3.1. Triangular	35
A2.3.2. Oblong pile.....	36
A2.4. EXPERIMENTAL TESTS.....	37
A2.4.1. Erosion tests.....	37
A2.4.2. Sand emission rate.....	38
A2.4.3. Wall shear stress tests	41
A2.4.3.1. Irwin probe.....	41
A2.4.4. Static pressure tests.....	42
CHAPTER A3. NUMERICAL MODELING	45
A3.1. COMPUTATIONAL FLUID DYNAMICS - CFD.....	46

A3.1.1.	Conservation Equations	48
A3.1.2.	Turbulence Modeling	49
A3.1.3.	Near-wall treatment.....	52
A3.1.4.	Discretization method.....	54
A3.1.4.1.	Spatial discretization	55
A3.2.	OPENFOAM.....	55
A3.3.	MODEL VERIFICATION AND VALIDATION (V&V).....	56
A3.3.1.	Model verification	57
A3.3.2.	Model validation	58
A3.4.	NUMERICAL SETUP	60
A3.4.1.	Computational domain and mesh parameters	60
A3.4.2.	Boundary conditions	63
A3.4.3.	Solver	64
CHAPTER A4.	TRIANGULAR PILES.....	67
A4.1.	CASE DESCRIPTION.....	68
A4.2.	EXPERIMENTAL RESULTS.....	70
A4.2.1.	Pressure coefficient distribution	70
A4.2.2.	Friction coefficient distribution.....	73
A4.2.3.	Free surface deformation.....	76
A4.2.4.	Sand emission rate (Φ)	78
A4.3.	NUMERICAL RESULTS.....	80
A4.3.1.	Pressure coefficient distribution	81
A4.3.2.	Friction coefficient distribution.....	82
A4.3.3.	Flow topology.....	84
A4.3.4.	Streamwise flux (q) and Sand emission rate (Φ).....	85
A4.4.	CONCLUDING REMARKS	90
CHAPTER A5.	OBLONG PILES.....	93
A5.1.	CASE DESCRIPTION.....	94
A5.2.	EXPERIMENTAL RESULTS.....	98
A5.2.1.	Free surface deformation.....	102
A5.2.2.	Sand emission rate	110
A5.3.	NUMERICAL RESULTS.....	118
A5.3.1.	Flow topology / Benchmark	118
A5.3.1.1.	Wall flow topology	119
A5.3.1.1.1.	Wind incidence angle of 90°	119
A5.3.1.1.2.	Wind incidence angle of 60°	124
A5.3.1.2.	Flow features around the piles.....	126
A5.3.1.2.1.	Wind incidence angle of 90°	126
A5.3.1.2.2.	Wind incidence angle of 60°	129
A5.4.	CONCLUDING REMARKS	132
CHAPTER A6.	CONCLUSIONS	137

REFERENCES	141
PART B. CALIBRATION OF IRWIN PROBES	149
CHAPTER B1. INTRODUCTION	151
B1.1. GOAL	153
B1.2. INTRODUCTORY CONCEPTS.....	153
B1.3. ENTRANCE REGION	155
B1.4. WALL SHEAR STRESS	156
CHAPTER B2. EXPERIMENTAL PROGRAM	157
B2.1. APPARATUS	158
B2.2. ENTRANCE LENGTH.....	159
B2.3. PRESTON TUBE	160
B2.4. <i>IRWIN</i> PROBE	161
CHAPTER B3. NUMERICAL SETUP.....	163
B3.1. COMPUTATIONAL DOMAIN	164
B3.2. MESH PARAMETERS.....	164
B3.3. CASE SETUP	165
B3.4. MESH DEPENDENCY STUDY	166
CHAPTER B4. RECTANGULAR DUCT WITH CONSTANT SECTION.....	169
B4.1. CASE DESCRIPTION	170
B4.2. EXPERIMENTAL RESULTS	171
B4.2.1. Repeatability and accuracy evaluation	171
B4.2.2. Pressure coefficient distribution.....	172
B4.2.3. Friction coefficient distribution	174
B4.2.4. Irwin probes	178
B4.2.4.1. Variation along the duct.....	178
B4.2.4.2. Calibration of the probes	180
B4.3. NUMERICAL RESULTS	184
B4.3.1. Pressure coefficient distribution.....	184
B4.3.2. Friction coefficient	185
B4.4. CONCLUDING REMARKS.....	187
CHAPTER B5. RECTANGULAR DUCT WITH VARIABLE SECTION	189
B5.1. CASE DESCRIPTION	190
B5.2. RESULTS AND DISCUSSION.....	191
B5.2.1. Pressure coefficient distribution.....	191
B5.2.2. Friction coefficient distribution	192
B5.2.3. Irwin probes - Calibration	193
B5.3. CONCLUDING REMARKS.....	195

CHAPTER B6. CONCLUSIONS	197
REFERENCES.....	199
CLOSURE	203
MAIN ACHIEVEMENTS	204
RECOMMENDATIONS FOR FUTURE WORK.....	207

LIST OF FIGURES

Part A - Numerical and experimental study of granular piles when subjected to wind erosion

Figure A1-1: Aeolian transport mechanisms.	15
Figure A1-2: Balance of forces applied to a particle subject to aerodynamic forces and cohesion.	16
Figure A1-3: Schematic representation of the relation between emission rate (F) and saltation flux (q).	21
Figure A2-1: Incident velocity profile for the undisturbed wind speed used in the experiments.	33
Figure A2-2: Schematic view of the wind tunnel and placement of the pile model (dimensions in mm).	33
Figure A2-3: Tested sand granulometry [59].	35
Figure A2-4: Geometry and dimensions of the triangular piles. The windward and lee side of the slope for the different configurations are indicated in red and black, respectively. (Dimensions in (mm); wind direction is from left to right) (Adapted from Faria et al. [12]).	36
Figure A2-5: Schematic representation of the tested oblong sand pile (dimensions in millimetres).	37
Figure A2-6: Scheme to calculate the emission rate for the 2D cases.	39
Figure A2-7: Scheme to calculate the emission rate for the 3D cases.	39
Figure A2-8: Distribution of <i>Irwin</i> probes and static pressure taps along the stoss side of a triangular model.	41
Figure A2-9: Geometry of the <i>Irwin</i> probes used (dimensions in millimetres).	42
Figure A2-10: Detail of the <i>Irwin</i> probes surface-mounted on one of the piles.	42
Figure A2-11: Distribution of static pressure taps along the lee side of a triangular model.	43
Figure A3-1: Finite control volume (a) and infinitesimal control volume (b) approaches [84].	48
Figure A3-2: Extend of modeling for different numerical models.	50
Figure A3-3: Boundary layer development.	52
Figure A3-4: Boundary layer regions.	53
Figure A3-5: Computational domain – triangular piles.	61
Figure A3-6: Oblong piles - computational domain for two wind incidence angles (90° (left) and 60° (right)).	61
Figure A3-7: Mesh detail – inflation layers (crest) and refined region around the pile.	62
Figure A3-8: Comparison of the performance of two turbulence models ($k-\epsilon$ and SST $k-\omega$) against experimental data of an illustrative triangular case (S150).	66
Figure A4-1: Geometry and dimensions of the three triangular piles tested. The windward slope of the various configurations is indicated in color and the lee side in black. (Dimensions in (mm); wind direction is from left to right).	68
Figure A4-2: Pressure coefficient repeatability tests: absolute deviation [%] distribution for all cases, for $U_0=9.9$ m/s.	71
Figure A4-3: c_p distribution for all tested cases, for $U_0=9.9$ m/s.	72
Figure A4-4: Influence of the Reynolds number on the pressure coefficient distribution (case S150).	73
Figure A4-5: <i>Irwin</i> probe pressure difference repeatability tests: absolute deviation [%] distribution for case S150, for $U_0=9.9$ m/s.	73
Figure A4-6: c_f distribution along the stoss side of the piles, for $U_0=9.9$ m/s.	74
Figure A4-7: c_f distribution along the stoss side of the piles – influence of the crest' height (cases S15 and S150).	75
Figure A4-8: Influence of the Reynolds number on the friction coefficient distribution (case S150).	75
Figure A4-9: Erosion profiles (initial profile - dotted line, average - continuous line, minimum and maximum - dashed lines) for $U_0=9.9$ m/s (vertical scale deliberately enlarged).	76
Figure A4-10: Normalized erosion profiles (z/h) at several erosion times (solid line: $t=1$ min; dash-dot-dot line: $t=2$ min and dashed line: $t=3$ min), and experimental measurements of the friction velocity across the stoss slope (markers) (dotted line corresponds to the ideal initial stoss slope).	77
Figure A4-11: Mean sand emission rate during three time intervals for each pile.	79

Figure A4-12: Comparison for the normal sand emission rate for the three geometries during the time interval $t=0$ to $t=1$ min.....	80
Figure A4-13: Experimental pressure coefficient distribution (markers) against predicted values by OpenFOAM (lines) for $U_0=9.9$ m/s.....	81
Figure A4-14: Influence of the Reynolds number on the pressure coefficient distribution predicted by OpenFOAM (case S150).	82
Figure A4-15: Experimental friction coefficient distribution (markers) against predicted values by OpenFOAM (lines) for $U_0=9.9$ m/s.....	83
Figure A4-16: Influence of the Reynolds number on the friction coefficient distribution predicted by OpenFOAM (case S150).	84
Figure A4-17: Flow topology predicted for $U_0 = 9.9$ m/s at $t=0$ (and also $t=1$ min for pile S10).	84
Figure A4-18: Predicted friction velocity along the windward slope of the three geometries (S10, S15 and S20) at $t=0$ for $U_0=9.9$ m/s.	85
Figure A4-19: Comparison of the normal sand emission rate between the three geometries (S10, S15 and S20) during the time interval $t=0$ to $t=1$ min.	86
Figure A4-20: Predicted shear velocity distribution along the windward surface of configuration S10 at instants $t = 0$ and $t = 1$ min.	87
Figure A4-21: Comparison of the measured sand emission rate (case S10) against the predicted values of calibrated Shao's [15] dust scheme (K – Kawamura (Equation (A1-8)); O – Owen (Equation (A1-9)) and L – Lettau and Lettau (Equation (A1-10)), during time interval $t = 0$ to $t = 1$ min; each model is based on the specific c_y value as listed in Table A4-4.	88
Figure A4-22: Comparison of the measured sand emission rate (markers) against the predicted values of calibrated Shao's [15] dust scheme (lines), using the Lettau and Lettau's [16] saltation model, for all cases, during time interval $t = 0$ to $t = 1$ min; each case is based on the specific c_y value as listed in Table A4-4.	89
Figure A5-1: Schematic of the oblong pile hopper.	94
Figure A5-2: View of the oblong pile hopper.	95
Figure A5-3: Oblong pile setup procedure (four steps).	96
Figure A5-4: Oblong sand pile tested (aerial and side views, respectively).	97
Figure A5-5: Angles of incidence tested	97
Figure A5-6: Initial measuring grid (top view).	98
Figure A5-7: Absolute deviation distribution along the pile (mean profile).	100
Figure A5-8: Measurement grid study: comparison between the refined and coarser grid.	101
Figure A5-9: Erosion profiles for $U_0=9.1$ m/s: initial profile and seven cumulative instants (left: mean profile; right: photos of the sand pile).	103
Figure A5-10: Free surface deformation for the two tested velocities ($U_0=9.1$ m/s and $U_0=9.9$ m/s) for first instant $t=1$ min: 3D plot (left) and plan view contours (right).	104
Figure A5-11: Free surface deformation for the two tested velocities ($U_0=9.1$ m/s and $U_0=9.9$ m/s) for first instant $t=2$ min: 3D plot (left) and plan view contours (right).	105
Figure A5-12: Free surface deformation for the two tested velocities ($U_0=9.1$ m/s and $U_0=9.9$ m/s) for first instant $t=3$ min: 3D plot (left) and plan view contours (right).	106
Figure A5-13: Free surface deformation for the two tested velocities ($U_0=9.1$ m/s and $U_0=9.9$ m/s) and two angles of incidence (90 and 60°) for first instant ($t=1$ minute).	107
Figure A5-14: Free surface deformation for the two tested velocities ($U_0=9.1$ m/s and $U_0=9.9$ m/s) and two angles of incidence (90 and 60°) for first instant ($t=2$ minutes).	108
Figure A5-15: Free surface deformation for the two tested velocities ($U_0=9.1$ m/s and $U_0=9.9$ m/s) and two angles of incidence (90 and 60°) for first instant ($t=3$ minutes).	109
Figure A5-16 – Comparison between the initial profile and erosion profile for $t=1$ minute, for velocity $U_0=9.1$ m/s	

and incidence angle $\beta=90^\circ$: plan view (initial profile – up left; t=1 minute – up right), height difference between initial profile and t=1 minute (down left) and sand emission rate [$\text{kg m}^{-2} \text{s}^{-1}$] during the test (down right).....	110
Figure A5-17 – Comparison between the initial profile and erosion profile for t=1 minute, for velocity $U_0=9.9$ m/s and incidence angle $\beta=90^\circ$: plan view (initial profile – up left; t=1 minute – up right), height difference between initial profile and t=1 minute (down left) and sand emission rate [$\text{kg m}^{-2} \text{s}^{-1}$] during the test (down right).....	111
Figure A5-18 - Comparison between the total sand erosion and sand deposition rate for two velocities ($U_0=9.1$ m/s and $U_0=9.9$ m/s) along time.	112
Figure A5-19 - Comparison between two velocities ($U_0=9.1$ m/s and $U_0=9.9$ m/s) for the total sand erosion and sand deposition rate along time.	113
Figure A5-20 – Comparison between the initial profile and erosion profile for t=1 minute, for velocity $U_0=9.1$ m/s and incidence angle $\beta=60^\circ$: plan view (initial profile – up left; t=1 minute – up right), height difference between initial profile and t=1 minute (down left) and sand emission rate [$\text{kg m}^{-2} \text{s}^{-1}$] during the test (down right).....	114
Figure A5-21 – Comparison between the initial profile and erosion profile for t=1 minute, for velocity $U_0=9.9$ m/s and incidence angle $\beta=60^\circ$: plan view (initial profile – up left; t=1 minute – up right), height difference between initial profile and t=1 minute (down left) and sand emission rate [$\text{kg m}^{-2} \text{s}^{-1}$] during the test (down right).....	115
Figure A5-22 - Comparison between the total sand erosion and sand deposition rate for two velocities ($U_0=9.1$ m/s and $U_0=9.9$ m/s) along time for a wind incidence angle of 60°	116
Figure A5-23 - Comparison between two velocities ($U_0=9.1$ m/s and $U_0=9.9$ m/s) for the total sand erosion and sand deposition rate along time with a wind incidence angle of 60°	116
Figure A5-24 - Comparison between two wind incidence angles (90° and 60°) for two velocities ($U_0=9.1$ m/s and $U_0=9.9$ m/s) and for the total sand erosion and sand deposition rate along time.....	117
Figure A5-25: Wall flow around the stockpile ($\beta = 90^\circ$): a Numerical contours of non-dimensional wall shear stress, b surface flow visualization [4].....	119
Figure A5-26: Numerical contours of non-dimensional wall shear stress ($\beta = 90^\circ$, $U_0=9.1$ m/s and $\tau_{ref} = 0.126$ Pa): a wall flow around the stockpile, b wall flow over the stockpile.	120
Figure A5-27: Numerical contours of the non-dimensional wall shear stress ($\beta = 90^\circ$, $U_0=9.9$ m/s and $\tau_{ref} = 0.146$ Pa): a wall flow around the stockpile, b wall flow over the stockpile.	121
Figure A5-28: Wall shear stress distribution over the stockpile - numerical predictions: a $U_0=9.1$ m/s, b $U_0=9.9$ m/s.	122
Figure A5-29: Numerical velocity vector field ($\beta = 90^\circ$): near-wall flow around the stockpile (vectors colored by velocity magnitude).	123
Figure A5-30: Wall flow around the stockpile ($\beta = 60^\circ$): a Numerical contours of non-dimensional wall shear stress, b surface flow visualization [4].....	124
Figure A5-31: Numerical contours of non-dimensional wall shear stress ($\beta = 60^\circ$, $U_0=9.1$ m/s and $\tau_{ref} = 0.126$ Pa): a wall flow around the stockpile, b wall flow over the stockpile.	125
Figure A5-32: Airflow topology over the stockpile – three dimensional streamlines($\beta = 90^\circ$): a Fluent results [4], b OpenFOAM results ($U_0=9.1$ m/s).	126
Figure A5-33: Airflow topology over the stockpile – path lines release from the ground (leeward)($\beta = 90^\circ$): a Fluent results [4], b OpenFOAM results ($U_0=9.1$ m/s).....	127
Figure A5-34: Airflow topology around the stockpile – streamlines in transversal plane ($x/h = 2.25$) for $\beta = 90^\circ$; Fluent results [4].	128
Figure A5-35: Airflow topology around the stockpile – streamlines in transversal plane ($x/h = 2.25$) for $\beta = 90^\circ$ and $U_0=9.1$ m/s; OpenFOAM results.....	128

Figure A5-36: Airflow topology around the stockpile – plot of non-dimensional wall shear stress in transversal plane ($x/h = 2.25$) ($\beta = 90^\circ$): a Fluent results [4], b OpenFOAM results ($U_0=9.1$ m/s).....	129
Figure A5-37: Airflow topology over the stockpile – three dimensional streamlines($\beta = 60^\circ$): a Fluent results [4], b OpenFOAM results ($U_0=9.1$ m/s).	130
Figure A5-38: Airflow topology around the stockpile – streamlines in transversal plane ($x/h = 2.875$) for $\beta = 60^\circ$; Fluent results [4].	131
Figure A5-39: Airflow topology around the stockpile – streamlines in transversal plane ($x/h = 2.875$) for $\beta = 60^\circ$ and $U_0=9.1$ m/s; OpenFOAM results.....	131
Figure A5-40: Airflow topology over the stockpile – plot of non-dimensional wall shear stress in transversal plane ($x/h = 2.875$) for $\beta = 60^\circ$: a Fluent results [4], b OpenFOAM results.	132

Part B - Calibration of Irwin probes

Figure B2-1: Schematic of experimental apparatus – top view (dimensions in meters).....	158
Figure B2-2: Experimental apparatus.	158
Figure B2-3: Placement of the used <i>Preston</i> tube.	161
Figure B2-4: <i>Irwin</i> probes (red dots) positioning. Test section with mean pressure sections (dashed lines) and static pressure taps (black dots) (in addition, see Figure B2-1) (dimensions in meters).	162
Figure B3-1: Computational domains (left – constant section duct; center – divergent duct; right – convergent duct).	164
Figure B3-2: Typical mesh (M7) with <i>simpleGrading</i> for one-quarter of the cross-section (constant section case).....	165
Figure B3-3 Mesh independency test - cross-section mean velocity. a cavity case; b pitzDaily case.....	166
Figure B3-4 Mesh independency study - near wall vertical velocity profile.	167
Figure B4-1: Normalized standard deviation (symbols – left vertical axle) and absolute deviation (bars – right vertical axle) of the repeatability tests: a) Mean static pressure and b) <i>Irwin</i> probe (Top face at $x/L_{max}=0.64$).	171
Figure B4-2: Influence of the Reynolds number on the pressure coefficient at $x/L_{max}=0.20$ (All cases).	173
Figure B4-3: Pressure coefficient distribution along the streamwise direction of the duct for different values of Re. (Case AR3 and Case AR4).....	173
Figure B4-4: Comparison of the present experimental data against smooth circular tube predictions [43] – Equation (B4-1).	174
Figure B4-5: Assessment of the influence of the characteristic length scale on the friction coefficient; markers correspond to the experimental values and lines (legend) represent values obtained with a semi-empirical relation [26] – Equation (B1-4).	176
Figure B4-6: Influence of the Reynolds number on the local friction coefficient at $x/L_{max}=0.60$ (case AR3), obtained through <i>Preston</i> measurements.	177
Figure B4-7: Assessment of longitudinal placement (a) and b)), transversal placement (c)) and comparison between top and bottom faces (d)) on the pressure measurement by the <i>Irwin</i> probes.	179
Figure B4-8: Calibration curve for the <i>Irwin</i> probes located at $x/L_{max} = 0.64$ (hollow markers correspond to top face and filled markers to the bottom face).	181
Figure B4-9: Comparison between experimental and correlated values of the wall shear stress; lines correspond to the calibration curve, Equation (B4-3), and markers were obtained with Equation (B1-9).....	182
Figure B4-10: Calibration curve for the <i>Irwin</i> probe located at $x/L_{max} = 0.60$ using <i>Preston</i> tube measurements for case AR3.	182
Figure B4-11: Comparison of the friction coefficient obtained through the measurements of the <i>Preston</i> tube (Equation (B2-2)) and the <i>Irwin</i> probe calibration curve (Equation (B4-4)) for case AR3.	183
Figure B4-12: Comparison of the calibration curves for the <i>Irwin</i> probe ($x/L_{max} = 0.60$) obtained using the <i>Preston</i>	

tube measurements (Equation (B4-4)) and the force balance for case AR3 (Equation (B4-5)).	183
Figure B4-13: Comparison of the experimental wall pressure distribution along the rectangular duct (case AR3) with OpenFOAM and CFX predicted values ($U_0=16.7$ m/s).	184
Figure B4-14: Wall pressure distribution. a) Velocity of $0.6 U_{max}$, b) Velocity of $0.3 U_{max}$.	185
Figure B4-15: Influence of the <i>Reynolds</i> number on the friction coefficient. <i>Preston</i> measurements against predicted values using OpenFOAM and CFX (Case AR3).	186
Figure B5-1: Schematic of experimental apparatus – Side View (dimensions in meters).	190
Figure B5-2: Experimental pressure coefficient distribution against predicted values by OpenFOAM and by CFX.	191
Figure B5-3: Influence of the Reynolds number on the friction coefficient. <i>Preston</i> measurements against predicted values using OpenFOAM and CFX and a power function.	192
Figure B5-4: Calibration curve for the <i>Irwin</i> probe located at $x/L_{max}=0.60$.	194
Figure B5-5: Comparison of the calibration curves (Table B5-3) for the <i>Irwin</i> probe located at $x/L_{max}=0.60$. Two different ranges of <i>Irwin</i> probe pressure difference (Δp_I): tested range in each case (left) and wider range (right).	195
Figure B5-6: Comparison of the friction coefficient obtained through the <i>Preston</i> tube and the <i>Irwin</i> probe.	195

LIST OF TABLES

Part A - Numerical and experimental study of granular piles when subjected to wind erosion

Table A3-1: Main meshes parameters ($U_0=9.9$ m/s).	63
Table A3-2: OF predefined solver characteristics.	65
Table A4-1: Main characteristics of the configurations used in the triangular pile study case.	69
Table A4-2: c_p repeatability tests: mean absolute deviation [%] for all cases and for $U_0=9.9$ m/s.	71
Table A4-3: Values of threshold friction velocity (calculated using Equation (A1-4) and observed experimentally (Figure A4-19)).	86
Table A4-4: Coefficient c_y for each saltation model and for each case.	88
Table A5-1: Repeatability tests: deviation and normalized deviation [%] of the measuring system.	99
Table A5-2: Repeatability tests: deviation [%], normalized deviation [%] and absolute deviation [mm] of the pile construction device.	100
Table A5-3: Main characteristics of the oblong piles used in Fluent (Furieri et al. [4]) and OpenFOAM.	118
Table A5-4: Analysis of the normalized distance between vortices (d_v/h) for the case with $\beta = 90^\circ$	123

Part B - Calibration of Irwin probes

Table B2-1: Entrance length for all cases.	160
Table B3-1: Structured meshes characteristics.....	165
Table B4-1: Main characteristics of the configurations with constant section.	170
Table B4-2: Mean relative errors for all cases (%).	175
Table B4-3: Local friction coefficient (at $x/L_{max} = 0.60$, for the maximum velocity - Table B4-1) predicted by OpenFOAM and by CFX and deviation relatively to <i>Preston</i> measurements.	186
Table B4-4: Local friction coefficient ($cf_x \cdot 10^3$) ($x/L_{max} = 0.56$) predicted by OpenFOAM and deviations from <i>Preston</i> measurements for two different velocities ($0.6 U_{max}$ and $0.3 U_{max}$).	187
Table B5-1: Main characteristics of the tested configurations (constant and variables sections).	190
Table B5-2: Local friction coefficient (at $x/L_{max} = 0.60$, and for the maximum velocity - Table B5-1) predicted by OpenFOAM and by CFX and deviation relatively to <i>Preston</i> measurements.	193
Table B5-3: Calibration curves, and respective R-square coefficient, for the <i>Irwin</i> probe located at $x/L_{max} = 0.60$	194

LIST OF ACRONYMS

2D	Two-dimensional
3D	Three-dimensional
ADAI	Association for the Development of Industrial Aerodynamics-University of Coimbra, Portugal
AR	Aspect Ratio
CFD	Computational Fluid Dynamics
CNC	Computer Numerical Control
CV	Control volume
DEM	Discrete Element Method
DES	Detached Eddy Simulations
DNA	Deoxyribonucleic acid
DNS	Direct Numerical Simulations
FDM	Finite Difference Method
FEM	Finite Element Method
FVM	Finite Volume Method
ISEC	Coimbra Institute of Engineering
LAI	Industrial Aerodynamics Laboratory
LES	Large Eddy Viscosity
OF	OpenFOAM® - Open Source Field Operation and Manipulation
RANS	Reynolds Averaged Navier Stokes Equations
RNG	Re-Normalized Group
RSM	Reynolds Stress Model
SST	Shear Stress Transport
USEPA	United States Environmental Protection Agency
V&V	Verification and Validation
VIM	International Vocabulary of Metrology

LIST OF SYMBOLS

Symbol	Units	Description
a	m	Longitudinal distance
A	-	Dimensionless coefficient (Bagnold [18])
A	m ²	Emission area
c_p	-	Pressure coefficient
c_y	-	Empirical parameter of Shao [15] model
C_{01}	-	Empirical constant of the Owen's saltation model
C_{02}	-	Empirical constant of the Owen's saltation model
C_B	-	Empirical constant of the Bagnold's saltation model
C_K	-	Empirical constant of the Kawamura's saltation model
C_L	-	Empirical constant of the Lettau and Lettau's saltation model
d	m	Grain diameter
D	m	Duct diameter
D	m	Reference grain diameter
d_p	m	Outside diameter of the <i>Preston</i> tube
d_v	m	Distance between the centers of the vortices
D_h	m	Hydraulic diameter
D_L	m	Laminar equivalent diameter
EF	g m ⁻² /year	Emission factor
F	kg m ⁻² s ⁻¹	Dust emission rate
\vec{F}	N	Force
g	m s ⁻²	Gravitational acceleration

h	m	Initial pile crest height
$h_{average}$	m	Average height of five measurements
$h_{measured}$	m	Measured height
H	m	Rectangular duct height
k	$m^2 s^{-2}$	Turbulent kinetic energy
k	-	Particle size multiplier
L	m	Length
l^*	m	Characteristic length scale
l_e	m	Entrance length
l_{salt}	m	Saltation length
L_c	m	Characteristic length
L_{max}	m	Maximum length
m	kg	Mass of the impacting particle
m_{Ω}	kg	Mass ejected by bombardment
N	-	Number of disturbances per year
p	Pa	Static pressure
P	Pa	Soil plastic pressure
P	m	Wet perimeter
p_{ref}	Pa	Reference static pressure
P_i	$g m^{-4}$	Erosion potential corresponding to the observed fastest mile of wind for the i -th period between disturbances
q	$kg m^{-1} s^{-1}$	Saltation (or streamwise) flux
Re	-	Reynolds number
R^2	%	R-square coefficient

S_i	m^2	Pile surface area
t	s	Time instant
u	m s^{-1}	Mean longitudinal velocity component
U	m s^{-1}	Axial mean velocity
u_{10}^+	m s^{-1}	Fastest mile value corrected to a reference anemometer height of 10 m
u_r	m s^{-1}	Reference velocity at 10 m height from the ground
u_s	m s^{-1}	Wind speed measured at 25 cm from the pile's surface
u_*	m s^{-1}	Friction velocity
u_{*t}	m s^{-1}	Threshold friction velocity on a flat bed
$u_{*t\theta}$	m s^{-1}	Threshold friction velocity on a surface with a slope angle θ
U_0	m s^{-1}	Undisturbed wind speed
U_{max}	m s^{-1}	Maximum flow velocity
U_t	m s^{-1}	Threshold undisturbed wind velocity
$U_{t\theta}$	m s^{-1}	Threshold undisturbed wind velocity for a tilted surface
V	m^3	Removed volume
w	m	Rectangular duct width
w_s	m s^{-1}	Settling velocity
x	m	Coordinate aligned with the undisturbed velocity
y	m	Distance to the closest wall
y^+	-	Dimensionless wall distance
z	m	Vertical distance above the ground
z_0	m	Aerodynamic roughness parameter

Greek letters

Symbol	Units	Description
α	°	Angle of repose
α_b	m ⁻¹	Sandblasting efficiency
α_v	-	Exponent of the velocity profile
β	°	Wind incidence angle
γ	-	Function of Shao [15] model
Δ	-	Severity of the pressure gradient parameter
δ	m	Boundary layer thickness
Δp	Pa	Pressure difference
Δp^+	-	Normalized pressure difference (<i>Preston</i> tube)
Δp_I	Pa	Pressure difference in the <i>Irwin</i> probe
Δt	s	Time interval
ε	m ² s ⁻³	Rate of dissipation of turbulence energy
ε	m	Absolute roughness
η	m	Bed elevation relative to a fixed level
η_c	-	Mass fraction resulting from aggregate disintegration
η_f	-	Total fraction of dust, which can be released from an unit of mass
η_m	-	Fraction of free dust
θ	°	Slope angle
κ	-	Von Kármán's constant
λ_p	kg m ⁻³	Bed porosity
ν	m ² s ⁻¹	Fluid kinematic viscosity

ρ	kg m ⁻³	Air density
ρ_b	kg m ⁻³	Bulk sand density
ρ_s	kg m ⁻³	Sand grain density
σ	-	Standard deviation of the measurements
σ_m	-	Bombardment efficiency - ratio between the mass ejected by bombardment (m_Ω) and the mass of the impacting particle (m)
σ_p	-	Free dust to aggregated dust ratio
τ^+	-	Normalized wall shear stress (<i>Preston</i> tube)
τ_{max}	Pa	Maximum value of the wall shear stress
τ_{ref}	Pa	Reference value of the wall shear stress
τ_w	Pa	Wall shear stress
ϕ	-	Generic variable
$\phi^*(w/h)$	-	Geometric function
Φ	kg m ⁻² s ⁻¹	Sand emission rate
ω	s ⁻¹	Specific turbulence rate

INTRODUCTION

The aim of the present work is to study the behavior of granular material stockpiles when subjected to wind erosion, for which both experimental tests and numerical simulations were performed. Regarding the experimental component, several tests were made, in particular, erosion experiments, where the evolution of the free surface of triangular and oblong piles was analyzed and the emission rate estimated. In addition, for the triangular configuration, tests were performed to obtain the static pressure and the wall shear stress distribution.

The numerical tool chosen to perform the simulations was the CFD open-source package OpenFOAM (OF) and the validation of the numerical model was performed against the results obtained in the experiments, as well as, in the case of the oblong piles, against a study performed by other authors, who employed a different CFD tool and oil film visualization.

Given the importance of the experimental data, not only in the assessment of the piles' behavior, but also due to its use in the model validation, the accuracy of the results should be attested. In view of the type of used equipment during the experimental tests, it was considered that the *Irwin* [1] probes deserved special attention and a new set of probes was constructed and calibrated. The developed study with these probes was so extensive and innovative that it was considered to deserve due attention, therefore, this additional work gave

rise to Part B of this thesis.

To perform the calibration of the probes a rectangular duct was fabricated, with six different configurations: four different constant cross-sections and two variable cross-sections (convergent and divergent) with a slope of 1° . Taking into account the versatility of the duct, in addition to the calibration of the probes, some questions were also addressed about the flow over rectangular sections, such as entrance length, symmetry, secondary flow or behavior when subjected to pressure gradients.

In summary, the present thesis is divided into two parts: Part A, which deals with the study of granular bed when subjected to wind erosion, and Part B where the flow through rectangular ducts is addressed and the calibration of the shear stress probes is performed.

In what concerns this "Introduction", it opens with the motivation behind the present work; it reports the main reasons that led to the present study which, among others, are related to the public health hazards due to particle emissions and/or economic and environmental impacts of the wind erosion.

In what follows, the research framework and the main goals of the entire work are presented, which include the objectives outlined for Part A, which deals with the piles of granular material, and for Part B, which is primarily devoted to the *Irwin* probes calibration. Moreover, the main contributions to the scientific field with the outcomes of this work are summarized. The structure of the present document is described in the Thesis outline section.

MOTIVATION

The transport of soil particles by wind is of high relevance in a wide range of areas from those related to agriculture (e.g., seed transport) to the formation and modification of the landscape, in particular, the typical example of sand dunes, which can be formed, moved, or entirely eroded due to aeolian processes. To be able to predict the phenomena associated with wind erosion is a major priority in the prevention of potential major threats such as, transportation safety, desertification, human health (air quality) and, even, climate changes.

At an industrial level, the knowledge of the phenomena of wind erosion is also very important, for instance in the electrical energy production sector, in particular the coal-fired power plants, where coal and resulting ashes are stored in open yards. To be able to predict the interaction between the wind and such granular stockpiles is important in economic and environmental terms.

In what concerns, coal-fired power plants, the coal is frequently transported over considerable

distances in open wagons yielding substantial losses [2]. Moreover, the coal stockpiles are also subjected to wind erosion leading to further losses and lowering of air quality, as the aeolian transport of the coal particles may extend their impact to several kilometers. In particular, when urban areas are affected, these particle emissions can become a public health hazard. Coal is a mixture of compounds and contains mutagenic and carcinogenic polycyclic aromatic hydrocarbons, and is considered as an important non-cellular and cellular source of reactive oxygen species that can induce DNA damage. Ultimately, the susceptibility to black lung around coal stockpiles increases due to the fact that coal is a respiratory toxicant [3].

To sum up, the environmental impacts, as well as the economic aspects, and regulation constraints related to wind erosion, motivate current efforts to model and quantify erosion.

One of the major obstacles to determine the dust emission is the high number of variables that are involved in this process. So, when the path is a theoretical or numerical approach, frequently several simplifications are assumed. If an empirical method is used, usually is restricted to a local, and due to that only includes a limited range of working conditions [3].

One of the empirical methods that are commonly employed is the, relatively simplified, methodology proposed by the United States Environmental Protection Agency (USEPA), which uses some data derived from wind tunnel studies, and shows a noticeable influence of the pile geometry and wind direction on the velocity distribution over the piles. The estimation of emission of particles is calculated for a limited group of pile shapes (conical and oval with flattop, and 37-degree side slope), flow directions and only during specific erosion events, such as bursts, when in reality emissions occur in many other occasions, thereby making this approach restrictive.

The USEPA methodology is focused in the velocity distribution near the stockpile surface, neglecting the flow topology and the wall shear stress distribution over and around the piles, both with influence on the particles emission phenomena. Considering the industrial sites, the understanding of near-wall flow behavior is essential when dealing with potential emissions of particles due to material handling and transportation. As reviewed by Furieri et al. [4], the airflow characteristics over and around piles are yet not fully known. Although there is a considerable body of literature dealing with the disturbance of the turbulent wind flow by obstacles, like buildings of several configurations; however, research directly related to the flow topology around stockpiles is rather scarce.

Often, wind erosion models, e.g., Zhang *et al.* [5], are not appropriate either due to their reliance on empirical modeling or due the amount of data required. Moreover, the influence of topography and different roughness levels resulting from diverse landscapes on the wind fields is almost impossible to measure at different scales with traditional methods. Numerical simulations prove to be an important way to study and model wind fields at different scales, as computational fluid dynamics (CFD) has been proven to be a cost-effective and powerful technology [5].

Over recent decades, the CFD approach is becoming widely used in wind erosion or related issues research. Studies over the role of pile shape or configuration and influence of flow conditions in the dust emission were carried out by Badr and Harion [6], Toraño et al. [7], Ferreira and Lambert [8], Furieri et al. [9], Furieri et al. [4], among others. Furieri et al. [10] predicted numerically the friction velocity distribution to evaluate the contributions of the pile surroundings to the total emission from an open stockyard. The effect of the non-erodible elements in aeolian research was investigated by Badr and Harion [11]. Many other related studies could be listed here, as the CFD is broadly used in this investigation area.

Most CFD codes with wide distribution are typically of types: commercial or open source. Their main differences are related to available documentation, user interface, cost and adaptability. Despite the lack of documentation that characterizes the open source software, usually there are large communities, which provide help. Commercial codes are, supposedly, easier to handle due to their user-friendly graphical interfaces, but are quite expensive. Besides being free of charge, the key advantage of the open source software is the fact that is open for enhancements and adaptation to different applications. This feature, which is freely exchanged, makes the open source software very appealing to the scientific community.

Open source CFD models are not yet extensively employed in wind erosion research; however, there are other research areas, such as the chemical engineering, marine science and industrial design, just to name a few, where they are already making considerable inroads. The wide application of open source CFD modeling demonstrates its powerful capability [5].

The lack of an appropriate methodology to study the airflow over and around stockpiles and consequent particle emissions over time led to the focus of the current project. Its aim is to understand the evolution of the free surface and, in this way, to contribute to the accuracy of the aeolian erosion prediction method. In order to accomplish it, a study will be conducted to analyze the flow features over 3D piles and their vicinity, and to observe the behavior of stockpiles free surface, when subjected to aeolian erosion mechanisms.

During the course of this work several configurations will be investigated, with increasing geometry complexity. The triangular geometry was chosen since, besides data being already available (Faria et al., [12]), new data obtained experimentally, will be used for the numerical model validation. Among the 3D configurations, the oblong geometry will be considered, since it is representative of coal stockpiles, commonly found in industrial sites [4].

RESEARCH FRAMEWORK

The experimental tests were carried out in the wind tunnel of the Industrial Aerodynamics

Laboratory (LAI) – a facility owned and operated by ADAI (Association for the Development of the Industrial Aerodynamics-University of Coimbra, Portugal).

Over the years, the ADAI team has developed considerable expertise in the area of Wind Engineering through numerous R&D projects. ADAI relevant publications to the present work are those addressing the free surface modeling of a loose granular bed exposed to wind flow, namely, e.g., Faria et al. [12], Ferreira and Fino [13], Ferreira and Lambert [8], Ferreira and Vaz [2] and Lopes et al. [14].

MAIN GOALS

The main goal of this study is assess the airflow characteristics over and around granular material 3D piles when subjected to wind erosion. However, there are several milestones that should be met toward this goal, having each one of them its own purpose. Therefore, the goals to be pursued within the context of the present project are:

- Triangular piles:
 - After proper familiarization with the CFD tool OpenFOAM (OF), benchmark the numerical model with the experimental data taking into account the pressure distribution, as well as the wall shear stress obtained with the *Irwin* [1] probes, along triangular piles;
 - Correlate the outcomes of the numerical model with the development of the erosion profiles;
 - Use Shao's [15] dust scheme to model sand emission flux, after proper calibration and selection of a suitable saltation model.
- Oblong piles:
 - Evaluate the behavior of such piles in what concerns the deformation of the free-surface, as well as the sand emission rate, when subjected to different undisturbed wind velocities and wind incident angles;
 - Study the airflow characteristics over a single oblong pile and in its surroundings for various wind velocities and incidence angles;
 - Benchmark the numerical model employed in the CFD tool OpenFOAM with the experimental data and studies from other authors, who employed a different CFD tool and oil film visualization.
- Rectangular duct:
 - Assess the applicability of *Irwin* [1] probes to measure the wall shear stress of fully developed, incompressible fluid flow in smooth-walled ducts of rectangular

- cross-section; and under pressure gradient conditions;
- Calibrate the *Irwin* [1] probes in different scenarios, i.e., under constant, adverse and favorable pressure gradients, with the aim of giving confidence to the measurements made on the triangular piles;
- Benchmark the OpenFOAM outcomes against other CFD tool, namely, ANSYS – CFX.

MAIN CONTRIBUTIONS

The main contribution of the present work is assessing the behavior of granular material 3D piles when subjected to wind erosion and of the airflow features over and around stockpiles. Aiming to fulfill the main goal of this work, several stages were accomplished; the following are the specific contributions of each one in the development of this thesis:

- Assessment of the applicability of the OpenFOAM in wind erosion applications, more specifically, in 2D transverse and 3D piles. Both triangular and oblong configurations were benchmarked against experimental data;
- Assessment of the interaction between the wind flow and the granular triangular piles. Influence of both slope angle and crest height on the pressure and friction coefficients was evaluated. Free surface deformation was monitored and then sand emission rate was calculated.
- Use of the calibrated Shao's [15] dust scheme to model sand emission flux with appropriate saltation model, namely, Lettau and Lettau's [16] model;
- Design and develop a device that allows oblong piles to form naturally for the experiments in the wind tunnel. Repeatability tests were performed to evaluate the precision of the pile shape;
- Evaluation of the influence of both wind velocity and incidence angle in the behavior of oblong piles, specifically, two different wind velocities and two different wind incidence angles;
- Assessment of potential areas of particles emission through the characterization of the airflow topology over and around oblong piles combined with the identification of high friction zones;
- Calibration of the *Irwin* probes, in order to assure the accuracy of the experimental results used in the numerical model validation. In addition, it was verified the applicability of *Irwin* probes to turbulent incompressible flow in smooth rectangular ducts. Six different configurations were used: constant cross-section with four aspect

ratios and variable cross-section, both convergent and divergent with 1° slope.

THESIS OUTLINE

As mentioned above, the thesis comprises two parts and it is organized as follows:

Part A- Numerical and experimental study of granular piles when subjected to wind erosion

Part A is focused on the main subject of the present work, which is the study of granular beds when subjected to the wind, and it is divided in six chapters as follows:

Chapter A1. Introduction

This is the introductory chapter where concepts and definitions that will be used along the thesis, are presented. In addition, the main reasons that justify the choice of OpenFOAM as the CFD tool used to perform the numerical simulations are discussed. The related literature is reviewed to evaluate the state of the art.

Chapter A2. Experimental setup

The present study includes a significant experimental component, which consists of erosion, wall shear stress and static pressure tests. The main characteristics of the facilities (wind tunnel) and material (sand) are presented. Moreover, the tested configurations - triangular and oblong piles, are described. Finally, the procedure and main features of the experimental tests are discussed.

Chapter A3. Numerical modeling

Besides the experimental tests, numerical simulations were also performed. Main features, assumptions and methodology are presented in this chapter. The selected CFD package, OpenFOAM, is summarily described and general considerations on the model verification and validation are given. In addition, it is reported the parameters employed in the numerical simulations.

Chapter A4. Triangular piles

As already mentioned, two different pile configurations were studied, and in this chapter, the triangular case is reported. It opens with the case description, where the main characteristics and parameters of the study are presented. Then the experimental and numerical results are discussed, and their comparison is evaluated. At the end of the chapter, the principal conclusions are made and the main findings commented.

Chapter A5. Oblong piles

This chapter has a structure similar to the previous one, considering that the same type of experiments and simulations were performed in both cases. Therefore, it starts with the description of the case, presenting the key characteristics and parameters; followed by the presentation and analysis of the results. As a closure, the main findings for oblong pile study are presented.

Chapter A6. Conclusions

The overall conclusions and findings concerning granular beds and their behavior when subjected to the wind are reported in this chapter.

Part B Calibration of Irwin probes

As mentioned in Part A, experimental tests were performed, and for the shear stress measurements, *Irwin* probes were used. With the aim of giving further credibility to the experimental results, the calibration of the *Irwin* probes was performed, as described in Part B. In addition, since the calibration was performed in a rectangular duct, it was required a more in-depth study to understand the secondary flows occurring in ducts of rectangular cross-section. Part B is organized as follows:

Chapter B1. Introduction

Along with the main goals of Part B, some introductory concepts are presented in what concerns flow in rectangular ducts. In addition, a few considerations about entrance region and wall shear stress are made.

Chapter B2. Experimental program

A plywood duct of rectangular cross-section was designed and built within the scope of the present work and it is described in this chapter. Some considerations and results concerning the entrance length are also discussed. The description of the probes used in the study - *Irwin* probe and *Preston* tube, is presented.

Chapter B3. Numerical setup

Similarly to Part A, the numerical simulations were performed using the open source CFD code OpenFOAM. The major features of the simulations, in particular computational domain, mesh parameters and the setup for the cases studied - rectangular duct with constant section and with variable section, are presented. The mesh dependency study is also discussed.

Chapter B4. Rectangular duct with constant section

The rectangular duct with constant cross-section, including its measurement equipment, is characterized. In the context of the experimental results, the repeatability and accuracy of the probes are discussed. In addition, the calibration of the *Irwin* probes was conducted and their performance along the length of the duct is analyzed. The numerical results obtained with OpenFOAM are compared against ANSYS CFX results, and the two sets are evaluated against

the experimental results. Considerations on Reynolds dependency are also given. Conclusions are presented at the end of the chapter.

Chapter B5. Rectangular duct with variable section

The structure of this chapter is similar to the previous one. First, the study case is described, and the main parameters are presented. Then, the results are analyzed and the comparison of the experimental measurements against the numerical predictions is evaluated. In addition, the calibration of the *Irwin* probes in the presence of pressure gradients is discussed. The chapter closes with the presentation of the main findings.

Chapter B6. Conclusions

Like Chapter A6, the final remarks of the study of flow through ducts of rectangular cross-section, and in particular the calibration of the *Irwin* probes, are presented.

Finally, a common chapter to both parts (A and B), named, “**Closure**”, presents an overview of the present work and it summarizes its main findings. Suggestions for future research work are also advanced.

PART A

NUMERICAL AND EXPERIMENTAL STUDY OF GRANULAR PILES WHEN SUBJECTED TO WIND EROSION

CHAPTER A1

INTRODUCTION

This is the introductory chapter of Part A, and it starts by presenting some introductory concepts and definitions that will be used in the present work (Section A1.1). They will cover granular material (Section A1.1.1), aeolian transport mechanisms (Section A1.1.2) and wind erosion (Section A1.1.3). In the latter, it is presented the friction velocity, which is a crucial variable in the understanding of aeolian processes and soil erosion. In addition, selected formulations among those most frequently used in aeolian studies are given for horizontal and vertical fluxes, as well as for saltation fluxes. In addition, these formulations will be employed in the estimation of the normal flux using the Shao's dust scheme.

In Section A1.2 , it is discussed the main reasons that justify the choice of OpenFOAM as the CFD tool to perform the numerical simulations.

Finally, in Section A1.3, it is made a state-of- the-art review of work relevant to the present investigation.

A1.1. INTRODUCTORY CONCEPTS

Concepts and definitions used in this thesis are presented in this section. Considering that the study of sand piles represents a major share of the investigation conducted, the classification of granular material along with some of its characteristics is presented. Subsequently, the main aeolian transport mechanisms are introduced and some variables and features of wind erosion are discussed.

A1.1.1. GRANULAR MATERIAL

Granular media are systems with a large number of particles and its constituents should be large enough so that they are not subject to thermal motion fluctuations [17]. Thus, the lower size limit for grains in granular material is about 1 μm .

Some examples of granular material are sand, snow, coal, fertilizers, cereals and other types of food, pharmaceutical products, several materials used in metallurgy (e.g., ceramic and metal powders), among others. In fact, they are ubiquitous materials in almost every human activity, with commercial significance in applications as diverse as pharmaceutical industry, agriculture or energy production, so of great economic relevance in the industrial sector.

Thus, research in granular materials is of high importance and has a wide applicability. Some of the first studies were of Charles-Augustin Coulomb, with its law of friction that was originally stated for granular materials. However, *The Physics of Blown Sand and Desert Dunes* [18] written by one of the pioneers of the physics of granular material - the soldier/physicist Brigadier Ralph Alger Bagnold, still is an important reference to the present day.

The evolution of the experimental and numerical techniques, especially in the recent years, made the granular media a target of great and renewed interest by the scientific community. Consequently, leading to a clear advance in the understanding of certain phenomena, like its behavior on a large-scale state, since they behave differently than solid, liquids or gases, taking many to characterize granular materials as a new form of matter; or some interesting characteristics from a small scale point of view, like collisions, which open up broad prospects for new and exciting research.

Besides the obvious interest of the industrial sector in the understanding of the behavior of the granular materials, there are evident applications in the geology and ecology domains, such as understanding of avalanche dynamics, the movement of dunes or displacement of snowflakes.

The transport and movement of the granular material are caused or influenced, by its

interaction with the wind. Aeolian processes represent an important role in landscape changes, since they are responsible for the development of aeolian dunes, sand sheets or erosive structures [19–22]. Still, they may cause serious damage in transportation, communications and severe environmental problems, such as desertification, degradation of air quality due to dispersion of pollutants from stockpiles, and even climate changes [e.g. ,2,23]

Thus, the capability of forecasting natural disasters can avoid the loss of material goods and ultimately loss of life. However, the study of the wind behavior, and more specifically its interaction with the Earth surface, can be very complex. There are many factors to be considered beyond the fact that, typically, the wind flow is 3D and turbulent.

A1.1.2. AEOLIAN TRANSPORT MECHANISMS

The motion of wind-driven granular material are classified in the pioneering work of Bagnold [18] into three distinct mechanisms, namely, suspension, saltation and creep, as depicted in Figure A1-1.

The transport mechanism adopted by each particle depends essentially on its diameter. Suspension is the typical mechanism for small particles, usually with diameters between 60 and 70 μm , as it is the case of clays and silts, and it is characterized by higher and longer trajectories.

The typical diameter range of the particles that move by saltation is between 60 and 500 μm (fine and medium grains). They travel short distances, and the trajectories are characterized by being initially very steep followed by a parabolic path, which makes them to return to the soil with relatively small angles, as depicted in Figure A1-1.

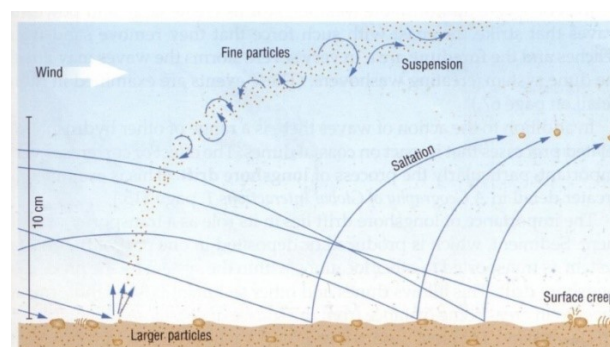


Figure A1-1: Aeolian transport mechanisms¹.

¹ <http://www.mrstevennewman.com>

Figure A1-2 displays schematically the forces involved in the saltation mechanism.

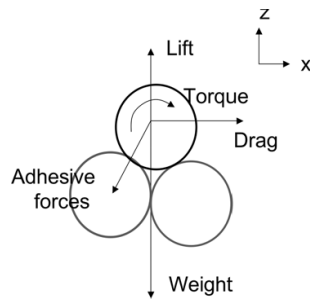


Figure A1-2: Balance of forces applied to a particle subject to aerodynamic forces and cohesion².

The aeolian transport of medium and coarse grains (diameter > 500 μm) is carried out mainly by creep. This mechanism is the one with the shortest trajectories. The movement of the particles is mainly due to impacts between the saltating grains and the surface (bombardment) - in this way, the kinetic energy of the saltating particles is transferred to the particles resting on the surface.

Considering the main transport mechanisms, the sand drive occurs essentially in a layer close to the ground with a typical thickness of 20-30 cm. The thickness of the layer is inversely proportional to the average diameter of the particles in movement.

A1.1.3. WIND EROSION

Wind is one of the most important natural contributors to geomorphological changes in both coastal and deserts regions, not only on Earth, but also on Mars, and possibly other planets [24].

Aeolian erosion of soils can influence not only the surface features but also the biological potential of the soils. Topographic changes can occur, like the formation or movement of dunes, and ecosystems can be put in jeopardy due to sandblasting of plants. Additionally, soil nutrients transportation by the wind can work for or against the biological potential of the soils (desertification). Furthermore, the suspended dust can alter the radiative properties of atmosphere, mostly by backscattering the received solar radiation [25].

² <http://www.informaworld.com>

The wind flow over complex terrain is very difficult to determine, essentially due to the considerable number of possible scenarios that can occur. Wind erosion depends strongly on the local wind flow characteristics and it is considerably affected by flow field changes caused by any modifications in terrain geometry. Thus, the recommended approach to their investigation is starting with simple configurations and known flow field and gradually increasing the complexity of the modifications [26]. In the past, several studies were conducted considering different scales and using diverse methods, from field case studies, to experimental and numerical simulations [26].

Besides Bagnold [18], numerous other investigators have been fundamental to a better understanding of the physics of wind-blown sand, like Iversen and Rasmussen [27], White and Tsoar [28], Dong *et al.* [24], among others.

The acquaintance of the existing interactions and of the several mechanisms existent in dust emissions is essential and very complex to achieve because of nonlinear and threshold processes involved. The knowledge of threshold friction velocity is very essential, since it controls not only the frequency but also the intensity of the erosion occurrences [25].

A1.1.3.1. FRICTION VELOCITY (u_*)

According to several authors, e.g. Iversen and Rasmussen [27], threshold friction velocity, defined as the minimum shear velocity required for the aerodynamic forces to overcome the opposing ones, is the crucial variable in the understanding of aeolian processes and soil erosion. Considerable research has been conducted on this parameter through theoretical analyses, wind-tunnel experiments and field investigations as reviewed by Huang *et al.* [20]. The present work will be on the analysis of loose or distributed soils, and in this case, as studied by Marticorena and Bergametti [29], Marticorena *et al.* [25], among others, the influence of the surface roughness and, consequently the aerodynamic roughness height, is the most important parameter that controls threshold friction velocity. But this parameter is affected by several other factors, such as surface moisture, specificities of the crust or vegetation characteristics [12].

Although great advances have been made, almost all studies refer to flat bed. Bagnold [18] derived the following equation for the threshold friction velocity:

$$u_{*t} = A \times \sqrt{\frac{\rho_s - \rho}{\rho} g d} \quad (\text{A1-1})$$

where u_{*t} [m s^{-1}] is the flat bed threshold friction velocity, ρ_s and ρ [kg m^{-3}] are the densities

of the granular material and of the air, respectively, d [m] is the grain diameter, g [m s^{-2}] is the gravitational acceleration and A is a general coefficient, that is nearly constant with the value of 0.1 in the case of air [18]. Equation (A1-1) is valid for particles with diameters greater than 100 μm , since it describes only the balance between drag and gravity forces. Greeley and Iversen [30] have considered lift and cohesive forces, thus obtaining a relation with a wider range of applicability. Other authors derived appropriate relations to estimate the threshold friction velocity, as mentioned by Faria et al. [12].

Experimentally the friction velocity can be obtained using wall shear stress probes, e.g., *Irwin* [1] probes (further details can be found in Section A2.4.3). The wall shear stress (τ_w) is related to the friction velocity, as follows:

$$u_* = \sqrt{\frac{\tau_w}{\rho}}, \quad (\text{A1-2})$$

The wall shear stress is commonly presented in the form of the friction coefficient (c_f) - a dimensionless parameter defined by the following expression:

$$c_f = \frac{\tau_w}{\frac{1}{2}\rho U_0^2} \quad (\text{A1-3})$$

where U_0 is the undisturbed wind velocity [m s^{-1}].

Bed slope is also an important factor to be considered in the study of particle entrainment processes, since most natural sand surfaces are not horizontal. Howard [31], among others, performed a theoretical analysis of the effects of slope on the threshold friction velocity. Based on this analysis, and neglecting some parameters [31], the threshold friction velocity ($u_{*t\theta}$) for initiation of the movement of a particle resting on a surface with a slope angle θ is given by:

$$u_{*t\theta} = \sqrt{u_{*t}^2 \left(\cos \theta + \frac{\sin \theta}{\tan \alpha} \right)}, \quad (\text{A1-4})$$

where α is the angle of repose that is defined as the steeper angle at which a pile of dissociated granular material is stable, i.e., without sliding, and it is controlled by the friction between grains. Particle size, roughness of the surface of the particle, sphericity of the particle, moisture and the uniformity of the pile, are some of the parameters that can influence the angle of repose.

Bagnold [18] also derived the threshold condition, on a flat bed, for wind velocity (U_t), which is the minimum wind speed necessary to drag a particle and can be described by:

$$U_t = 5.75 \times u_{*t} \times \ln \left(\frac{z}{z_0} \right), \quad (\text{A1-5})$$

being z [m] the height above the ground and z_0 [m] the aerodynamic roughness.

Correspondingly, to the case of a tilted surface, the threshold wind velocity ($U_{t\theta}$) is given by:

$$U_{t\theta} = 5.75 \times u_{*t\theta} \times \ln\left(\frac{z}{z_0}\right), \quad (\text{A1-6})$$

The relation between the friction velocity (u_*) and the saltation flux (q) is also a very important matter in the study of the aeolian sand transport [32], as it will be discussed in the following section.

A1.1.3.2. HORIZONTAL AND VERTICAL FLUX

The core matter of sand transport is the assessment of the material quantity being carried away by the wind. Since the early 1930s, several efforts were made toward the development of models to predict aeolian transport. These models are divided in three categories: theoretical, numerical and statistical models. The main difference between them is discussed by Dong et al. [24], along with a review of the most representative transport models.

In order to increase both usability and versatility of the sand transport models, they should rely on a theoretical basis, have a minimal number of empirical coefficients, be of easy access to input data, and, in the process, their accuracy should not be compromised. According to Dong et al. [24], these requirements are the main reason why the Bagnold type and modified Bagnold-type models are still used and object of enhancement.

Bagnold [33] introduced a cubic relation between the shear velocity and the sand flux, regardless the threshold condition, which impose a minimum speed for erosion to occur. The use of the threshold friction velocity in the flux relations was one of the most important improvements introduced by the several authors that follow Bagnold [33] in this subject.

The horizontal (or streamwise) sand flux indicates the intensity of saltation, defined as the vertical integral of the streamwise flux of the saltating particles. In the present work, tests are conducted for four saltation flux models, proposed by Bagnold [18], Kawamura [34], Owen [35], and Lettau and Lettau [16], respectively, selected among those most frequently used in aeolian studies [e.g. ,14,24,36]. It is intended to assess which model is the most suitable to the present application.

The above-mentioned flux models are formulated, respectively, as follows:

$$q_B = C_B \sqrt{\frac{d}{D} \frac{\rho}{g}} u_*^3 \quad (\text{A1-7})$$

$$q_K = C_K \frac{\rho}{g} (u_* - u_{*t})(u_* + u_{*t})^2 \quad (\text{A1-8})$$

$$q_O = \frac{\rho}{g} u_*^3 \left(1 - \frac{u_{*t}^2}{u_*^2}\right) \left(C_{O1} + C_{O2} \frac{w_s}{u_*}\right) \quad (\text{A1-9})$$

$$q_L = C_L \sqrt{\frac{d}{D}} \frac{\rho}{g} (u_* - u_{*t}) u_*^2 \quad (\text{A1-10})$$

In equations (A1-7) to (A1-10), the empirical constants are $C_B=1.8$, $C_K=2.78$, $C_{O1}=0.25$, $C_{O2}=0.33$, $C_L=6.7$, and D is a reference grain diameter ($D=0.25$ mm, according to Bagnold [33]), while d is the saltating grain diameter (in the present work $d=0.5$ mm, as reported in Section A2.2). In addition, $w_s=2.42$ m/s is the settling velocity [37].

The magnitude of the emission rate is a function of many parameters, such as wind speed, particle size distribution, soil packing, clay content, vegetation, fetch length, among others [as mentioned in, e.g., 29,38,39]. The emission (vertical) flux, with units of $[\text{kg m}^{-2} \text{s}^{-1}]$, is considered here as perpendicular to the emitting surface, and it assumes different designations, namely “dust flux” (F), or “sand flux” (Φ), for particle diameters, d , smaller than $63 \mu\text{m}$, and up to 2 mm, respectively [40].

Saltation bombardment is considered the main mechanism that influences emission rate; therefore, Gillette [41], Marticorena and Bergametti [29], Grini et al. [42], and others, proposed a direct relation between emission rate (F) $[\text{kg m}^{-2} \text{s}^{-1}]$ and the saltation flux (q) $[\text{kg m}^{-1} \text{s}^{-1}]$, namely:

$$F = \alpha_b \cdot q, \quad (\text{A1-11})$$

According to Shao [15], the α_b coefficient, named “sandblasting efficiency” [29,41,43,44, among others], with units of $[\text{m}^{-1}]$, depends on the diameter of the saltating particles. In fact, as claimed by several authors, the main source of dust emission is the kinetic energy delivered to granular beds and dust aggregates through saltatory impacts and the subsequent ejection of soil particles. Typically, the order of magnitude of α_b ranges between 10^{-5} and 10^{-2} [39,45,46]. Most of the models calculate the emission flux as a function of the third or fourth power of the shear velocity, u_* , which is in agreement with most saltation flux models [24].

According to several authors, such as Marticorena and Bergametti [29], Toraño et al. [7], Kok et al. [39], there are many parameters that influence the magnitude of the emission rate (F), for example, wind speed, fetch length, particle size distribution, and soil packing, among others. For loose soils, Shao [15] claimed that “(...) the dust emission rate is proportional to u_*^4 but not necessarily so in general”.

The estimation of the normal flux, perpendicular to a granular surface, is usually computed using the saltation length (l_{salt}), which is defined as the length of trajectories of particles that

have rebounded from the surface [e.g. ,47,48],and this relation is schematically represented in Figure A1-3.

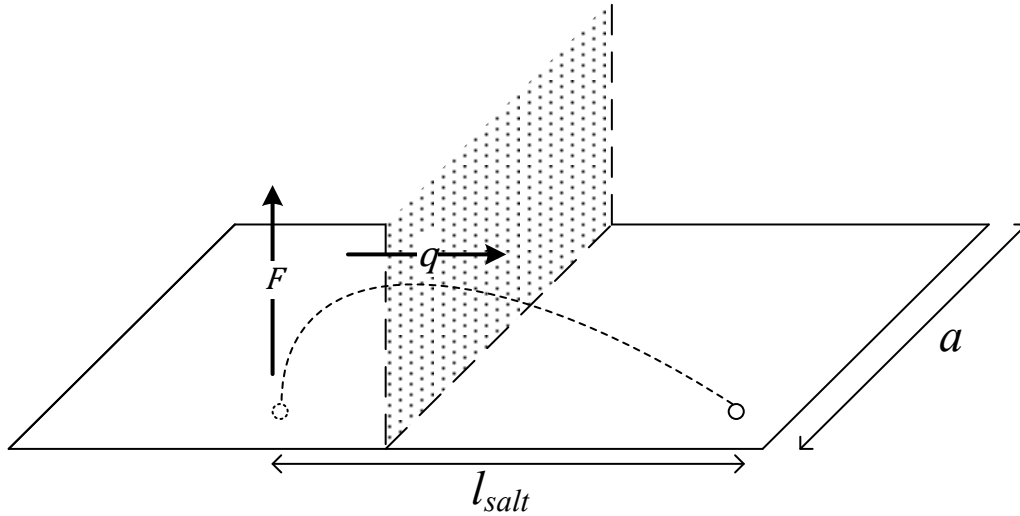


Figure A1-3: Schematic representation of the relation between emission rate (F) and saltation flux (q).

The representation depicted in Figure A1-3, infers the following relation:

$$F \cdot l_{salt} \cdot a = q \cdot a \Leftrightarrow F = q / l_{salt}, \quad (\text{A1-12})$$

Another approach to compute the free surface evolution of piles is based on the mass conservation equation of Exner [49]. Considering unidirectional flow in the x-direction over an erodible bed, the standard form of the Exner equation of bed sediment continuity is given by:

$$(1 - \lambda_p) \frac{\partial \eta}{\partial t} = - \frac{\partial q}{\partial x} \quad (\text{A1-13})$$

where λ_p represents the bed porosity and t time. η is the bed elevation relative to a fixed level and q is the volume transport rate of bed material load per unit width.

One of the direct applications of the study of normal flow rate is the estimation of the released dust from open stockyards, which, as mentioned before, is a problem with a wide range of impacts. In the present work, it is intended to explore the applicability of a dust emission scheme, when appropriately calibrated, as an alternative method to estimate the normal flux. The chosen model is the dust emission flux (F) model of Shao [15], a simplification of the Shao's [50] scheme, and can be described as follows:

$$F = c_y \eta_f [(1 - \gamma) + \gamma \sigma_p] (1 + \sigma_m) \frac{g}{u_*^2} q \quad (\text{A1-14})$$

where q is the streamwise saltation flux, as already mentioned, c_y is a dimensionless

parameter, and γ is a function specified as:

$$\gamma = \exp \left[-(u_* - u_{*t})^3 \right] \quad (\text{A1-15})$$

$\sigma_m = m_\Omega/m$ is the ratio between the mass ejected by bombardment (m_Ω) and the mass of the impacting particle (m), and can be interpreted as the bombardment efficiency [15]. Moreover, $\sigma_p = \eta_m/\eta_f$ is the free dust to aggregated dust ratio. According to Shao [15], σ_m can be estimated using the following relation:

$$\sigma_m = 12u_*^2 \frac{\rho_b}{P} \left(1 + 11.63 \cdot u_* \sqrt{\frac{\rho_b}{P}} \right) \quad (\text{A1-16})$$

where ρ_b is the soil bulk density and P the soil plastic pressure [51] (in the present work $\rho_b=1500 \text{ kg/m}^3$, $\rho_s=2650 \text{ kg/m}^3$ and $P =15000 \text{ Pa}$, as reported in Section A2.2 and Section A4.3.4).

In Equation (A1-14), η_f is the total fraction of dust, which can be released from an unit of mass, equal to mass fraction of free dust (η_m) plus the mass fraction (η_c) resulting from aggregate disintegration ($\eta_f = \eta_m + \eta_c$). In the present work, as detailed in Section A2.2, the experiments were performed using dried and sieved sand; therefore, it can be assumed that $\eta_c = 0$ implying that $\eta_f = \eta_m = 1$ and consequently $\sigma_p = 1$.

This allows a further simplification of Equation (A1-14), leading to the following expression for the normal sand flux (Φ):

$$\Phi = c_y(1 + \sigma_m) \frac{g}{u_*^2} q \quad (\text{A1-17})$$

The underlying assumption when using Shao [15] model is that sand emission, as a first approximation, has similar behavior to dust.

The experimental normal sand emission fluxes are calculated based on the profiles measured, and then compared against the outcome of the dust scheme of Shao [15] in order to determine the appropriate adjustment for the c_y parameter. The distribution of the surface shear velocity required, to calculate the streamwise flux is obtained through a computational fluid dynamics (CFD) approach.

A1.2. CFD PACKAGE

From the freely available open sources CFD codes, the two more representative are Gerris³ [52] and OpenFOAM (Open Field Operation and Manipulation - OF⁴ [53]), which are easily available worldwide comparatively to some other CFD codes. Both of them are known to have high accuracy and reliability, being applied in a wide range of research areas.

In order to perform a full evaluation of the CFD wind code CFD-WEM [54], Zhang et al. [5] performed a comparative study between this software and the two open source CFD codes mentioned above (Gerris and OpenFOAM). The study had its purpose the verification of the suitability of *CFD-WEM* wind code to investigate a particular site (*Xilingele* grassland in Inner Mongolia). Since open source codes are still not widely used in to simulate wind erosion, Zhang et al. [5] also aimed to provide a perspective about the use of these type of codes, like OpenFOAM, in this particular area of research. An important conclusion of their work is that the two open source codes prove to be a powerful and reliable technology to simulate wind fields.

Zhang et al. [5] compared various parameters between the three open source CFD codes (CFD-WEM, Gerris and OpenFOAM), and their main conclusions are that OF was the most difficult to handle in terms of defining the mesh structure and obstacles, but was the one that produced the best results in terms of accuracy. According to Zhang et al. [5], OF, despite being the code with the most complex algorithm of the three codes under comparison, did not had the slowest processing. Furthermore, the study concludes that in what concerns the viability of using OF for wind erosion research, it is advantageous considering that OF offers a high number of solvers that can resolve various types of problems related to CFD. Clear program structure and helpful documentation are other factors favoring the use of OF.

These are some of the reasons leading to the choice of OpenFOAM as the CFD Package being used in the present work. Further details about OF will be presented in Section A3.2.

A1.3. STATE OF THE ART

As mentioned, granular material's aeolian transport is an issue with a wide range of applications, and to be able to study and modeling wind fields at different scales, as well as their interaction with the ground is of high importance. Besides the work already cited in the

³ http://gfs.sourceforge.net/wiki/index.php/Main_Page

⁴ <http://www.openfoam.com/>

previous sections, this section consists of a literature review in the field of wind erosion, more specifically on the main topics of interest for this study, in particular wind erosion; dust emission from stockpiles and free surface deformation of piles. In addition, studies in other areas, like coastal engineering processes and scour modeling, are presented due to their similarity to the process (or processes) that occur in the time-changes of free surface morphology.

The literature reviewed consists of experimental studies and numerical modeling, in this case with commercial and open source CFD tools. It will be given a higher emphasis to the OpenFOAM software, since this is the tool that will be used to perform the numerical simulations.

Numerical modeling has established itself as a cost-effective and powerful technology tool in a wide range of applications including design of industrial equipment and processes, and prediction of eventual environmental hazards [14]. However, some pitfalls persist, which indicates that further development is necessary.

Prior to the study of the actual effect of wind erosion, it is necessary to know and understand the wind behavior. Examples of the simulation of atmospheric flows over complex terrain are found in the work of Tapia [55], Martinez [56] and Sumner et al. [57]. All three studies used OpenFOAM as modeling tool.

The study of Tapia [55] is performed in the context of the *Vattenfall's*⁵ project aiming to increase from 2% to 12% by 2030 the wind power share of the company's energy sources. A great expansion of onshore wind power capacity is one of the goals of *Vattenfall* in the future; however, the best locations are already taken. Therefore, it is high priority the identification and evaluation of new potential locations, many of them over complex terrain.

The wind potential in a site is usually based on long-term onsite measurements of the wind speed. According to Tapia [55], in order to get reliable results the data collection should be conducted over a period from one to four years, with expected uncertainty levels for the wind speed values from 12% to 7%, respectively. Consequently, to further improve the precision of the power predictions (proportional to the velocity to the power of three); it is common the use of wind tunnel experiments and numerical modeling.

Most numerical tools to assess the wind potential have limitations, becoming more reliable for simple terrains or bodies of water, which is the case of offshore wind farms. Tapia [55] chose OF to model the wind field over the possible complex terrain sites to install wind turbine farms.

Martinez [56] conducted a study to validate OF as a CFD tool for flow over complex terrain applications, and to do so, a series of test cases were carried out and the outcomes compared with an already benchmarked in-house CFD code (EllipSys). The test cases used are a 2D flat

⁵ <http://corporate.vattenfall.com>

terrain, 2D and 3D bump, and the results of the well-known *Askervein hill* project. Sumner et al. [57] used the *Bolund*⁶ experiment to assess OF as a tool to simulate flow over complex terrain.

Gartmann et al. [58] used OF to analyze the wind field characteristics of a portable wind tunnel. The results allowed the study in detail of flow conditions and the determination of spatial distributions of derived measures of shear stress and turbulence characteristics.

In what concerns wind erosion studies, other CFD codes are frequently employed to perform simulations in this area, like the commercial code CFX used by Faria et al. [12] to study the stoss slope effect on the aeolian erosion of transverse sand dunes and Ferreira et al. [59] to evaluate the wind flow near sinusoidal piles. Ferreira et al. [60] investigate the shear velocity distribution along a single and two closely spaced transverse dunes, also using CFX to perform the numerical simulations. Another example is the work of Beyers and Waechter [61], who use Fluent to simulate the snowdrift development over several configurations.

On the other hand, CFD–WEM is an open source software who was specifically developed to evaluate the wind erosion in *Xilingele* grassland in Inner Mongolia, which was successfully validated against wind tunnel data [5].

Open storage yards for bulk material, like iron ore or coal, are frequently found at industrial sites or power plant facilities. Dust emission from stockpiles is a relevant environmental problem, with consequent effects on human health varying according to the diameter of the particles released. Additionally, it can be faced as an economical issue, since dust emission is a problem to be solved, for both new installations, in order to get licensing from the involved authorities, and existing stockyards that are allowed to maintain operation through compliance with the regulations[62].

Moreover, the study of dust emission from stockpiles is rather complex due to number of variables necessary to take into account. To overcome this, theoretical – numerical simulations usually assume several simplifications. Other approach is the use of empirical models, which have the shortcoming of limited range of applicability as they were developed for specific working conditions at a given site, and even these conditions may vary [7].

In general, the methodologies available to predict the dust emissions require two main steps - the first one the wind flow analysis, and the second one the use of an appropriate model for the emission rates with these wind fields [62].

Two common methods to estimate the dust emission from stockpiles are field measurements and mathematical models, being the most widely used the one proposed by the United States Environmental Protection Agency (USEPA) [63], which also covers other diffuse sources, such as unpaved roads or explosives detonation. USEPA [63] methodology provides not only

⁶ http://www.bolund.vindenergi.dtu.dk/the_bolund_experiment

emission factors and control methods, but also techniques to predict, among others, the total emission. It is focused on several conditions, in particular wind direction and pile shape. The disadvantage is related to flexibility, as it may not evaluate the most convenient way of storing the material considering area restrictions and stacking means.

Brief explanation of USEPA (2006) methodology:

The methodology applied to estimate the emissions from stockpiles can be found in Section 13.2.5 of AP-42 Compilation of Air Pollutant Emission Factors [63], and is summarized as follows.

The emission factor (EF) [$g\ m^{-2}/year$] for surface airborne dust subject to disturbances can be obtained as follows:

$$EF = k \sum_{i=1}^N P_i S_i, \quad (A1-18)$$

where k is the particle size multiplier, N is the number of disturbances per year, P_i is the erosion potential corresponding to the observed fastest mile of wind for the i -th period between disturbances in $g\ m^{-4}$, and S_i is the pile surface area in m^2 .

The erosion potential function for a dry, exposed surface is:

$$P = \begin{cases} 58(u_* - u_{*t})^2 + 25(u_* - u_{*t}), & u_* > u_{*t} \\ 0, & u_* \leq u_{*t} \end{cases} \quad (A1-19)$$

where u_{*t} is the threshold friction velocity and u_* the friction velocity. For the case of flat piles or those with little penetration into the surface wind, friction velocity is given by:

$$u_* = 0.053 \times u_{10}^+ \quad (A1-20)$$

where u_{10}^+ is the fastest mile value corrected to a reference anemometer at a height of 10 m. Equation **Erro! A origem da referência não foi encontrada.** assumes a typical roughness height of 0.5 cm and height-to-base ratio not exceeding 0.2. If the pile exceeds this value, the pile surface area is divided into isosurfaces of friction velocity, which are treated as distinctive sources and Equation **Erro! A origem da referência não foi encontrada.** is employed to each one of them. The total dust emission is the sum of the emissions from each area.

$$u_* = 0.1 \times \left(\frac{u_s}{u_r} \right) \times u_{10}^+ \quad (A1-21)$$

According to USEPA [63], for two representative pile shapes (conical and oval top flat 37° side slope), the ratio of the wind speed measured at 25 cm from the pile's surface (u_s) and the reference velocity at 10 m height from the ground (u_r) (both for real scale) are derived from wind tunnel studies.

In several publications, the USEPA's model is used to quantify the emission rate from stockpiles and evaluate the influence of various parameters on the emission rate, such as the role of pile configurations and influence of flow conditions. Since erosion studies are increasingly turning to CFD technology, it is common to use numerical simulations coupled with the USEPA [63] methodology, regardless the focus of the research.

Badr and Harion [6] employed a numerical model (validated with wind tunnel measurements by Badr and Harion [64]), for various wind conditions, to predict the wind field near the piles and concluded that the proper pile configuration can reduce the dust emissions. Similarly, Toraño et al. [7] compared the semi-circular shape with the flattop oval and conical piles; the semi-circular configuration has the lowest emission rate. Due to the configuration of the piles, the tests were carried out for several wind directions. Besides studying the sensitivity of the stockpiles' wind exposure to geometry, location and wind conditions, Badr and Harion [11] assessed, assuming a non-erodible surface, the influence of the size distribution of granular material on the flow characteristics and friction velocity distribution. Badr and Harion [11] performed the quantification of the dust emission by using an upgraded version of the USEPA model, which takes into account several parameters such as, dust size distribution and meteorological data.

Turpin and Harion [65], taking into consideration the stockpile shape and configuration, concluded that the influence of flattening of its crest on pollution is low. Diego et al. [62] implemented the USEPA model in a commercial CFD code to calculate the total emission rate from complex yards, specifically, two parallel oblong sharp or flat-crested piles. It was confirmed that one pile works as a protection to the other, reducing the wind speed over the second pile, causing a different contribution from each pile to the total dust eroded. Similarly, Furieri et al. [9], investigated the global emissions from oblong piles, and since piles are rarely isolated in a stockyard, they analyzed the influence of a second successive pile, changing the distance between them on the global dust emissions. They conducted the fluid flow numerical simulations by using the open source Code Saturne. In their study, it was found that with the increase of the gap between the two parallel piles, the dust emission from the upstream pile increases while it decreases for the downstream pile. Thus, regardless the gap, the overall dust emission was similar. In addition, they showed that the total dust emission from two closely placed piles is higher than twice the emission of an isolated stockpile.

Like Toraño et al. [66], Furieri et al. [4] evaluated the influence of the wind flow direction on the study of the airflow over and around a single oblong pile. Both wind tunnel experiments, employing respectively oil-film surface coating and PIV measurements, were carried out and compared against numerical results.

Toraño et al. [66] performed numerical simulations, together with USEPA methodology, to study the influence of wind barriers on the dust emission from stockpiles and the predictions agreed well with data from the literature and industrial measurements. Ferreira and Lambert

[8], in addition to numerical simulations, also performed experimental erosion measurements in conical piles sheltered by wind barriers.

Turpin and Harion [67] used USEPA [63] model to investigate the influence of surrounding buildings in industrial sites, specifically, a power plant. The influence of the buildings in the emission rate from the stockpiles was assessed.

The above-mentioned studies investigated the influence of several parameters on the dust emission from stockpiles; however, they do not take into account the emissions of the surroundings of the piles. Even though the USEPA model is typically employed to calculate the amount of fugitive particles from stockpiles, Furieri et al. [10] use it to quantify the contributions of dust re-emissions from the ground surface around oblong piles in the overall emission rate of an open storage yard.

Except Furieri et al. [9], which use the open source Code Saturn to simulate isolated and parallel piles, the remaining mentioned studies resorted to commercial CFD codes in their work. The commercial CFX code was employed by Toraño et al. [7], Toraño et al. [66], Diego et al. [62] and Ferreira and Lambert [8], while other authors performed their simulations using Fluent [4,6,10,11,64,65,67].

Furieri et al. [68], instead of employing the referred methodologies, like USEPA [63], perform wind tunnel experiments and the emission mass flux was obtained through the weighing of emitted mass. The purpose was to evaluate the influence of non-erodible particles on aeolian erosion. Since all studies to evaluate the influence of non-erodible particles were executed in configurations like flat beds, sinusoidal or conical piles, Furieri et al. [68] selected the oblong pile to their study, because is the most frequently encountered in industrial sites, such as steel productions.

Aeolian erosion arises in the most ordinary situations, like drifting of sand or snow, wind exposed piles in stockyards or even granular materials kept or carried in open containers.

The primary objective of determining the emission rate of particles (dust or sand) is predicting the free surface evolution caused by the wind erosion with time due to the entrainment and deposition phenomena [e.g. ,23].

The possibility of having the control over the environment for studying the physical processes associated to wind erosion is the main advantage of wind tunnels over field tests; therefore, the environmental wind tunnel has proven a valuable tool for investigating the basic physics of aeolian processes [69].

Although field and wind tunnel experiments are a valuable help to the understanding of the flow characteristics, a lack of information persists regarding its interaction and relation with the reshape of the piles' free surface. Numerical modeling is a versatile and effective method that allows the improvement of the wind field knowledge and consequently the inherent processes [70].

Most authors qualitatively analyze the wind erosion over piles, since they base their conclusions in velocity values, instead of considering the continuous erosion of the piles, i.e., the deformation of the free surface and its interaction with the wind field. [71].

Although some attempts were made, such as Beyers and Waechter [61], the behavior of the shape of the piles with changeable free surface still is a research area requiring further development, both experimental and numerically. Ferreira and Lambert [8] obtained experimentally the evolution of a conical pile's shape deformation with the aim to relate it with the velocity distribution, and also to be used as a dataset to benchmark numerical models for transient wind erosion of stockpiles. Also, Faria et al. [12] conducted experimental work aiming to model the temporal wind erosion of sand dunes, and it is intended to use such data as benchmark of the computational models used within the present work.

Discrete Element Method (DEM) is increasingly being used by researchers to model fluid flow-particles interaction, for instance, Derakhshani et al. [72] used CFD and DEM as a coupled method to model the air flow over a stockpile and study the dust emission and consequent surface deformation. Both models were implemented using open source software packages, LIGGGHTS and OpenFOAM for DEM and CFD, respectively. The results obtained by the CFD-DEM modeling were compared against experimental data, and it was demonstrated that the use of this method is an interesting possibility to illustrate erosion and deformation of stockpiles.

Ji et al. [73] presented a convection–diffusion mixture model for estimating particle transport, including the influence of saltation and suspension along loose boundaries, which can be incorporated within the framework of CFD solution. It has revealed good agreement with both experimental and analytical results. Lopes et al. [14] proposed a numerical method, implemented in a home-made code, to compute the erosion progress of sand dunes when exposed to the wind, adopting various entrainment models and corresponding deposition fluxes.

Most aeolian erosion studies using OF software indicate that it does not take into consideration the continuous deformation of the free surface, thus does not evaluate the contributions of the boundary air-particle changes in the wind field along time, and consequent influence on erosion. Other works, which consider the changeability of the pile's shape, use OF to calculate the flow field, but coupled with different software to predict the particle transport, such as DEM, as previously mentioned. On the other hand, some authors, like Liu and Garcia [74], use only OpenFOAM to modeling scour and calculate the fluid-solid interactions. Although some similarities can be found between scour and the free surface movement due to wind erosion, the approach used by Liu and Garcia [74] still requires further evaluation and eventual development.

In the present state of the art review, applications are also presented that, despite not being directly related to the topic under study, deal with processes involving phenomena similar to

those that occur in aeolian erosion, such as, among others, coastal engineering and scour processes.

In the recent years, OF began to be recognized as a valuable tool for coastal engineering applications, since it is able to solve 3D domains and two-phase flows. An example is the work performed by Higuera et al. [75], which upgraded OF with the developing of wave energy generation and active absorption boundary conditions. This model was then validated by Higuera et al. [76] using comparisons with relevant experimental benchmark cases, revealing a truthful wave generation and achieving a very good agreement with regard to wave breaking, run up and undertow current.

Scouring can be defined as the removal of granular material from the base of a water flow's obstacle, i.e., bed erosion, which occurs due to swiftly moving water, compromising the integrity of a structure. It occurs not only during floods but also in normal flow conditions. Scour intensity is directly proportional to flow velocity, as aeolian erosion is proportional to the wind speed.

The assessment of two different approaches to scour modeling, namely, mesh deformation techniques and multiphase models, to evaluate which was the most appropriate one for this type of study was performed by Melling et al. [77]; both approaches were implemented in OF.

Stahlmann and Schlurmann [78] investigated scouring in order to gain better understanding of its evolution at the foundations (tripod) of offshore wind turbines, aiming to improve the scour prediction and also to reduce the uncertainties in the dimensioning of the constructions. Pasiok and Stilger-Szydło [79] studied the mechanisms involved in local scour associated with bridge pier impact, in particular the mass trajectories around a pier.

A numerical model for scour modeling with free-surface and automatic mesh deformation was developed by Liu and Garcia [74]. Two sharp interfaces were defined, water-air and water-sediment, and in order to solve both problems, a new solver for OF -called foamScour, was developed.

CHAPTER A2

EXPERIMENTAL SETUP

In this chapter, the experimental setup will be presented. The experimental part of the present study comprises three different types of experiments, namely erosion, static pressure and wall shear stress tests.

In the present work, several wind erosion tests for different cases of granular material piles were conducted with the purpose of analysing the erosion evolution, i.e., the piles' free surface changes with time.

Additionally, using rigid models, both pressure and wall shear stress distribution along the piles' surface were measured, with static pressure taps and a set of calibrated (Part B) *Irwin* [1] probes, respectively.

The experimental tests were performed in a wind tunnel, which, according to Iversen and White [69], among others, has proven to be a valuable tool to investigate the physical basis of aeolian processes and modeling of some of these processes on a small scale. The tunnel main features are presented in Section A2.1.

In the present work there are no special conditions that must be replicated (like scalable models, wind fields, etc.); therefore, the only concern is to maintain (as close as possible) the

experimental conditions and use them in the CFD simulations due to numerical model validation purposes.

The tested piles are made of sand as the granular material, which is characterized in Section A2.2. Several pile configurations were tested in the present work, with increasingly complex geometry, and are presented in Section A2.3. Finally, the main features of the performed experimental tests are described in Section **Erro! A origem da referência não foi encontrada..**

A2.1. WIND TUNNEL

The tests were carried out in the wind tunnel of the Industrial Aerodynamics Laboratory (LAI) – a facility owned and operated by ADAI (Association for the Development of the Industrial Aerodynamics-University of Coimbra, Portugal). The main characteristics of the tunnel are described in Section A2.1.1. A discussion about the similarity criteria can be found in Section A2.1.2.

A2.1.1. TUNNEL DESCRIPTION

The cross-section of the nozzle of the wind tunnel is 2x2 m² and it is followed by an open (without enclosing walls) test chamber with a length of 5 m. Both turbulence intensity and wind profile of the mean longitudinal velocity component (u) were measured in the empty test section, at half-width, and at a distance of 2.4 m downstream of the nozzle. A power law can approximate the wind profile at that location, as follows:

$$\frac{u}{U_0} = \left(\frac{z}{\delta}\right)^{\alpha_v} \quad (\text{A2-1})$$

where U_0 [m s⁻¹] is the undisturbed wind speed, u [m s⁻¹] is the mean longitudinal velocity component, z [m] is the vertical distance above the ground. The boundary layer thickness (δ) has the value of 0.1 m, based on its measurement, and the best fit is obtained with $\alpha_v=0.11$. The turbulence intensity of the longitudinal velocity component remains nearly unchanged with the height, and a reasonable approximation is to take its value equal to 1.2%. This value was obtained through velocity measurements with a hot wire probe, and is within the order of magnitude of other wind tunnels [80].

Depending on the pile configuration tested, different undisturbed wind speeds (U_0) for a range from 6.60 to 12.95 m s^{-1} were tested; the resulting normalized velocity profile is given in Figure A2-1.

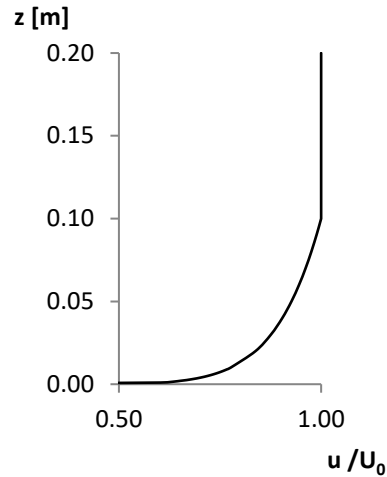


Figure A2-1: Incident velocity profile for the undisturbed wind speed used in the experiments.

The sand piles studied were placed, equidistant to the sidewalls of the wind tunnel, on its test section. The crest of the configurations is positioned 2.5 m downstream of the nozzle, and the main flow direction is perpendicular to the outflow plane. As an example, Figure A2-2 depicts the triangular pile case.

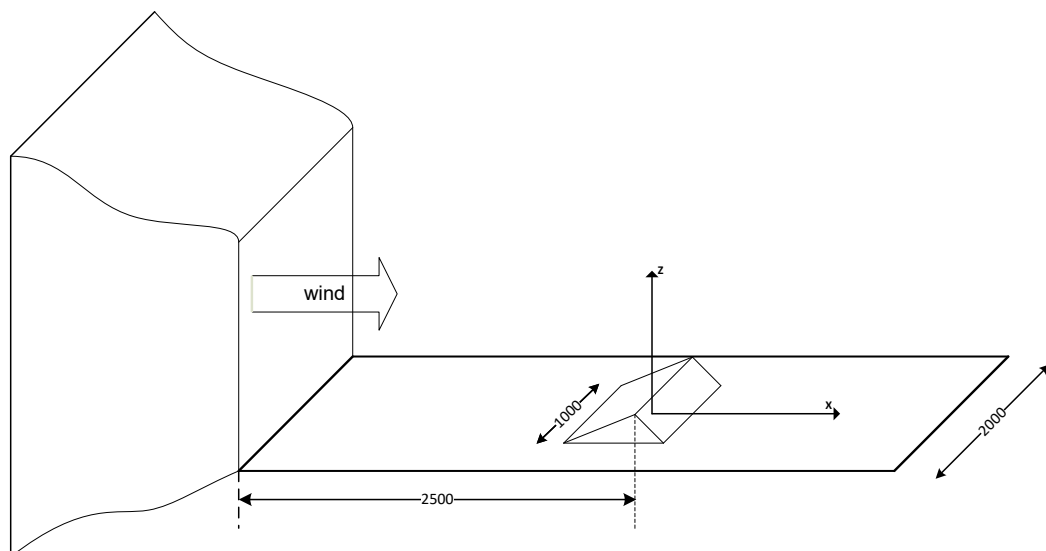


Figure A2-2: Schematic view of the wind tunnel and placement of the pile model (dimensions in mm).

A2.1.2. SIMILARITY CRITERIA

Similarity criteria should be taken into consideration, when testing scaled models in a wind tunnel. However, to satisfy these criteria, several dimensionless parameters should be within prescribed limits – a requirement, which is normally very difficult or even impossible. According to White [81], probably the most important requirement to be met is the Reynolds number (Re), which is determined as:

$$Re = \frac{U_0 \times L_c}{\nu} \quad (\text{A2-2})$$

where L_c is a characteristic length [m], U_0 is the already mentioned undisturbed wind velocity and ν is the fluid kinematic viscosity [$\text{m}^2 \text{s}^{-1}$] (equal to $\nu_{air} = 1.5 \times 10^{-5} \text{ m}^2 \text{ s}^{-1}$, in the present study).

According to several references [e.g. ,71,81], the required equality between model and full-scale can be relaxed if Re exceeds a minimum critical value of approximately 10^4 , which occurs in all cases of the present work. Further details on this topic can be found in White [81].

Another important issue related to wind tunnel tests is the ratio between the pile height and the thickness of the wind tunnel boundary layer (h/δ). White [81] indicates that it would be desirable to keep the tunnel model in the lower 20% of the boundary layer. Extrapolation of the results to full-scale conditions may not be reliable, when this requirement is not met.

The wind tunnel results, even when the last requirement is not satisfied, are useful as benchmark data for computational models. The experimental results may provide important information for the validation of the computational predictions and contribute to the understanding of the dynamics of aeolian erosion of sand dunes, in particular the free surface time-development of stockpiles of granular material.

A2.2. SAND

Sand is a material with a mineral origin, composed mainly by silicon dioxide, aka silica, whose size varies between $64 \mu\text{m}$ (1/16 mm) and 2 mm, according to the Wentworth [40] scale.

The tests were performed over sand piles, with various initial configurations, as already mentioned. The sand piles, usually known as dunes, are dynamic natural structures that grow, move and change shape, essentially due to aeolian erosion. This behavior is common to all types of granular material stockpiles.

All the sand piles considered in this study are made out of sieved sand with a prevailing grain

diameter of $d = 0.5$ mm, according to the granulometry tests conducted by Ferreira et al. [59], as reported in Figure A2-3.

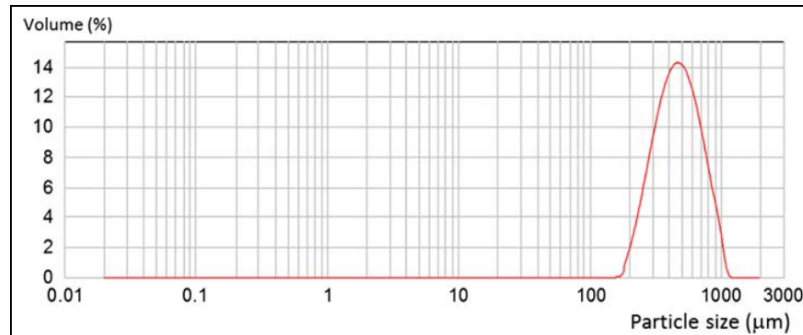


Figure A2-3: Tested sand granulometry [59].

The particles for this prevailing grain diameter, according to Wentworth [40], can be classified as medium to coarse sand grains. The bulk sand density (ρ_b) for this particular granulometry is approximately equal to 1500 kg m^{-3} . However, the value for the sand grain density (ρ_s) is taken to 2650 kg m^{-3} , as the sand used consists mainly of silica grains, usually in the form of quartz [18].

A2.3. STUDIED CONFIGURATIONS

The present work has its focus on the study of non-horizontal geometries, such as triangular profile's transverse piles and three-dimensional topography models. Both rigid plywood models and sand piles were used in the present work, except for the oblong configuration (3D).

All studied configurations were experimentally and numerically tested, as will be discussed in Chapter A3.

A2.3.1. TRIANGULAR

Since some of the experimental values of Faria et al. [12] are used in the present study for model validation purposes, the simplest configuration to be used is the constant slope geometry, i.e. triangular profile pile.

The geometry of the triangular piles studied is shown in Figure A2-4. The lee side has a declivity equal to the angle of repose (α), which, according to Ferreira and Lambert [8], is around 33.2° , and besides the configurations tested by Faria et al. [12], other slopes were used in the stoss side. Furthermore, two different crest heights (h) were tested.

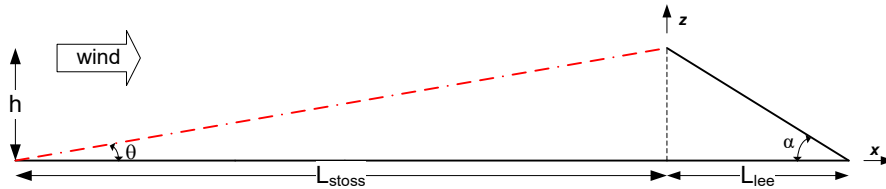


Figure A2-4: Geometry and dimensions of the triangular piles. The windward and lee side of the slope for the different configurations are indicated in red and black, respectively. (Dimensions in (mm); wind direction is from left to right) (Adapted from Faria et al. [12]).

Additional specific details about the tested configurations of the triangular piles are provided in Chapter A4.

A2.3.2. OBLONG PILE

The three-dimensional pile configuration is selected to perform the erosion tests is the oblong geometry, because it is representative of stockpiles of granular material, for instance coal piles, commonly found in industrial sites.

As will be explained in Section A5.1, in the scope of this work, a specific device was projected and manufactured to build the oblong sand pile in the working chamber of the wind tunnel. Due to that, only one geometric configuration was tested and the general dimensions of the oblong pile are: 74 mm (height), 226 mm (width), 635 mm (length), and 33.2° of angle of repose [8]. A schematic representation of the pile is depicted in Figure A2-5.

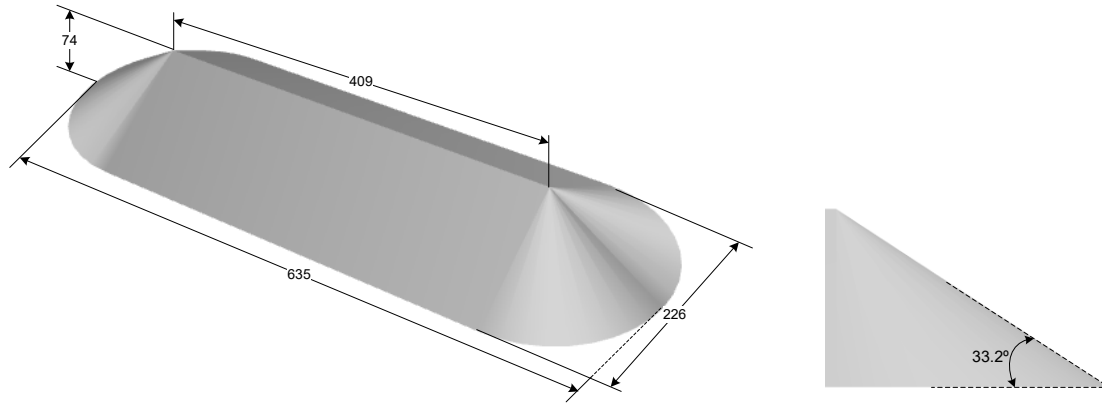


Figure A2-5: Schematic representation of the tested oblong sand pile (dimensions in millimetres).

A2.4. EXPERIMENTAL TESTS

The experimental trials were conducted over two types of prototypes: granular material (sand) piles and rigid wooden models. Due to its characteristics, different experimental tests were performed for each one of them. The sand piles were used for the erosion tests and the rigid models for the wall shear stress measurements and pressure distribution along the surface.

The main goal of the erosion tests is to measure the erosion profiles, i.e., to obtain the time-evolution of the free surface shape of the piles, as described in Section A2.4.1. Based on these results, in Section A2.4.2, the deformation rate was then computed to determine the sand emission rate.

For the shear stress tests, the local wall shear stress is obtained using *Irwin* [1] probes distributed along the surface of the piles, as explained in Section A2.4.3. The study and calibration of this type of probes are discussed in Part B of this thesis. Additionally, a set of pressure taps distributed along the surface of the models allowed the measurement of the pressure coefficient distribution, as presented in Section A2.4.4.

A2.4.1. EROSION TESTS

The erosion tests, as already mentioned, were conducted for the granular material models, namely, triangular and oblong sand piles. In order to perform this type of tests, the first step is to build the pile in the working chamber. Due to the geometry of the models, some differences

can be noticed in the experimental procedure, in particular related to the pile setup. Therefore, the details of the piles' construction technique will be described in the respective chapters, namely, Chapter A4 for triangular piles and Chapter A5 for oblong piles.

Prior to the erosion test itself, the initial profile is scanned using a distance laser sensor Dimetix-model DLS-B15 [82]. The distance sensor is mounted on a traversing system working on a plane parallel to the base of the model. The traversing system carries the laser in two perpendicular directions, and the entire process is controlled from a computer-based platform, which was developed by Gonçalves [83].

After the initial pile scan, the sand dune is exposed to the desired wind speed and the wind tunnel is stopped at cumulative times (which can vary according to the pile configuration), for registering the erosion profile; such data will be then used to determine the deformation rate of the pile. Since the triangular case is a 2D model, the erosion profile is measured only in the centerline of the pile, whereas in the oblong case (3D model) a grid of points scattered along the surface is used to register the evolution of the free surface.

Each one of the models was tested five times (as performed by Ferreira and Fino [13]), to properly characterize the time evolution of the pile profile. Thus, the profile that will be used for each time instant is the mean profile obtained from the five experiments.

A2.4.2. SAND EMISSION RATE

As described, in the erosion tests, the free surface profile is measured, and the data can be used to calculate the sand emission rate

For the computation of the sand emission rate, in the 2D configuration, during the time interval (Δt), i.e., between instants (t) and ($t + \Delta t$), and per unit of depth (1 meter) and length (L), as depicted in Figure A2-6, the following expression was used:

$$\Phi = \frac{[(z_i + z_{i-1})_t - (z_i + z_{i-1})_{t+\Delta t}] \frac{\Delta x}{2} \cdot 1}{\left[\frac{(L_t + L_{t+\Delta t})}{2} \cdot 1 \right]} \times \frac{\rho_b}{\Delta t} \quad (\text{A2-3})$$

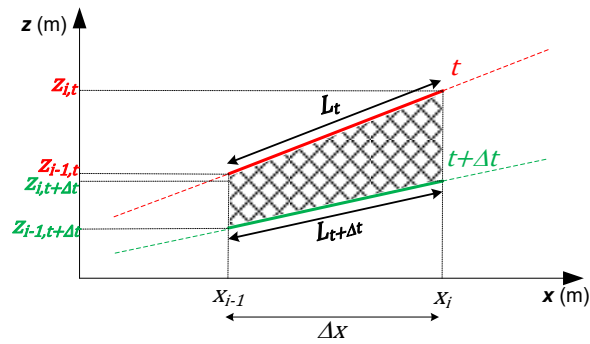


Figure A2-6: Scheme to calculate the emission rate for the 2D cases.

The calculated fluxes correspond to the average value during such time interval, since the surface profiles were measured only at discrete instants (e.g., $t=1, 2, \dots, n$ minutes). For example, the mean flux, between $t=1$ and $t=2$ minutes is calculated using the pile contours measured at those instants.

Similar method is employed for the 3D piles, between instants (t) and ($t + \Delta t$), and per unit of emission area (A), as depicted in Figure A2-7, the following expression was used:

$$\Phi = \frac{[V_t - V_{t+\Delta t}]}{\left[\frac{(A_t + A_{t+\Delta t})}{2}\right]} \times \frac{\rho_b}{\Delta t} \tag{A2-4}$$

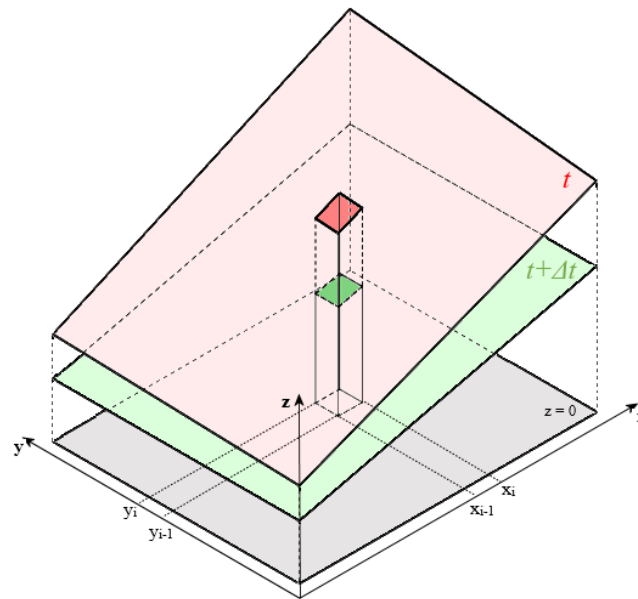


Figure A2-7: Scheme to calculate the emission rate for the 3D cases.

where V [m³] is the removed volume.

In Figure A2-7 the red plane symbolizes a portion of the pile's surface at instant t and the green plane for instant $t + \Delta t$. In grey is represented the ground level ($z=0$). The darker red and green rectangles correspond to the emission areas of instant t (A_t) and $t + \Delta t$ ($A_{t+\Delta t}$), respectively.

The spacing of the measuring grid was equal for all cases (Section A5.1), and, as mentioned, the distance sensor is mounted parallel to the ground, therefore, the x and y coordinates of the measured points are the same for all instants.

Due to the irregularity of the pile's surface during the erosion tests, the methodology employed to obtain the emission areas and, consequently, the removed volume, requires the following steps:

- For each time instant:
 - Using four points (x y z), contiguous rectangles are created along the measuring grid, like those depicted in Figure A2-7 (darker red and green);
 - For each rectangle, the mean edge length along the x - and y -axis is calculated. The following expression, as an example, is used to calculate this length along the x -axis:

$$x_{mean} = \frac{(d_{xy_{i-1}} + d_{xy_i})}{2} \quad \text{(A2-5)}$$

where, $d_{xy_{i-1}}$ represents the length ($d = \sqrt{(x_2 - x_1)^2 + (y_2 - y_1)^2 + (z_2 - z_1)^2}$) of the edge of the rectangle for y_{i-1} and d_{xy_i} the edge on y_i ;

- The mean height of each rectangle, i.e., the mean z coordinate of the four vertices of each rectangle (z_{mean}), is calculated;
- The mean area of each rectangle, i.e., the emission area, is computed as follows:

$$A = x_{mean} \times y_{mean} \quad \text{(A2-6)}$$

- The volume under each rectangle is calculated using:

$$V = A \times z_{mean} \quad \text{(A2-7)}$$

- For consecutive time instants (t and $t + \Delta t$):
 - For corresponding rectangles, i.e., for the same x and y coordinates, the equation (A2-4) is used to obtain the sand emission rate.

A2.4.3. WALL SHEAR STRESS TESTS

The wall shear stress was measured along the centerline of the stoss face of the triangular piles. Rigid models, made out of wood, were used for the placement of the probes, more specifically, *Irwin*-type [1] pressure probes.

The wall shear stress for each geometric configuration is measured for the same free stream wind speeds selected for the sand erosion tests. Depending on the size and geometry of the models, the number of probes is variable, since the available length, in each stoss face is different. Figure A2-8 shows, as an example, the distribution of the *Irwin* probes on the stoss side of one of the tested piles.

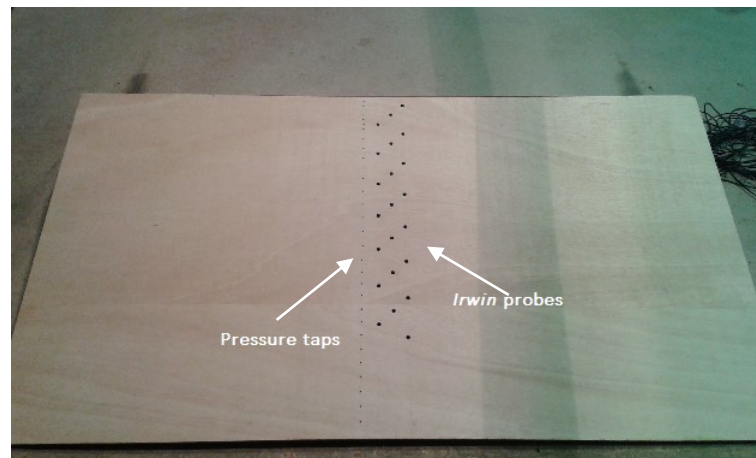


Figure A2-8: Distribution of *Irwin* probes and static pressure taps along the stoss side of a triangular model.

The pressure taps of the *Irwin*-probes, two per sensor, will be connected to a 48 channel Scanivalve, and the full measuring process is controlled by a personal computer/based platform. Pressure is measured using a Multur pressure transducer. Further details are given in Faria et al. [12] and in Part B of the present work.

A2.4.3.1. IRWIN PROBE

Considering the geometries studied and tested in the work of Irwin [1], a set of identical *Irwin*-type pressure probes was built for the present project; the geometric characteristics of a probe are presented in Figure A2-9.

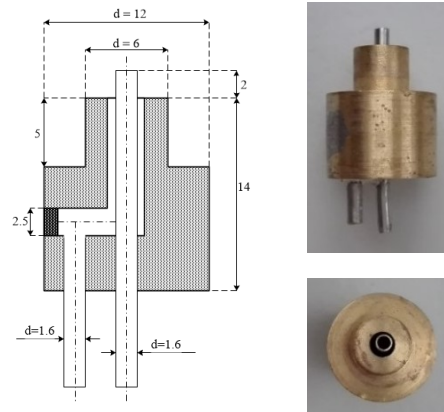


Figure A2-9: Geometry of the *Irwin* probes used (dimensions in millimetres).

Irwin probes consist essentially of two concentric pressure taps (Figure A2-9), and the pressure difference (Δp_I) between these two taps can be related to the wall shear stress (τ_w) by calibration, as it will be discussed in Sections B4.2.4.2 and B5.2.3.

The *Irwin* probes are surface-mounted, with one of the taps levelled with the face of the pile and the other 2 mm above (Figure A2-10).



Figure A2-10: Detail of the *Irwin* probes surface-mounted on one of the piles.

Based on the calibration of the probes, the wall shear stress (τ_w) is related to the pressure difference by the following relation:

$$\tau_w = 0.0266 \times \Delta p_I^{0.8478} \quad (\text{A2-8})$$

A2.4.4. STATIC PRESSURE TESTS

The rigid models were also instrumented with pressure taps, distributed alongside the *Irwin* probes (25 mm apart), to measure the pressure distribution. The taps are spaced 20 mm

between them, starting in the leading edge and covering the entire surface of the model (stoss and lee sides), as shown in Figure A2-8 and Figure A2-11. Due to the structure of the flow near the crest, a spacing of 10 mm was adopted in that area.

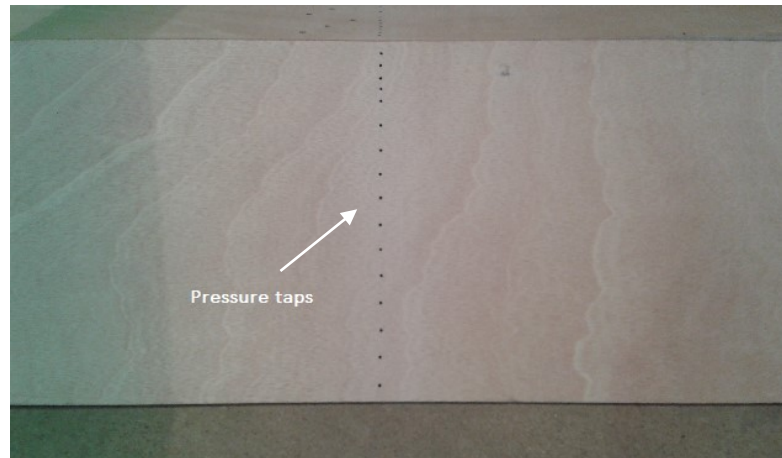


Figure A2-11: Distribution of static pressure taps along the lee side of a triangular model.

In order to evaluate the influence of the Reynolds number in the measurements, three different free stream velocities were tested. Prior to the actual experiments, the sensors were evaluated by conducting repeatability tests for the intermediate velocity.

The pressure distribution results will be presented in dimensionless form using the pressure coefficient (c_p), which is defined as follows:

$$c_p = \frac{p - p_{ref}}{\frac{1}{2}\rho U_0^2} \quad (\text{A2-9})$$

where p [Pa] is the static pressure at the measuring point and p_{ref} [Pa] is the reference static pressure.

CHAPTER A3

NUMERICAL MODELING

Numerical simulation, beyond the physical modeling, requires that particular attention be given to four main steps: Geometry, Mesh Generation, Processing and Post-processing.

The first step is mapping with appropriate software the domain geometry for the case under study. It should be noticed that at this step, often, some geometrical simplifications are made to avoid complexities that are irrelevant for a first evaluation. The next step is the mesh generation, which involves the discretization in finite volumes of the computational domain. The mesh generation should take into account regions of high gradients; moreover, the process should be guided through appropriate mesh convergence tests in close coordination with the processing stage, in which the actual simulation is conducted. In the simulation step, the discretized conservation equations are solved with an appropriate solver after the implementation of the boundary conditions. The results are treated in the last stage, the post-processing, if issues of the previous stages are identified, such as inconsistencies in the geometry, low level of mesh refinement in regions of large gradients, or errors in the determination of boundary conditions, it should be corrected and the analysis is restarted.

The main characteristics of the numerical model, assumptions employed and followed approaches are presented in Section A3.1. The chosen CFD package, the open source

OpenFOAM toolbox, is summarily characterized in Section A3.2. It is essential to have confidence in the results obtained through the simulations, consequently, to have the guarantee that the results translate reliably what happens in reality; therefore, verification and validation (V&V) are key steps to be considered in the model evaluation. In Section A3.3, some general considerations about these processes, as well as their application in the present work are discussed. Regarding the numerical simulations, only the general and common parameters at all study cases will be presented in Section A3.4, since, for the sake of clarity the specificities of the numerical setup of the triangular and oblong piles will be reported in Chapter A4 and Chapter A5, respectively.

A3.1. COMPUTATIONAL FLUID DYNAMICS - CFD

Computational Fluid Dynamics (CFD) is the term given to the group of mathematical, numerical and computational techniques used to obtain, view and interpret computational solutions of the equations of conservation of physical quantities of interest in a given flow. Thus, CFD can be summarized as the set of techniques of computer simulation used for predicting the physical or physicochemical phenomena that occur in a flow.

The great advances in processing capacity and data storage that computers achieved in recent decades has allowed a great diffusion of CFD techniques, both in the scientific community (e.g. universities) and industry. In both cases, the objective is the research and development of products and processes in which one or more flow fluid is involved.

CFD models and software can be divided into two main categories: commercial and open source. The commercial CFD packages are provided with detailed documentation, and are relatively easy to handle with the user-friendly graphical interfaces (e.g. CFD packages CFX and Fluent owned by ANSYS, Inc.). On the other hand, open source software can be used free of charge, the quality of the implemented methods is often advanced and around the open source software there are strong communities, which provide well-qualified support. Other aspects, that turn open source very appealing for the scientific community are related to being open for adaptation and enhancements, and the updates are freely exchanged [5].

Modeling the problem is a key issue in a numerical study and, in a general way, can be divided into six steps:

Definition of the problem

Define the physical domain to be studied, and select a suitable coordinate system. Identify relevant magnitudes, boundary conditions, and intervening phenomena, among others.

Representation of the physical model

Represent by using a schematic drawing of the domain under study indicating simplifying assumptions that were eventually made to facilitate the resolution of the problem.

Construction of the mathematical model

Translate the physical model in terms of mathematical expressions: connection between the relevant magnitudes - conservation equations (mass, momentum, energy, chemical species, e.g.) and boundary conditions, initial and "mathematical closure", inherent to the specific problem.

Resolution of the mathematical model

Perform mesh grid and temporal discretization independence tests, and verify the evolution of the dependent variables as function of the independent variables (time, space coordinates) and other parameters of the problem, including those of a physical and geometric nature.

Analysis of results

Conduct the data treatment of the results, use appropriate visualization tools to assess the physical meaning of the results, and extract conclusions.

Model validation

Evaluate numerical predictions versus experimental data, versus numerical results of other work, other authors: accuracy, reliability, range of applicability, limitations of the method.

Despite the investment costs of CFD software in license fees and add-ins, the overall expense is usually lower than a high-quality experimental facility, although with inherent limitations. Additionally, CFD over an experimental approach has other advantages as reduction of deadlines and costs of new designs; capability to study systems where controlled experiments are difficult such as systems operating in conditions at and beyond their normal performance limits (e.g. safety studies and accident scenes).

Regardless all these advantages, CFD simulation it is not a replacement of experimental data, considering that the models need to be evaluated and the data enables their benchmark and validation.

Furthermore, usually CFD software has a friendly graphical user interface with robust algorithms, which allow producing very attractive displays, even for inconsistent solutions. This represents a serious trap to the untrained user, who may lack the critical ability to assess the result; therefore, CFD should not be dealt as a "black box" and its analyses should be conducted by skilled labor.

A3.1.1. CONSERVATION EQUATIONS

As mentioned above, to obtain the basic equations of fluid motion, the fundamental physical principles should be followed, then applied to a suitable model of the flow leading to the mathematical governing model, which is typically described by conservation equations and the initial and boundary conditions. When reference is made to the equations of conservation is not more than a system of equations that reflect the exact conservation of mass, momentum, energy, and chemical species.

Contrarily to a solid body, which is rather easy to define and, if under a translational motion the entire body moves at the same velocity, a fluid do not maintain its form and if in motion, the velocity field is not constant. Therefore, the model of the fluid requires careful consideration. For a continuum fluid, usually one of the following approaches can be employed: the finite control volume or the infinitesimal control volume (top and bottom in Figure A3-1).

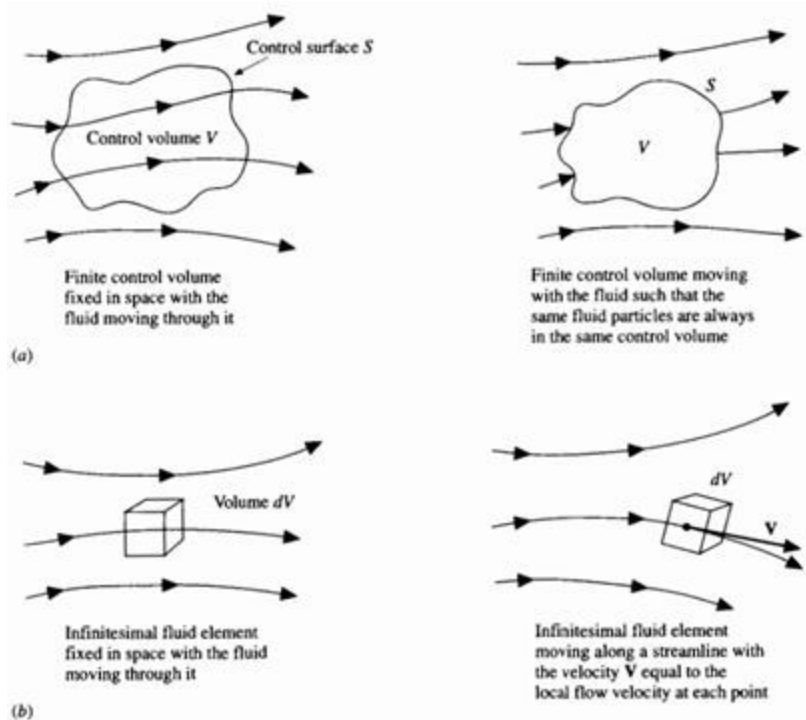


Figure A3-1: Finite control volume (a) and infinitesimal control volume (b) approaches [84].

In both approaches, instead of analyzing the entire flow field at once, the study is performed in a small portion of the fluid. Furthermore, the control volume (CV) can be fixed in space with the fluid flowing through it (left images of Figure A3-1) or moving along with the fluid in the way that the fluid particles inside the control volume are always the same (right hand images of Figure A3-1) [84].

Almost all differential conservation equations can be represented in the following generic form - also called general conservation equation in Cartesian coordinates and tensor notation [85]:

$$\frac{\partial(\rho\phi)}{\partial t} + \frac{\partial}{\partial x_j} \left(\rho u_j \phi - \Gamma \phi \frac{\partial \phi}{\partial x_j} \right) = S_\phi \quad (\text{A3-1})$$

↑ Advection
↑ Diffusion

↓ Local variation rate
↓ Sources / Sinks

The conservation equation reflects a balance of ϕ (generic variable, which can be replaced with different variables depending on the intended study) to an infinitesimal control volume (CV). The first parcel represents the transient term, i.e., a local variation rate; the second reflects the balance between the in and out ϕ fluxes through the faces of the CV, for combined diffusion (movement of particles down a concentration gradient) and advection (movement of particles by bulk motion), and the source term S_ϕ represents all the sources and sinks.

Due to the characteristics of the work under study, only the mass and momentum conservation equations are used. Thus, the generic variable (ϕ) should be replaced by 1 (Mass equation (A3-2)) and u_i (Momentum equation (A3-3)), respectively, leading to following expressions:

$$\frac{\partial \rho}{\partial t} + \frac{\partial \rho u_j}{\partial x_j} = 0 \quad (\text{A3-2})$$

$$\frac{\partial(\rho u_i)}{\partial t} + \frac{\partial}{\partial x_j} \left(\rho u_j u_i - \mu \frac{\partial u_i}{\partial x_j} \right) + \frac{\partial p}{\partial x_j} = S'_{u_i}$$

with (for Newtonian fluids) $S'_{u_i} = S_{u_i} + \frac{\partial}{\partial x_j} \left[\mu \left(\frac{\partial u_j}{\partial x_i} - \frac{2}{3} \frac{\partial u_k}{\partial x_k} \delta_{ij} \right) \right]$, where $\delta_{ij} = \begin{cases} 0, & \text{if } i \neq j \\ 1, & \text{if } i = j \end{cases}$ (A3-3)

A3.1.2. TURBULENCE MODELING

Turbulence is characterized by apparently random and chaotic three-dimensional fluctuations of a variable. When in the presence of turbulence, this normally dominates all other phenomena and results as an increase in, for example, energy dissipation, heat and mass transfer and drag. Thus, models that attempt to reproduce the haphazard manner in which turbulence influences the properties of the fluid are required.

As reviewed by Tapia [55], a large number of numerical turbulence models are available:

Reynolds – Average Navier Stokes (RANS): modeling of whole scales of turbulence. Attention is

focused on the mean flow and the effects of turbulence on mean flow properties. It is the most recognized and employed approach for practical engineering applications.

Large Eddy Simulation (LES): larger scales are computed while smaller scales are modeled.

Detached Eddy Simulation (DES): hybrid model with RANS and LES elements, taking advantage of particular features of both approaches. The latter is only used to model the regions with separation.

Direct Numerical Simulations (DNS): distinguishes itself from the previous models in the sense that does not require turbulence modeling as it solves the complete set of Navier Stokes equations. In this way, the whole range of spatial and temporal scales of the turbulence must be resolved. Because the large computational effort, it is employable only in cases of quite small domains and low Reynolds number.

The choice of the model to employ should depend on the assessment between accuracy and computational resources, since these and time consumption will increase with the number of turbulence scales compute instead of modelled. A schematic comparison between the three more representative models is depicted in Figure A3-2.

DNS is the ideal method, however hardly feasible for high Reynolds number cases in the immediate future; RANS has inherent limitations, leaving LES as the best option, but with high computational capabilities needed.

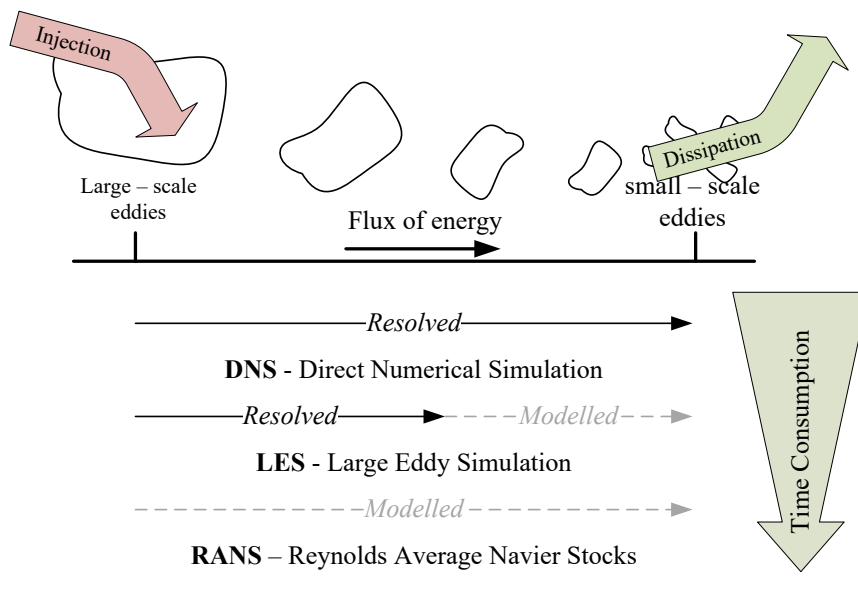


Figure A3-2: Extend of modeling for different numerical models⁷.

⁷ Adapted from <http://naimhossain.blogspot.pt/2012/08/turbulence-modeling.html>

Therefore, and besides RANS restrictions, considering the type of problem and the configurations that are intended to study, this simulation type is the best option due to its lower computing requirements and time consuming. Additionally, RANS models had proven to be adequate to study wind erosion applications as demonstrated by its widespread use by the scientific community.

One of the characteristics of the RANS methodology, is the additional number of transport equations required to be solved, such as: zero-equation model (Mixing-length), one-equation model, two-equation model (k - ϵ , k - ϵ RNG, k - ω , SST k - ω), seven-equations (RSM - Reynolds Stress Model), among others. The use of the two-equation turbulence models is well established and in the present work, these models will be employed.

The two variables of the k - ϵ standard model [86] represent the turbulent kinetic energy (k) and the rate of dissipation of turbulence energy (ϵ). When the Reynolds number is high, near-wall functions are needed (Section A3.1.3). A variation of this model, called Re-Normalization Group (RNG), was introduced by Yakhot et al. [87], which removed the small scales of motion from the equations and their effects were represented in the large scales. Also Wilcox [88] proposed an alternative to k - ϵ , using, as second variable, the specific turbulence rate ($\omega = \epsilon/k$). SST k - ω is a hybrid model between k - ϵ and k - ω , suggested by Menter [89], developed in order to overcome the main shortcomings of both models, namely, the severe limitations k - ϵ in the near-wall region and strong sensitivity of the k - ω solution to free stream values for ω outside the boundary layer. Therefore, in this hybrid model, the k - ω is implemented in near-wall zones, and k - ϵ is used in the fully turbulent area of the flow.

Considering the phenomena under study, the SST k - ω model, alongside with the k - ϵ standard model are the ones most often used among the two-equation models. Studies on the performance of turbulence models pointed out some of the shortcomings if the k - ϵ standard model is employed, namely, the overestimation of k or the inaccurate surface pressure distribution. Moreover, k - ϵ standard model has proven to be more appropriate for analysis of mean flow fields under constant and favorable pressure gradients, going towards the model's applicability tested by Launder and Spalding [86][90,91].

The work of Menter et al. [92] dealing with the SST k - ω model, revealed that, although this model was developed to overcome the issues related to the accurate prediction of aeronautical flows, rapidly widened its range of usability to most industrial, commercial and scientific applications. This model has proven to be accurate in the near wall layers, even in the case of strong adverse pressure gradients flows or with pressure induced separation. Additionally, it incorporates blending functions to ensure the proper selection of the k - ω or k - ϵ models without user interaction (so as to make the most of the advantages of each model), and has an automatic near wall treatment [93] which allows a reduction in the near wall grid resolution requirements.

Therefore, in view of the above, and the scope of the present work, the proper choice for the

numerical simulations is the numerical model RANS with the SST $k-\omega$ turbulence model, for which further details are given in Menter [89] and Menter and Esch [93].

A3.1.3. NEAR-WALL TREATMENT

In regions of the domain where turbulence is low, especially near the solid surfaces, the equations of turbulence models are not applicable.

The no-slip condition for viscous flows is often considered, it assumes that at a solid boundary, the fluid velocity goes to zero relatively to the surface. The layer near to the wall resists the motion of the adjacent layers and it slows them down gradually causing progressive thickening of the boundary layer until it is fully developed, as can be observed in the schematics of Figure A3-3.

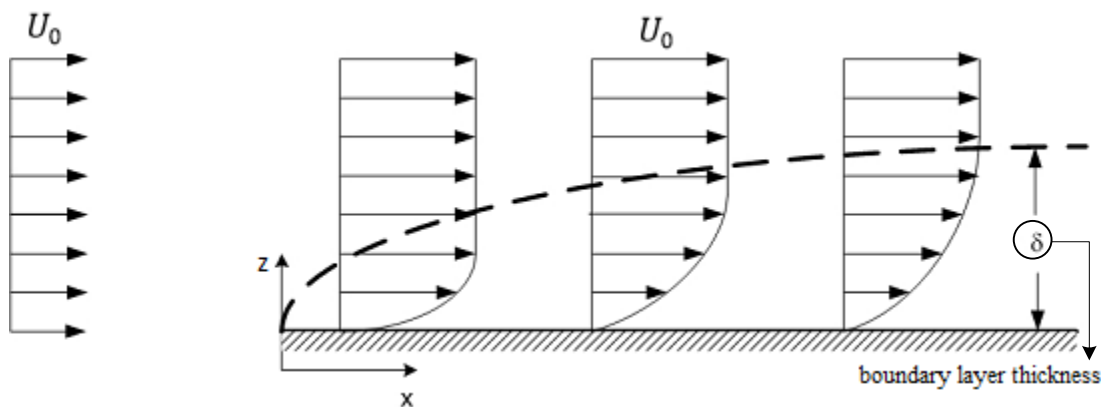


Figure A3-3: Boundary layer development⁸.

In the near-wall regions, algebraic equations are used, and these expressions are only valid in a small region of the flow close to the wall. The nodes of the elements near the wall should be located at a certain distance range so that the adoption of the models is valid. The so called "dimensionless wall distance" (y^+ or y plus), based on the distance between the wall and first node of the mesh and the local friction velocity, is given by:

$$y^+ = \frac{u_* y}{\nu} \tag{A3-4}$$

where y [m] is the distance to the closest wall and ν [$\text{m}^2 \text{s}^{-1}$] is the local kinematic viscosity of the fluid.

⁸ Adapted from <https://sites.google.com/site/scientiaestpotentiaplus>

As can be observed in Figure A3-4, the boundary layer is divided in different contiguous regions, which can be characterized, according to Schlichting [94], by the dimensionless wall distance range. Closer to the wall, specifically, the viscous sublayer occurs for $y^+ < 5$.

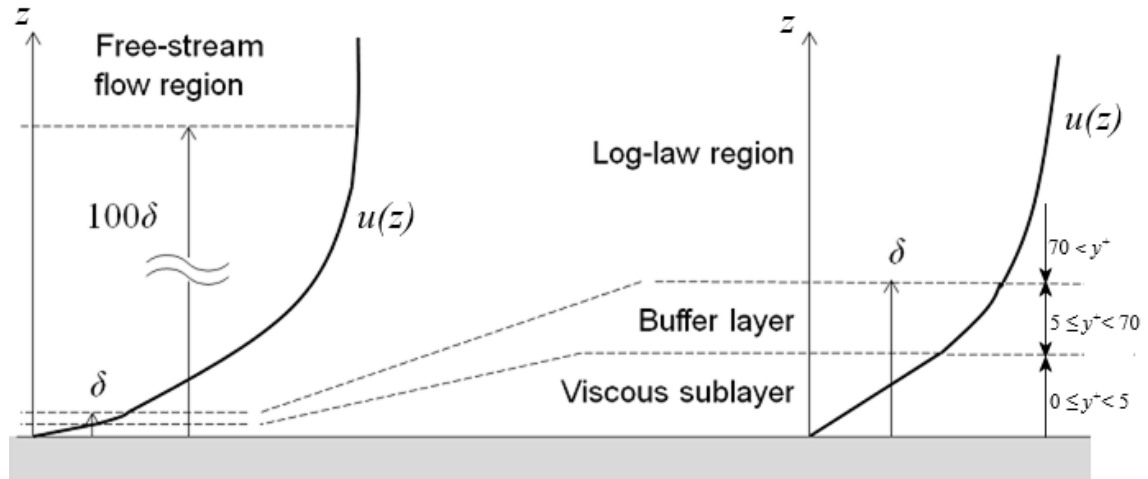


Figure A3-4: Boundary layer regions⁹.

The treatment of the equations near the wall is a very important element in the numerical simulations and there are a few methods. The most widely used is the wall function approach, used in many industrial CFD simulations, which uses the known velocity logarithmic profile of the boundary layer and bridges the viscous sublayer. This method allows coarser grids in the near-wall region; however, it imposes severe restrictions in the grid generation due to the imposition of an upper limit on mesh density ($y^+ > Y_{low}^+$ - value that depends on the numerical formulation) in order to stay in the logarithmic part of the boundary layer.

To avoid this limitation, Grotjans and Menter [95], introduced the scalable wall function approach, later optimized by Menter and Esch [93], that permits the use of indiscriminately fine near-wall grids without the first grid point slide into the linear profile; interpreting the wall as if is the limit of the viscous sub-layer.

Nevertheless, for flows with low Reynolds numbers, the applicability of the wall functions approach can be problematic, since it neglects the viscous sub-layer, which can have a substantial effect on the solution. Therefore, with the aim of allowing higher flexibility in the selection of a proper grid, Menter and Esch [93] developed an automatic near-wall treatment for ω -equation based models. The purpose of this method is to shift gradually between the viscous sublayer (low-Re - $y^+ < 5$) formulation and the wall function approach ($70 < y^+$), considering the grid density, due to the importance to solve the equations all the way to the surface. Between the two regions (buffer layer), a mix of the two methods is used.

⁹ Adapted from <https://www.comsol.com/blogs>

Since the ω -equation offers analytical solutions for both sublayer and logarithmic regions, this models are the most appropriate to employ the automatic near-wall treatment, and, to do so, Menter and Esch [93] proposed a blending function using the solutions of ω in the viscous sublayer and logarithmic region in terms of y^+ , as follows:

$$\omega(y^+) = \sqrt{\omega_{vis}^2(y^+) + \omega_{log}^2(y^+)}, \text{ where} \quad (\text{A3-5})$$

$$\omega_{vis} = \frac{6\nu}{0.075y^2} \quad (\text{A3-6})$$

$$\omega_{log} = \frac{1}{0.3\kappa} \frac{u_*}{y} \quad (\text{A3-7})$$

being κ the Von Kármán's constant.

Regarding the velocity profile near the wall an analogous procedure is used. Further details can be found in Menter and Esch [93] and Menter et al. [92].

The latter introduced method, the automatic near-wall treatment proposed by Menter and Esch [93], is used in the numerical simulations performed in the present work, considering the advantage of requiring minimal user's handling on the mesh generation and of being already implemented in the OpenFOAM package.

A3.1.4. DISCRETIZATION METHOD

Discretization transforms the differential conservation equations into algebraic equations, making them solvable; the process requires intrinsic approximations. Generally, both spatial and temporal discretization are performed dividing the time and space domains in well-identified discrete parts, namely instants and nodes, respectively [85].

Due to the characteristics of the cases simulated in the present work, only considerations on spatial discretization are presented in this section.

A3.1.4.1. SPATIAL DISCRETIZATION

In the spatial discretization, a node represents each fraction of the domain. Together, the nodes and the lines connecting them form a network, which can be more or less irregular, more or less structured. The discretization equations relating the values of the generic variable (ϕ) for a certain group of the mesh nodes are obtained from the differential conservation equations, assuming some kind of variation of ϕ between nodes. This variation is one of the main differences between discretization methods.

Among the existing methods (finite difference method (FDM); finite volume method (FVM); finite element method (FEM), among others), in the present work, due to the chosen CFD package, the adopted method is the Finite Volume Method (FVM).

In a simple way, the first step of the FVM is to divide the domain in contiguous control volumes (CV), in a way that each node is involved by a CV. Then, the differential equation is integrated for each of these volumes, resulting from them the discretization equation, which expresses the conservation principle in the finite CV, as the original differential equation had expressed the conservation principle for the infinitesimal CV.

The more evident advantages of the FVM are simplicity and immediate physical interpretation. Furthermore, the solution implies that the condition of integral conservation of the variables is exactly satisfied across the calculation domain. So, even a solution obtained for a coarse mesh satisfies exact integral balances (important in an initial stage of a calculation program) [85].

A3.2. OPENFOAM

From the early inception of the present project, the intention is to use an open source CFD package for several reasons, such as: is free usage and usually there are strong communities that provide help, which can be very useful from the point of view of a new user. Additionally, the packages are open for adaptation and development, which allows the users to create new applications suitable to their work.

Among the most used packages, and as mentioned before, the CFD software chosen was the *OpenFOAM* (**O**pen **S**ource **F**ield **O**peration and **M**anipulation). *OpenFOAM* was originally developed by a group at Imperial College (London) in the late 1980s, is written in C++ and it uses an object oriented approach which makes the code to be understandable and permits the user to implement its own files in order to adapt it to each specific case, bringing great flexibility and suitability for the users.

This software has been developed with a set of predefined solvers, libraries for pre and post-processing (e.g. ParaView) for several kinds of CFD applications. The mesh generation and the setting up of the boundary conditions and fluid properties are made in the pre-processing stage, the solver is responsible for the flow analysis, i.e., calculations, and the calculated results are displayed in the post-processing stage, using suitable visualizations tools [55]. Meshing in OF can be performed “manually” or resorting to the utilities to generate, convert or handle meshes [5].

Like other CFD tools, a study using OF passes through three main stages:

Pre-processing - mesh generation and setting up the boundary conditions, as close as possible of the real application. If a similar case already exists in the OF library, the files can be used and only alterations will be made to fit the specific case.

Calculation – run the solver to perform the flow analysis and obtain the results. It is a crucial stage, since it is very important to choose the optimal solver for the specific applications between the ones available in the OF library, or adapt an existing solver to the case under study.

Post-processing – analyzes of the results. It is also an important phase, since with the usage of the appropriate visualization tools, the user can observe the results obtained in the numerical simulations, and, perform mesh independency studies (model verification) and assess if the values are coherent (model validation).

The main assumptions and features used in the first two stages, i.e., pre-processing and calculation are presented in Section A3.4. The results visualization and analysis are performed in the chapters relating to each of the cases studied, namely, Chapter A4 for triangular piles and Chapter A5 for the oblong piles.

A3.3. MODEL VERIFICATION AND VALIDATION (V&V)

The main purpose of the model verification and validation is to determine the accuracy of a code, so it can be used with confidence and produce reliable results, which can support, for instance, design decisions. In other words, if V&V assessment attains satisfactory levels of error and uncertainty, the credibility of the code is demonstrated.

A proper appraisal of errors and uncertainties is crucial when CFD codes are employed, since they are used to model intervening, elaborated phenomena usually in complex geometries. Among the many guides (for instance, AIAA G-077-1998 [96], originally published in 1998, which was the first standard document available to the engineering community V&V of simulations) and other works published on this matter, is the notable book on verification and

validation by Roache [97]. The continuous evolution of the computational resources and consequent CFD codes, as well as the range of applications, force the V&V procedures to be in continuum progress (Guide AIAA G-077-1998 [96] is currently under update). Furthermore, the V&V is a throughout procedure in code development, i.e., before the code releasing and then in the growth phases.

In a CFD study, the credibility required can vary according to the desired use of the results, namely, qualitative information, incremental or absolute quantities [98]. The levels of uncertainties and errors are obtained through a V&V analysis.

In general, is quite common to use indifferently the terms uncertainty and error, however, regarding CFD simulation results, the AIAA Guidelines [96] provide two distinctive definitions:

- **Uncertainty:** *A potential deficiency in any phase or activity of the modeling process that is due to the lack of knowledge.*
- **Error:** *A recognizable deficiency in any phase or activity of modeling and simulation that is not due to lack of knowledge.*

The uncertainties may or may not occur, and the lack of knowledge often falls on the physical processes of the model, like the turbulence modeling. In these cases, a possible approach to estimate the level of uncertainty is to simulate the same problem with different turbulence models and evaluate its influence in the results.

In contrast, the error can be detected upon scrutiny. Errors can be classified as acknowledged or unacknowledged. The first one can be identified through proper procedures, and then removed or in the impossibility, be estimated and listed, namely, physical approximation or convergence errors. Concerning those that are unknown, such as programming or usage errors, they are hard to find and can remain in the code or simulation.

However, if what is under analysis is experimental data, both definitions are slightly different and are linked to each other:

- **Error:** *difference between the measured value and the exact value.*
- **Uncertainty:** *estimate of error.*

A3.3.1. MODEL VERIFICATION

According to AIAA G-077-1998 [96], verification can be defined as: *“the process of determining that a model implementation accurately represents the developer's conceptual description of the model and the solution to the model”*. Thus, and according to Roache [97] it has two strands: the verification of the code, to attest if the computational models correctly mimic the

phenomena under study; and the verification of the calculation, to assess the usability and accuracy of the solution.

The verification assessment is more directed towards mathematical rather than engineering problems with the intention to seek errors in both programming and models implementation. In the code verification, an error evaluation is performed and, usually, is executed prior to a code's release. This certification can be obtained by comparing the results of two different codes or with grid refinement studies. These tests are made in order to evaluate if the refinement of the mesh will influence the results, since as smaller the mesh elements are, hence in higher number, more time consuming will become the calculation process.

Whereas, in the verification of the calculation, an error estimation is made in order to attain the accuracy of the calculation. In this methodology, grid convergence studies should be performed.

The verification assessment consists in an initial scrutiny stage, where code, iterative convergence, consistency, spatial and temporal convergence are examined, then the CFD results are compared against known and accurate solutions.

A3.3.2. MODEL VALIDATION

Once again, according to AIAA G-077-1998 [96], validation can be defined as: *the process of determining the degree to which a model is an accurate representation of the real world from the perspective of the intended uses of the model*". Thus, the validation assessment evaluates the agreement between the computational simulation and the physical reality through the comparison with experimental data. Therefore, the range of applicability of a CFD code is limited by the used experimental data, beyond that range only predictions can be obtained. Nevertheless, even the experimental data have errors associated, which should be quantified in the comparisons, and, therefore, the precision attained through the validation depends on the application and the levels of accuracy should be chosen accordingly.

Model validation is one of the most important tasks in a numerical simulation, and seeks the increase of the credibility and consequently the reduction of the lack of trust, in order to substitute the experiments and raise the level of reliability and acceptance of the model, so it can be used in future investigations.

The numerical model validation process will be transverse to the entire work; since it will be performed using the various cases of study that it will be implemented.

The first step is the assessment of the applicability of the OpenFOAM software in wind erosion

studies of simple configurations, which in the present work will be performed for the geometry with constant slope, i.e., the triangular profile piles. This stage includes four phases:

- I. Attainment of the experimental data:
 - a. Erosion profiles, i.e., free surface deformation of the transverse triangular sand piles;
 - b. Wall shear stress and static pressure distributions through *Irwin* probes and pressure taps measurements, respectively, along the surfaces of the rigid models.
- II. Quasi-steady state numeric prediction (i.e., considering a rigid shape of the pile) of the wall shear stress (τ_w) and static pressure.
- III. Analysis of the obtained values in I and II with the purpose of calibrating and validating the numerical model:
 - a. Comparison of the measured static pressure distribution against the pressure coefficient predicted numerically;
 - b. Comparison of the measured wall shear stress distribution against the friction coefficient predicted numerically;
 - c. Correlation of the experimentally measured erosion profiles with the friction coefficient distribution, i.e., verify if erosion only occurs where the threshold condition, numerically predicted, is exceeded;
 - d. Comparisons with outcomes of other authors.
- IV. Adjustment of the numerical setup, if necessary, and return to step II.

The second step concerns the oblong piles, since only the sand models were tested in the wind tunnel, the model validation procedure has some differences, as can be observed in the following phases:

- I. Attainment of the free surface deformation and granular material emission flux through the evolution of the profiles of the piles experimentally obtained.
- II. Quasi-steady state numeric prediction (i.e., considering a rigid shape of the pile) of the wall shear stress (τ_w);
- III. Analysis of the obtained results with the purpose of calibrating and validating the numerical model:
 - a. Comparison of the experimentally measured erosion evolution and computed sand emission rate (obtained in I) against the wall shear stress distribution (obtained in II).
 - b. Benchmark the airflow features around and over the pile, obtained in II, against:
 - i. Experimental data obtained in I, specifically, correlate the free surface deformation and pile's contour with the wall shear stress distribution over and around the pile;
 - ii. Other CFD packages (Fluent);

- iii. Oil-film visualization outcomes of other authors.
- IV. Alteration of the numerical setup, if necessary, and return to step II.

A3.4. NUMERICAL SETUP

Of the main stages presented in Section A3.2, the numerical setup comprises the pre-processing, where the computation domain (Section A3.4.1) is drawn, the mesh generated (Section A3.4.1) and the case defined (Section A3.4.2) and the calculation, where the resolution of the equations is performed (solver – Section A3.4.3). The post-processing stage is performed to visualize and assess the veracity or coherence of the results and will be presented in Chapter A4 and Chapter A5.

A3.4.1. COMPUTATIONAL DOMAIN AND MESH PARAMETERS

Two cases were studied in the present work, and consequently two specific computational domains were used. Due to the characteristics of the cases, for the triangular piles a 2D domain could be used (Figure A3-5), whereas for the oblong piles, regardless the wind incidence angle, a 3D computational domain was employed (Figure A3-6).

In the case of the triangular piles, the experimental measurements were only performed along the centerline of the model, and actions were taken to reduce the edge effects and improve the two-dimensional character of the flow. Therefore, in order to reduce the number of elements in the mesh, the width of the domain is very thin, with only one element in the transverse direction. Due to that, in Figure A3-5 only the side view is depicted:

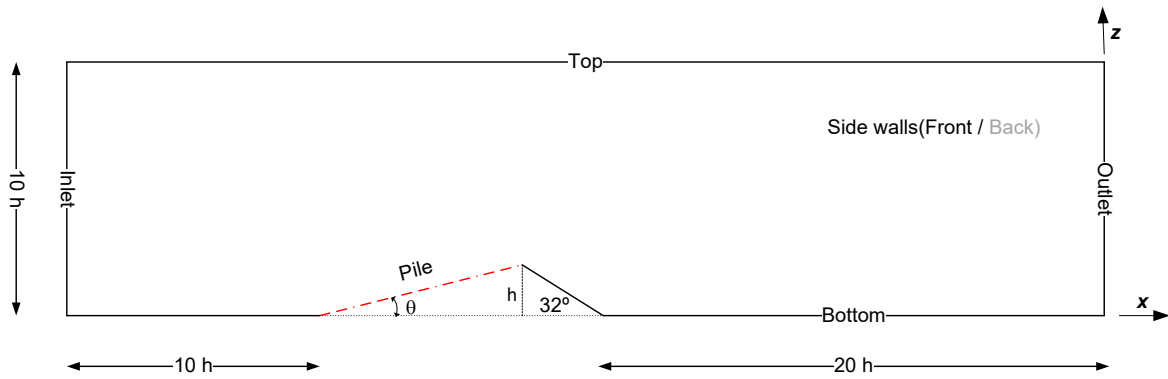


Figure A3-5: Computational domain – triangular piles.

In what concerns the oblong piles, due to the multiple wind incidence angles (β), two different approaches were followed to create the computational domains. In the case of a wind incidence angle equal to 90° , i.e., perpendicular to the pile’s crest, due to the symmetry of the geometry, only half of the physical domain was simulated, being the symmetry plane coincident with the centerline of the pile. This approach was not possible to use in the cases with a wind incidence angle of 60° due to the fact that, despite the pile’s geometry be symmetric, the interaction with the flow is not, so, the entire physical domain was simulated. Both computational domains are shown in Figure A3-6.

Wind incidence angle (β)

$\beta = 90^\circ$

$\beta = 60^\circ$

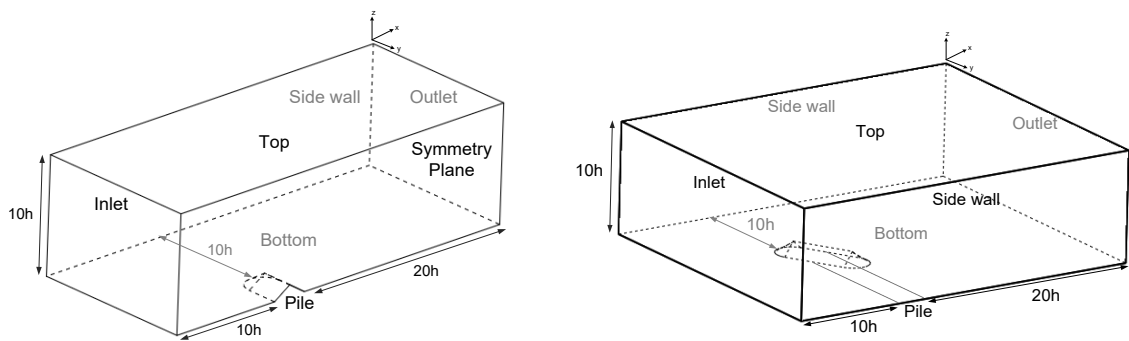


Figure A3-6: Oblong piles - computational domain for two wind incidence angles (90° (left) and 60° (right)).

As can be observed in Figure A3-6, the main difference between the oblong pile’s domains is that in the cases where the wind hits perpendicularly to the pile (90°), only half of the physical domain is simulated. Since what is intended is to replicate the test conditions of the wind tunnel, for the cases with $\beta = 60^\circ$, the wind orientation is obtained by the rotation of the pile,

therefore, the computational domain mimics the experimental setup. Thus, except the existence of a symmetry plane in the case with $\beta=90^\circ$, all remain regions, namely, inlet, outlet, bottom and sidewall, are similar.

The mesh generation of the triangular piles was performed using the OpenFOAM's utility *snappyHexMesh*. To ensure that only one element is generated in the direction perpendicular to the flow (y-axis - Figure A3-5), due to the 2D condition, the *extrudeMesh* utility of OpenFOAM was used. As the name implies, this utility was used to perform a linear perpendicular extrusion of the mesh of a specific boundary (sidewall) with a given thickness.

Additionally, another mesh generation utility, specifically, *cfMesh*, was used to create the mesh for the oblong pile cases. This utility was employed for the oblong geometry, since, after several tests and attempts executed with the *snappyHexMesh* utility, a higher quality mesh was achieved with *cfMesh*.

Regardless the case under study, layers were added in the bottom region (wall) in order to capture in the better way possible the boundary layer, even though the automatic near wall treatment of the SST $k-\omega$ turbulence model is being used. Additionally, a parallelepipedic region was added to allow further refinement around the pile. As an example, Figure A3-7 depicts the inflation layers and the refined region around the triangular pile.

The mesh study, as it will be presented Part B (Section B3.4), along with the CFD community recommendation for the most suitable value of y^+ to calculate the wall-bounded quantities, especially when employing the SST $k-\omega$ turbulence model, led to the use of the value $y^+ \approx 1$ in all meshes. The main mesh parameters, like the number of elements or the mean y^+ of the tested cases, are shown in Table A3-1. Illustratively, only the values for the simulations with the undisturbed wind velocity of $U_0=9.9$ m/s, are presented in Table A3-1.

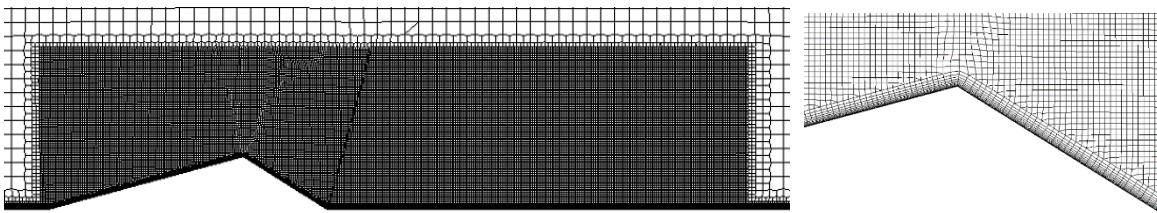


Figure A3-7: Mesh detail – inflation layers (crest) and refined region around the pile.

Table A3-1: Main meshes parameters ($U_0=9.9$ m/s).

	Case*	Elements	Mean y^+	Iterations	Calculation time [s]*
Triangular	S10	62670	1.16	2049	188
	S15	53200	1.12	2521	234
	S150	121556	0.93	4548	741
	S20	60115	0.72	2919	248
Oblong	90°	1515370	1.25	1553	5008
	60°	1446693	1.75	1442	3626

* triangular cases designation in Section A4.1

It can be observed in Table A3-1 that, as expected, the number of cells in the triangular pile's cases is substantially lower than the oblong pile's cases, since those are 2D cases, with only one element in the transversal direction (y-axis).

Considering the triangular cases, both iterations and calculation time increase with the slope angle, the opposite occurs for the y^+ values, which decrease. Although the S150 case has the same slope angle as the S15 case, since the crest height is twice the value, a larger computational domain was tested, and therefore the behavior is not directly compared with the remainder.

Concerning the oblong pile, although only half of the physical domain was simulated in the case with 90° incidence angle, the number of cells is quite similar in both cases (60° and 90°). Several meshes were tested, and, due to the airflow characteristics when the pile is not perpendicular to the streamwise direction, no convergence was achieved in refined grids. Therefore, less elements and a slightly higher y^+ value was used in the $\beta=60^\circ$ case, leading to a lower calculation time and number of iterations.

A3.4.2. BOUNDARY CONDITIONS

Although different geometries and computational domains were used for the triangular and oblong cases, similar boundary conditions were employed with the proper suitability.

As implicit in the designation, *symmetry* condition is employed in boundaries that behave as

symmetry surfaces (or planes). The *Dirichlet* (or first-type) boundary condition specifies the value of a quantity (e.g., pressure and velocity), which a specific boundary requires to take and in OpenFOAM, the keyword employed is *fixedValue*. On the other hand, the *Neumann* (or second-type) boundary condition differs from the *Dirichlet* condition because it specifies the value of the derivative of a certain quantity in the normal direction. Due to the characteristics of the problems under study, regarding the second-type boundary conditions, only gradients equal to zero (fully developed conditions – extrapolates the quantity to the boundary from the nearest cell value) are employed, being the keyword in OpenFOAM *zeroGradient*.

Considering the characteristics of the several regions of the domains presented in Figure A3-5 and Figure A3-6, at the inlet, the boundary conditions are: *zeroGradient* for pressure and *fixedValue* for the other properties; the turbulence intensity was considered 1.2% to match the experimental conditions. The experimental tests performed in all cases occurred in the same wind tunnel; therefore, although a *fixedValue* was used as the velocity condition, a discrete field considering the tunnel's wind profile (Equation (A2-1)) was employed.

In the outlet, *zeroGradient* was assumed for all dependent variables, except pressure, which was set equal to a constant value (*fixedValue*). The bottom faces are all treated as smooth walls, with a no-slip condition. Since OpenFOAM works with 3D domains by default, in the triangular piles cases (Figure A3-5), to switch from 3D to 2D, it was necessary to specify the *empty* condition on the sidewalls. This condition – *empty* – is used in reduced dimensions cases (1D or 2D), and is applied in the boundaries that are perpendicular to the geometric direction that do not constitute a solution direction. Symmetry conditions were imposed in all remain boundaries, namely, the top faces, in the symmetry plane of the oblong pile with $\beta=90^\circ$ (as shown in Figure A3-6), and sidewalls of the oblong's domains.

A3.4.3. SOLVER

As stated, the OF software comes equipped with a set of predefined solvers. In order to choose the most suitable solver it is necessary to take into consideration some parameters, which, in a first analysis, are, among others: type and number of fluids and flow regime.

Considering such parameters, the present case is dealing with incompressible and turbulent flow over a rigid model. Concerning the state, the flow field is calculated with a quasi-steady approach, i.e., it is assumed that over a short period it is a steady-state case, more specifically, the problem was solved for the initial time. From the solvers available in OF (*OpenFOAM - The Open Source CFD Toolbox: User guide* – Table 3.5), the following ones are some of widely used and possible choices (Table A3-2). Regarding each parameter, the crosses represent the range

of applicability of the presented solvers.

Table A3-2: OF predefined solver characteristics.

	Predefined solver	<i>simpleFoam</i>	<i> pisoFoam</i>	<i> pimpleFoam</i>	<i> interFoam</i>
State	Steady	<input checked="" type="checkbox"/>	<input type="checkbox"/>	<input type="checkbox"/>	<input type="checkbox"/>
	Transient	<input type="checkbox"/>	<input checked="" type="checkbox"/>	<input type="checkbox"/>	<input checked="" type="checkbox"/>
	Transient (large time-step)	<input type="checkbox"/>	<input type="checkbox"/>	<input checked="" type="checkbox"/>	<input type="checkbox"/>
Fluid	Compressible	<input type="checkbox"/>	<input type="checkbox"/>	<input type="checkbox"/>	<input type="checkbox"/>
	Incompressible	<input checked="" type="checkbox"/>	<input checked="" type="checkbox"/>	<input checked="" type="checkbox"/>	<input checked="" type="checkbox"/>
Phase	Single-phase	<input checked="" type="checkbox"/>	<input checked="" type="checkbox"/>	<input checked="" type="checkbox"/>	<input type="checkbox"/>
	Multiphase	<input type="checkbox"/>	<input type="checkbox"/>	<input type="checkbox"/>	<input checked="" type="checkbox"/>
Flow	Laminar	<input type="checkbox"/>	<input type="checkbox"/>	<input type="checkbox"/>	<input type="checkbox"/>
	Turbulent	<input checked="" type="checkbox"/>	<input checked="" type="checkbox"/>	<input checked="" type="checkbox"/>	<input checked="" type="checkbox"/>

Besides the predefined solvers presented, there are other possibilities; OF users develop their own code and make contributions into the public domain or not available the code but have publications which explain the developments made, which is the case of Liu and Garcia [74], already mentioned.

Due to the characteristics of the problem under study, a steady-state solver for incompressible flow can be employed to solve the flow equations, considering the free surface of the granular pile as a rigid wall. Therefore, the standard solver *simpleFOAM* was employed, to solve the RANS equations using the FVM discretization method. A parallelized computation with six processors was employed, and numerical convergence was assumed satisfied, when all the normalized residuals were lower than 1×10^{-5} .

As mentioned in Section A3.1.2, considering the phenomena under study, the most widely employed turbulence models are SST $k-\omega$ model and $k-\epsilon$ standard model, and, besides all the evidences point to SST $k-\omega$ model be the most suitable model of the two, some preliminary performance tests were carried out and are depicted in Figure A3-8.

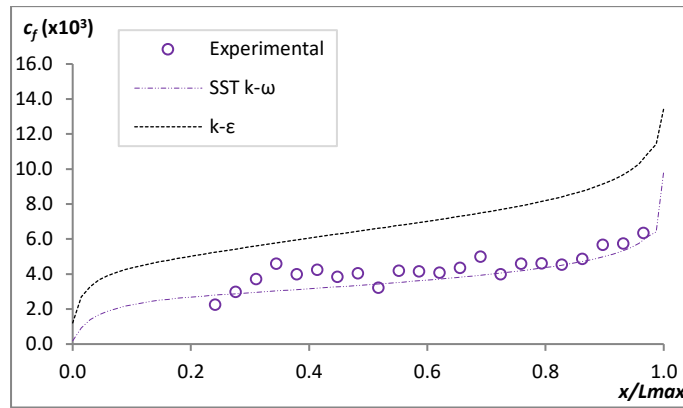


Figure A3-8: Comparison of the performance of two turbulence models ($k-\epsilon$ and SST $k-\omega$) against experimental data of an illustrative triangular case (S150).

It can be observed in Figure A3-8 that, as expected, the best agreement was achieved with the SST $k-\omega$ model. Therefore, this turbulence model was the one used in the numerical simulations with the automatic near-wall treatment.

Further details of each case can be found in the descriptions presented in the respective chapters, specifically, Chapter A4 for triangular piles and Chapter A5 for oblong piles.

CHAPTER A4

TRIANGULAR PILES

As already mentioned, the present work focuses on the study of piles with increasingly complex geometry. The first configuration to be studied is the triangular profile's transverse pile, which has a constant slope. The main characteristics of the numerical setup, e.g., mesh, boundary conditions and solver, were already presented in Chapter A3.

The flow around this configuration is investigated for different values of the stoss slope and the height of the crest. The experimental trial considered both rigid models and sand piles, as it will be described in Section A4.1.

Different measurements were performed, in particular shear stress, using the *Irwin* probes, pressure distribution and free surface deformation, and the results are presented in Section A4.2.

In Section A4.3, the predicted values by OpenFOAM are reported and evaluated by comparing them against the experiments. The analysis leads to preliminary conclusions, which are presented in section A4.4.

A4.1. CASE DESCRIPTION

In this section is described the triangular pile study case, namely the dimensional characteristics of the tested configurations and the experimental tests and procedures performed.

Besides the sand piles built in the wind tunnel to perform the erosion tests, rigid wooden models were also constructed for the measurements of pressure and the wall shear stress distribution along the piles' surface.

Three shapes were considered for the parametric study of the deformation of the free surface (erosion tests). Their geometry consists of a triangular prism, mimicking slopes, with windward inclinations of 10°, 15° and 20°, respectively (Figure A4-1). These configurations will be designated, hereinafter, as **S10**, **S15** and **S20**, respectively, regarding the stoss slope. To ensure identical conditions in the lee side, a leeward slope equal to the angle of repose ($\alpha=33.2^\circ$), was adopted for all configurations tested. The crest height (h) of 75 mm was imposed by the length of the traversing system on which the distance laser sensor was mounted (Section A2.4.1). The width of all shapes tested in the wind tunnel, in the spanwise direction, is equal to 1 m.

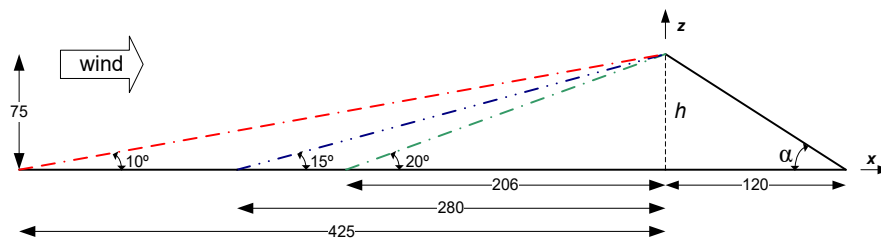


Figure A4-1: Geometry and dimensions of the three triangular piles tested. The windward slope of the various configurations is indicated in color and the lee side in black. (Dimensions in (mm); wind direction is from left to right).

It should be noted that in all figures of the present chapter, the value of $x = 0$ refers to the horizontal location of the crest of the different piles (Figure A4-1).

In order to build the triangular sand piles in the test chamber of the wind tunnel, it was used two wooden guides with the same dimensions of the models' profile. They were placed one meter apart, and then the space between them was filled with dried and sieved sand (Section A2.2). After, a ruler supported on the guides swept the sand to obtain the final shape of the dune's model. The placement of the piles in the test chamber is shown in Figure A2-2 (Section A2.1).

In the course of erosion tests, the piles are subjected to the airflow and the wind tunnel is stopped at cumulative time instants (1 minute each) to allow the profiles recording. The

measurement of each profile was processed over the section along the centerline located half-way the width of the pile to ensure that the edges effects can be neglected.

As mentioned, the wall shear stress and the pressure distribution along the pile's surface were measured with *Irwin* probes and pressure taps, respectively, distributed along the rigid models' surfaces. Besides the configurations presented in Figure A4-1, another model was built with a windward slope of 15°, but with a crest height (h) of 150 mm, called hereinafter as **S150**. This higher configuration was built only in wood (rigid model), due to the traversing system limitations. The main characteristics of the tested piles are summarized in Table A4-1.

Table A4-1: Main characteristics of the configurations used in the triangular pile study case.

Model	S10	S15	S20	S150
<i>Crest height</i> [mm]	75	75	75	150
<i>Stoss angle</i> [°]	10	15	20	15
<i>Stoss base length</i> (L_{max}) [mm]	425	280	206	560
<i>Lee base length</i> [mm]	120	120	120	240

Furthermore, the blockage ratio (frontal area of the model divided by the crosswise wind-tunnel section) was calculated for all triangular configurations and the highest value and consequently the worst case, corresponding to **S150**, is 3.75%. Even this value satisfies recommended values which should be less than 5% [99,100].

The same free stream wind speed was used in all experimental tests, specifically, $U_0=9.9$ m/s. However, in some of the tests, different velocities were considered in order to evaluate the influence of the Reynolds number. Thus, where justified, the value of the employed velocities will be indicated.

The numerical predicted wall shear stress and static pressure distributions in the surface of the piles were obtained for the initial shape of the pile. These results are discussed in Section A4.3, including the comparison with the experimental measurements and the correlation with the erosion profiles.

A4.2. EXPERIMENTAL RESULTS

The results measured on the rigid models are presented first, in particular the pressure coefficient (Section A4.2.1) and the wall shear stress (Section A4.2.2) distribution. In the erosion tests, only the evolution of the free surface deformation is measured, and these results are presented in Sections A4.2.3 and A4.2.4. In addition, the threshold friction velocity (u_{*t}) correlation with the free deformation rate is presented in Section A4.2.3.

A4.2.1. PRESSURE COEFFICIENT DISTRIBUTION

The pressure coefficient distribution was measured in all rigid models for three different undisturbed wind velocities. In order to assess the repeatability of the measurements obtained with the pressure taps, as defined by VIM3: International Vocabulary of Metrology [101], five tests were conducted for the intermediate velocity ($U_0=9.9$ m/s). The deviation was calculated with Equation (A4-1) and similar results were obtained in all configurations, as presented in Figure A4-2.

$$deviation = \left| \frac{\sum_{i=1}^n (c_{p_i} - c_{p_m})}{n \cdot c_{p_m}} \right| \times 100 \quad (\text{A4-1})$$

where n is the number of tests, the index i corresponds to each test and the index m is the mean value of all performed tests.

In this section, to allow an easier interpretation of the charts, the dependent variables, namely deviation and c_p , are plotted against the distance normalized with the total length of the piles. It should be noticed that the L_{max} values are different upstream and downstream of the crest, and vary according to the configuration (Table A4-1).

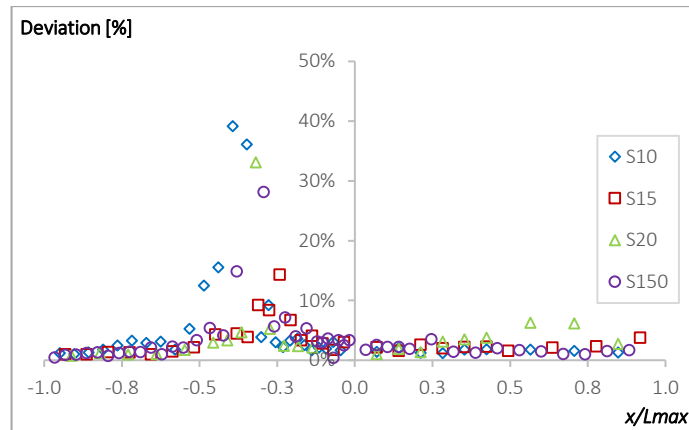


Figure A4-2: Pressure coefficient repeatability tests: absolute deviation [%] distribution for all cases, for $U_0=9.9$ m/s.

It can be noted in Figure A4-2 that higher discrepancies were registered in the stoss side of the models, and, interestingly, in a small area between half-length and the crest of the model ($-0.5 < x/L_{max} < -0.3$). The location of this variation can be related to the acceleration of the flow towards the pile's crest, as observed by several authors [20,102,103].

In order to compare the results of all tested physical models, a mean absolute deviation of the measurements, computed along the entire stoss surface of the pile, is presented in Table A4-2.

Table A4-2: c_p repeatability tests: mean absolute deviation [%] for all cases and for $U_0=9.9$ m/s.

Model	Mean absolute deviation [%]
S10	5.12
S15	3.36
S20	4.16
S150	6.85

Due to the higher deviations observed in the region $-0.5 < x/L_{max} < -0.3$ of the stoss side (Figure A4-2), the mean values tend to be increased; even so, taking into consideration the results presented in Table A4-2, the measurements present good level of repeatability.

Figure A4-3 depicts, for each tested case, the pressure coefficient distribution along the piles.

Model

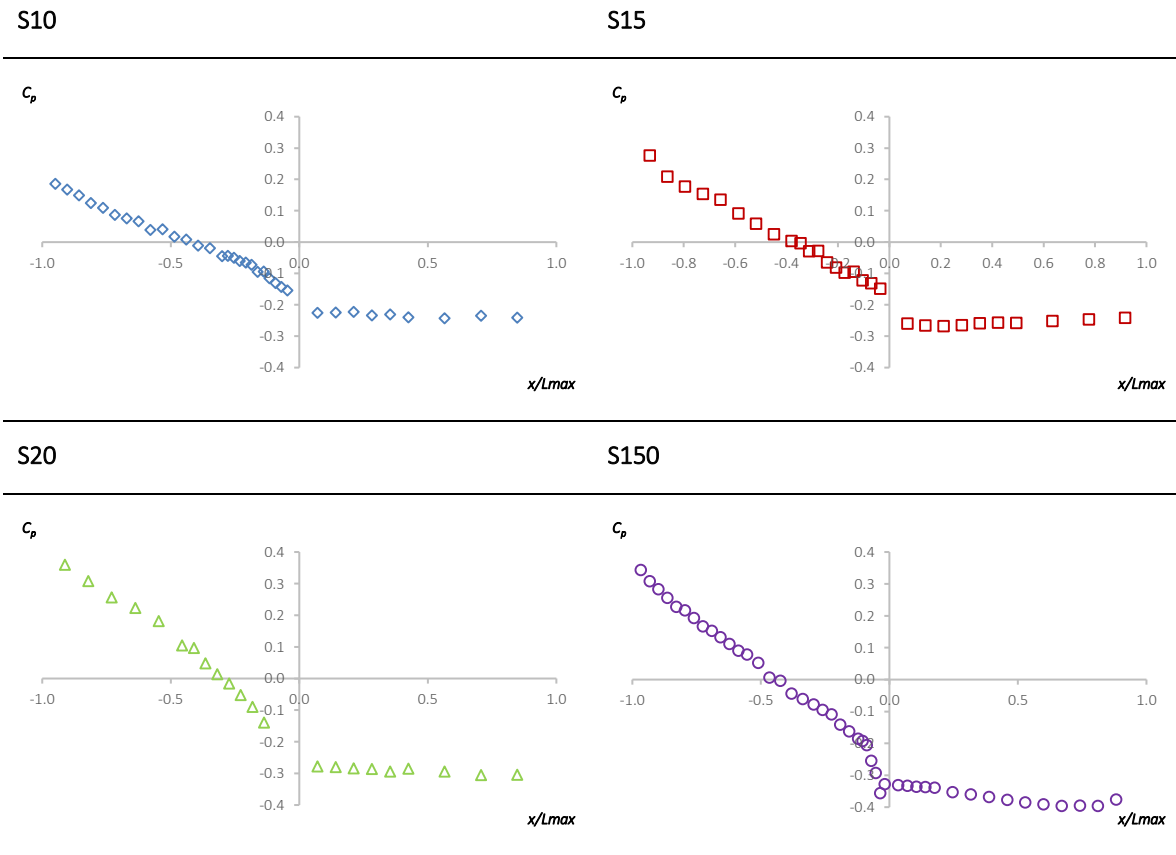


Figure A4-3: c_p distribution for all tested cases, for $U_0=9.9$ m/s.

The behavior on the stoss side of the piles is similar for all configurations, as shown in Figure A4-3; with **S10** presenting the lowest pressure gradient corresponding to the lowest value of the stoss angle, while **S20**, for similar reasons, presents the highest pressure gradient. For the cases studied, the shift to negative values of the pressure coefficient occurs at approximately the same location, which corresponds to the region where higher deviation values were observed, when conducting the repeatability tests (Figure A4-2).

Regarding the leeward side, similar behavior occurs for all cases. Due to the recirculation zone, the pressure gradient is nearly constant, with the cases **S10** and **S20**, again, with the lowest and highest values, respectively. These results are consistent with those reported by Lee and Park [104].

In order to evaluate the Reynolds number dependency on the pressure distribution, tests were conducted for two additional undisturbed wind velocities, specifically, $U_0=6.60$ m/s ($Re=6.2 \times 10^4$) and $U_0=12.95$ m/s ($Re=1.2 \times 10^5$). Similar results were achieved for all four configurations, consequently, Figure A4-4 only reports case **S150**, as the representative case.

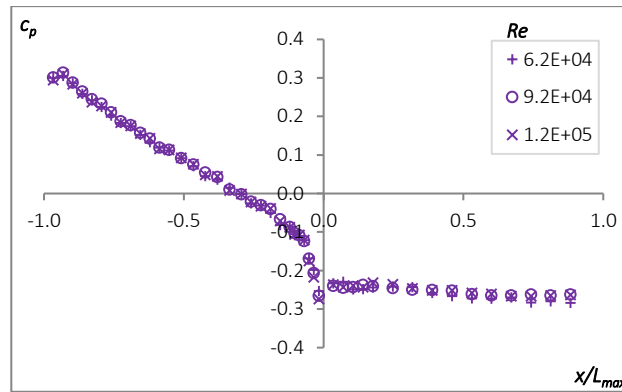


Figure A4-4: Influence of the Reynolds number on the pressure coefficient distribution (case **S150**).

It can be observed in Figure A4-4 that, regardless the Reynolds number value, the measured pressure coefficient along the entire model's profile is approximately equal, which is indicative of the Reynolds number independence condition.

A4.2.2. FRICTION COEFFICIENT DISTRIBUTION

The wall shear stress (τ_w) was measured along the stoss side of all rigid models using *Irwin* probes. The probes were placed only on the stoss side, and the number of probes distributed depends on the available surface of each pile, as already mentioned in Section A4.2.3.

The repeatability tests of these sensors for this kind of piles were conducted by performing the measurements five times, for case **S150** and $U_0=9.9$ m/s. The deviation was calculated with Equation (A4-1) and the corresponding results are reported in Figure A4-5.

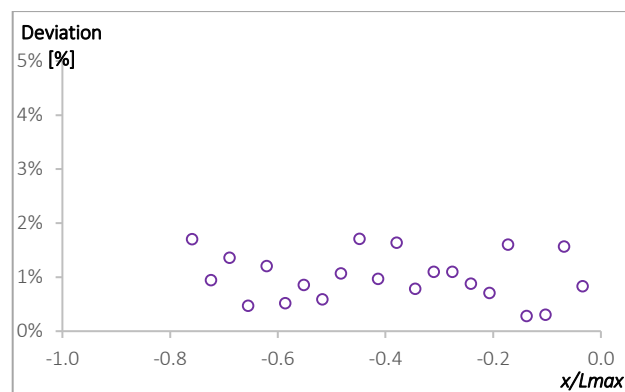


Figure A4-5: *Irwin* probe pressure difference repeatability tests: absolute deviation [%] distribution for case **S150**, for $U_0=9.9$ m/s.

It can be concluded that the probes have good level of repeatability, considering that the mean absolute deviation is around 1%, with a variation range from 0.27% to 1.70%.

Figure A4-6 depicts the distribution of the friction coefficient (c_f) along the stoss side of the piles (all cases) for $U_0=9.9$ m/s.

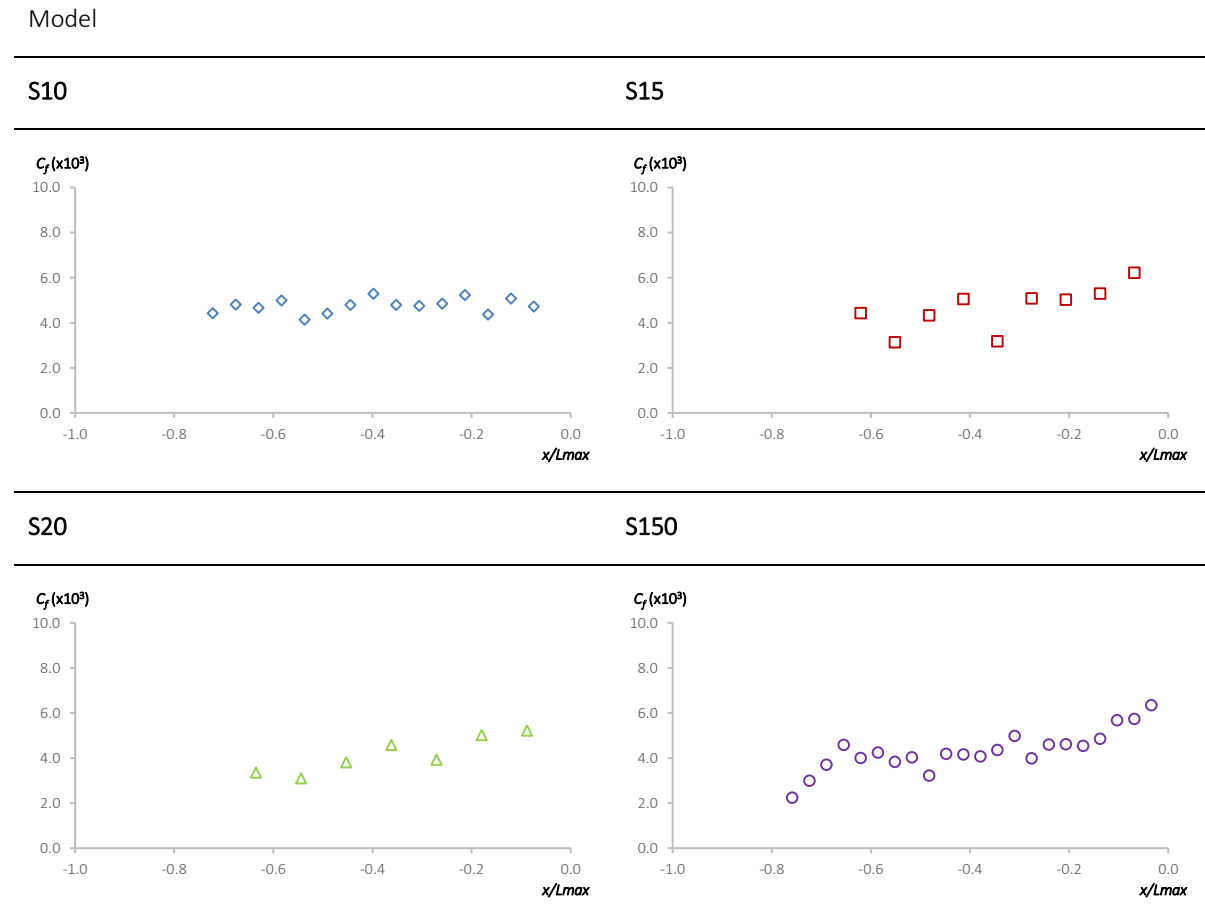


Figure A4-6: c_f distribution along the stoss side of the piles, for $U_0=9.9$ m/s.

It can be observed in Figure A4-6 that the general behavior of all configurations is analogous, where the wall shear stress increases toward the pile’s crest and the range of registered values is similar.

Moreover, a slightly scatter behavior can be seen in all geometries, which may be due to different degrees of intrusion of the probes into the flow or due to their leveling with the surface.

Additionally, a direct comparison of cases **S15** and **S150** is presented in Figure A4-7 to assess the crest’s height influence. Despite the scattering, it can be noted that similar values were measured along the stoss face of both models.

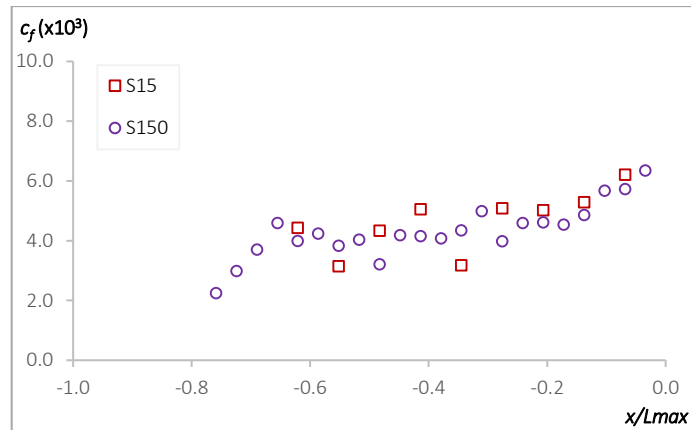


Figure A4-7: c_f distribution along the stoss side of the piles – influence of the crest' height (cases **S15** and **S150**).

Similar to the pressure tests, the dependence of friction results on the Reynolds number was also evaluated for $U_0=6.60$ m/s ($Re=6.2 \times 10^4$) and $U_0=12.95$ m/s ($Re=1.2 \times 10^5$). Due to their representativity, only the results obtained with model **S150** are presented in Figure A4-8.

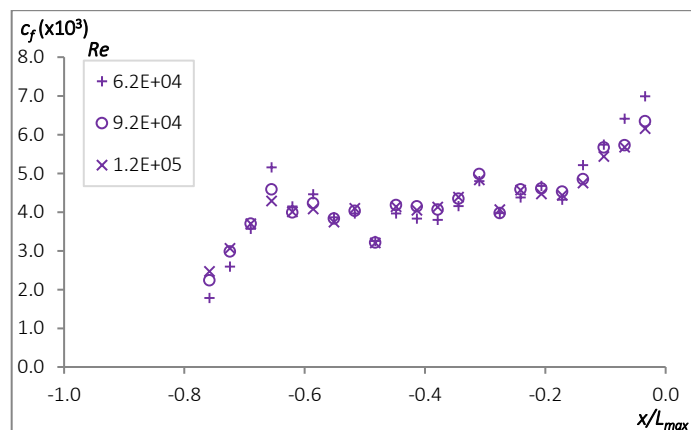


Figure A4-8: Influence of the Reynolds number on the friction coefficient distribution (case **S150**).

Regardless of the Reynolds number value and as already observed in Figure A4-4, similar friction coefficient results were obtained along the entire model.

In section A4.2.3, it is presented the threshold friction velocity (u_{*t}) correlation with the free deformation rate.

A4.2.3. FREE SURFACE DEFORMATION

The erosion tests were only performed in the piles with crest height of 75 mm, i.e. models **S10**, **S15** and **S20**. Figure A4-9 reports the measured profiles for all configurations for the three first cumulative time instants (time interval of erosion: 1 minute), as mentioned in Section A4.1. In each graph, it is presented the mean, highest and lowest profile. The initial (triangular) profile is also depicted as a reference contour.

Based on visual observation, the eroded profile of (**S10**, $t=3$ min) spreads beyond $x>240$ mm; however, such region was not measured due to length restrictions of the traversing system used.

The mean contour was calculated based on five trials performed for each case. All profiles were measured up to $x=240$ mm, being $x=0$ mm, as already mentioned, the horizontal coordinate of the crest of the piles. The mean profiles are those used for the computation of the normal fluxes.

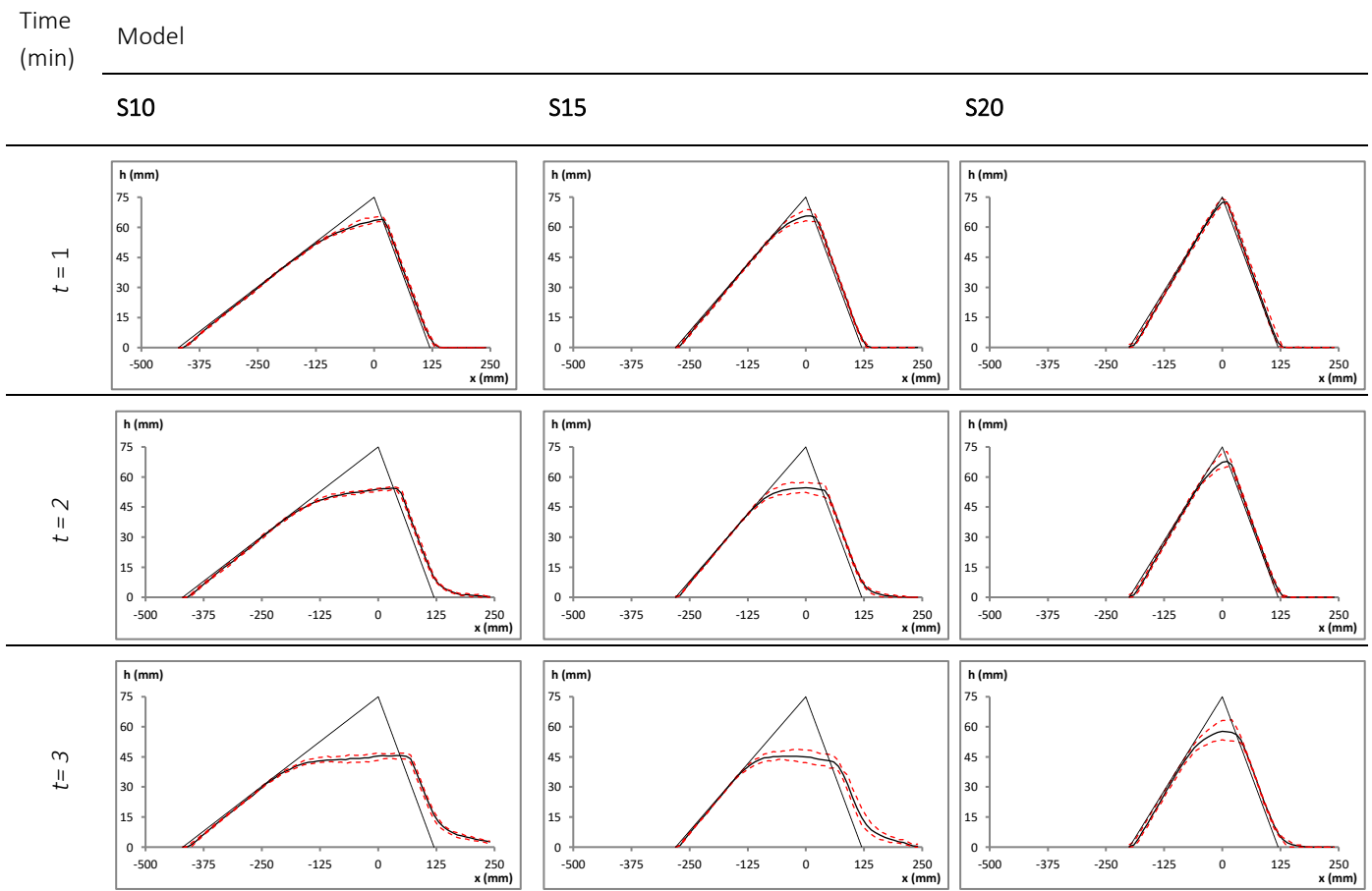


Figure A4-9: Erosion profiles (initial profile - dotted line, average - continuous line, minimum and maximum - dashed lines) for $U_0=9.9$ m/s (vertical scale deliberately enlarged).

As discussed in Section A1.1.3.1, the threshold wind speed is proportional to the slope of the pile (Equation (A1-6)), and taking into consideration that the results presented in Figure A4-9 were obtained for the same undisturbed wind speed of $U_0 = 9.9$ m/s, the highest deformation rate occurs for case **S10**.

Figure A4-10 presents the erosion contours (as in Figure A4-9) along with the friction velocity results (Figure A4-6), to verify an eventual correlation.

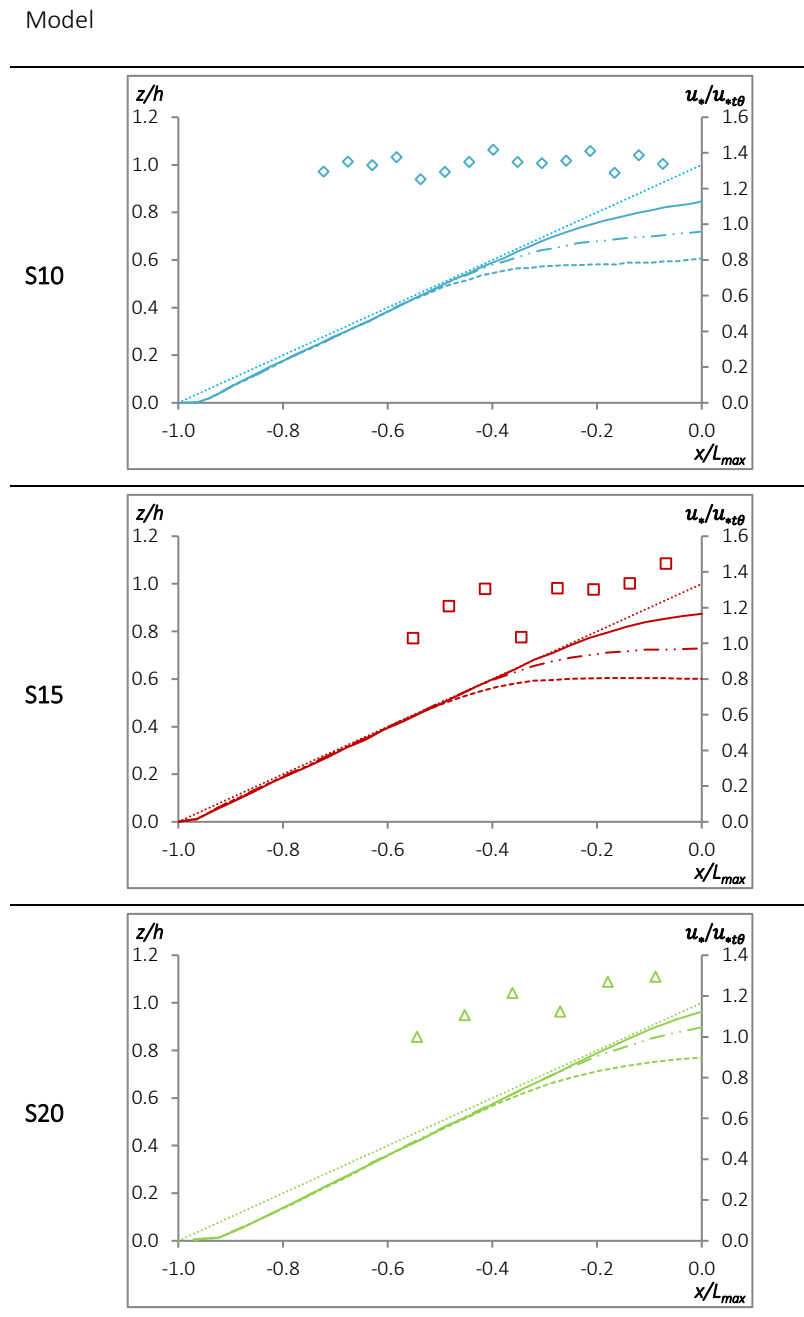


Figure A4-10: Normalized erosion profiles (z/h) at several erosion times (solid line: $t=1$ min; dash-dot-dot line: $t=2$ min and dashed line: $t=3$ min), and experimental measurements of the friction velocity across the stoss slope (markers) (dotted line corresponds to the ideal initial stoss slope).

As expected, the erosion occurs mainly in the region where the friction velocity exceeds its threshold value (Equation (A1-4)), i.e., $u_* / u_{*t\theta} > 1$. Nevertheless, it should be emphasized that the *Irwin* probes were placed in the rigid models (fixed triangular shape), while the erosion contours are continuously changing over time. Furthermore, the threshold value used for each case, will be the one reported in Figure A4-19, as it will be discussed in the following section (Section A4.2.4)

It can be observed in Figure A4-10 that for case **S10**, most of the $u_* / u_{*t\theta}$ values are higher than 1, which is indicative that erosion is susceptible to occur in the entire stoss face; however, only the area near the crest has eroded ($x/L_{max} > -0.4$). The modification of the pile's profile during the tests can affect the wind pattern over the leading edge and, consequently, the friction velocity, leading to the behavior seen in case **S10**. In case of a longer erosion test, most likely the erosion would extend to the leading region of the windward surface.

In the remaining cases, the threshold condition is overcome essentially in the crest area, and such data correlates well with the erosion profiles. Due to the erosion, the piles' profile changes over time and, as already stated, the friction velocity was measured in rigid models, so, beyond a certain erosion time, it is no longer realistic to correlate these two sets of results.

A4.2.4. SAND EMISSION RATE (Φ)

As mentioned in Section A2.4.2, for the computation of the sand emission rate, during the time interval (Δt), i.e., between instants (t) and ($t + \Delta t$), and per unit of depth and length (L), Equation (A2-4) was used.

As the surface profiles were measured at several discrete instants ($t=1, 2$ and 3 minutes), the computed erosion fluxes correspond to the average value during each time interval. For example, the mean flux, between $t=1$ and $t=2$ minutes, represented here by Φ_{12} , is calculated using the pile contours measured at those two instants.

Figure A4-11 presents the mean flux during the first three time intervals for each pile. Positive flux values indicate erosion, whereas negative values correspond to areas where deposition occurs. In general, it can be stated that the mean flux intensity increases as time goes by, which can be justified by the fact that, as the pile gets eroded near the crest, its slope decays leading to a lower threshold shear velocity, as described by Equation (A1-4). Figure A4-11 also reveals that the increase of the pile slope yields a rise of the erosion time necessary to achieve the maximum flux rate. For example, while the maximum emission rate for **S10** is observed during the first time interval – from $t=0$ to $t=1$ min, for pile **S15** it occurs during the second period – $t=1$ min to $t=2$ min. In what concerns the steeper shape (**S20**), the largest flux value is displayed

only during the third time interval - $t=2$ min to $t=3$ min.

Model

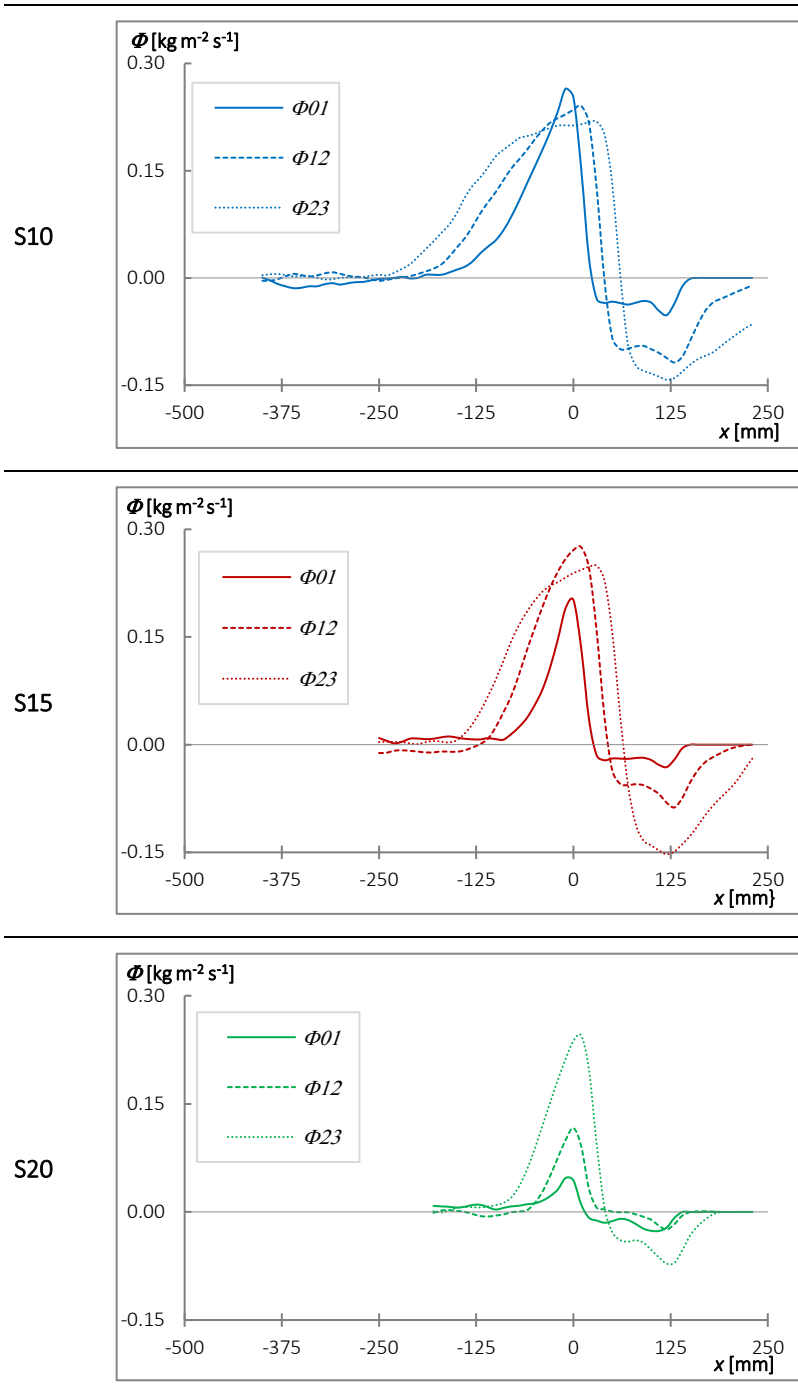


Figure A4-11: Mean sand emission rate during three time intervals for each pile.

It can be observed in Figure A4-11, that, only in case **S10**, the highest emission rate occurs on $x=0$, i.e., on the location of the initial crest (at $t=0$). This can be explain by the fact that, as time goes by, piles **S15** and **S20** get flattened and their crests are gradually shifted to the right.

In Figure A4-12, it is presented the comparison between the three geometries for the first time interval (Φ_{01}). The maximum erosion rate was observed on the **S10** configuration; in contrast, as expected, the steeper configuration (**S20**) shows the smallest rate. These three experimental data sets corresponding to the average fluxes during that time interval will be used to calibrate Shao's [15] model (Section A4.3.4).

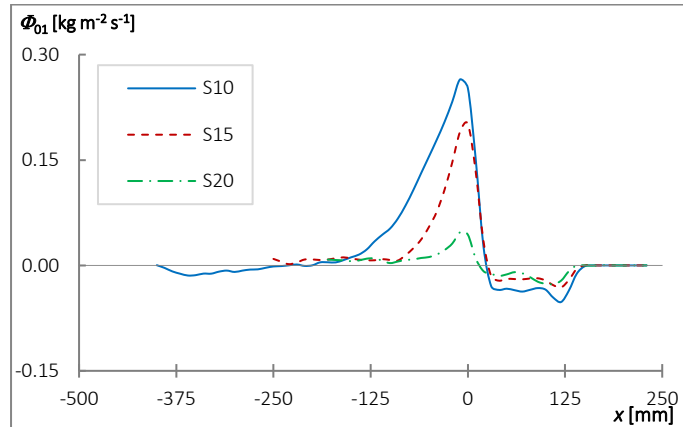


Figure A4-12: Comparison for the normal sand emission rate for the three geometries during the time interval $t=0$ to $t=1$ min.

A4.3. NUMERICAL RESULTS

The results presented in this section were obtained using the open source CFD toolbox OpenFOAM. The main characteristics of the numerical simulations in what concerns mesh generation, boundary conditions and solver are presented in Chapter A3.

In order to validate the numerical model, the predicted values by OpenFOAM were compared against the experimental results already presented and discussed in Section A4.2.

The sequence that will be followed in this section will be similar to that used in the presentation of the experimental results, so, the distribution of the pressure coefficient in the various simulated configurations will be presented and discussed first (Section A4.3.1). In Section A4.3.2, the friction coefficient is compared against the values measured experimentally. Then, some observations on the flow topology are made in Section A4.3.3. Finally, a comparison of the streamwise flux (q) obtained with several models (Equations (A1-7) to (A1-10)) is discussed in Section A4.3.4, as well as a calibration of the Shao's [15] dust scheme.

A4.3.1. PRESSURE COEFFICIENT DISTRIBUTION

The four configurations presented in Table A4-1 are also used in the numerical simulations. The comparison between the experimental measured pressure coefficient distribution in the rigid models and the predicted values by OpenFOAM are depicted in Figure A4-13. As in Section A4.2.1, all the variables are plotted against the normalized distance with the respective total length of the stoss and lee sides.

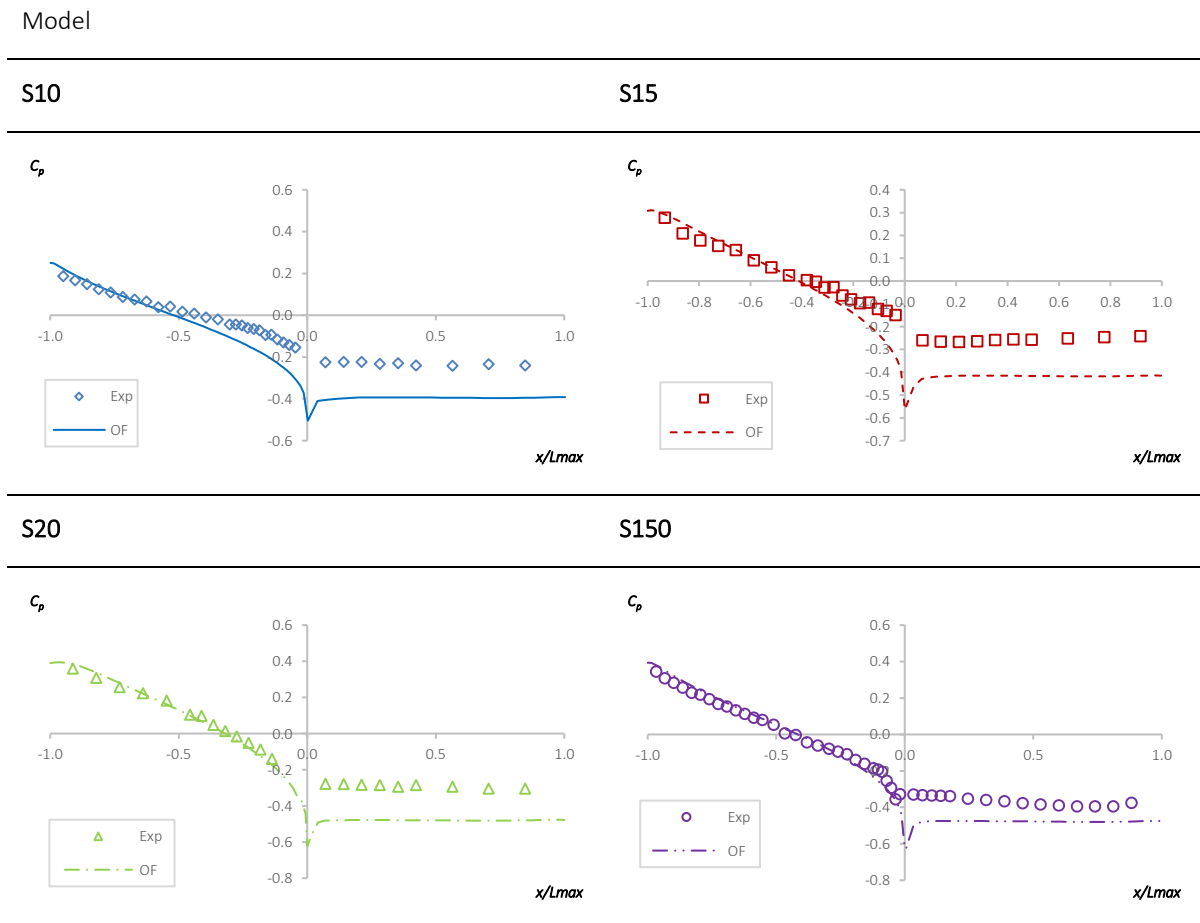


Figure A4-13: Experimental pressure coefficient distribution (markers) against predicted values by OpenFOAM (lines) for $U_0=9.9$ m/s.

Considering the windward side of the cases presented in Figure A4-13, there is good agreement between the experimental results and the predicted values by OpenFOAM. The values up half-length of the stoss face and the location where the pressure coefficient turns negative are well predicted by the numerical tool. Beyond this position, until the crest, the agreement for the less steep (**S10** and **S15**) cases worsens. In all cases, the larger values of the discrepancies occur at the area near the crest and downstream.

Regarding the leeward side of the models, although the behavior of the predicted values is similar to the experimental results, i.e., a constant pressure along the entire surface; the predicted pressure coefficient has a magnitude nearly two times that obtained experimentally.

The overall comparison between the experimental and numerical results clearly indicates that the agreement worsens in the regions where negative values of pressure coefficient occur; this observation may be due to the limitations of the turbulence model used in predicting flows with separation and favorable pressure gradients.

Also, the influence of the Reynolds number on the flow was assessed through the numerical simulations. The predictions are similar to the experimental results (Figure A4-4), as it can be observed in Figure A4-14. As expected, once again the Reynolds number independence condition prevails.

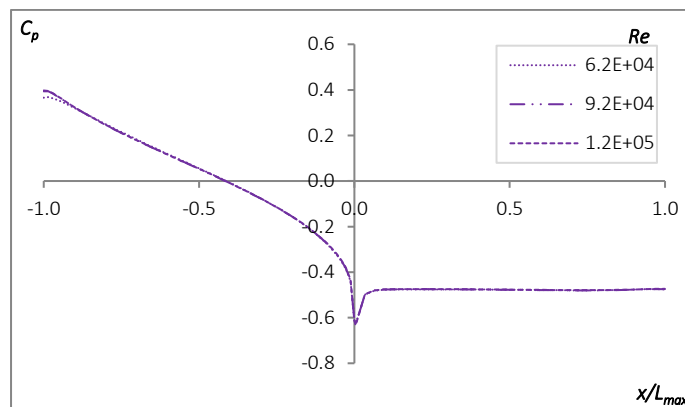


Figure A4-14: Influence of the Reynolds number on the pressure coefficient distribution predicted by OpenFOAM (case **S150**).

A4.3.2. FRICTION COEFFICIENT DISTRIBUTION

The friction coefficient distribution along the stoss side predicted by OpenFOAM for all configurations was compared against the experimental values, as presented in Figure A4-15. It should be noticed that the c_f values presented in Figure A4-15 are multiplied by the factor 10^3 .

It can be observed in Figure A4-15 that OpenFOAM predicts well the distribution of c_f , being the flatter configuration (**S10**) where the agreement between predictions and experiments is the least favorable. Furthermore, as mentioned in Section A4.2.2, the technical issues associated with the experimental measurements with the *Irwin* probes may contribute to the augmentation of the observed deviations.

Case

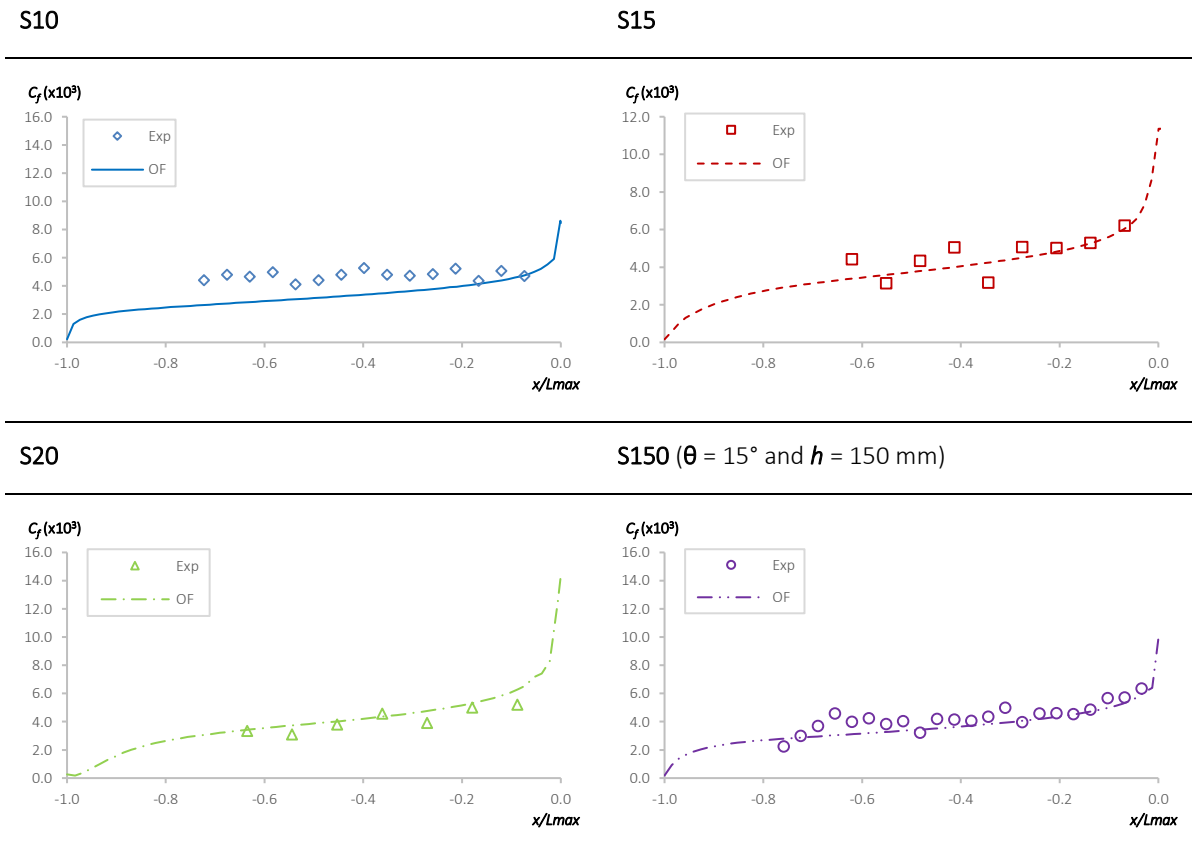


Figure A4-15: Experimental friction coefficient distribution (markers) against predicted values by OpenFOAM (lines) for $U_0=9.9$ m/s.

In what concerns the CFD values, the higher differences between the four configurations occur close to the leading edge and near the crest, being the values half-length quite similar. Comparing the physical models with the same crest height (**S10**, **S15** and **S20**), the steeper is the stoss side, the higher is the friction coefficient in the crest. The opposite effect takes place on the leading edge, where the highest values of C_f occur for the smallest slopes. The results of case **S150** are very interesting; in the leading edge, the friction coefficient is very similar to that of case **S15**, since the slope angle is the same, so the shape of the piles is the same. Regarding the values around the crest, they are close to those of case **S10**, which is a consequence of cases **S150** and **S10** having similar length of the stoss face (Table A4-1).

Figure A4-16 depicts the friction coefficient distribution for three different undisturbed wind velocities, and minor differences occur between the profiles. Likewise in Figure A4-8, once again, the Reynolds number independence condition is observed.

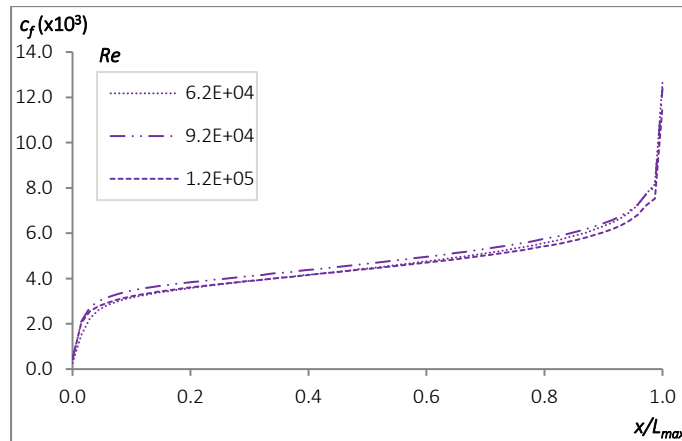


Figure A4-16: Influence of the Reynolds number on the friction coefficient distribution predicted by OpenFOAM (case **S150**).

A4.3.3. FLOW TOPOLOGY

Figure A4-17 reports the flow topology predicted computationally; the region in the vicinity of the piles is of particular interest to the present study; the predicted local data may be critical to the evaluation and adjustment of the model. It can be noticed that the recirculation zone starts right at the crest of the pile ($x = 0$ mm) as expected, and the wake region extends well downstream. Furthermore, the size of the recirculation zone grows with the increase of the upwind slope angle. All streamline contours are calculated for the configuration at time $t=0$, except for case **S10**, for which the profile at $t=1$ min (Figure A4-9) is also presented

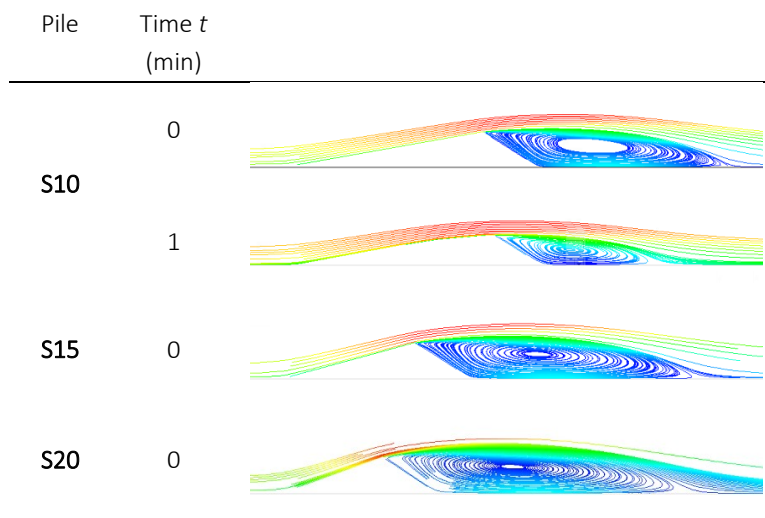


Figure A4-17: Flow topology predicted for $U_0 = 9.9$ m/s at $t=0$ (and also $t=1$ min for pile **S10**).

It can be observed for case **S10**, after 1 min of erosion, the recirculation zone decreases substantially. The main difference between the two profiles, $t=0$ and $t=1$ min, respectively, of case **S10** (Figure A4-17) is concerned with the region around the crest, where the free surface profile is flattened; the initial sharp vertex disappears, causing a major modification of the flow topology in the wake.

A4.3.4. STREAMWISE FLUX (q) AND SAND EMISSION RATE (Φ)

The sand flux magnitude is directly related to the wall shear stress and, therefore, associated with friction velocity (u_*) and threshold friction velocity (u_{*0}). According to Equation (A1-4), u_{*0} is calculated using the threshold friction velocity on a horizontal surface, affected by a factor dependent on the surface's slope and angle of repose. The wall shear stress and, more specifically, the friction coefficient is the quantity selected to perform the comparisons between the experimental and the predicted values by OF; nevertheless, it is directly related to u_* as described by Equation (A1-2). Considering only the cases with $h=75\text{mm}$, Figure A4-15 was rearranged and Figure A4-18 reports the comparison of the shear velocity distribution predicted numerically along the windward face of configurations **S10**, **S15** and **S20**, for $U_0=9.9$ m/s.

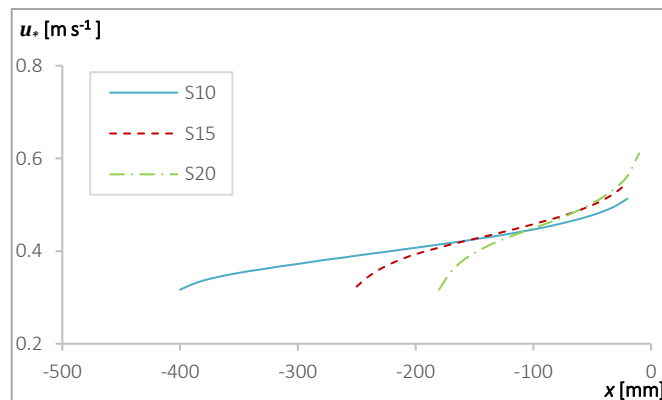


Figure A4-18: Predicted friction velocity along the windward slope of the three geometries (**S10**, **S15** and **S20**) at $t=0$ for $U_0=9.9$ m/s.

As discussed in Section A1.1.3.2, the model of Shao [15] requires the adoption of a saltation model (q), and, among those most frequently used in aeolian studies, four models were selected, namely, Bagnold [18] (Equation (A1-7)), Kawamura [34] (Equation (A1-8)), Owen [35] (Equation (A1-9)), and Lettau and Lettau [16] (Equation (A1-10)). Apart from the Bagnold's

model (Equation (A1-7)), all the remaining models to compute the streamwise flux require the specification of the threshold shear velocity ($u_{*t\theta}$).

Figure A4-19 depicts the sand emission rate during the first time interval, and it results from the combination of the data sets reported in Figure A4-11 (experimental sand emission rate) and in Figure A4-18 (friction velocity prediction). As usual, the threshold friction velocity, above which erosion occurs, is defined as the minimum shear velocity required for aerodynamic forces to overcome the opposing forces. In this way, Figure A4-19 allows the observation of the threshold shear velocity necessary to initiate erosion in the experiments. These values (“Experimental”) are given in Table A4-3 along with $u_{*t\theta}$ “Calculated” results obtained from Equation (A1-4)).

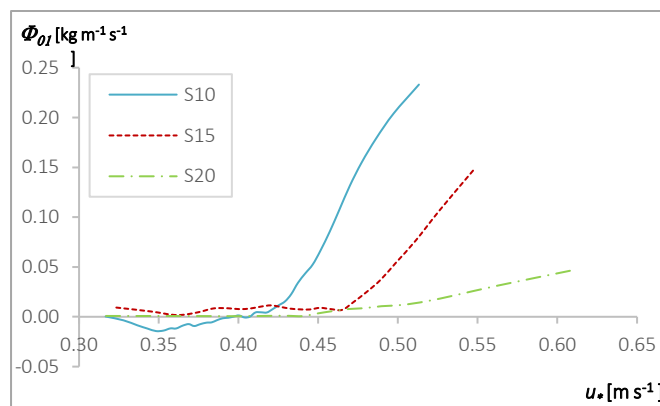


Figure A4-19: Comparison of the normal sand emission rate between the three geometries (S10, S15 and S20) during the time interval $t=0$ to $t=1$ min.

Table A4-3: Values of threshold friction velocity (calculated using Equation (A1-4) and observed experimentally (Figure A4-19)).

Case	$u_{*t\theta}$	
	Calculated	Experimental
S10	0.37	0.418
S15	0.39	0.465
S20	0.40	0.440

Close observation of Table A4-3 indicates that the “Experimental” values are larger than those “Calculated”. Most likely, the discrepancy is related to the size and configuration of the piles studied here, namely to the relatively short distance between the windward pile toe and the onset erosion location, which affects the flow development along the stoss slope. In addition, the CFD tool used in the present study does not consider the effect of saltating particles (saltators), which, when are present in the flow field, tend to reduce the threshold friction velocity. This aspect is taken into account through the Bagnold’s threshold parameter (A) in

Equation (A1-1). The “Experimental” values of $u_{*\theta}$ will be those used in the Shao’s [15] model calibration procedure.

The simplified dust emission scheme of Shao [15] is calibrated against the present experimental results. The best fitting is obtained by adjusting the empirical c_y parameter of Equation (A1-17), which, obviously, depends on the selected saltation model (Equations (A1-7) to (A1-10)). The need to calibrate the dust emission scheme of Shao [15] relies on the intention to use it to model, not dust, but a sand emission flux and on the underlying assumption that, as a first approximation, sand emission has similar behavior to dust.

To demonstrate the usefulness and applicability of the calibrated Shao’s [15] model, the calibration is illustrated for the first time interval, using the experimental data of Φ_{01} (Figure A4-12). The selection of the initial pile shape is due to the fact that, as already mentioned, only instant $t=0$ was numerically simulated.

As a simplification, it is assumed that the shear velocity computed for the initial instant (i.e., at $t=0$; triangular configuration) is constant and representative of the first entire time interval. To assess this assumption various sensitivity CFD tests were conducted, modeling the wind flow at two instants, as illustrated by the two plots presented in Figure A4-17, for configuration **S10**, showing the predicted flow topology at instants $t=0$ and $t=1$ min, respectively. Figure A4-20 presents the friction velocity distribution, along the windward slope of S10, at $t=0$ and $t=1$ min. As observed, the variation between those two instants can be considered relatively small, in spite of the noticeable reduction of the recirculation bubble length observed in Figure A4-17.

It should be noticed that the larger variation in Figure A4-20 occurs at $x \approx -100$ mm and near the pile’s crest, due to the local modification of the pile’s profile once eroded. The relatively small difference of u_* , between $t=0$ and $t=1$ min, supports the simplification made in the present work by considering the flow characteristics at $t=0$ as representative of the first time interval.

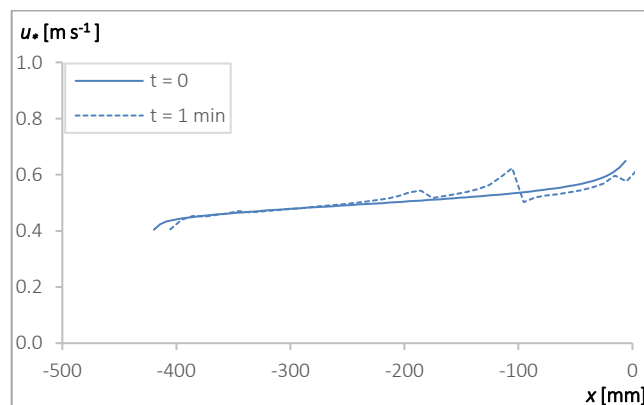


Figure A4-20: Predicted shear velocity distribution along the windward surface of configuration **S10** at instants $t = 0$ and $t = 1$ min.

Figure A4-21 shows, for case **S10**, the comparison between the measured values of the sand emission flux against those predicted by Shao’s [15] model. The three curves shown (corresponding to the saltation models of Owen [35]; Kawamura [34] and Lettau and Lettau [16]), were adjusted to determine its specific “best” c_y value, listed in Table A4-4, which corresponds to the minimum absolute deviation between computed and experimental flux results.

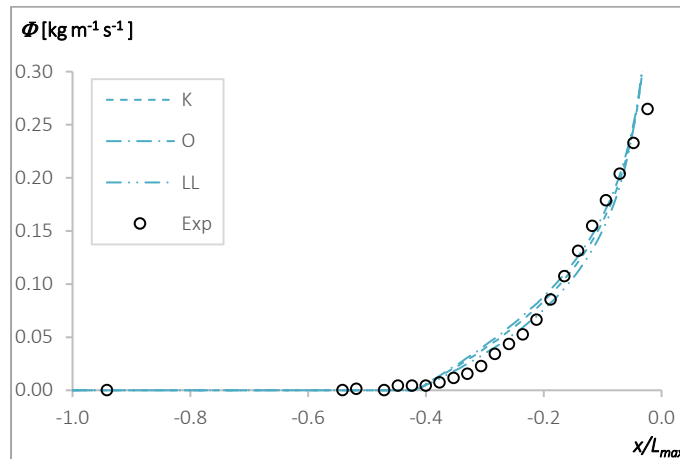


Figure A4-21: Comparison of the measured sand emission rate (case **S10**) against the predicted values of calibrated Shao’s [15] dust scheme (K – Kawamura (Equation (A1-8)); O – Owen (Equation (A1-9)) and L – Lettau and Lettau (Equation (A1-10)), during time interval $t = 0$ to $t = 1$ min; each model is based on the specific c_y value as listed in Table A4-4.

Table A4-4: Coefficient c_y for each saltation model and for each case.

Saltation model	S10	S15	S20
Kawamura (K)	0.1	0.14	0.02
Owen (O)	0.3	0.42	0.06
Lettau & Lettau (LL)	0.1	0.14	0.02

As it can be observed in Figure A4-21, the three calibrated curves are similar; therefore, only the results with the saltation model of Lettau and Lettau [16] are presented in Figure A4-22, considering that this model is one that yields the best comparison.

The c_y magnitude (Table A4-4) is much larger than the Shao’s [15] value ($c_y=5 \times 10^{-5}$); however, it should be pointed out the difference in the soil plastic pressure (P) [51] - while Shao [15] used 10^3 Pa (for dust), in the present work, such parameter was set equal to 15×10^3 Pa (for sand). In order to obtain the soil plastic pressure, compression tests were performed adapting the procedure described by Rice et al. [51] to that used granular material (dry sieved sand) in the present work. However, differences in the sample preparation and penetrometer type along with the material tested may have led to the discrepancy between the soil plastic

pressure values.

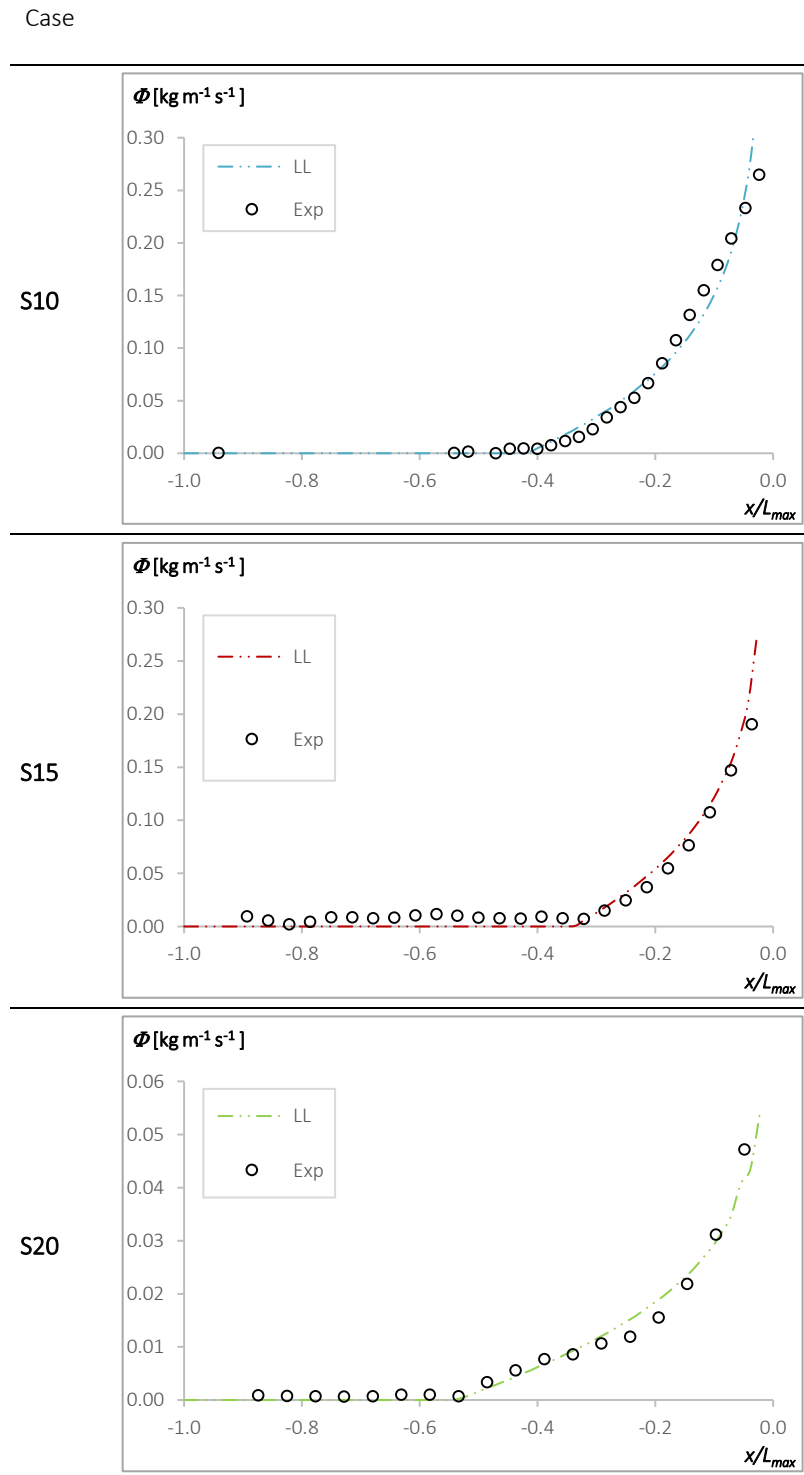


Figure A4-22: Comparison of the measured sand emission rate (markers) against the predicted values of calibrated Shao's [15] dust scheme (lines), using the Lettau and Lettau's [16] saltation model, for all cases, during time interval $t = 0$ to $t = 1$ min; each case is based on the specific c_y value as listed in Table A4-4.

The original formulation of Bagnold, i.e. Equation (A1-7), does not consider a threshold value,

which could suggest that erosion would always occur regardless the value of u_* , as long as it is different from zero. That is not the case for the other three saltation models; as indicated by the experimental measurements, this would lead to high discrepancy values in several regions, and in particular near the upstream pile toe. Therefore, Bagnold's formulation is not suitable for the calibration procedure tested in this study - reason why Bagnold's c_y values are not listed in Table A4-4.

Figure A4-21 demonstrates the validity of the present method, regardless of the saltation model being used, to estimate the normal sand flux, when the appropriate c_y is employed. It is important to reiterate that the use of this methodology in conditions different from those presented in this study requires some caution, due to the need of always determining the appropriate value of c_y .

Although Figure A4-22 only depicts the results using the Lettau and Lettau's [16] saltation model; for all cases the calibration of the remaining models was performed and the c_y parameter determined, as listed in Table A4-4. Interestingly, in all configurations, Kawamura's [34] and Lettau and Lettau's [16] models use the same c_y parameter, whereas for the Owen's [35] model a value three times higher was found.

A4.4. CONCLUDING REMARKS

The purpose of the present chapter is to evaluate the behavior of two-dimensional granular transverse dunes. This work comprises the comparison between OpenFOAM predicted and experimentally-derived values, respectively, for pressure and friction coefficients with the aim of validating the numerical model and the study of the emission flux from sandy sloped surfaces, including the calibration of the simplified dust model of Shao [15].

Three geometries were selected, all of them corresponding to triangular prisms mimicking transverse sand piles, with stoss slopes of 10°, 15°, and 20°, respectively cases **S10**, **S15** and **S20**; all with a leeward slope equal to angle of repose and crest height of 75mm. The three sand pile configurations were tested in a wind tunnel, and their eroded profiles were measured at different time instants. The emission rate was computed based on those profiles.

Rigid wooden models were built representing the tested above-mentioned sand models, and besides these configurations, another model was made with a windward slope of 15°, but with a crest height (h) of 150 mm (**S150**). Using pressure taps and *Irwin* probes, these models were also tested in the wind tunnel in order to obtain the distributions of the pressure and friction coefficients.

Moreover, the pressure and friction distributions along the initial triangular profile of the four referred cases were numerically obtained by the simulations performed with the CFD package OpenFOAM. In order to validate the employed numerical model, the predicted values by OpenFOAM were compared against the experimental results measured in the wind tunnel.

It what concerns to the pressure coefficient distribution along the models, in the windward side good agreement between the experimental and numerical results was observed, being the lowest deviations up to half-length of the face and in the location where the pressure coefficient turns negative. Although the behavior is quite similar to the experimental results, in the leeward side, the pressure magnitude predicted by the numerical tool is different, in some cases, twice higher. The values from OpenFOAM predicted quite well the friction coefficient distribution measured with the *Irwin* probes, being **S10** the case with the worst agreement. In all performed tests and simulations, the Reynolds number independence condition had prevailed.

Regarding the flow topology, it was noticed that the recirculation zone starts right at the crest of the pile and the wake region extends well downstream. Moreover, the size of the recirculation zone grows with the stoss slope angle. For case **S10** both initial shape and erosion profile after 1 minute were simulated, and it was observed a significantly reduction in the recirculation bubble after 1 minute of erosion. This behavior occurs mainly due to the flattening of the crest during erosion, making the sharp vertex disappear.

Shao's model required a calibration procedure since it is a dust emission scheme and, in the present work, it was used to model sand emission flux. The shear velocity distributions, along the initial triangular profile, obtained through the CFD numerical simulation were incorporated into the specific selected saltation model to determine the normal sand emission flux using the model of Shao [15]. These predictions were then benchmarked against the experimental results, and the best fit for the parameter c_y was determined for the three pile geometries considered. It was demonstrated that these c_y values are specific to the saltation model selected and slope angle. Interestingly, regardless the configuration, it was observed that two of the models, specifically, Kawamura's [34] and Lettau and Lettau's [16], used the same c_y parameter, while for the Owen's [35] model a value three times higher was found.

CHAPTER A5

OBLONG PILES

The three-dimensional transverse pile selected to perform the present study has an oblong geometry, considering that it is representative of stockpiles of granular material, such as coal piles, commonly found in industrial sites. Furthermore, there is a clear lack of studies with this configuration, in particular about the free surface deformation.

Due to the procedure of the pile setup in the test chamber of the wind tunnel, only one configuration of the oblong geometry was tested. Its dimensions, as well other features of the experimental conditions, in particular, the pile setup procedure and the wind velocities tested, are presented in Section A5.1.

Both experimental and numerical simulations were performed for this particular case. In what concerns the experimental tests, measurements were conducted only for the free surface deformation. Similarly to the triangular case, those values were employed in Equation (A2-5) in order to calculate the sand emission rate at each time interval, and the results are reported in Section A5.2.

The numerical simulations were performed with OpenFOAM for the initial shape of the pile and the results are presented in Section A5.3. The airflow over and around the pile is compared

against the results of Furieri et al. [4] and correlated with the erosion profiles registered in the wind tunnel experiments.

A5.1. CASE DESCRIPTION

In this section, a description of the oblong pile case study is presented, in particular the procedure to conform the pile in the wind tunnel, the geometric characteristics of the models, and the main features of the experimental tests and numerical simulations performed.

The oblong pile setup in the test chamber of the wind tunnel is quite different from the methodology employed in the triangular piles. There was no previous experience about the pile setup procedure, as it was the first time this kind of tests was performed in the LAI laboratory; therefore, a development and design phase was necessary prior to the experimental tests. Several designs were considered concerning the feasibility and expediency of the oblong pile construction in the wind tunnel test chamber. Figure A5-1 and Figure A5-2 depict the specific device that was built for this purpose at the workshop of the Department of Mechanical Engineering - Coimbra Institute of Engineering (ISEC).

Schematic views

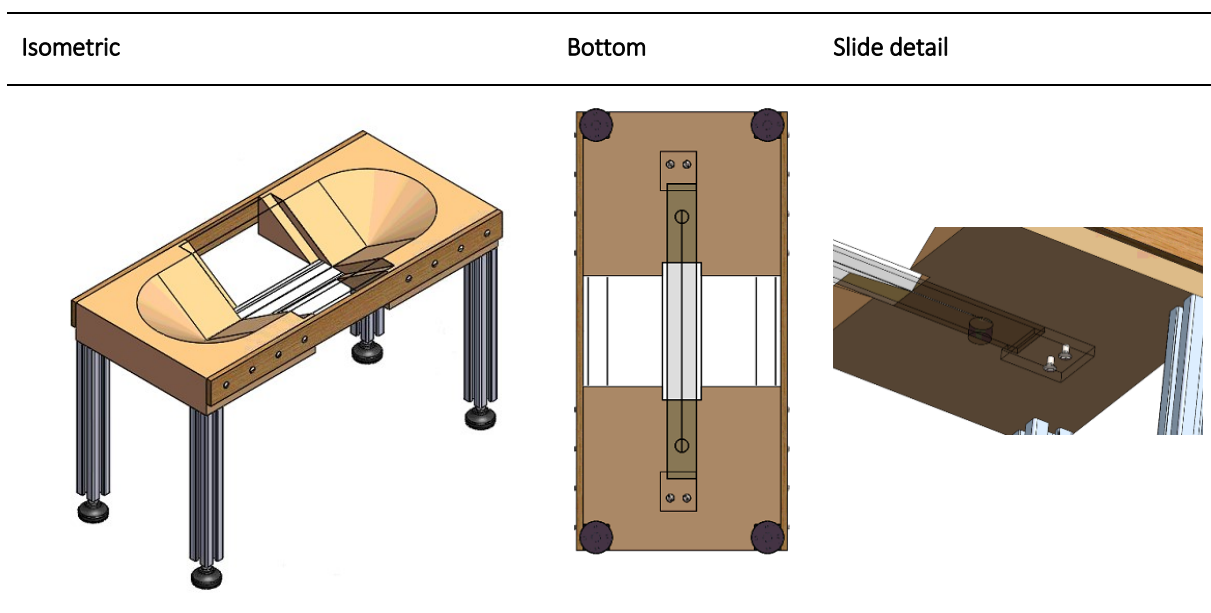


Figure A5-1: Schematic of the oblong pile hopper.

Device

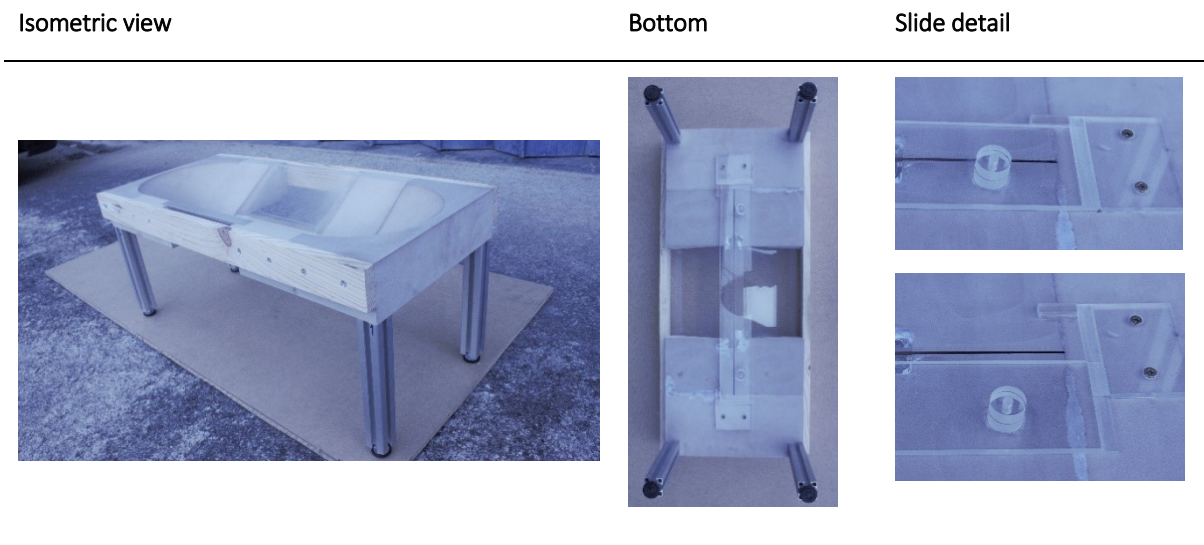
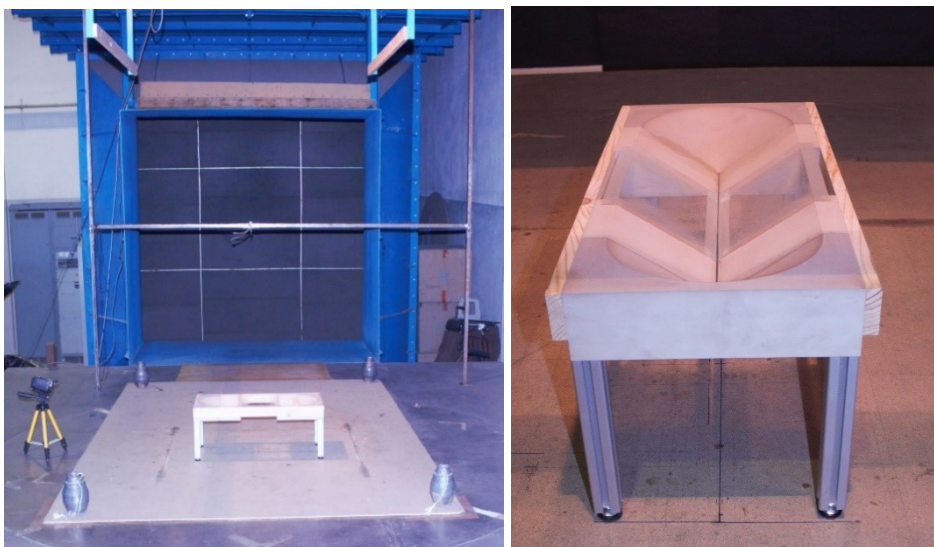


Figure A5-2: View of the oblong pile hopper.

Since the equipment works as a hopper, it was designed to accommodate the same volume of sand necessary to build the intended pile. In addition, tests were carried out to evaluate the most suitable size for the sand run-through and the best results were obtained with 1 mm. A slide was placed underneath of the device to cover the opening (slot) (Figure A5-1) during the filling phase.

The procedure to build the oblong sand pile in the wind tunnel is quite simple, consisting of four steps (illustrated in Figure A5-3):

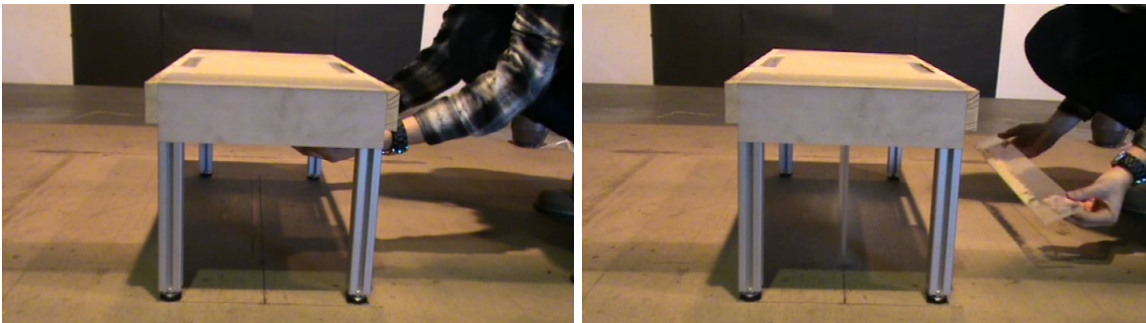
Step 1) Place the device in the proper location of the test chamber



Step 2) Fill the total volume of the mold with sand;



Step 3) Remove the slide to allow the sand to pass through the slot;



Step 4) Wait for the pile to form naturally.

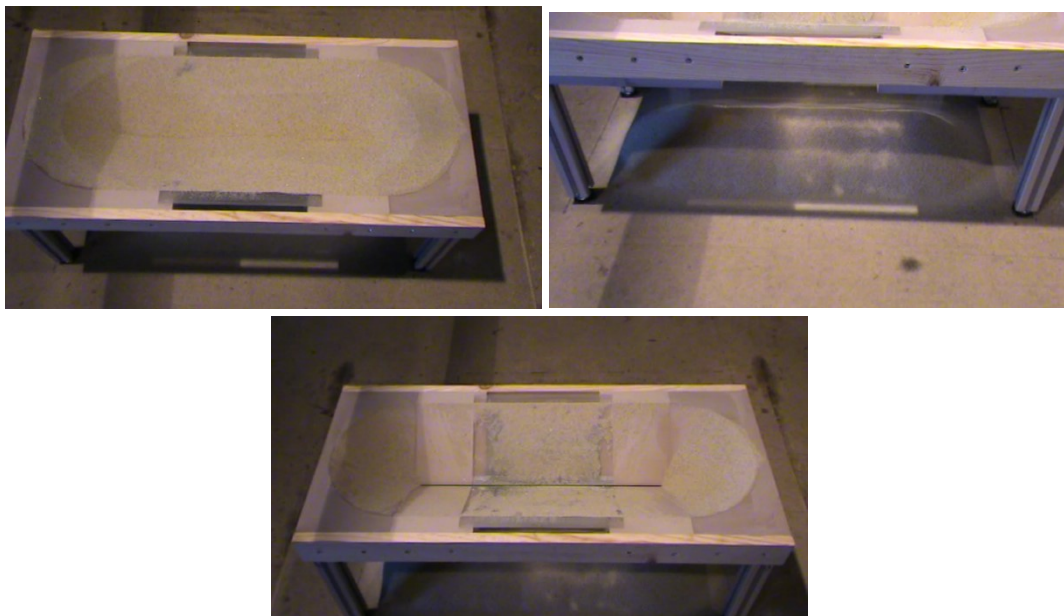


Figure A5-3: Oblong pile setup procedure (four steps).

After removing the specific device from the test chamber, the resulting oblong sand pile can be seen in Figure A5-4.

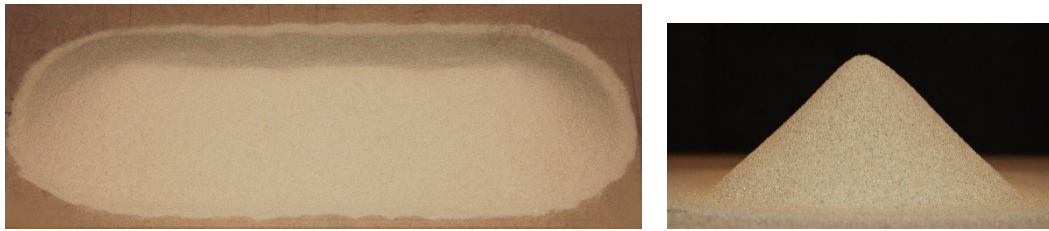


Figure A5-4: Oblong sand pile tested (aerial and side views, respectively).

Prior to the erosion experiments, several tests were performed with the device used to build the pile, in order to check the repeatability of the pile geometry and dimensions, and the corresponding results are discussed in Section A5.2.

Similar to the triangular pile case, the blockage ratio was calculated for the oblong piles in order to ensure that it was in agreement with the recommended value of less than 5% [99,100]; the obtained blockage value is 0.97%.

Taking into consideration this result, the pile was allowed to be built naturally with all the lateral faces of the pile having a slope equal to the angle of repose; the threshold undisturbed wind velocity can be predicted by using Equation (A1-6). Preliminary tests were performed and two undisturbed velocities were selected to carry out the erosion trials, $U_0=9.1$ m/s and $U_0=9.9$ m/s, respectively.

The influence of the wind direction was also tested and two angles of incidence (β) were tested, namely 90° (perpendicular to the pile's crest) and 60° , as schematically presented in Figure A5-5.

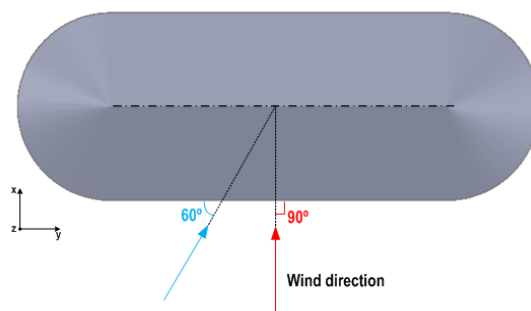


Figure A5-5: Angles of incidence tested

As mentioned in Section A2.4.1, during the erosion tests, the piles are exposed to the wind and the wind tunnel is stopped at cumulative times to allow the measurement of the eroded profile. The total erosion time was 10 minutes, for each velocity, being the first five time intervals of 1 minute each, and then, due to the evolution of the pile, 2 and 3 minutes. This is: the eroded

profile was measured at cumulative instants: 1, 2, 3, 4, 5, 7, and 10 minutes.

Since this is a 3D geometry, the data acquisitions cannot be only made along the centerline of the pile, as it was done for the triangular pile case; instead, grid points were used, as schematically represented in Figure A5-6. This particular arrangement leads to an increase of the duration of each experiment.

In addition, an extension beyond the pile's limit (downstream) was considered in order to record the sand deposition.

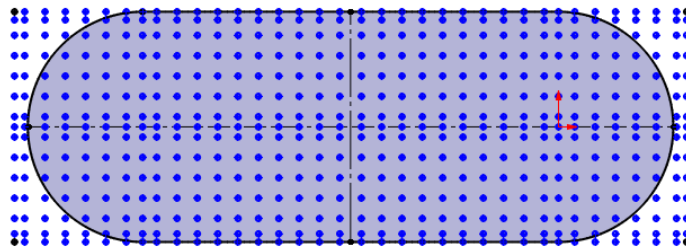


Figure A5-6: Initial measuring grid (top view).

Besides the free surface deformation with time, the erosion profiles also allowed obtaining the sand emission rate by using Equation (A2-5), and the results are discussed in Section A5.2.1 and Section A5.2.2, respectively.

The numerical simulations were performed for the initial shape of the pile in order to attain the wall shear stress distribution in the surface of the pile. These results are discussed in Section A5.3, including the correlation with the free surface deformation of the piles and the comparison of the flow topology against studies performed by other authors, specifically, with different CFD tools and with oil film visualization tests.

A5.2. EXPERIMENTAL RESULTS

The study of the oblong piles only involved erosion tests to obtain the time evolution of the free surface deformation and of the sand emission rate.

As already mentioned, repeatability tests were performed to ensure the shape and dimensions of the pile built with the new device in the wind tunnel. Five different tests were conducted (Figure A5-3), and for each one of them, the pile was measured five times with the distance laser sensor (Figure A5-6).

In order to present the repeatability results, in each test, the deviation was obtained by dividing the absolute deviation (*absdev*) by the average value of the five measurements ($h_{average}$), as given by Equation (A5-1).

$$deviation = \frac{absdev}{h_{average}} = \frac{|h_{measured} - h_{average}|}{h_{average}} \times 100 \quad (A5-1)$$

In a few grid points the deviation reaches very high values, due to the small values of the average, thus, a different approach was used (Equation (A5-2)), normalizing the absolute deviation by the initial crest height ($h = 74\text{mm}$).

$$normalized\ deviation = \frac{absdev}{h} = \frac{|h_{measured} - h_{average}|}{h} \times 100 \quad (A5-2)$$

Table A5-1 depicts the results of deviation and normalized deviation, in the five performed tests, relatively to the measuring system.

Table A5-1: Repeatability tests: deviation and normalized deviation [%] of the measuring system.

Test	Approach	Measurement					Mean value
		M1	M2	M3	M4	M5	
T1	Normalized	0.74%	2.04%	0.55%	0.39%	1.12%	0.97%
	Deviation	5.94%	12.60%	5.48%	3.98%	8.14%	7.23%
T2	Normalized	0.92%	1.02%	0.70%	1.94%	0.73%	1.06%
	Deviation	5.04%	8.21%	4.47%	10.46%	4.43%	6.52%
T3	Normalized	2.31%	0.65%	0.66%	1.13%	1.07%	1.16%
	Deviation	16.10%	4.54%	5.06%	7.27%	7.85%	8.16%
T4	Normalized	0.81%	0.53%	0.46%	0.40%	1.70%	0.78%
	Deviation	6.12%	4.58%	3.80%	4.95%	12.08%	6.31%
T5	Normalized	0.81%	0.33%	1.39%	1.54%	0.53%	0.92%
	Deviation	7.89%	2.88%	8.89%	12.68%	5.45%	7.56%

It can be observed in Table A5-1 that similar behavior occurs for all tests, and the deviation is around 7%, with the normalized deviation close to 1%.

In order to evaluate the repeatability of the pile setup procedure, a comparison of the mean profiles (mean value of the five measurements made in each test) was performed. In this case, besides of the two approaches already mentioned, the absolute deviation [mm] is also presented in Table A5-2.

Table A5-2: Repeatability tests: deviation [%], normalized deviation [%] and absolute deviation [mm] of the pile construction device.

Approach	Test					Mean value
	T1	T2	T3	T4	T5	
Normalized	0.84%	1.27%	1.15%	1.39%	0.91%	1.11%
Deviation	5.59%	7.93%	7.99%	8.98%	5.40%	7.18%
Absolute	0.62 mm	0.94 mm	0.85 mm	1.03 mm	0.68 mm	0.82 mm

Regarding the deviation and normalized deviation of the mean profiles, similar performance to Table A5-1 was observed. In what concerns the absolute deviation, a mean value of less than 1 millimeter was obtained and it was considered good level of repeatability.

Figure A5-7 depicts the distribution of the absolute deviation, in each grid point relative to the mean profile of the pile.

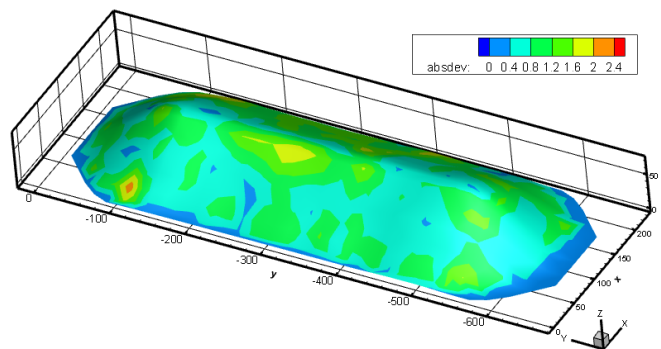


Figure A5-7: Absolute deviation distribution along the pile (mean profile).

Considering that the pile is made of granular material, several factors can contribute to the deviations presented in Table A5-2 and Figure A5-7, such as particle size and sphericity; roughness of the surface of the particle; moisture and the compaction of the pile. Some of the parameters are difficult to control, in particular those concerning the characteristics of the

particle; nevertheless, as mentioned in Section A2.2, the material used was dry sieved sand with a prevailing grain diameter (d) of 0.5 mm; therefore, the particle size and moisture content of sand were known. On the other hand, the ambient conditions and the experimental procedure may also influence the results obtained. In fact, these parameters were closely monitored; moreover, the tests were performed in the same place and day to assure uniform atmospheric conditions in the laboratory. In addition, markers to guarantee the positioning of the device were drawn in the test chamber of the wind tunnel; the tests were performed by the same operator, who took due care that the piles were naturally built. Vibrations were avoided, as they may cause the change of the angle of repose. After the pile was built, the device was removed from the wind tunnel to proceed with the measurements; no pile compaction was made.

Taking into consideration the experimental procedure and the results for the five tests, which are presented in Table A5-2 and Figure A5-7, it was judged that the device is capable of ensuring the shape and dimensions of the piles.

Alongside with the repeatability tests for the new device, a study was performed to evaluate the best measuring grid. The procedure comprises the use of two different grids, a refined grid with 10 mm spacing and a coarser grid with double this spacing. After the measurement of the pile, the values of the coarser grid were interpolated to the refined mesh and the points were directly compared, as can be observed in Figure A5-8. Only half of the pile is depicted in Figure A5-8 due to its symmetry.

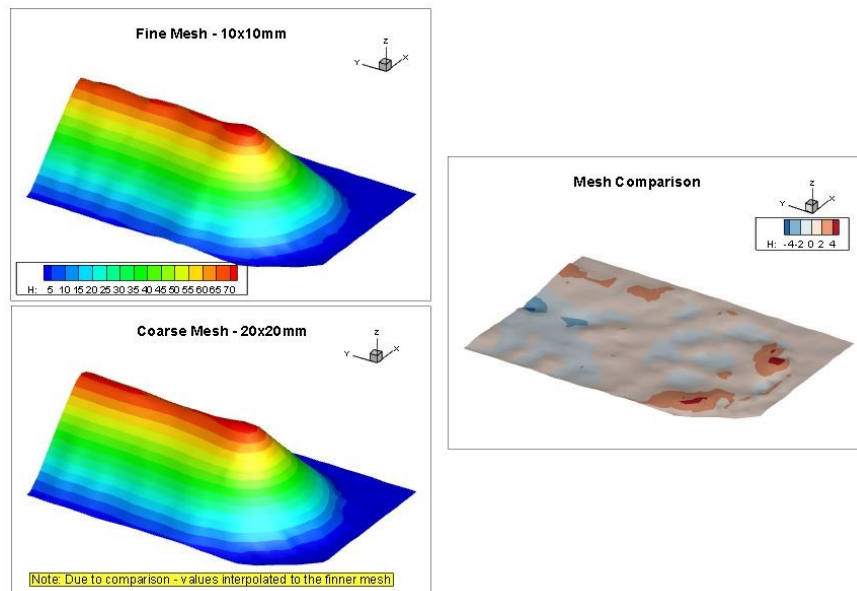


Figure A5-8: Measurement grid study: comparison between the refined and coarser grid.

It can be observed in Figure A5-8 that the differences between the two grids are small (right

hand side image); therefore, considering the number of grid points (and consequently the measuring time), it was selected the use the coarser grid to measure all the erosion profiles.

A5.2.1. FREE SURFACE DEFORMATION

As previously mentioned, regarding the oblong piles, only one configuration was tested; however, tests were conducted with two different velocities. Figure A5-9 shows the measured profiles for $U_0=9.1$ m/s, in the seven cumulative instants. For each instant, it is depicted the mean profile (calculated based on the five trials – left hand image) and a photograph of the obtained sand pile (right hand image). The initial limit edge of the pile is also represented as a reference contour.

It can be observed in Figure A5-9 that small changes occur in the measurement grid during the tests, in particular concerning its extension downstream. This strategy was used to make the measuring procedure more effective as, earlier on the downstream extension of the pile is practically negligible.

Time (min)	Representation	
	Graph	Photo
t = 0		
t = 1		

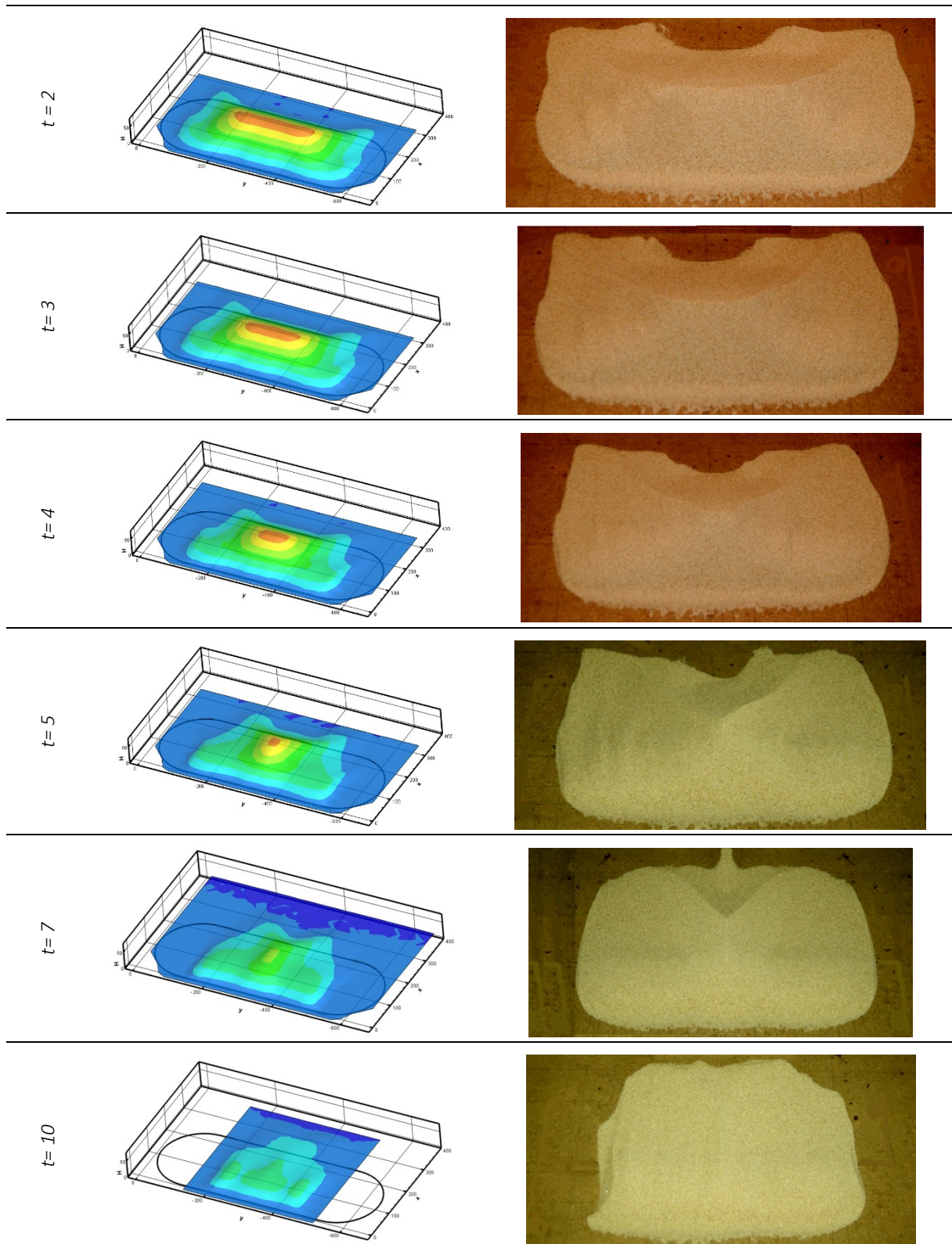


Figure A5-9: Erosion profiles for $U_0=9.1$ m/s: initial profile and seven cumulative instants (left: mean profile; right: photos of the sand pile).

The erosion process is gradual along time as it can be observed in Figure A5-9. However, the most significant modifications in the shape occur in the initial time instants, since it is when the

pile is steeper. The images of the sand piles clearly indicate that the crest line is the last feature to disappear; it recedes over time and tends to a V-shape over the symmetry plane of the pile with the highest height at the centerline.

Similar behavior occurs with the higher wind velocity ($U_0 = 9.9$ m/s); however, the erosion is more significant for the corresponding time instants. In order to facilitate the analysis, three different figures are presented, specifically, Figure A5-10, Figure A5-11 and Figure A5-12, to allow the comparison of the free surface deformation between the two tested velocities ($U_0=9.1$ m/s and $U_0=9.9$ m/s) for $t=1, 2$ and 3 minutes, respectively.

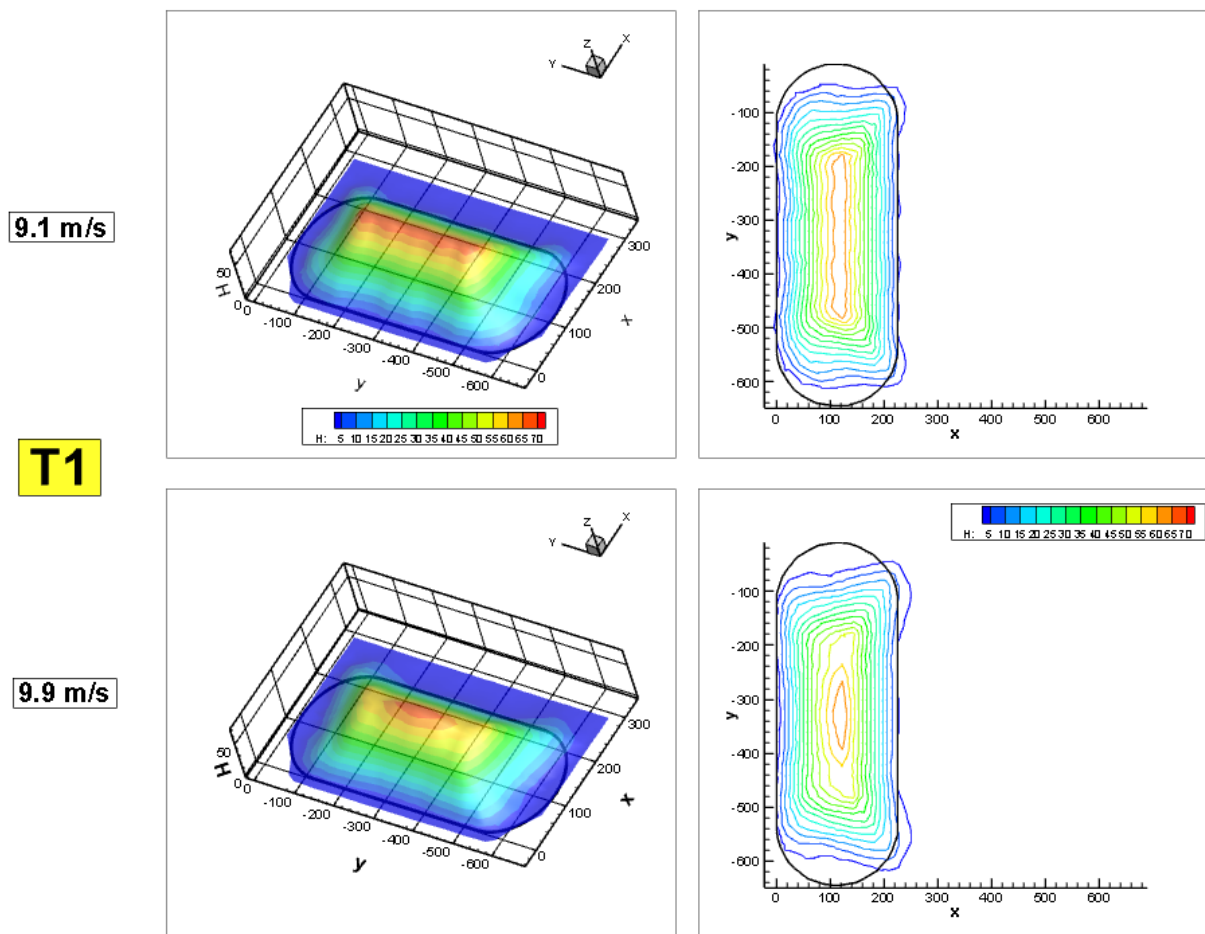


Figure A5-10: Free surface deformation for the two tested velocities ($U_0=9.1$ m/s and $U_0=9.9$ m/s) for first instant $t=1$ min: 3D plot (left) and plan view contours (right).

After the first instant, the differences between the two tests are clearly noticeable in Figure A5-10. Whereas for the lower velocity minor changes occur in the shape of the pile; for 9.9 m/s, the initial crest almost disappears and the leeward side starts to extend toward the downstream direction of the wind flow.

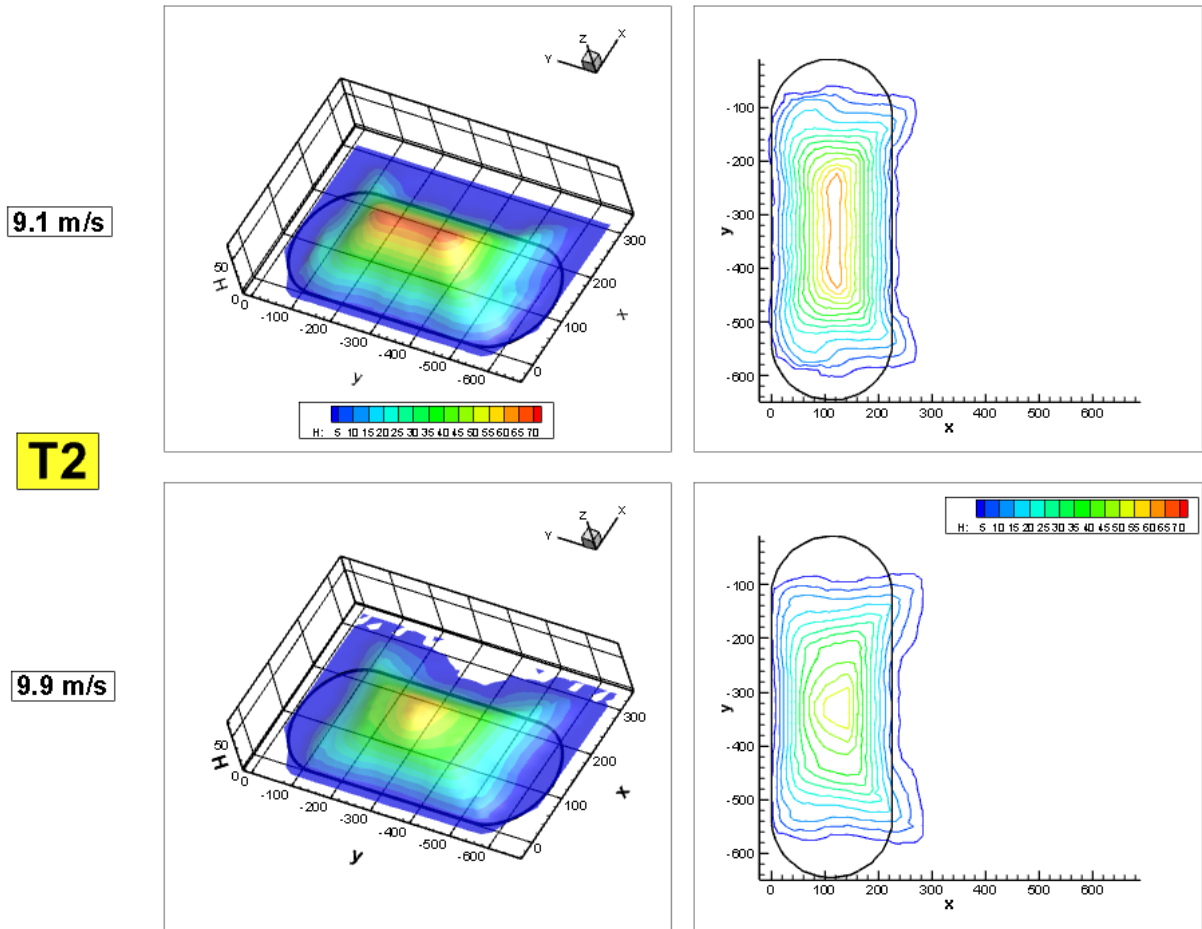
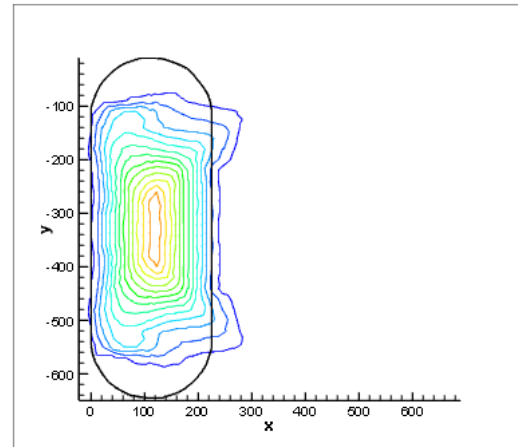
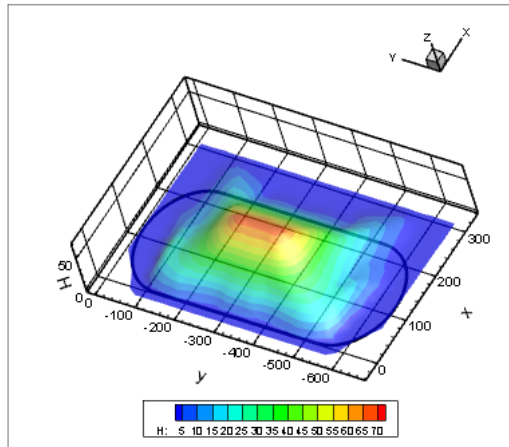


Figure A5-11: Free surface deformation for the two tested velocities ($U_0=9.1$ m/s and $U_0=9.9$ m/s) for first instant $t=2$ min: 3D plot (left) and plan view contours (right).

It can be observed in Figure A5-11 that, after 2 minutes of erosion, the geometry of the pile in the test with $U_0=9.1$ m/s, although narrower and with a crest better defined, is similar to the one presented in Figure A5-10 for $U_0=9.9$ m/s. Additionally, it can be seen that after $t=2$ minutes, for velocity $U_0=9.9$ m/s, the initial crest resembles a peak.

For both cases depicted in Figure A5-12, the piles became slenderer, although, in the case of the higher velocity, the pile is almost flat. A portion of the initial crest line is still visible for the lower velocity and for $U_0=9.9$ m/s, the crest line has a much reduced height and it is nearly aligned with the flow.

9.1 m/s



T3

9.9 m/s

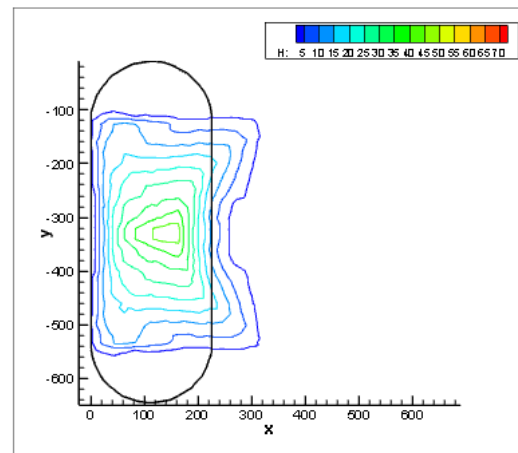
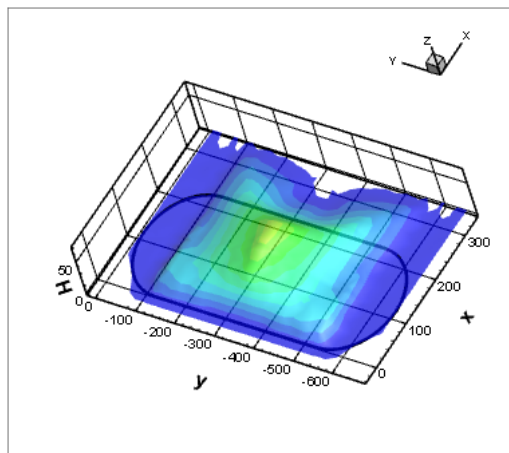


Figure A5-12: Free surface deformation for the two tested velocities ($U_0=9.1$ m/s and $U_0=9.9$ m/s) for first instant $t=3$ min: 3D plot (left) and plan view contours (right).

Considering the three time instants, as expected, the erosion is higher for the larger velocity. Along the erosion tests, both piles extended themselves toward downstream, in particular, as expected, for the higher velocity ($U_0=9.9$ m/s). Regardless of the test velocity, the leeward edge tends to a symmetric V-shape.

In addition, as already mentioned, the influence of the wind direction was also evaluated, and two different incidences were tested, namely, 90° and 60° (relatively to the original crest line). Figure A5-13, Figure A5-14 and Figure A5-15 depict a comparison of the free surface deformation for those two incidence angles, and for the two tested velocities ($U_0=9.1$ m/s and $U_0=9.9$ m/s), at instants $t=1, 2$, and 3 minutes, respectively. Similarly to the cases where the wind is flowing normal to the pile, a reference contour was also added.

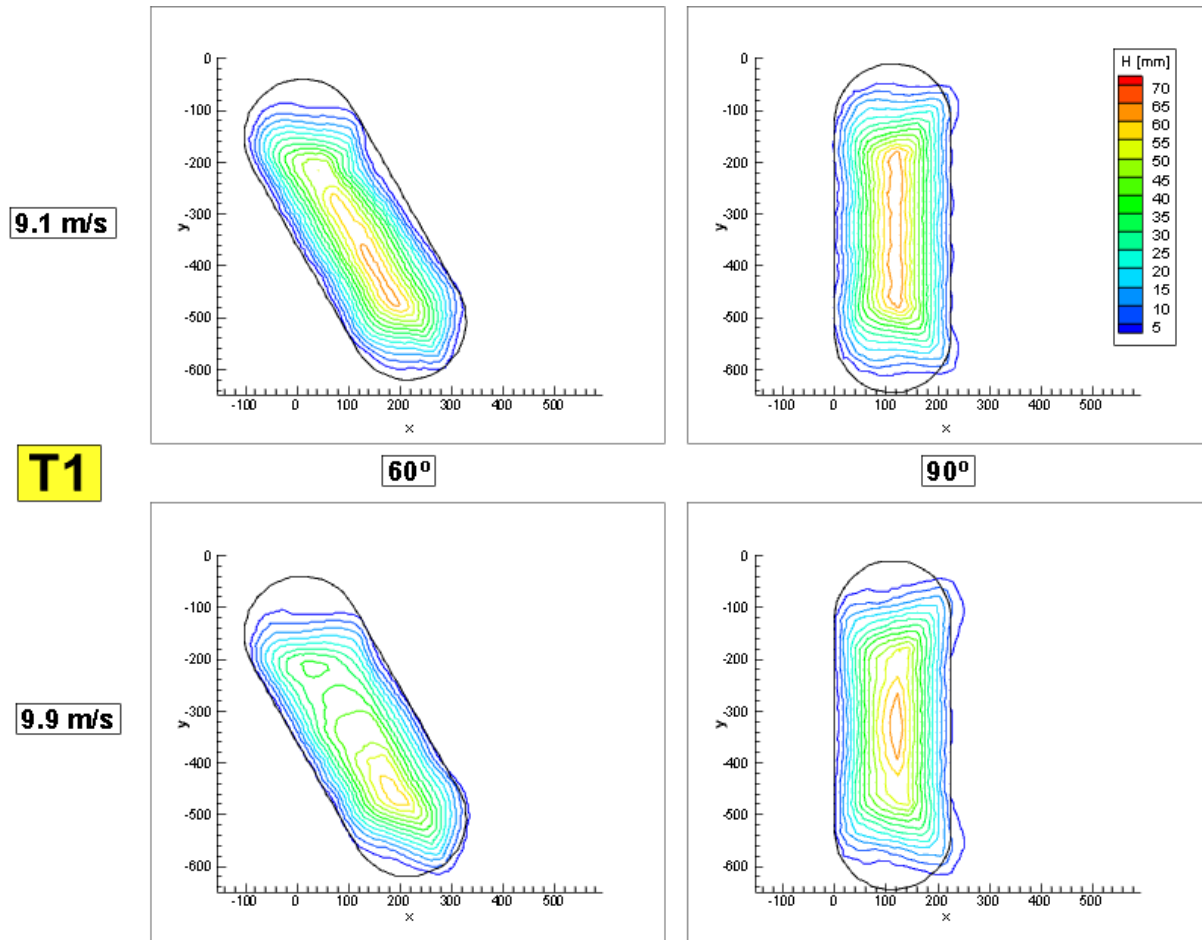


Figure A5-13: Free surface deformation for the two tested velocities ($U_0=9.1$ m/s and $U_0=9.9$ m/s) and two angles of incidence (90° and 60°) for first instant ($t=1$ minute).

For $t=1$ minute, Figure A5-13 presents that the most evident differences between the two angles of incidence (for both velocities) is the shape of the pile's contour and of the crest, which shift towards the leeward side. Despite some erosion, the piles keep their contour close to the initial one.

By considering only the half of the pile further away from the tunnel nozzle, it can be noted that the values and distribution of the height levels for the two incidence angles are similar.

For the 60° wind incidence, the higher the velocity yields higher erosion, as indicated by the levels of surface deformation. However, the contour of the pile for both velocities is similar, which differs from the observations for the cases with 90° wind incidence.

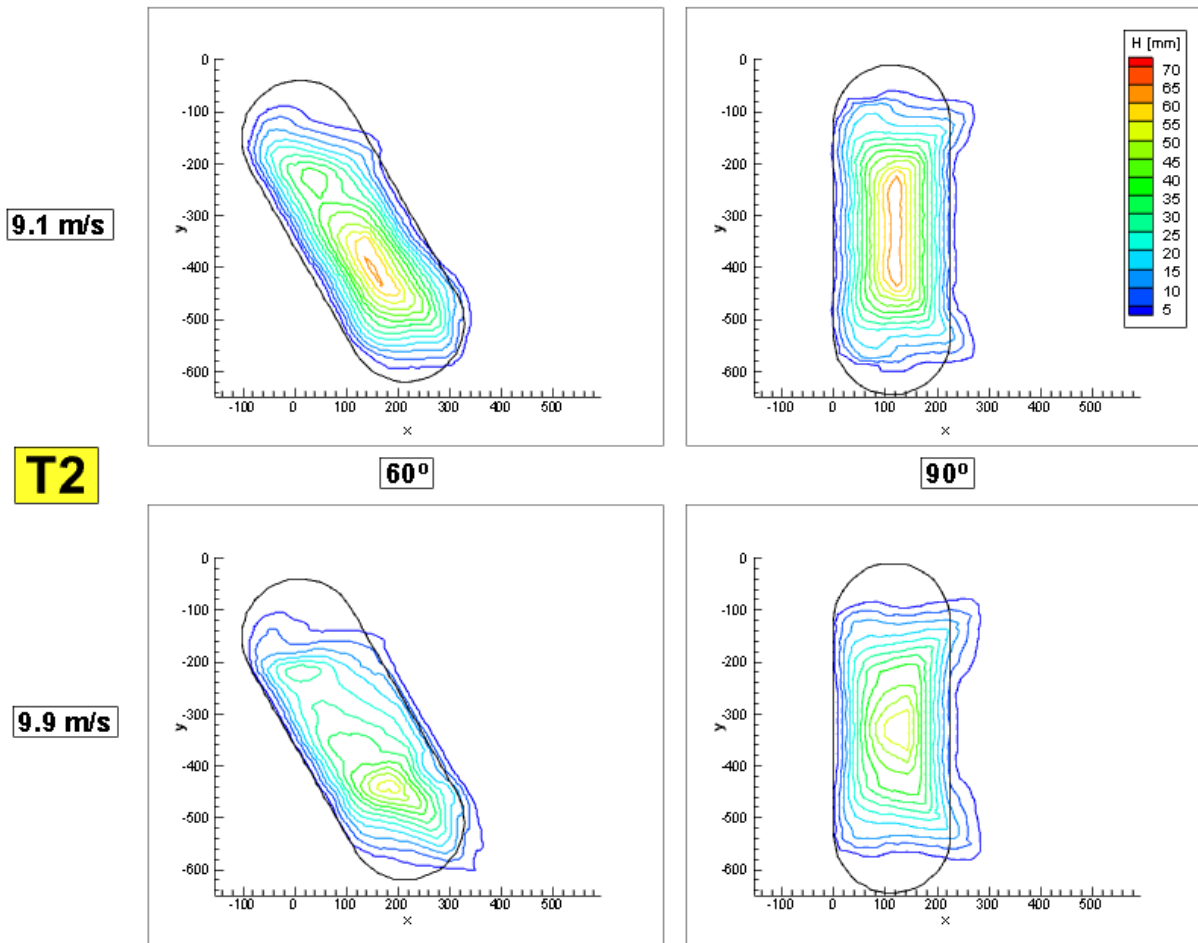


Figure A5-14: Free surface deformation for the two tested velocities ($U_0=9.1$ m/s and $U_0=9.9$ m/s) and two angles of incidence (90 and 60°) for first instant ($t=2$ minutes).

In Figure A5-14, there is still some resemblance between the 60° and 90° cases in what concerns the height levels for the downwind portion of the pile.

Regarding the 60° cases, in particular for the higher velocity, the downwind contour starts to extend beyond the initial contour.

Figure A5-15 depicts $t=3$ minutes and, considering only the cases with 60° of incidence, it can be observed that the shape of the piles changes markedly. The extension of the pile away from the initial contour starts with the lower velocity and it becomes clearly noticeable for $U_0=9.9$ m/s, but not as accentuated as in the cases where in wind flows normal to the pile.

Moreover, for $U_0=9.1$ m/s and both angles of incidence, although with different shapes, there are still traces from the crest, while in the higher velocity the piles are practically flattened.

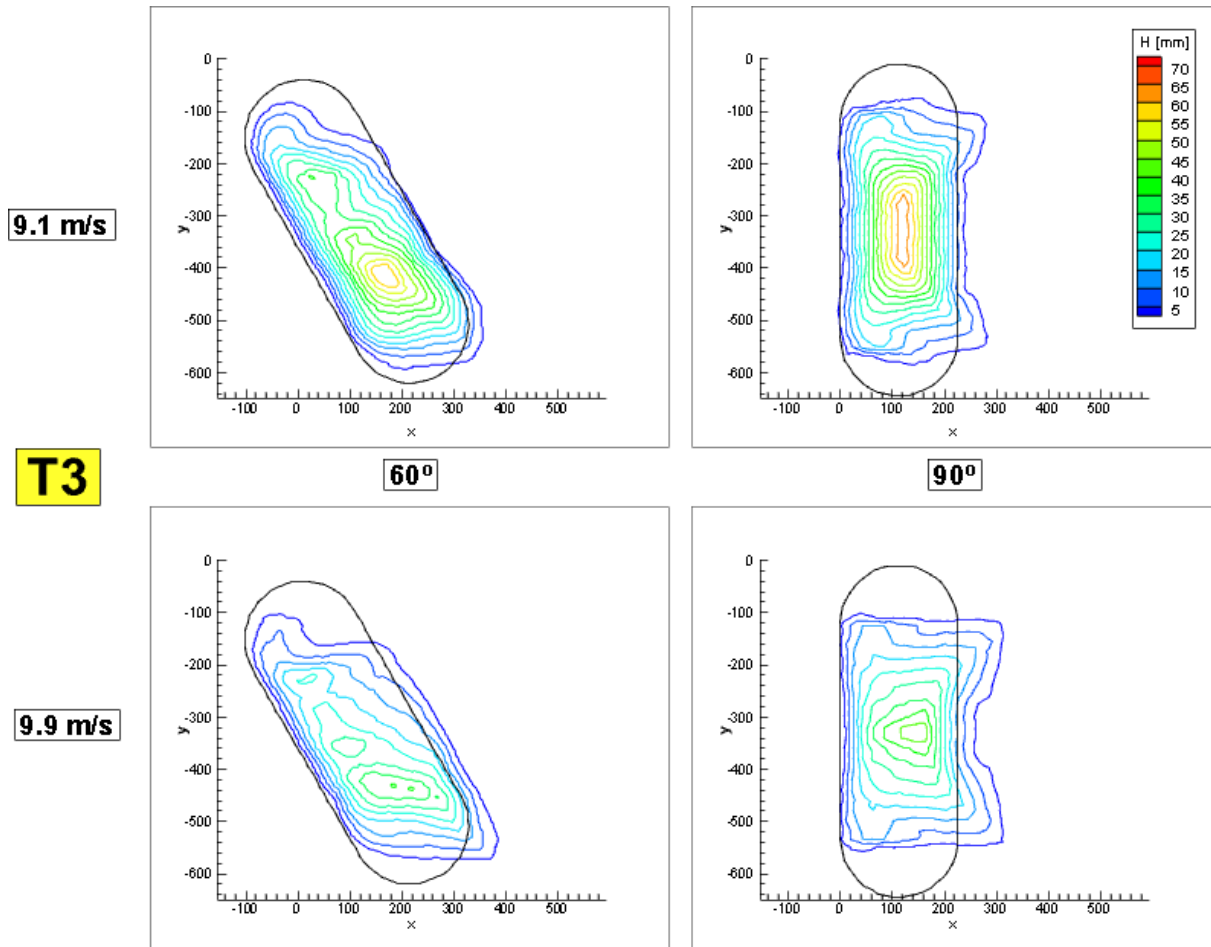


Figure A5-15: Free surface deformation for the two tested velocities ($U_0=9.1$ m/s and $U_0=9.9$ m/s) and two angles of incidence (90° and 60°) for first instant ($t=3$ minutes).

Based on an overall analysis of the results for the three time instants, it can be stated that the pile height reduction is augmented when wind flows at an incidence angle lower than 90° ; however, the extension of the pile beyond the initial contour is more accentuated for the angle of 90° .

Earlier on the experiment, the downwind portion of the pile with 60° of wind incidence has similar morphology values as the cases with 90° of wind incidence, however, as the test progresses, this resemblance fades away.

For the 60° of wind incidence, the erosion and consequent alteration of the initial contour of the pile is rather pronounced at the upwind boundary close to the y-axis origin, whereas in the case where the wind is normal to the pile, the modification of the pile is practically symmetrical. This behavior can be explained by the influence of the pile in the wind pattern, since the fully developed flow in the test chamber of the tunnel faces an obstacle that is not symmetric in the streamwise direction. Further development of this topic will be discussed in Section A5.3.1, where the numerical results of the flow topology will be presented.

A5.2.2. SAND EMISSION RATE

As mentioned in Section A2.4.2, for the computation of the sand emission rate, during the time interval (Δt), i.e., between instants (t) and ($t + \Delta t$), and per unit of emission area (A), Equation (A2-4) was used. Likewise the free surface deformation analysis, both velocity and wind incidence angle were evaluated in the case of the sand emission rate

The calculation of the removed volume and of the emission area depends mainly on two parameters, the measured height difference of the two instants in each point of the measuring grid and the spacing of the grid itself (Section A2.4.2). Therefore, to compute sand emission rate, in the grid points where was measured a reduction of the height of the pile, a volume of sand was removed and consequently, erosion occurred (positive sand emission rate), whereas an increase in the height implies that deposition took place (negative sand emission rate).

Figure A5-16 depicts the sand emission rate for the first instant ($t=1$ minute) with the velocity $U_0=9.1$ m/s.

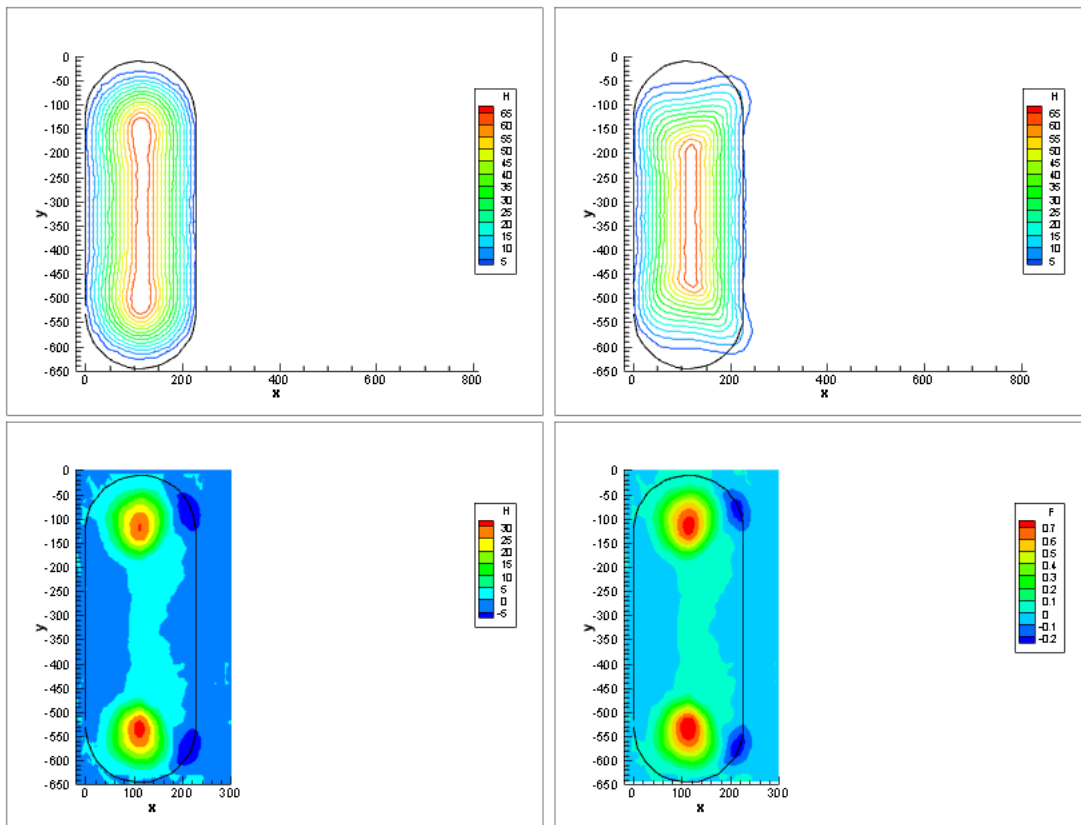


Figure A5-16 – Comparison between the initial profile and erosion profile for $t=1$ minute, for velocity $U_0=9.1$ m/s and incidence angle $\beta=90^\circ$: plan view (initial profile – up left; $t=1$ minute – up right), height difference between initial profile and $t=1$ minute (down left) and sand emission rate [$\text{kg m}^{-2} \text{s}^{-1}$] during the test (down right).

In order to evaluate the dependency between the variation in the erosion profile and the sand emission rate, Figure A5-16 depicts the plan view of the initial profile and the erosion profile for $t=1$ minute; the height difference in each grid point between $t=0$ and 1 minute; and the sand emission rate that occurred during the test. Once again, to support the visualization, Figure A5-16 depicts the limiting edge of the pile as a reference contour.

As mentioned, it can be observed in Figure A5-16 that the plots of the height difference and sand emission rate are quite similar in what concerns the spatial distribution of the maximum and minimum values areas. As expected, the higher values of erosion occur in the peaks of the crest, while the deposition is more accentuated where the pile contour exceeds the reference contour in the leeward. Similar behavior is maintained for the entire test as well as for the other tested flow velocity (Figure A5-17).

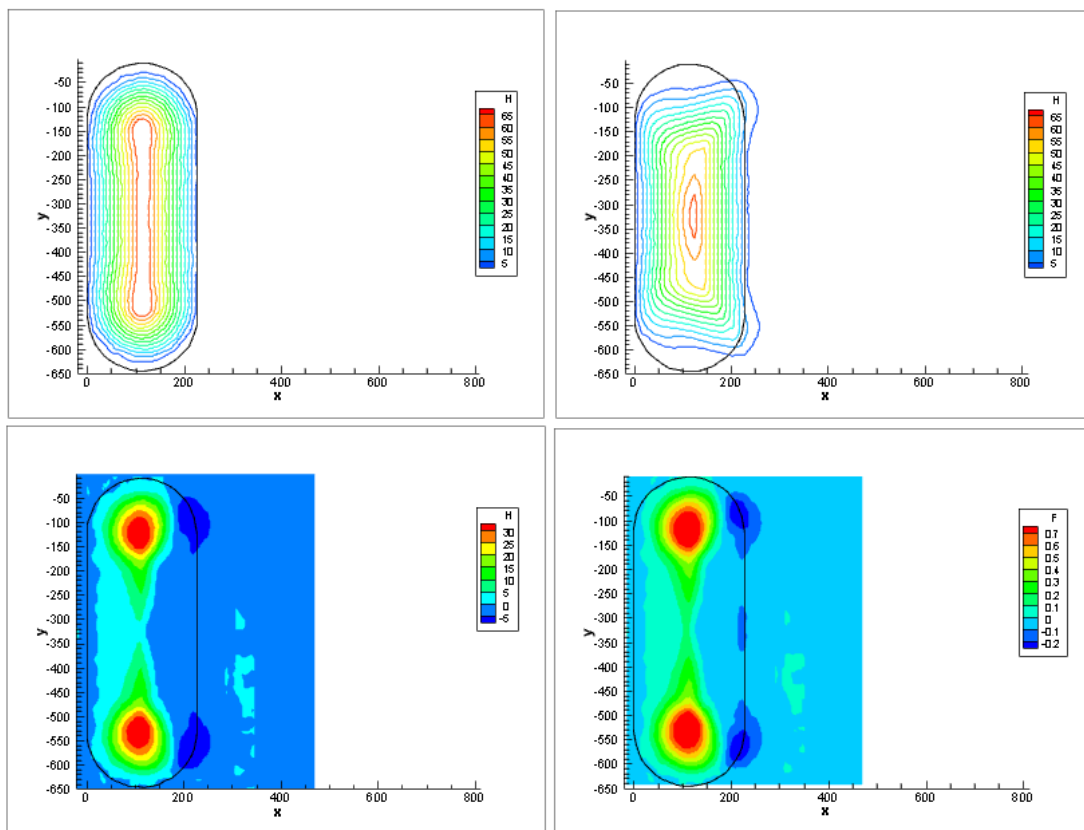


Figure A5-17 – Comparison between the initial profile and erosion profile for $t=1$ minute, for velocity $U_0=9.9$ m/s and incidence angle $\beta=90^\circ$: plan view (initial profile – up left; $t=1$ minute – up right), height difference between initial profile and $t=1$ minute (down left) and sand emission rate [$\text{kg m}^{-2} \text{s}^{-1}$] during the test (down right).

Further analysis results are reported in Figure A5-18, where, for each velocity, a comparison between the total erosion and deposition fluxes along the entire test (measured at each time interval) is performed. The total fluxes (erosion and deposition) were obtained by the sum of the discrete values of the measuring grid.

Flow velocity

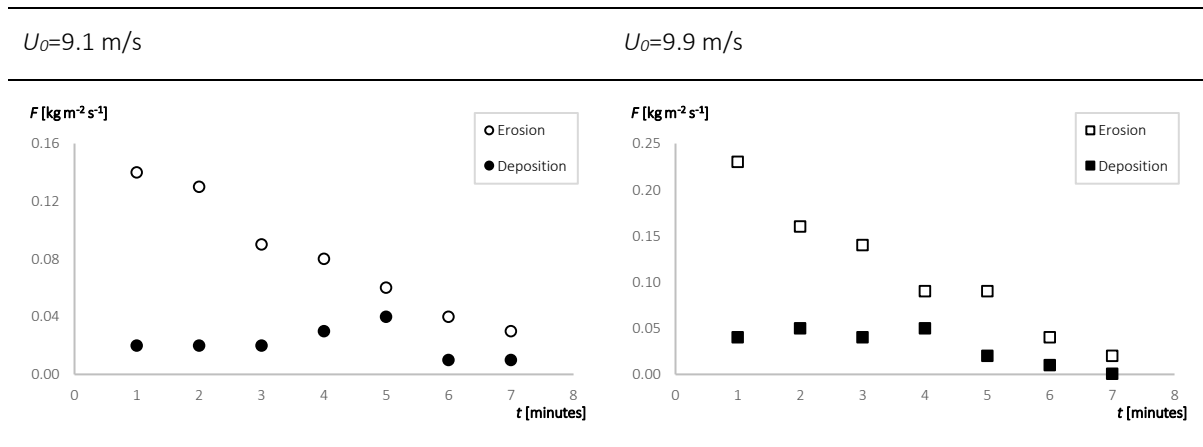


Figure A5-18 - Comparison between the total sand erosion and sand deposition rate for two velocities ($U_0=9.1$ m/s and $U_0=9.9$ m/s) along time.

Close observation of Figure A5-18 indicates that for both velocities the erosion flux decreases over the duration of the experiment, a phenomenon, which can be explained taking into consideration the continuous change of the shape of the pile; the consequent decrease of the slope leading to reduction of flow recirculation and wake turbulence resulting in lower friction velocity values.

As already mentioned, the sand emission rate is obtained through the height measurements in the chosen grid and this grid was changed along the erosion tests in order to improve the effectiveness of the measuring process. Due to the saltation – the aeolian erosion mechanism, the sand particles travel far beyond the spectrum of the measuring area, which leads to the deposition flux be considerably lower than the erosion one, regardless the test velocity.

In addition, it can be noticed in Figure A5-18 that in the beginning of the test the deposition flux increase and after a period of time (depending on the velocity) it starts to decrease. This effect may be due to the fact that, as time progresses, most of the sand was already been eroded and the pile is practically flat and with a considerable extension downstream beyond the initial limiting edge, as shown in Figure A5-9 for the lower velocity.

In order to evaluate the velocity influence in both total deposition and erosion fluxes, Figure A5-18 was rearranged, and now a direct comparison between the two tested velocities is reported in Figure A5-19.

Rate

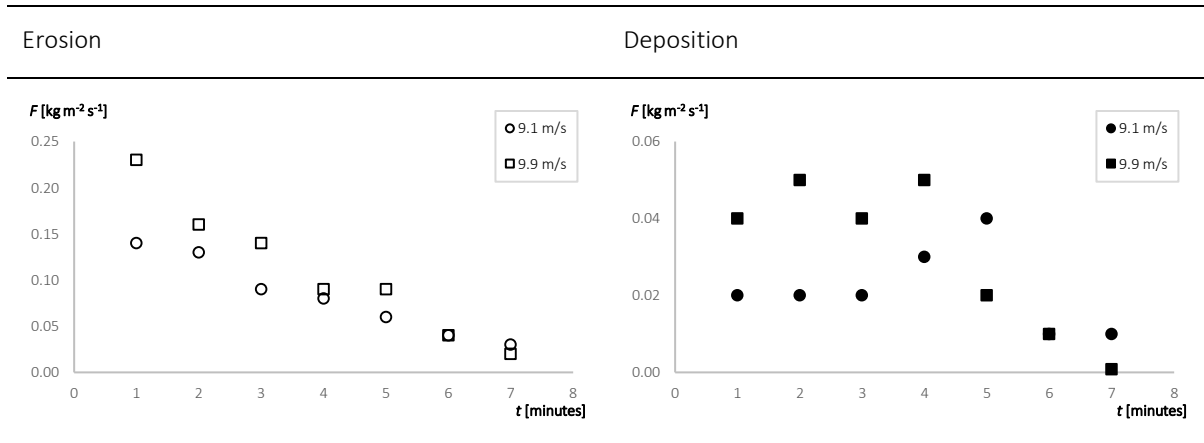


Figure A5-19 - Comparison between two velocities ($U_0=9.1$ m/s and $U_0=9.9$ m/s) for the total sand erosion and sand deposition rate along time.

As expected, Figure A5-19 shows a higher erosion flux for the greater velocity, specially in the initial time interval. Since the initial shape of the pile is similar, this discrepancy occurs mainly due to the difference from the threshold wind velocity ($U_{t\theta} \approx 9.2$ m/s – Equation (A1-6)). The erosion fluxes for the two velocities converge as the test progresses, and by the end of the test, they are very similar.

In what concerns, the deposition rate, once again, higher values were obtained for the velocity $U_0 \approx 9.9$ m/s, as shown in Figure A5-19. Furthermore, different behavior was observed for the two velocities, whereas, in the first part of the test, for $U_0 \approx 9.1$ m/s an increase of the deposition rate occurred; for the higher velocity, an oscillatory performance was registered. After the $t=5$ minutes, in both cases, the deposition flux decreased.

A similar analysis was performed for the cases where the wind incidence angle was 60° , and Figure A5-20 depicts not only the sand emission rate, but also its dependency with the variation in the isolines of the pile height for the $U_0=9.1$ m/s.

It can be observed in Figure A5-20 that, similarly to what was presented in Figure A5-16, the distribution of the levels of height difference and sand emission rate along the pile (bottom figures) are identical, as expected, due to the direct relation between the two magnitudes.

As already discussed, the crest is the region where the erosion is more evident; however, due to the positioning of the model in the test chamber of the tunnel for wind incidence angle of 60° , more accentuated emission rate occurs on the crest location closer to the nozzle. In addition, it can be observed that the erosion regions present nearly symmetrical patterns; however, these regions are skewed downstream from the crest. It can be observed on the upper pictures of Figure A5-20 that the limiting edge of the pile is kept, which is in agreement with the areas where deposition (negative emission rate) occurs, in particular near to the leeward contour. Moreover, the deposition is more accentuated near the peak with less

erosion, due to several factors: particles that travel beyond the measuring grid through saltation, particles that roll due to entrainment and accumulate at the foot of the pile and the recirculation / vortices occurring in the wake of the pile, as it will be discussed in Section A5.3.1.

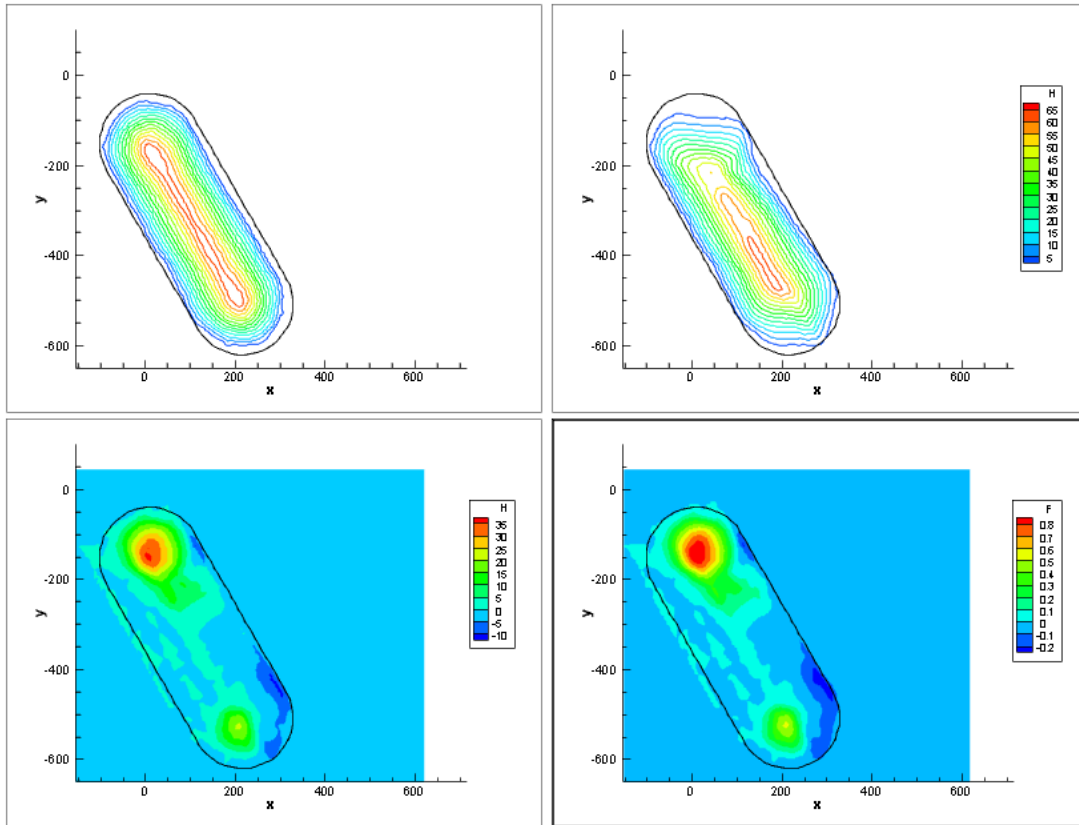


Figure A5-20 – Comparison between the initial profile and erosion profile for $t=1$ minute, for velocity $U_0=9.1$ m/s and incidence angle $\beta=60^\circ$: plan view (initial profile – up left; $t=1$ minute – up right), height difference between initial profile and $t=1$ minute (down left) and sand emission rate [$\text{kg m}^{-2} \text{s}^{-1}$] during the test (down right).

The geometric behavior during the erosion test with the velocity of $U_0 \approx 9.9$ m/s is similar to that with the lower velocity, as can be observed in Figure A5-21. Obviously, there are differences in the recorded values of the sand emission rate, since the value of the velocity of the flow is higher and consequently with a greater difference from the threshold wind speed, as previously mentioned. Nonetheless, a small shift of the erosion area around the peak near to the nozzle exit towards the crest line is visible, whereas, on the other peak, the erosion area continues located in the upstream face of the pile.

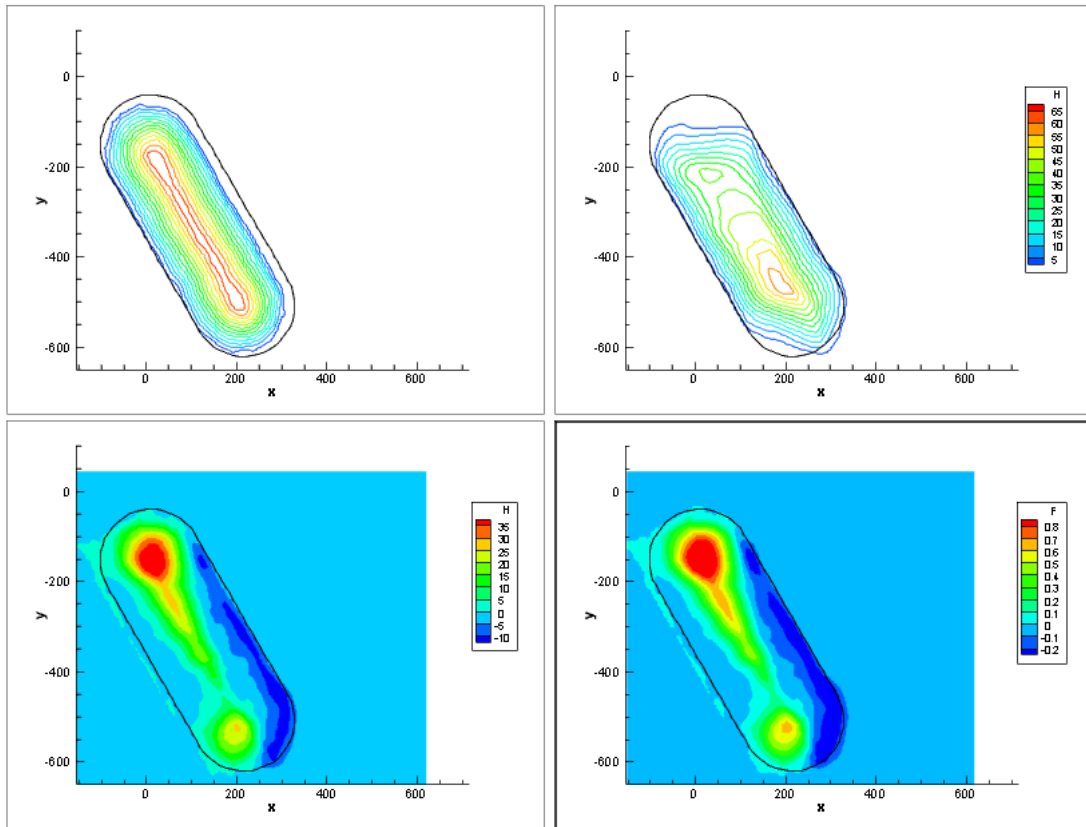


Figure A5-21 – Comparison between the initial profile and erosion profile for $t=1$ minute, for velocity $U_0=9.9$ m/s and incidence angle $\beta=60^\circ$: plan view (initial profile – up left; $t=1$ minute – up right), height difference between initial profile and $t=1$ minute (down left) and sand emission rate [$\text{kg m}^{-2} \text{s}^{-1}$] during the test (down right).

For the cases with a wind incidence angle of 60° , and for each velocity, a comparison between the total erosion and deposition fluxes along the entire test is presented in Figure A5-22.

Due to the size of the sand particles, the main aeolian mechanisms are saltation and creeping. As already mentioned, the trajectory of the saltating particles goes beyond the measuring grid, which explains why for both velocities the erosion fluxes are higher than the deposition ones. Furthermore, for $U_0 = 9.9$ m/s, the difference between erosion and deposition is more accentuated and both fluxes have an unceasing decrease along the entire test. That was not observed for the lower velocity, since, although the erosion flux reduces its value during the test, in what concerns the deposition, an oscillatory behavior occurred in the first part of the trial (until $t=4$ minutes).

Flow velocity

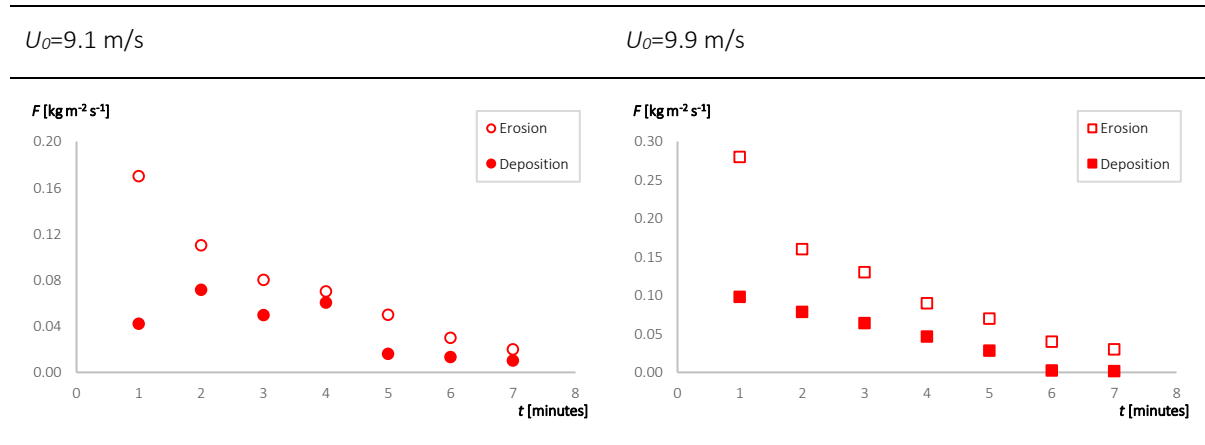


Figure A5-22 - Comparison between the total sand erosion and sand deposition rate for two velocities ($U_0=9.1$ m/s and $U_0=9.9$ m/s) along time for a wind incidence angle of 60° .

To assist the analysis of the velocity influence on both erosion and deposition processes, Figure A5-22 was reorganized to obtain Figure A5-23.

Considering the threshold wind velocity and the tested velocities, once again, during the entire trial, the higher erosion fluxes were obtained for the higher velocity, having a decreasing difference throughout the test.

Regarding the deposition fluxes, despite the large difference at the first time instant, the fluxes for both velocities are quite similar, starting $U_0 = 9.9$ m/s with higher values of flux, to then be overcome by the values of the lower velocity ($U_0 = 9.1$ m/s) at the end of the test ($t \geq 6$ minutes).

Rate

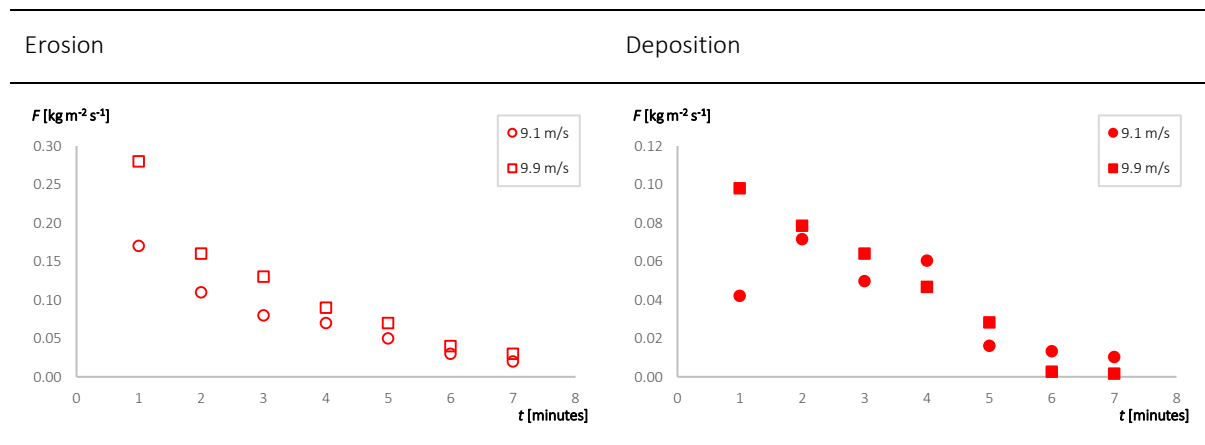


Figure A5-23 - Comparison between two velocities ($U_0=9.1$ m/s and $U_0=9.9$ m/s) for the total sand erosion and sand deposition rate along time with a wind incidence angle of 60° .

The sum up of the erosion and deposition fluxes obtained for both velocities and both wind incidence angles is presented in Figure A5-24, being this way simpler to perform a comparison.

In what concerns to the erosion fluxes, regardless the wind velocity, it can be observed in Figure A5-24 that the behavior for the two wind incidence angles is quite similar. At the first time instant, the erosion is more accentuated in the case where the wind does not strike the pile perpendicularly, the remaining values are very close to each other, being the flux slightly higher in the 90° case for the lower velocity.

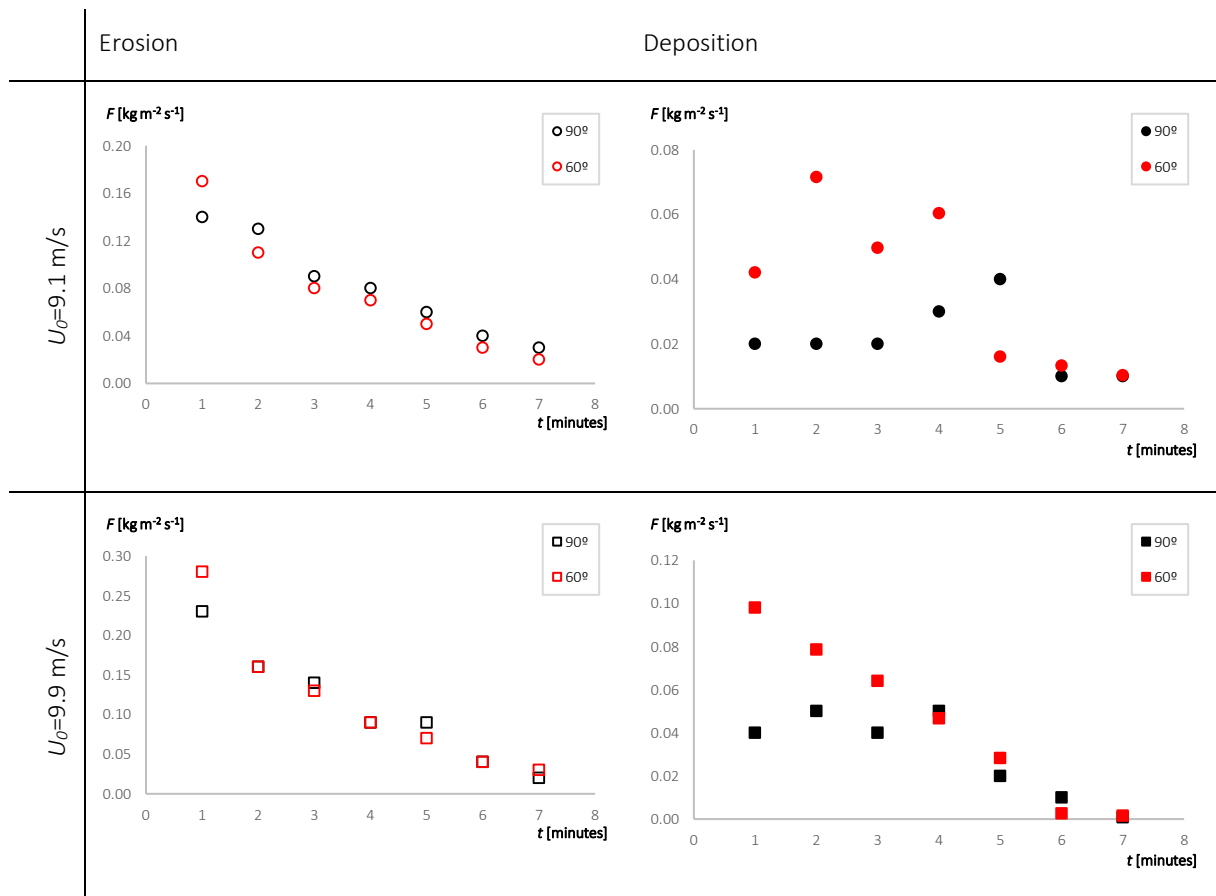


Figure A5-24 - Comparison between two wind incidence angles (90° and 60°) for two velocities ($U_0=9.1$ m/s and $U_0=9.9$ m/s) and for the total sand erosion and sand deposition rate along time.

From the comparison of the deposition fluxes, it can be observed in Figure A5-24 that, in the beginning of the test, the higher values were registered for the incidence angle of 60°, whereas at the final time instants, when, in both cases, the piles are practically shapeless, the values became analogous. The observed discrepancies between the two angles in the initial part of the experimental test may be explained in terms of the particles that roll along the leeward face of the pile (creeping), becoming trapped in the pile's foot due to the flow topology in the wake of the piles.

A5.3. NUMERICAL RESULTS

The numerical simulations were performed using the open source CFD Package OpenFOAM, as mentioned in Section A3.2. For both wind incidences, only the initial profile of the piles was tested. In order to correlate the numerical results with the experimental measurements (Section A5.2), both velocities ($U_0 = 9.1$ m/s and $U_0 = 9.9$ m/s) were employed.

Additionally, the flow topology over and around the piles is benchmarked against the oil-film visualization tests and numerical results of Furieri et al. [4]. Although the pile’s characteristics are slightly (Table A4-1) different due to the used material (sand) in the present experimental tests, the flow features numerically predicted are quite similar, as it will be discussed.

Table A5-3: Main characteristics of the oblong piles used in Fluent (Furieri et al. [4]) and OpenFOAM.

Model	Fluent (Furieri et al. [4])	OpenFOAM
<i>Crest height (h) [mm]</i>	80	74
<i>Crest length [mm]</i>	373	409
<i>Pile width (y/h)</i>	3.75	4.30
<i>Undisturbed wind velocity(U_0) [m/s]</i>	5.26	9.1 (and 9.9)
<i>Angle of repose [°]</i>	38 (coal)	33.2 (sand)

A5.3.1. FLOW TOPOLOGY / BENCHMARK

In this section, the flow topology and wall shear stress distribution over and around the oblong pile is analyzed. With the intent to assess the numerical model, the flow features obtained within the present work are confronted against numerical results and oil-film surface coating records from other authors. Additionally, the correlation of the wall shear stress predicted in the simulations performed using OpenFOAM with the wind tunnel’s experiments is assessed.

The discussion of the results will start by the analysis of the wall flow topology followed by the fluid flow features around the piles. It should be noted that the term “wall” refers to the

“surface” of the pile or its surrounding.

A5.3.1.1. WALL FLOW TOPOLOGY

As previously stated, this study was performed for two different wind incidence angles, namely, $\beta = 60^\circ$ and $\beta = 90^\circ$, which will be analyzed separately.

A.5.3.1.1.1. WIND INCIDENCE ANGLE OF 90°

Figure A5-25 depicts the surface flow visualization results (oil-film mixture coating) and the numerical predictions of the wall shear stress distributions obtained by Furieri et al. [4]. Like those authors, who compared their results to support the numerical model employed, in the present work it is intended to perform a similar analysis, since the shape of the piles is quite similar.

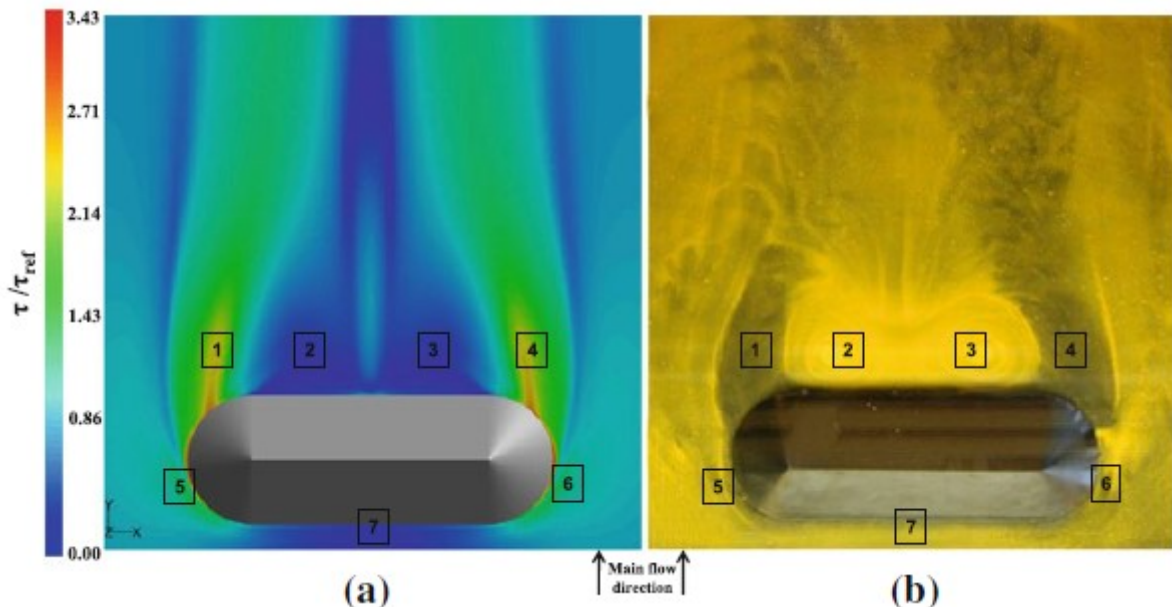


Figure A5-25: Wall flow around the stockpile ($\beta = 90^\circ$): **a** Numerical contours of non-dimensional wall shear stress, **b** surface flow visualization [4].

Figure A5-25(b) presents the surface flow visualization results with varying color intensities:

bright yellow indicates areas of low friction while the darkest regions correspond to higher values of wall shear stress. Similar surface flow structures were observed in the numerical results (Figure A5-25(a), with four different flow features, corresponding to seven areas due to the symmetry of the pile’s shape.

The values of the wall shear stress distribution shown in Figure A5-25 were obtained for $U_0=5.26$ m/s and are normalized with a reference value chosen by those authors ($\tau_{ref} = 0.07$ Pa). Therefore, in order facilitate the comparison, the numerical results obtained in the present work presented in Figure A5-26, are also normalized. The chosen value was the one registered in the areas undisturbed by the wall-mounted obstacle, specifically, $\tau_{ref} = 0.126$ Pa. Furthermore, since the present study uses velocities different from that of Furieri et al. [4], the comparison will be conducted only for the lower velocity, $U_0=9.1$ m/s, as presented in Figure A5-26. As stated in Chapter A3, due to the symmetry of the piles, only half of the domain was evaluated, consequently only half of the pile is depicted in Figure A5-26.

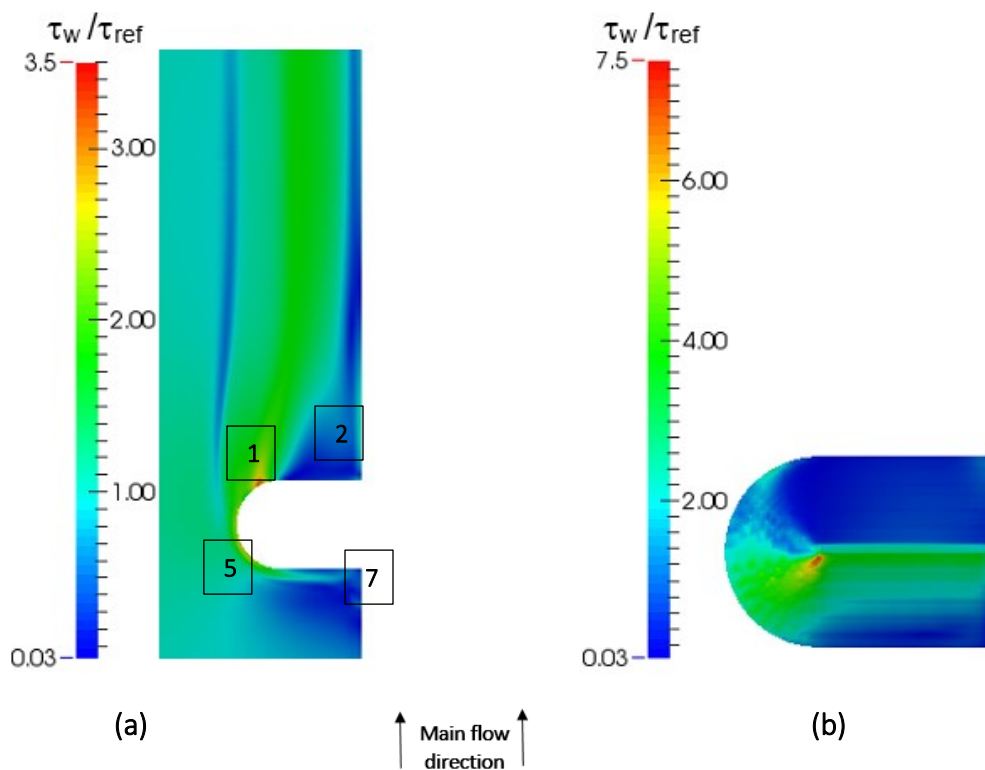


Figure A5-26: Numerical contours of non-dimensional wall shear stress ($\beta = 90^\circ$, $U_0=9.1$ m/s and $\tau_{ref} = 0.126$ Pa): **a** wall flow around the stockpile, **b** wall flow over the stockpile.

By comparing Figure A5-25(a) and Figure A5-26(a), it is clear that the results are analogous. Not only the maximum normalized wall shear stress is similar, but also the identified surface flow structures by Furieri et al. [4] can be observed in Figure A5-26(a). The areas where the counter-rotating vortices occur are clearly located downstream the pile’s limit (zone 2), like the

acceleration flow area, which starts on the side of the pile (zone 5) and extends downstream, towards zone 1 where the highest wall shear stress occurs ($\tau_w \approx 3.5\tau_{ref}$). The lowest values of τ_w appear upstream the leading edge of the pile, being zone 7 a stagnation area.

The wall shear stress is critical in the particles take-off mechanisms; therefore, as a first step to correlate the pile free-surface deformation experimental data with the numerical results, the wall shear stress distribution on the surface of the pile is presented in Figure A5-26(b).

The comparison between the erosion profile and the sand emission rate at $t=1$ minute presented in Figure A5-9 (and Figure A5-10) and Figure A5-16, respectively, clearly indicates the influence of the τ_w on the erosion process. The higher values of wall shear stress shown in Figure A5-26(b) correspond to the regions where the erosion is more intense, in particular the crest region away from the centerline and on the sides of the pile close to the limiting edge (Figure A5-10). Upstream the pile, in the stagnation region, practically no alteration occurs on the pile's contour and the evolution of the pile's profile (Figure A5-9) agrees with the presence of the counter-rotating vortices - the particles appear to be trapped downstream the pile.

As described in Section A5.1, two different velocities were tested, and, in order to analyze the influence of the main flow velocity, Figure A5-27 reports the wall shear stress numerical contours for the velocity $U_0=9.9$ m/s. The reference value selected for the wall shear stress is $\tau_{ref}=0.146$ Pa.

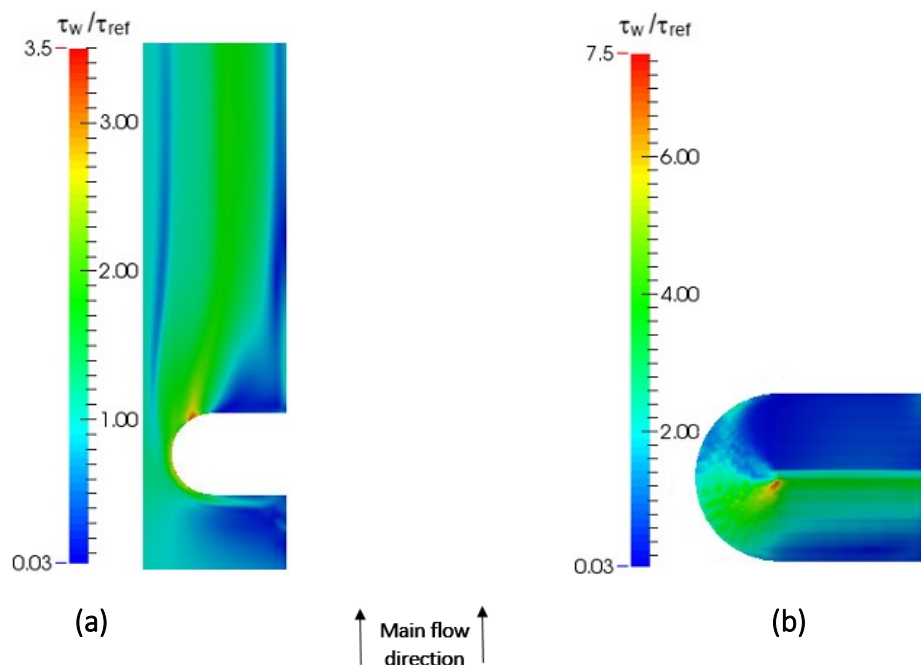


Figure A5-27: Numerical contours of the non-dimensional wall shear stress ($\beta = 90^\circ$, $U_0=9.9$ m/s and $\tau_{ref}=0.146$ Pa): **a** wall flow around the stockpile, **b** wall flow over the stockpile.

The results reported in Figure A5-26 and Figure A5-27 present similar contours, although they

were obtained with different undisturbed flow velocities.

As expected, the wall shear stress increases with the wind speed, as it can be noticed in Figure A5-28, particularly in the acceleration regions.

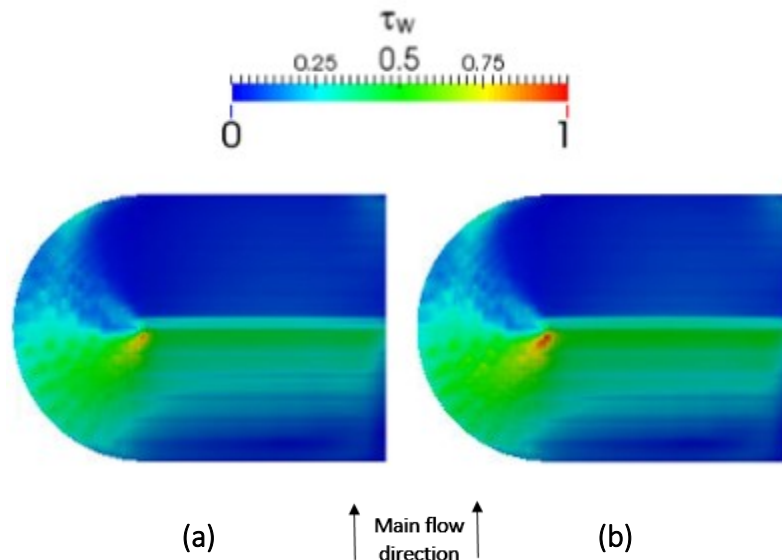


Figure A5-28: Wall shear stress distribution over the stockpile - numerical predictions: **a** $U_0=9.1$ m/s, **b** $U_0=9.9$ m/s.

In Figure A5-28 it can be noted that the values of the wall shear stress increase along with the main flow velocity; it should be further noted that the contour over the stockpile for both velocities is identical, specifically, $\tau_{max} = 0.968$ Pa and $\tau_{max} = 1.107$ Pa were registered for $U_0=9.1$ m/s and $U_0=9.9$ m/s, respectively. These results are in physical agreement with the observations made during the erosion tests (Figure A5-10).

Similar behavior is verified for the flow around the piles; the maximum values of the wall shear stress (τ_{max}) are registered downstream the leeward edge of the pile (zone 1 – Figure A5-26(a)) and they are 0.425 Pa and 0.490 Pa for the undisturbed main flow velocities (U_0) of 9.1 m/s and 9.9 m/s, respectively.

In order to perform a more quantitative analysis and comparison of the flow around the stockpile, Figure A5-29 depicts the velocity vector field in the vicinity of the pile. This analysis is only conducted for the cases where the stockpile is normal to the wind direction.

Once again, there is clear evidence of the presence of the vortices downstream the pile's edge. This visualization of the vector field allows the measurement of the distance (d_v) between the centers of the vortices.

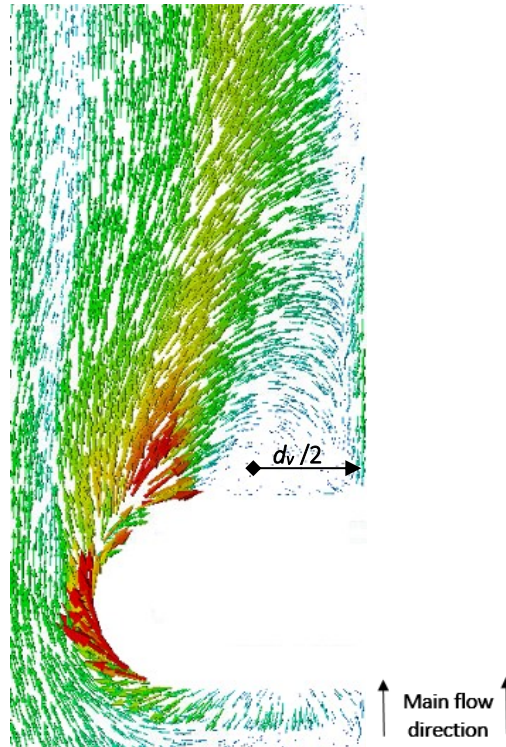


Figure A5-29: Numerical velocity vector field ($\beta = 90^\circ$): near-wall flow around the stockpile (vectors colored by velocity magnitude).

In Figure A5-29 only the distance between the center of the vortices and the middle plane is represented ($d_v/2$). A comparison with the results obtained by Furieri et al. [4] is reported in Table A5-4.

Table A5-4: Analysis of the normalized distance between vortices (d_v/h) for the case with $\beta = 90^\circ$.

	Numerical Simulation		Experimental work
	OpenFOAM	Fluent [4]	Furieri et al. [4]
d_v/h	3.541	3.788	3.156
Difference [%]	10.9	16.7	

It can be observed in Table A5-4 that the normalized distance between vortices in the OpenFOAM simulation is closer to the one performed with the flow visualization [4] tests, leading to a difference of approximately 11%, almost 7% less than the Fluent predictions.

A.5.3.1.1.2. WIND INCIDENCE ANGLE OF 60°

A similar study was made for the wind incidence angle of 60°. Figure A5-30 depicts the results obtained by Furieri et al.[4] in what concerns the distribution of the wall shear stress around the stockpile, as well as, the surface flow visualization obtained with the oil film tests.

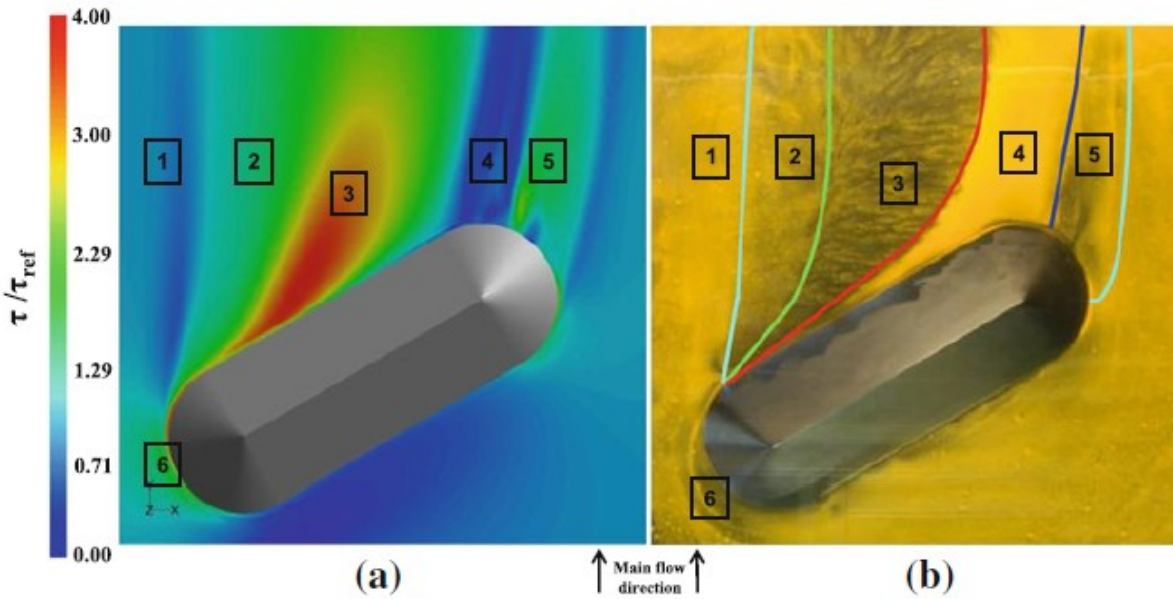


Figure A5-30: Wall flow around the stockpile ($\beta = 60^\circ$): **a** Numerical contours of non-dimensional wall shear stress, **b** surface flow visualization [4].

Comparing Figure A5-25 and Figure A5-30, it is noticeable that the positioning of the pile causes flow asymmetry and high disturbance of the main flow.

In Figure A5-30 it can be observed the six different zones identified by Furieri et al. [4]. Considering the normalized wall shear stress values, it can be noted that the flow accelerates on the sides of the pile, having zone 5 reduced strength and extension as compared to those of zone 6. The region with the highest wall shear stress values, which differs from that of that of the incidence angle of 90° (Figure A5-25), was registered downstream to the pile's edge and it extends itself up to the wake zone (zone 3). Still in the leeward side, an increasing of the wall shear stress towards the center is visible on the left side of the pile, from zones 1 to 3; and the lowest wall friction was attained on zone 4 (right hand side). Similar pattern can be observed in Figure A5-30(b), in this particular zone occurs an accumulation of the oil-film mixture.

The wall shear distribution predicted by the OpenFOAM for $U_0=9.1$ m/s is reported in Figure A5-31.

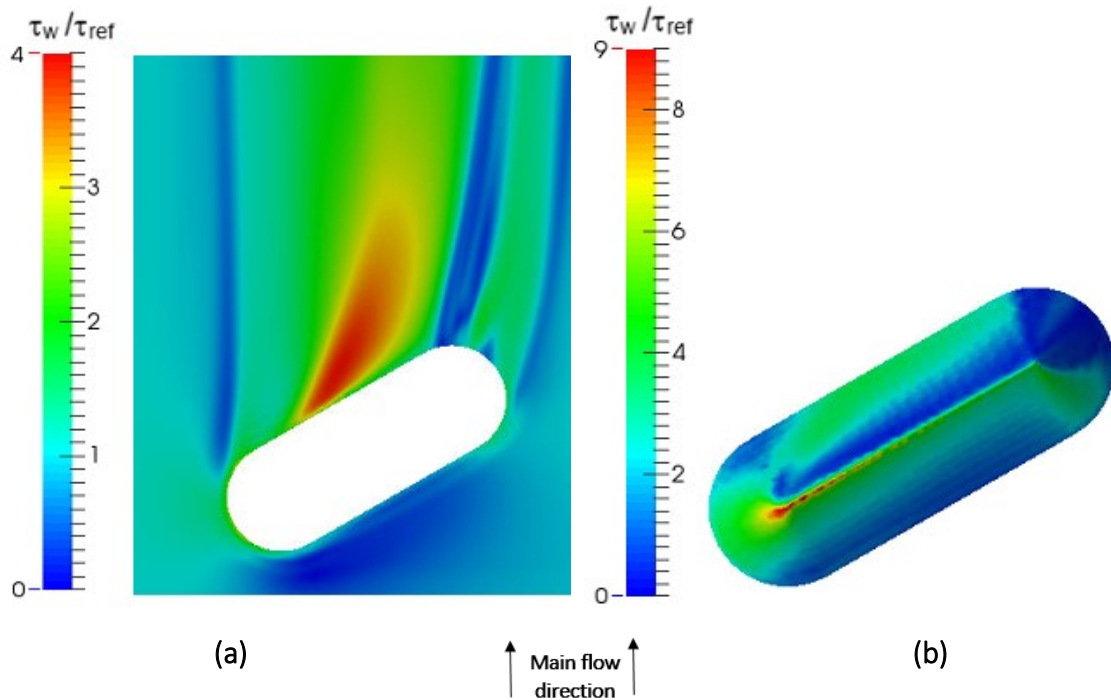


Figure A5-31: Numerical contours of non-dimensional wall shear stress ($\beta = 60^\circ$, $U_0 = 9.1$ m/s and $\tau_{ref} = 0.126$ Pa): **a** wall flow around the stockpile, **b** wall flow over the stockpile.

It can be observed in Figure A5-31(a) that, the wall shear stress contours around the stockpile depicted are similar to those presented in Figure A5-30; in addition, the range of values is comparable and, in particular, the maximum value for both cases is around $\tau_w \approx 4.0\tau_{ref}$.

In what concerns the shear stress features for the flow over the pile, they are depicted in Figure A5-31(b), and once again the higher values were registered in the crest's vicinity. In addition, it is visible the flow acceleration in both sides of the pile, with the left side experiencing higher values and, in this aspect, differing for the situation in which the flow direction is normal to the pile (Figure A5-27(b)), where a speed up area is also present in the leeward face of the pile.

Comparison of the free surface deformation registered in the erosion tests (Figure A5-13) with the wall shear stress contours lends credibility to the shape of the pile's edge observed after the first minute of erosion. Although almost all sand had stayed within the initial contour, it can be observed that on both sides the pile was wind-swept, but with higher intensity on the left side. Furthermore, it appears that the crest was washed out to the right, which agrees with the decreasing values of the wall shear stress along the crest.

A5.3.1.2. FLOW FEATURES AROUND THE PILES

In addition to the study of wall shear stress caused by the flow over and around the piles (Section A5.3.1.1), the knowledge of the flow features around stockpiles is also of major importance to support the understanding of the phenomena occurring not only with the stockpiles, but also with their surroundings.

In this section, with the aim of evaluating the performance of the proposed numerical model using the OpenFOAM, its predictions are compared against those produced with Fluent [4]. Once again, this study was carried out for both wind incidence angles ($\beta = 90^\circ$ and $\beta = 60^\circ$), and, due to the similarity of the flow features observed with the two velocities tested, only the results for $U_0=9.1$ m/s are reported.

A.5.3.1.2.1. WIND INCIDENCE ANGLE OF 90°

As previously mentioned, the computational domain was designed to mimic the sand piles tested in the wind tunnel. Therefore, the dimensions of the present simulated models differ slightly from those used by Furieri et al. [4]. Nevertheless, the flow features are comparable and both sets of results are presented in Figure A5-32.

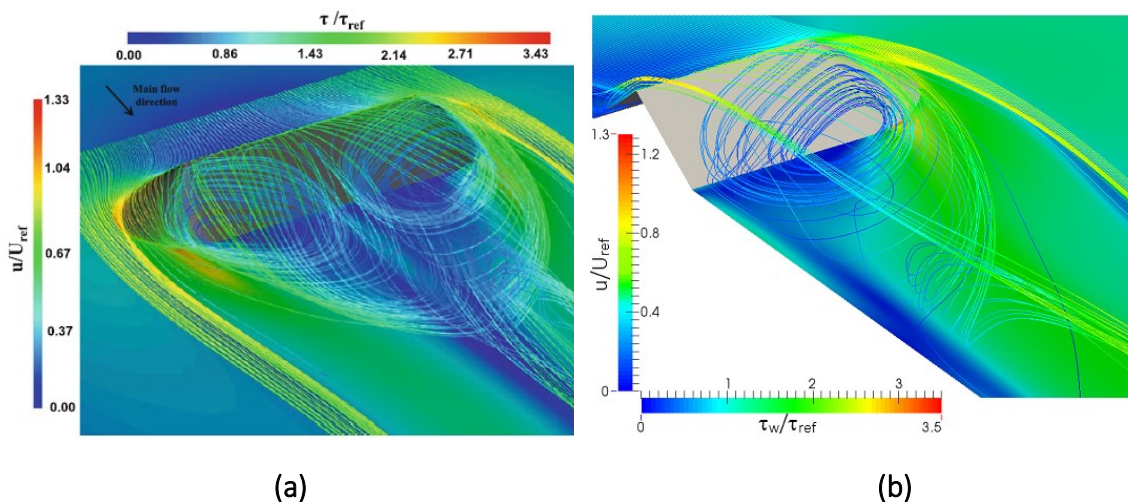


Figure A5-32: Airflow topology over the stockpile – three dimensional streamlines($\beta = 90^\circ$): **a** Fluent results [4], **b** OpenFOAM results ($U_0=9.1$ m/s).

In Figure A5-32 the three-dimensional streamlines are colored by the velocity magnitude and

the ground with the wall shear stress distribution, which was already analyzed in the previous section.

In Figure A5-32, the OpenFOAM results, which are depicted only for half of the pile due to symmetry, are in good agreement with those produced by Fluent in what concerns to the range of values and flow features. It is clearly visible the flow bending and acceleration on the lateral surfaces, as well as the flow separation at the crest and sides of pile, leading to slow vortices downstream the model. Furthermore, some of the main flow passes over the pile curving the rotation axis of the vortical structures, which are perpendicular to the ground in the region near to the pile, as shown in Figure A5-33.

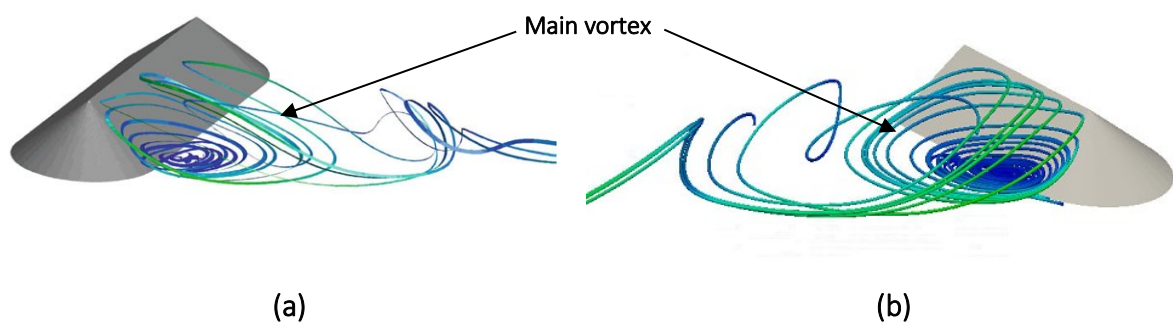


Figure A5-33: Airflow topology over the stockpile – path lines release from the ground (leeward) ($\beta = 90^\circ$): **a** Fluent results [4], **b** OpenFOAM results ($U_0 = 9.1$ m/s).

Once again, despite some differences due to the post-processing tools employed, good agreement was obtained between the features predicted by the simulations using the two modeling software tools.

The detail of the recirculation flow contour depicted in Figure A5-33 agrees well with the vortices revealed by the experimental visualization technique presented in Figure A5-25(b) and with the erosion profiles shown in Figure A5-9. During the erosion tests some of the sand released from the pile was trapped between the main vortices (Figure A5-32 and Figure A5-33), and, although this phenomenon occurred throughout the tests, it was difficult to capture it in the pictures; however, it can be clearly observed at $t = 7$ minutes for Figure A5-9.

Another approach was used to study the airflow topology, namely the analysis of a vertical plan downward the pile, in the wake zone, specifically at $x/h = 2.25$. Figure A5-34 and Figure A5-35 depict the streamlines, as well as the velocity vectors in that particular plan as predicted by Fluent and OpenFOAM, respectively.

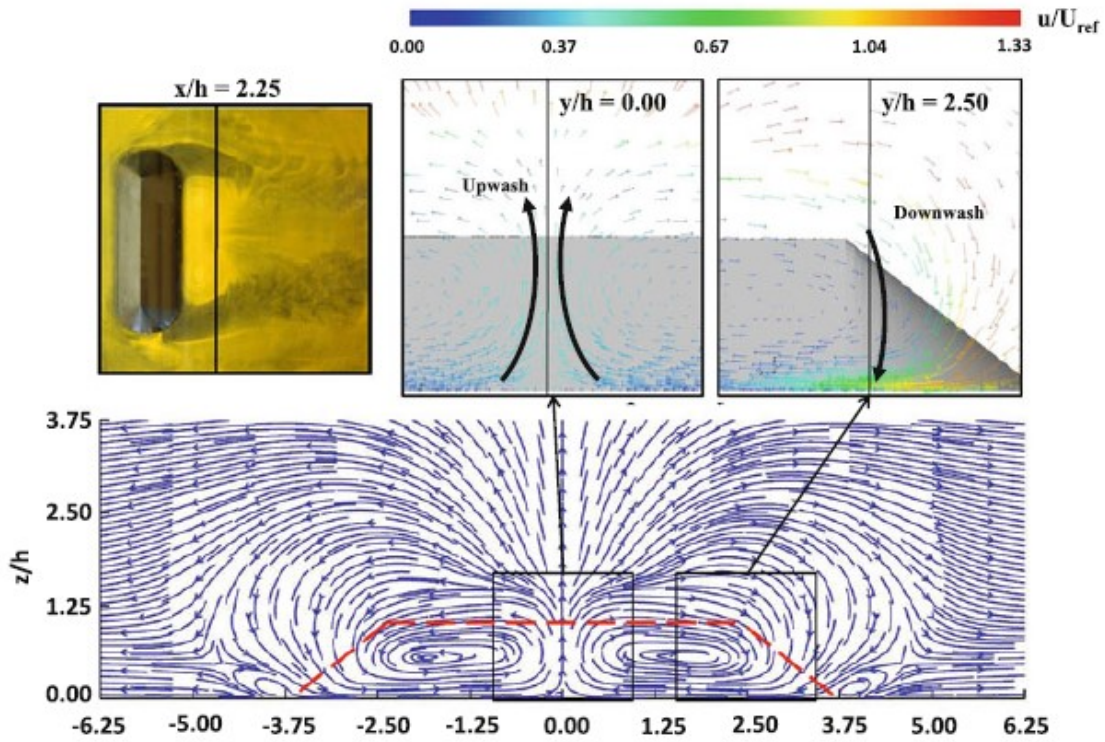


Figure A5-34: Airflow topology around the stockpile – streamlines in transversal plane ($x/h = 2.25$) for $\beta = 90^\circ$; Fluent results [4].

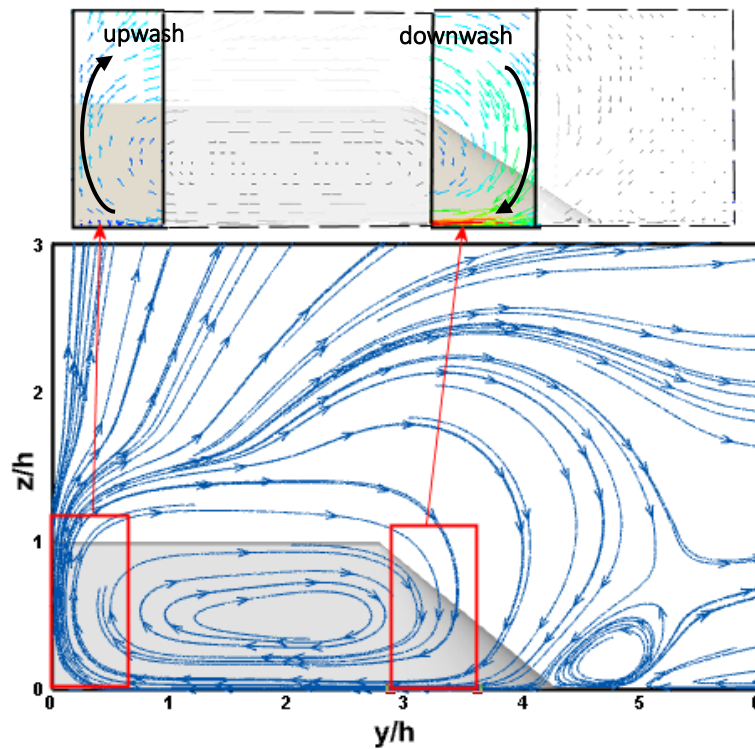


Figure A5-35: Airflow topology around the stockpile – streamlines in transversal plane ($x/h = 2.25$) for $\beta = 90^\circ$ and $U_0=9.1$ m/s; OpenFOAM results.

It can be stated that the outcomes of both simulations are quite similar; the main vortex is visible in both figures and the upwash and downwash zones are in relatable areas, i.e., the fluid moves upwards in the symmetry plan and downwards on the side of the pile (black and red rectangles in Figure A5-34 and Figure A5-35, respectively).

Additionally, in the same location ($x/h = 2.25$), the spanwise variation of the wall shear stress profile was plotted with the intention to relate it with the airflow topology, and is depicted in Figure A5-36.

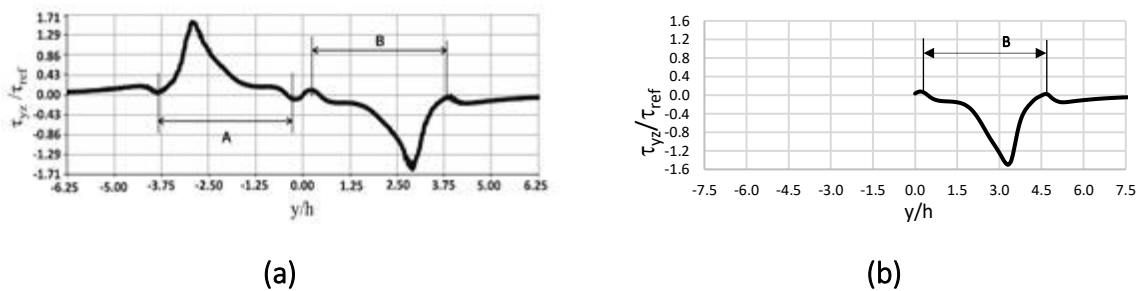


Figure A5-36: Airflow topology around the stockpile – plot of non-dimensional wall shear stress in transversal plane ($x/h = 2.25$) ($\beta = 90^\circ$): **a** Fluent results [4], **b** OpenFOAM results ($U_0=9.1$ m/s).

Through Figure A5-36 it can be seen that the zones of high wall shear stress corresponds to the vortical structures highlighted by the streamlines in the vertical plane. Due to the already mentioned difference in the dimensions of the pile (Table A4-1), zones B are slightly different, namely, $0.625 < y/h < 4.375$ and $0.22 < y/h < 4.75$, for Fluent and OpenFOAM, correspondingly.

As expected, it can be observed that in the upwash zone (symmetry plan – $y/h = 0$), where the fluid leaves the surface, the wall shear stress is zero. The higher values were registered where the fluid had a downward movement to the ground, i.e., on the sides of the pile, specifically, $y/h = 3.125$ and $y/h = 3.31$ in Figure A5-36(a) and Figure A5-36(b), respectively. This downwash zones were already identified in Figure A5-25 and Figure A5-26, namely, zones 1 and 4.

Finally, the plots in Figure A5-36 also allowed identifying the beginning of the zone where the flow is no longer disturbed by the model, specifically, $y/h = 5.5$ and $y/h = 6.5$, in Fluent and OpenFOAM results, respectively. In this zone, the wall shear stress in the spanwise direction returns to zero, since the only contribution to it is oriented with the inward flow.

A.5.3.1.2.2. WIND INCIDENCE ANGLE OF 60°

A similar analysis to the previous is now performed for the incidence angle of 60° . Figure A5-37

depicts the flow topology obtained by Furieri et al. [4] and within the present work.

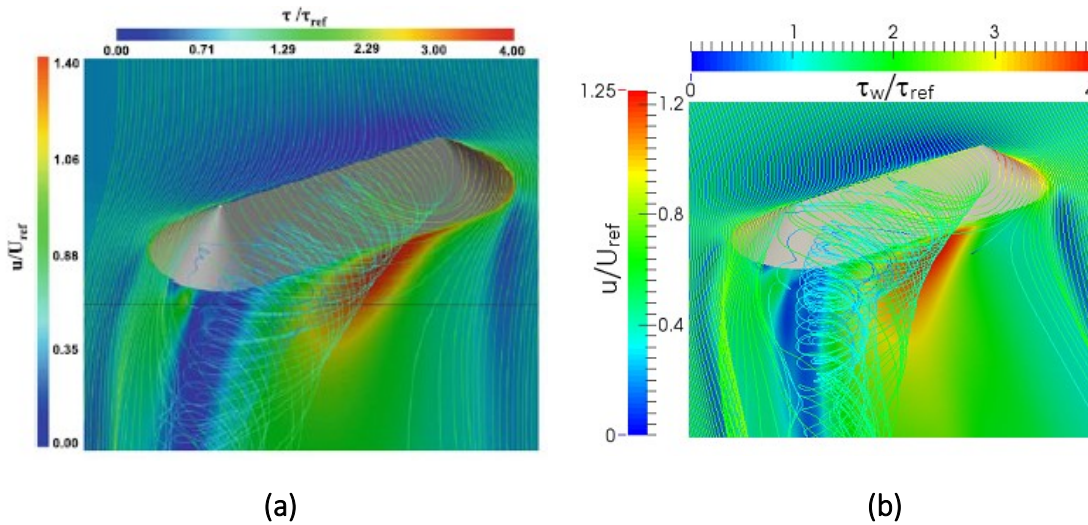


Figure A5-37: Airflow topology over the stockpile – three dimensional streamlines($\beta = 60^\circ$): **a** Fluent results [4], **b** OpenFOAM results ($U_0=9.1$ m/s).

In Figure A5-37 it is visible the wall shear stress distribution in the ground around the piles and the three-dimensional streamlines, which are colored by the velocity magnitude.

The pile's placement influence in the main flow stream is clear in Figure A5-37. Contrarily to what was observed in the previous case ($\beta = 90^\circ$), despite the flow separation also occurring near the pile's crest, in this case, a main helical vortex is formed, and its rotation axis tends, further downstream, to the main flow direction.

Comparing Figure A5-37(a) and Figure A5-37(b), the similarities between the two plots are evident, and considering the benchmarking of the Fluent results against the oil-film visualization, it can be stated that the OpenFOAM predictions are also in a good agreement with the experimental results. Additionally, considering the erosion profiles shown in Figure A5-13, the direction of rotation axis of the vortex formed in the separation zone, agrees well with the deformity of the pile's contour.

Likewise the previous case (Section A.5.3.1.2.1), a study of a vertical plane in the wake zone, specifically at $x/h = 2.875$, was made, and the streamlines, as well as, the velocity vectors in that particular plan, calculated through Fluent and OpenFOAM simulations, are depicted in Figure A5-38 and Figure A5-39, respectively.

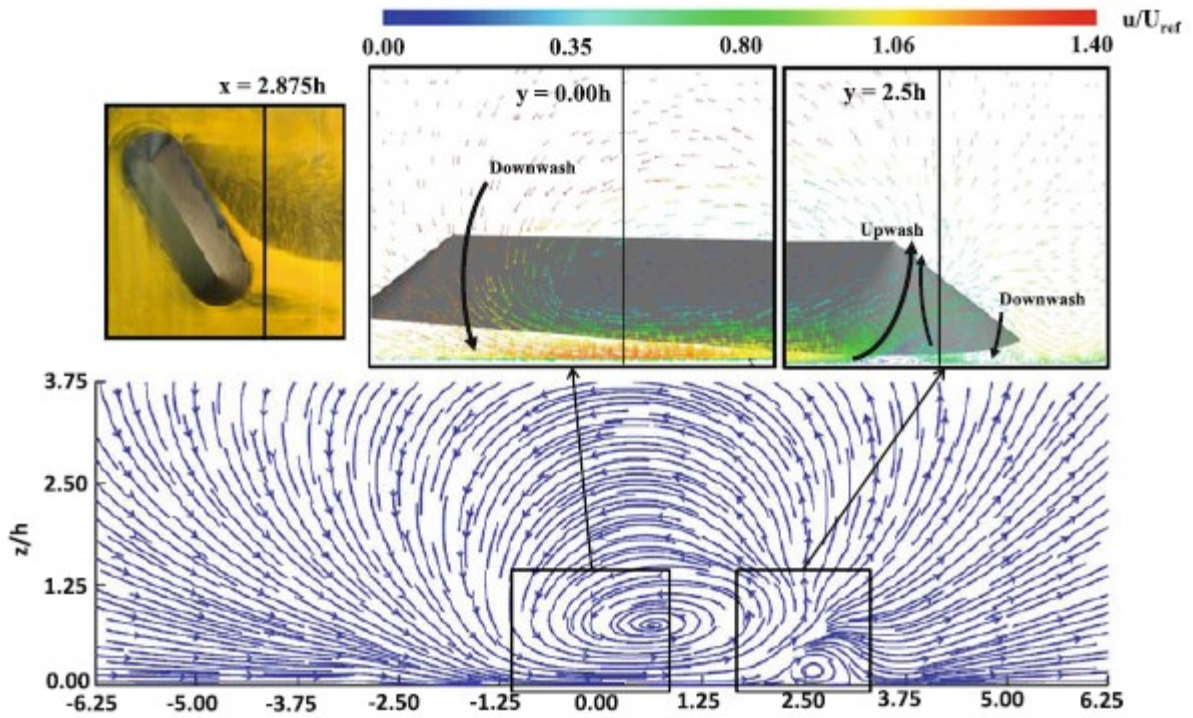


Figure A5-38: Airflow topology around the stockpile – streamlines in transversal plane ($x/h = 2.875$) for $\beta = 60^\circ$; Fluent results [4].

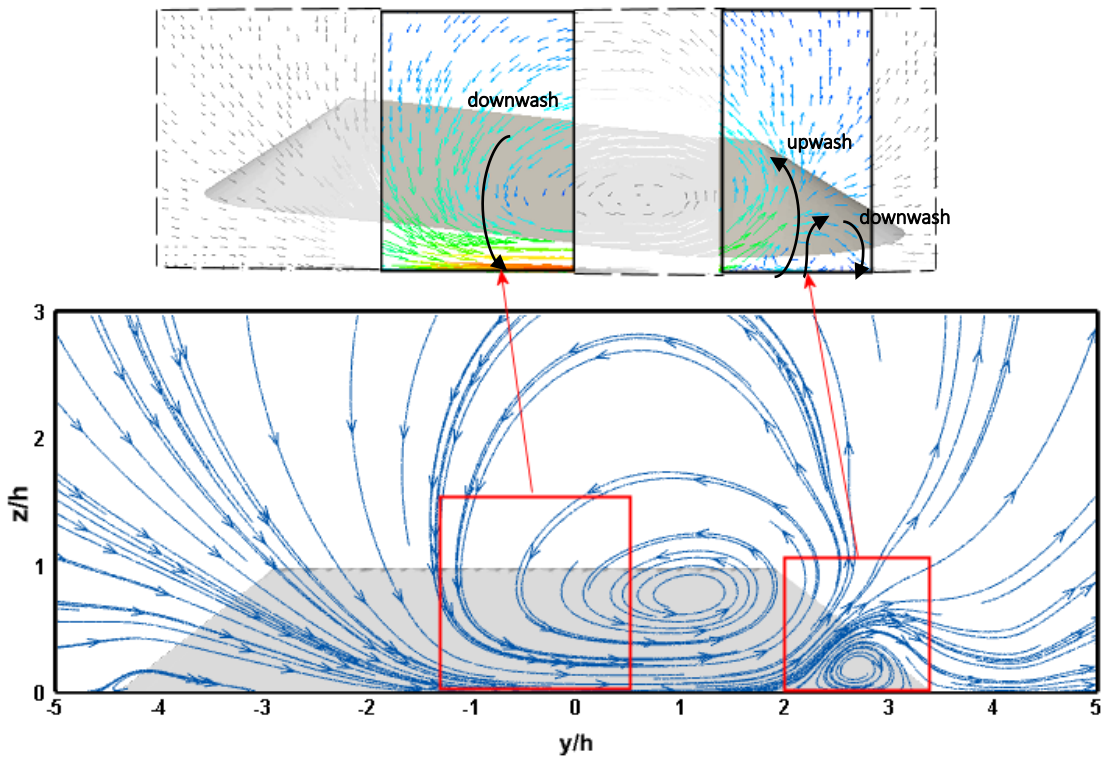


Figure A5-39: Airflow topology around the stockpile – streamlines in transversal plane ($x/h = 2.875$) for $\beta = 60^\circ$ and $U_0 = 9.1$ m/s; OpenFOAM results.

Once again, the flow features predicted by OpenFOAM (Figure A5-39) are analogous to those obtained with Fluent (Figure A5-38). To support this analysis, Figure A5-40 depicts the spanwise wall shear stress profile in the same location ($x/h = 2.875$), and the similarity between the two plots is evident.

It can be observed two counter-rotating vortices; one more intensive, with maximum values of $\tau_w \approx 3.5\tau_{ref}$ and $\tau_w \approx 3.6\tau_{ref}$ for Fluent and OpenFOAM, respectively, as shown in the corresponding Figure A5-38 and Figure A5-39. The smaller vortex, closer to the side of the pile and induced by the main one, registered lower maximum values for the ratio of τ_w / τ_{ref} , as reported in Figure A5-40.

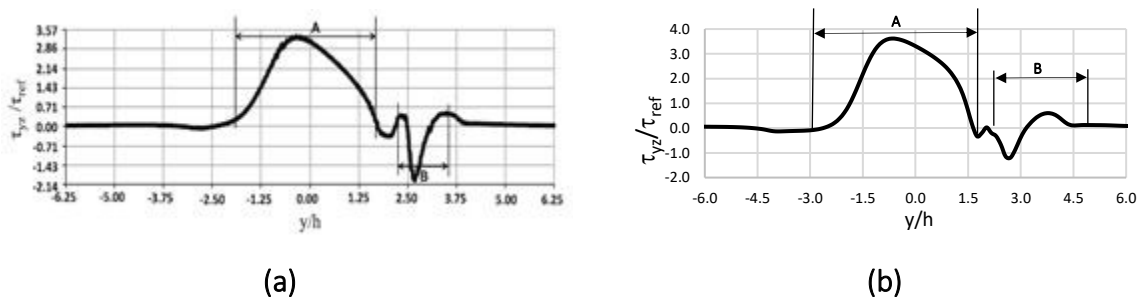


Figure A5-40: Airflow topology over the stockpile – plot of non-dimensional wall shear stress in transversal plane ($x/h = 2.875$) for $\beta = 60^\circ$: **a** Fluent results [4], **b** OpenFOAM results.

In addition, the relation between the airflow topology and the spanwise wall shear stress is evident. This can be observed in the comparison of the inserts of Figure A5-38 and Figure A5-39 with the profiles plotted in Figure A5-40, in what concerns the downwash zones, which correspond to the peaks in the wall shear stress, and the upwash zones between the two vortices located around $y/h = 2.5$.

Moreover, and as supported by the visualization and analysis of the three-dimensional streamlines (Figure A5-37), both plotted streamlines in Figure A5-38 and Figure A5-39 and wall shear stress profiles depicted in Figure A5-40, agree well with the pile limiting edge deformation observed in the erosion tests (Figure A5-13). In the region near the main vortex the sand was wind-swept and on the other side (near the secondary vortex), the pile’s contour was stretched and the sand is trapped near the edge.

A5.4. CONCLUDING REMARKS

The aim of the present chapter is to assess the airflow features over and around oblong piles

and its interaction with the free surface and consequent evolution of the deformation. This work includes erosion tests for two wind speeds ($U_0=9.1$ m/s and $U_0=9.9$ m/s) and two wind incidence angles ($\beta=60^\circ$ and $\beta=90^\circ$).

It was required to design and develop a device for the setup of the sand pile. Several tests were made and it was considered that the projected device was able to ensure the repeatability of the piles' shape and dimensions. In addition, it was performed the evaluation of the best measuring grid for the erosion profiles. Due to the small differences registered between the two tested grids, the coarser grid with 20 mm spacing was selected.

Regarding the free-deformation observed in the erosion tests, as expected, the erosion process was gradual along time, being the most significant modifications in the shape during the early stages of the process. For the cases where the wind is flowing normal to the pile, despite eroding throughout the test, the crest was the last feature to disappear, receding over time and tending to a V-shape over the symmetry plane of the pile. Similar behavior occurred along time with the higher test velocity; however, the erosion was much more significant for the corresponding times. Over the duration of the erosion tests, both piles extended themselves toward downstream, being more accentuated for $U_0=9.9$ m/s.

The influence of the wind direction was also evaluated, and a wind incidence angle of 60° in relation to the crest line was tested. Comparing the two orientations, the height reduction of the pile is more intense for the angle of 60° ; however, the extension of the pile beyond the initial contour is more evident for the angle of 90° .

A resemblance between the morphology values in the downwind portion of the pile with 60° of wind incidence and the 90° incidence cases was observed, although it faded away as the test progresses. Also, due to the influence of the piles in the wind pattern, in the cases where the wind is normal to the pile, its changeability is symmetrical, whereas for incidence of 60° , a rather pronounced alteration of the initial contour was observed at the upwind boundary closer to the tunnel's exit.

As expected, in all cases the areas where lowering of the pile surface was registered a positive sand emission occurred (erosion), and an increase of the height corresponds to deposition.

In the cases where the pile was placed normal to the main flow, regardless of the velocity, the higher values of erosion were registered in the peaks of the crest, while deposition is more accentuated where the sand exceeds the initial reference contour in the leeward.

By analyzing the sand fluxes along the entire erosion tests for both velocities, it can be noted a continuous decrease of the erosion fluxes; however, these fluxes are always higher than those associated with the deposition. Also for both velocities, the deposition flux increases in the beginning of the test, and as it progresses this trend changes, depending on the velocity. Erosion and deposition flux values, as observed, are larger for the higher tested velocity ($U_0=9.9$ m/s).

In what concerns the study with the wind incidence angle of 60° , and regardless the velocity, the higher erosion values occur at the crest, being more accentuated at the peak near to the wind tunnel's exit.

From the analysis of the sand emission rate during the erosion tests, for both velocities the erosion flux is higher than the deposition flux; this observation results from the fact that some particles travel beyond the measuring area limits. Interestingly, there is a clear decreasing trend for the deposition flux with $U_0=9.9$ m/s, whereas for $U_0=9.1$ m/s it presents a somewhat erratic behavior.

The numerical simulations were performed with the OpenFOAM, and the results were benchmarked against oil-film visualization tests and numerical results from other authors, who used Fluent, as well as against the experimental measurements carried out in the context of the present work. Flow topology and flow features over and around the piles were considered for both velocities and incidence angles.

For all cases and flow features analyzed, it was found good agreement between the OpenFOAM and Fluent predictions. The minor discrepancies observed are mainly due to geometric differences between the pile models used in the present work and in that selected for comparison. It should be noted that Fluent predictions were validated against oil-film visualization tests; therefore, giving further credibility to the OpenFOAM results. Moreover, the numerical results obtained in the present work were compared against the experimental measurements, and the flow features are physically sound and consistent with the erosion contours observed.

In what concerns the flow topology, for $\beta = 90^\circ$, a symmetrical behavior was observed downstream the pile, being the lower values of the wall shear stress registered at the center of the wake zone. For $\beta = 60^\circ$, an enhanced disturbance of the main flow was observed, and in opposition to $\beta = 90^\circ$, the higher wall shear stress value was attained downstream the pile.

Regarding the flow features around the piles, their analysis was conducted by using three-dimensional streamlines over the piles and two-dimensional plots of streamlines, vector fields and spanwise wall shear stress profile over a vertical plan downward the pile. The influence of the wind incidence angle was clearly noticed in the vortical structures formed in the leeward of the pile. Two symmetrical counter-rotating vortices were observed for $\beta = 90^\circ$, being its rotation axis initially perpendicular to the ground and then curved by the main flow passing over the pile's crest. For the models positioned at an angle of $\beta = 60^\circ$, also two counter-rotating vortices formed in the separation zone, with one more intense than the other, being the latter induced by the main vortex. In addition, the rotation axis of the helical main vortex tends toward the main flow direction.

It was enlightening to investigate the evolution of the deformation of the free surface of the sand piles. In particular, the case with $\beta = 60^\circ$, in opposition to the piles positioned normal to

the main flow where features phenomena like symmetry in the wake zone was expected, the behavior of the pile's contour and profile were to a great extent unexpected.

The assessment of the flow topology over and around the piles makes a good contribution toward the understanding of the intervening phenomena associated with the wind erosion of stockpiles and their surroundings, in particular the vortical structures in the wake zone.

Finally, the good agreement of the OpenFOAM predictions with those obtained with Fluent and their experimentally validation using oil film visualization and erosion tests gives further credibility to the proposed numerical model and it provides sure confidence about the usability of OpenFOAM in this type of applications.

CHAPTER A6

CONCLUSIONS

The present study triangular piles were also analyzed aiming to understand airflow features over and around granular piles and their relation with the free surface erosion. The choice of this simpler geometry is two-fold: need of getting acquainted with the procedures and methodologies involved, while facilitating their validation.

The piles - triangular and oblong - were tested in a wind tunnel facility. Three different experimental tests were carried out: erosion; wall shear stress and pressure measurements. The erosion experiments were performed using sand piles, while for the wall shear stress and pressure measurements rigid models were used. Pressure taps were distributed along both leeward and windward faces of the models, while the *Irwin* probes were placed only on the stoss side. From the erosion tests, based on the evolution of the erosion profiles, it was possible to compute the sand emission rate.

Due to construction limitations, only one configuration was considered for the oblong pile, and with these only erosion tests were carried out. Regarding the triangular piles, three different stoss angles were used (10° , 15° and 20°) and two crest heights (75 and 150 mm), leading to four different configurations (the crest with 150mm was only used for stoss angle of 15°). All triangular configurations were subjected to the three experimental tests (pressure, wall shear

stress, and erosion), except the pile with $h=150\text{mm}$, for which it was not possible to perform erosion tests due to limitations of the measuring system. Two different velocities ($U_0=9.1\text{ m/s}$ and $U_0=9.9\text{ m/s}$) and incidence angles ($\beta=60^\circ$ and $\beta=90^\circ$) were employed for the oblong piles erosion tests, while in the triangular cases, only the higher velocity was used ($U_0=9.9\text{ m/s}$) and the piles crests were oriented normal to the streamwise flow.

A device to build the oblong pile in the test chamber of the wind tunnel was designed and developed. The device was evaluated through different tests to guarantee the repeatability of the shape and dimensions of the piles. In addition, it was conducted a study to determine the most suitable measuring grid and a grid with 20 mm spacing was selected.

Numerical simulations were performed with all configurations using the CFD Package OpenFOAM. The main reasons associated with the selection of this code are free of charge availability, flexibility and the adaptability, and the large communities contributing to its forums.

In what concerns the triangular piles, the purpose of this case was to evaluate the behavior of 2D sand piles, comparing the predicted values by OpenFOAM with the experimentally-derived results. In addition, the study of the evolution of the free-surface deformation, as well as sand emission flux, which included the calibration of the dust model of Shao [15], were also considered.

Good agreement between the numerical results and the experimental measurements was attained for both pressure and friction coefficients. In what concerns the pressure coefficient, the lower deviations were observed between the foothill and half-length of the windward surface, and, although with similar behavior, the predicted values in the leeward face exceeded the experimental measurements in some cases, by as much as twice higher. OpenFOAM predictions agree well the friction coefficient for all configurations, the case with the lowest angle (10°) is the one with the least favorable agreement. The Reynolds number independency condition is evidenced by the predictions and experimental results.

The relevant finding of the triangular pile cases is the validation of the methodology used, considering the good agreement between the experimental results and the Shao [15] model predictions after appropriate calibration. Therefore, it can be concluded that the simplified model of Shao [15] can be used to estimate the sand emission rate from tilted surfaces, when the appropriate values of the model empirical coefficient are employed.

In what concerns the oblong case, the aim of its study was to assess the airflow features over and around such pile and its interaction with the free surface and consequent evolution of the deformation.

The erosion process of the oblong pile was gradual along time, being more intense in the initial period of time. Similar behavior was observed in the two tested velocities, being, as expected, more accentuated for the highest one ($U_0=9.9\text{ m/s}$). In the cases with $\beta=90^\circ$, although eroding

during the course of the tests, the crest was the last feature to disappear, receding over time and tending to a V-shape relatively to the symmetry plane of the pile.

Evaluating the wind direction influence, the erosion was more significant for $\beta=60^\circ$, whereas the extension of the pile beyond the initial contour was more evident in the cases where the wind strikes normal to the pile ($\beta=90^\circ$). In addition, due to the influence of the pile in the wind pattern, as anticipated, when $\beta=90^\circ$ the pile shape changed symmetrically, while a more pronounced alteration at the first area subjected to the incoming flow was observed in the cases with $\beta=60^\circ$.

The study of the free-surface deformation of the oblong pile, in particular for $\beta=60^\circ$, led to interesting results as, contrary to the piles positioned normal to the main flow, the contour in the wake zone is not symmetric and does not exceed the initial reference contour in the leeward.

The analysis of the sand fluxes along the entire erosion tests for both velocities and incidence angles indicates a continuous decrease of the erosion fluxes. Mainly due to the particles that travel beyond the measuring area limits, the erosion fluxes are always higher those of the deposition. Moreover, for both velocities tested, similar erosion fluxes were registered regardless of the wind incidence angle.

However, for close observation of the deposition fluxes, it noticeable the influence of the wind incidence angle upon them, as higher values were registered for $\beta=60^\circ$ independently of the velocity. The behavior for the cases with $\beta=90^\circ$ was consistent with both velocities -, an increase of the deposition flux at the beginning of the test, and after a few time instants, the initial trend changes. For $\beta=60^\circ$, the deposition flux presents a lowering trend for the higher velocity, while for the lower velocity ($U_0=9.1$ m/s) it is observed an erratic behavior.

The computational results obtained for the oblong pile cases were compared against oil-film visualization tests and numerical results from other author, who used the commercial code Fluent. They were also evaluated against the experimental measurements carried out in the present work. The flow topology and flow features over and around the piles for both velocities ($U_0=9.1$ m/s and $U_0=9.9$ m/s) and incidence angles ($\beta=60^\circ$ and $\beta=90^\circ$) were analyzed.

Good agreement between the OpenFOAM and Fluent predictions was obtained, giving greater confidence to the results obtained with OpenFOAM in the present work. In addition, the predicted flow features are in close consonance with the experimentally-obtained erosion contours.

The influence of the incidence angle was evident in the behavior of the flow pattern. For $\beta=60^\circ$ higher disturbance was present and the higher wall shear stress values were observed downstream the pile, starting near the pile contour and extending to the wake zone.

In what concerns the flow features around the oblong piles, the influence of the wind direction

was noticed on the vortical structures formed in the leeward of the pile. Although two counter-rotating vortices were observed for both incidence angles, differences were encountered in their size, symmetry and rotation axis.

The present work makes an important contribution towards further confidence on the usability of OpenFOAM in this type of applications.

Finally, it should be stated that the present work was a very important learning process toward the understanding of the phenomena involved in the wind erosion of stockpiles and its surroundings.

REFERENCES

- [1] Irwin, H. P. A. H., 1981, "A Simple Omnidirectional Sensor for Wind-Tunnel Studies of Pedestrian-Level Winds," *J. Wind Eng. Ind. Aerodyn.*, **7**(3), pp. 219–239.
- [2] Ferreira, A. D., and Vaz, P. A., 2004, "Wind Tunnel Study of Coal Dust Release from Train Wagons," *J. Wind Eng. Ind. Aerodyn.*, **92**(7–8), pp. 565–577.
- [3] Topi, N., and Itnik, M., 2012, "Fugitive Dust Emissions from a Coal-, Iron Ore- and Hydrated Alumina Stockpile," *Air Pollution - Monitoring, Modelling and Health*, D.M. Khare, ed., InTech.
- [4] Furieri, B., Russeil, S., Harion, J. L., Turpin, C., and Santos, J. M., 2012, "Experimental Surface Flow Visualization and Numerical Investigation of Flow Structure around an Oblong Stockpile," *Environ. Fluid Mech.*, **12**(6), pp. 533–553.
- [5] Zhang, Z., Wieland, R., Reiche, M., Funk, R., Hoffmann, C., Li, Y., and Sommer, M., 2011, "Wind Modelling for Wind Erosion Research by Open Source Computational Fluid Dynamics," *Ecol. Inform.*, **6**(5), pp. 316–324.
- [6] Badr, T., and Harion, J. L., 2007, "Effect of Aggregate Storage Piles Configuration on Dust Emissions," *Atmos. Environ.*, **41**(2), pp. 360–368.
- [7] Toraño, J. A., Rodriguez, R., Diego, I., Rivas, J. M., and Pelegry, A., 2007, "Influence of the Pile Shape on Wind Erosion CFD Emission Simulation," *Appl. Math. Model.*, **31**(11), pp.

2487–2502.

- [8] Ferreira, A. D., and Lambert, R. J., 2011, “Numerical and Wind Tunnel Modeling on the Windbreak Effectiveness to Control the Aeolian Erosion of Conical Stockpiles,” *Environ. Fluid Mech.*, **11**(1), pp. 61–76.
- [9] Furieri, B., Russeil, S., Harion, J. L., Santos, J. M., and Milliez, M., 2012, “Comparative Analysis of Dust Emissions: Isolated Stockpile vs Two Nearby Stockpiles,” *Air Pollution XX*, pp. 285–294.
- [10] Furieri, B., Santos, J. M., Russeil, S., and Harion, J. L., 2014, “Aeolian Erosion of Storage Piles Yards: Contribution of the Surrounding Areas,” *Environ. Fluid Mech.*, **14**(1), pp. 51–67.
- [11] Badr, T., and Harion, J. L., 2007, “Quantification of Diffuse Dust Emissions from Open Air Sources on Industrial Sites,” *Proceedings of the 3rd IASME/WSEAS Int. Conf. on Energy, Environment, Ecosystems and Sustainable Development*, Agios Nikolaos, Greece, pp. 276–280.
- [12] Faria, R., Ferreira, A. D., Sismeiro, J. L., Mendes, J. C. F., and Sousa, A. C. M., 2011, “Wind Tunnel and Computational Study of the Stoss Slope Effect on the Aeolian Erosion of Transverse Sand Dunes,” *Aeolian Res.*, **3**(3), pp. 303–314.
- [13] Ferreira, A. D., and Fino, M. R. M., 2012, “A Wind Tunnel Study of Wind Erosion and Profile Reshaping of Transverse Sand Piles in Tandem,” *Geomorphology*, **139–140**, pp. 230–241.
- [14] Lopes, A. M. G., Oliveira, L. A., Ferreira, A. D., and Pinto, J. P., 2013, “Numerical Simulation of Sand Dune Erosion,” *Environ. Fluid Mech.*, **13**(2), pp. 145–168.
- [15] Shao, Y., 2004, “Simplification of a Dust Emission Scheme and Comparison with Data,” *J. Geophys. Res. D Atmos.*, **109**(10), pp. 1–6.
- [16] Lettau, K., and Lettau, H. H., 1978, “Experimental and Micrometeorological Field Studies of Dune Migration,” *Exploring the World’s Driest Climates. Institute of Environmental Science Report 101*, H.H. Lettau, and K. Lettau, eds., Center for Climatic Research, University of Wisconsin, Madison, WI, USA, pp. 110–147.
- [17] de Gennes, P. G., 1998, “Reflections on the Mechanics of Granular Matter,” *Phys. A Stat. Mech. its Appl.*, **261**(3–4), pp. 267–293.
- [18] Bagnold, R. A., 1941, *The Physics of Blown Sand and Desert Dunes*, Methuen, London.
- [19] Sherman, D. J., and Farrell, E. J., 2008, “Aerodynamic Roughness Lengths over Movable Beds: Comparison of Wind Tunnel and Field Data,” *J. Geophys. Res. Earth Surf.*, **113**(2), pp. 1–10.
- [20] Huang, N., Shi, F., and Pelt, R. S. Van, 2008, “The Effects of Slope and Slope Position on Local and Upstream Fluid Threshold Friction Velocities,” *Earth Surf. Process. Landforms*, **33**(12), pp. 1814–1823.
- [21] Pye, K., and Tsoar, H., 2009, *Aeolian Sand and Sand Dunes*, Springer-Verlag, Berlin, Heidelberg.
- [22] Durán, O., Claudin, P., and Andreotti, B., 2011, “On Aeolian Transport: Grain-Scale Interactions, Dynamical Mechanisms and Scaling Laws,” *Aeolian Res.*, **3**(3), pp. 243–270.

- [23] Ferreira, A. D., and Oliveira, R. A., 2009, "Wind Erosion of Sand Placed inside a Rectangular Box," *J. Wind Eng. Ind. Aerodyn.*, **97**(1), pp. 1–10.
- [24] Dong, Z., Liu, X., Wang, H., and Wang, X., 2003, "Aeolian Sand Transport: A Wind Tunnel Model," *Sediment. Geol.*, **161**(1–2), pp. 71–83.
- [25] Marticorena, B., Bergametti, G., Gillette, D., and Belnap, J., 1997, "Factors Controlling Threshold Friction Velocity in Semiarid and Arid Areas of the United States," *J. Geophys. Res. Atmos.*, **102**(D19), pp. 23277–23287.
- [26] Ferreira, A. D., Silva, M. C. G., Viegas, D. X., and Lopes, A. M. G., 1991, "Wind Tunnel Simulation of the Flow around Two-Dimensional Hills," *J. Wind Eng. Ind. Aerodyn.*, **38**(2–3), pp. 109–122.
- [27] Iversen, J. D., and Rasmussen, K. R., 1994, "The Effect of Surface Slope on Saltation Threshold," *Sedimentology*, **41**(4), pp. 721–728.
- [28] White, B. R., and Tsoar, H., 1998, "Slope Effect on Saltation over a Climbing Sand Dune," *Geomorphology*, **22**(2), pp. 159–180.
- [29] Marticorena, B., and Bergametti, G., 1995, "Modeling the Atmospheric Dust Cycle: 1. Design of a Soil-Derived Dust Emission Scheme," *J. Geophys. Res.*, **100**(D8), p. 16415.
- [30] Greeley, R., and Iversen, J. D., 1985, *Wind as a Geological Agent on Earth, Mars, Venus and Titan.*, Cambridge University Press, Cambridge - London - New York - New Rochelle - Melbourne - Sydney.
- [31] Howard, A. D., 1977, "Effect of Slope on the Threshold of Motion and Its Application to Orientation of Wind Ripples," *Geol. Soc. Am. Bull.*, **88**(6), p. 853.
- [32] Zhang, Z., Wieland, R., Reiche, M., Funk, R., Hoffmann, C., Li, Y., and Sommer, M., 2011, "Wind Modelling for Wind Erosion Research by Open Source Computational Fluid Dynamics," *Ecol. Inform.*, **6**(5), pp. 316–324.
- [33] Bagnold, R. a., 1936, "The Movement of Desert Sand," *Proc. R. Soc. A Math. Phys. Eng. Sci.*, **157**(892), pp. 594–620.
- [34] Kawamura, R., 1972, "Study on Soil Movement by Wind," *NASA-TT-F-14215. Translation of "Hisa_no Kenkyu". Tokyo Daigaku Rikogaku Kenkyusho Hokoku (Reports of Physical Sciences Research Institute of Tokyo University), Vol. 5, No. 3-4, Oct. 1951, 95-112.*, Tokyo, p. 48.
- [35] Owen, P. R., 1964, "Saltation of Uniform Grains in Air," *J. Fluid Mech.*, **20**, pp. 225–242.
- [36] Sherman, D. J., and Li, B., 2012, "Predicting Aeolian Sand Transport Rates: A Reevaluation of Models," *Aeolian Res.*, **3**(4), pp. 371–378.
- [37] Chen, W., and Fryrear, D. W., 2001, "Aerodynamic and Geometric Diameters of Airborne Particles," *J. Sediment. Res.*, **71**(2), pp. 365–371.
- [38] Lu, H., and Shao, Y., 1999, "A New Model for Dust Emission by Saltation Bombardment," *J. Geophys. Res.*, **104**(D14), p. 16,827-16,841.
- [39] Kok, J. F., Parteli, E. J. R., Michaels, T. I., and Karam, D. B., 2012, "The Physics of Wind-Blown Sand and Dust," *Reports Prog. Phys.*, **75**(10), p. 106901.
- [40] Wentworth, C. K., 1922, "A Scale of Grade and Class Terms for Clastic Sediments," *J.*

Geol., **30**(5), pp. 377–392.

- [41] Gillette, D. A., 1979, “Environmental Factors Affecting Dust Emission by Wind Erosion,” *Sahar. dust mobilization, Transp. Depos.*, pp. 71–91.
- [42] Grini, A., Zender, C. S., and Colarco, P. R., 2002, “Saltation Sandblasting Behavior during Mineral Dust Aerosol Production,” *Geophys. Res. Lett.*, **29**(18), pp. 15-1-15–4.
- [43] Alfaro, S. C., and Gomes, L., 2001, “Modeling Mineral Aerosol Production by Wind Erosion: Emission Intensities and Aerosol Size Distributions in Source Areas,” *J. Geophys. Res.*, **106**(D16), pp. 18075–18084.
- [44] Shao, Y., Raupach, M. R., and Findlater, P. A., 1993, “Effect of Saltation Bombardment on the Entrainment of Dust by Wind,” *J. Geophys. Res.*, **98**(D7), p. 12719.
- [45] Shao, Y., Raupach, M., and Leys, J., 1996, “A Model for Predicting Aeolian Sand Drift and Dust Entrainment on Scales from Paddock to Region,” *Aust. J. Soil Res.*, **34**(3), p. 309.
- [46] Gomes, L., Arrúe, J. L., López, M. V., Sterk, G., Richard, D., Gracia, R., Sabre, M., Gaudichet, A., and Frangi, J. P., 2003, “Wind Erosion in a Semiarid Agricultural Area of Spain: The WELSONS Project,” *Catena*, **52**(3–4), pp. 235–256.
- [47] Sauermann, G., Kroy, K., and Herrmann, H. J., 2001, “Continuum Saltation Model for Sand Dunes,” *Phys. Rev. E*, **64**(3), p. 31305.
- [48] Almeida, M. P., Parteli, E. J. R., Andrade, J. S., and Herrmann, H. J., 2008, “Giant Saltation on Mars,” *Proc. Natl. Acad. Sci.*, **105**(17), pp. 6222–6226.
- [49] Exner, F. M., 1925, “Über Die Wechselwirkung Zwischen Wasser Und Geschiebe in Flüssen (in German),” *Sitz Acad Wiss Wien Math. Naturwiss*, **Abt. 2**³(134), pp. 165–203.
- [50] Shao, Y., 2001, “A Model for Mineral Dust Emission,” *J. Geophys. Res. Atmos.*, **106**(D17), pp. 20239–20254.
- [51] Rice, M. a., Mullins, C. E., and McEwan, I. K., 1997, “An Analysis of Soil Crust Strength in Relation to Potential Abrasion by Saltating Particles,” *Earth Surf. Process. Landforms*, **22**(9), pp. 869–883.
- [52] Popinet, S., 2003, “Gerris: A Tree-Based Adaptive Solver for the Incompressible Euler Equations in Complex Geometries,” *J. Comput. Phys.*, **190**(2), pp. 572–600.
- [53] “The Open Source CFD Toolbox - OpenFOAM” [Online]. Available: <https://www.openfoam.com/>.
- [54] Zhang, Z., Wieland, R., Reiche, M., Funk, R., Hoffmann, C., Sommer, M., and Li, Y., 2010, “A CFD Wind Model for Simulation of Wind Erosion in Inner Mongolia,” *Modellierung Und Simulation von Oekosystemen: Workshop Koelpinsee 2009*, A. (Ed. . Gnauck, ed., Aachen (Shaker), pp. 27–48.
- [55] Tapia, X. P., 2009, “Modelling of Wind Flow over Complex Terrain Using OpenFoam,” M.S. thesis, Department of Techonology and Built Environment, University of Gälve.
- [56] Martinez, B., 2011, “Wind Resource in Complex Terrain with OpenFOAM,” M.S. thesis, Risø DTU, National Laboratory for Sustainable Energy, Technical University of Denmark.
- [57] Sumner, J., Masson, C., Odemark, Y., and Cehlin, M., 2010, “OpenFOAM Simulations of Atmospheric Flow over Complex Terrain,” *5th OpenFOAM Work.*, pp. 1–45.

- [58] Gartmann, A., Fister, W., Schwanghart, W., and Müller, M. D., 2011, "CFD Modelling and Validation of Measured Wind Field Data in a Portable Wind Tunnel," *Aeolian Res.*, **3**(3), pp. 315–325.
- [59] Ferreira, A. D., Farimani, A., and Sousa, A. C. M., 2011, "Numerical and Experimental Analysis of Wind Erosion on a Sinusoidal Pile," *Environ. Fluid Mech.*, **11**(2), pp. 167–181.
- [60] Ferreira, A. D., Pinheiro, S. R., and Francisco, S. C., 2013, "Experimental and Numerical Study on the Shear Velocity Distribution along One or Two Dunes in Tandem," *Environ. Fluid Mech.*, **13**(6), pp. 557–570.
- [61] Beyers, M., and Waechter, B., 2008, "Modeling Transient Snowdrift Development around Complex Three-Dimensional Structures," *J. Wind Eng. Ind. Aerodyn.*, **96**(10–11), pp. 1603–1615.
- [62] Diego, I., Pelegry, A., Torno, S., Toraño, J., and Menendez, M., 2009, "Simultaneous CFD Evaluation of Wind Flow and Dust Emission in Open Storage Piles," *Appl. Math. Model.*, **33**(7), pp. 3197–3207.
- [63] USEPA, 2006, "13.2.5 Miscellaneous Sources; Industrial Wind Erosion," *Compil. Air Pollut. Emiss. Factors, Vol. I Station. Point Area Sources, AP-42*, pp. 1–15 [Online]. Available: <http://www.epa.gov/ttn/chief/ap42/ch13/final/c13/final/c13s0205.pdf>. [Accessed: 20-Apr-2005].
- [64] Badr, T., and Harion, J. L., 2005, "Numerical Modelling of Flow over Stockpiles: Implications on Dust Emissions," *Atmos. Environ.*, **39**(30), pp. 5576–5584.
- [65] Turpin, C., and Harion, J.-L., 2009, "Numerical Modeling of Flow Structures over Various Flat-Topped Stockpiles Height: Implications on Dust Emissions," *Atmos. Environ.*, **43**(35), pp. 5579–5587.
- [66] Toraño, J., Torno, S., Diego, I., Menendez, M., and Gent, M., 2009, "Dust Emission Calculations in Open Storage Piles Protected by Means of Barriers, CFD and Experimental Tests," *Environ. Fluid Mech.*, **9**(5), pp. 493–507.
- [67] Turpin, C., and Harion, J. L., 2010, "Effect of the Topography of an Industrial Site on Dust Emissions from Open Storage Yards," *Environ. Fluid Mech.*, **10**(6), pp. 677–690.
- [68] Furieri, B., Russeil, S., Santos, J. M., and Harion, J. L., 2013, "Effects of Non-Erodible Particles on Aeolian Erosion: Wind-Tunnel Simulations of a Sand Oblong Storage Pile," *Atmos. Environ.*, **79**, pp. 672–680.
- [69] Iversen, J. D., and White, B. R., 1982, "Saltation Threshold on Earth, Mars and Venus," *Sedimentology*, **29**(1), pp. 111–119.
- [70] Parsons, D. R., Walker, I. J., and Wiggs, G. F. S., 2004, "Numerical Modelling of Flow Structures over Idealized Transverse Aeolian Dunes of Varying Geometry," *Geomorphology*, **59**(1–4), pp. 149–164.
- [71] Stunder, B. J. B., and Arya, S. P. S., 1988, "Windbreak Effectiveness for Storage Pile Fugitive Dust Control: A Wind Tunnel Study," *JAPCA*, **38**(2), pp. 135–143.
- [72] Derakhshani, S. M., Schott, D. L., and Lodewijks, G., 2013, "Dust Emission Modelling around a Stockpile by Using Computational Fluid Dynamics and Discrete Element Method," *Powders & Grains*, pp. 1055–1058.

- [73] Ji, S. B., Gerber, A. G., and Sousa, A. C. M., 2004, "A Convection-Diffusion CFD Model for Aeolian Particle Transport," *Int. J. Numer. Methods Fluids*, **45**(8), pp. 797–817.
- [74] Liu, X., and Garcíá, M. H., 2006, "Numerical Simulation of Local Scour with Free Surface and Automatic Mesh Deformation," *World Environmental and Water Resource Congress 2006*, American Society of Civil Engineers, Reston, VA, pp. 1–10.
- [75] Higuera, P., Lara, J. L., and Losada, I. J., 2013, "Realistic Wave Generation and Active Wave Absorption for Navier-Stokes Models. Application to OpenFOAM®," *Coast. Eng.*, **71**, pp. 102–118.
- [76] Higuera, P., Lara, J. L., and Losada, I. J., 2013, "Simulating Coastal Engineering Processes with OpenFOAM®," *Coast. Eng.*, **71**, pp. 119–134.
- [77] Melling, G., Dix, L. K., Turnock, S. R., and WhiteHouse, R., 2011, "CFD-Based Methods for Numerical Modelling of Scour," *Numerical Towing Tank Symposium*, Geology & Geophysics, Civil Maritime & Env. Eng & Sci Unit, United Kingdom, p. 6.
- [78] Stahlmann, A., and Schlurmann, T., 2012, "Numerical and Experimental Modeling of Scour at Tripod Foundations for Offshore Wind Turbines," *ICSE6*, Paris, pp. 1019–1026.
- [79] Pasiok, R., and Stilger-Szydło, E., 2010, "Sediment Particles and Turbulent Flow Simulation around Bridge Piers," *Arch. Civ. Mech. Eng.*, **10**(2), pp. 67–79.
- [80] Shaw, R., Lewkowicz, A. Z., and Gostelow, J. P., 1966, *Measurement of Turbulence in the Liverpool University Turbomachinery Wind Tunnels and Compressor*, H.M. Stationery Office.
- [81] White, B. R., 1996, "Laboratory Simulation of Aeolian Sand Transport and Physical Modeling of Flow around Dunes," *Ann. Arid Zone*, **35**(3), pp. 187–213.
- [82] "Dimetix" [Online]. Available: <http://www.dimetix.com/>.
- [83] Gonçalves, E. L., 2008, "Development of an Experimental Facility for Continuous Measurement of the Free Surface Profile of a Granular Bed," M.S. thesis, Department of Mechanical Engineering, University of Coimbra.
- [84] Anderson, J. D., 1995, *Computational Fluid Dynamics - The Basics with Applications*, McGraw-Hill, Inc., New York, NY.
- [85] Patankar, S. V., 1980, *Numerical Heat Transfer and Fluid Flow*, McGraw-Hill Company.
- [86] Launder, B. E., and Spalding, D. B., 1974, "The Numerical Computation of Turbulent Flows," *Comput. Methods Appl. Mech. Eng.*, **3**(2), pp. 269–289.
- [87] Yakhot, V., Orszag, S. A., Thangam, S., Gatski, T. B., and Speziale, C. G., 1992, "Development of Turbulence Models for Shear Flows by a Double Expansion Technique," *Phys. Fluids A-Fluid Dyn.*, **4**(7), pp. 1510–1520.
- [88] Wilcox, D. C., 1988, "Reassessment of the Scale-Determining Equation for Advanced Turbulence Models," *AIAA J.*, **26**(11), pp. 1299–1310.
- [89] Menter, F., 1993, "Zonal Two Equation K-W Turbulence Models For Aerodynamic Flows," *23rd Fluid Dynamics, Plasmadynamics, and Lasers Conference*, American Institute of Aeronautics and Astronautics, Reston, Virginia.
- [90] Murakami, S., 1993, "Comparison of Various Turbulence Models," *J. Wind Eng. Ind.*

- Aerodyn., **47**, pp. 21–36.
- [91] Wilcox, D. C., 1993, “Comparison of Two-Equation Turbulence Models for Boundary Layers with Pressure Gradient,” *AIAA J.*, **31**(8), pp. 1414–1421.
- [92] Menter, F. R., Kuntz, M., and Langtry, R., 2003, “Ten Years of Industrial Experience with the SST Turbulence Model,” *Turbul. Heat Mass Transf.*, **4**, pp. 625–632.
- [93] Menter, F. R., and Esch, T., 2001, “Elements of Industrial Heat Transfer Predictions,” *16th Brazilian Congress of Mechanical Engineering (COBEM)*, pp. 117–127.
- [94] Schlichting, H., and Gersten, K., 2017, *Boundary-Layer Theory*, Springer-Verlag, Berlin, Heidelberg.
- [95] Grotjans, H., and Menter, F. R., 1998, “Wall Functions for Industrial Applications,” *Proceedings of the Fourth European Computational Fluid Dynamics Conference*, K.D. Papailiou, ed., John Wiley Sons, Athens, Greece, pp. 1112–1117.
- [96] AIAA G-077-1998, 2002, “Guide for the Verification and Validation of Computational Fluid Dynamics.”
- [97] Roache, P. J., 1998, *Verification and Validation in Computational Science and Engineering*, Hermosa Publishers, Albuquerque, New Mexico.
- [98] Benek, J. A., Kraft, E. M., and Lauer, R. F., 1998, “Validation Issues for Engine-Airframe Integration,” *AIAA J.*, **36**(5), pp. 759–764.
- [99] Takeda, K., and Kato, M., 1992, “Wind Tunnel Blockage Effects on Drag Coefficient and Wind-Induced Vibration,” *J. Wind Eng. Ind. Aerodyn.*, **42**(1–3), pp. 897–908.
- [100] Chen, T. Y., and Liou, L. R., 2011, “Blockage Corrections in Wind Tunnel Tests of Small Horizontal-Axis Wind Turbines,” *Exp. Therm. Fluid Sci.*, **35**(3), pp. 565–569.
- [101] JCGM, 2012, *International Vocabulary of Metrology – Basic and General Concepts and Associated Terms (VIM - 3rd Ed.)*.
- [102] Sauermann, G., Andrade, J. S., Maia, L. P., Costa, U. M. S., Araújo, A. D., and Herrmann, H. J., 2003, “Wind Velocity and Sand Transport on a Barchan Dune,” *Geomorphology*, **54**(3–4), pp. 245–255.
- [103] Qian, G., Dong, Z., Luo, W., and Wang, H., 2009, “Variations of Horizontal and Vertical Velocities over Two-Dimensional Transverse Dunes: A Wind Tunnel Simulation of the Effect of Windward Slope,” *J. Arid Environ.*, **73**(12), pp. 1109–1116.
- [104] Lee, S., and Park, C., 1998, “Surface-Pressure Variations on a Triangular Prism by Porous Fences in a Simulated Atmospheric Boundary Layer,” *J. Wind Eng. Ind. Aerodyn.*, **73**(1), pp. 45–58.

PART B

CALIBRATION OF IRWIN PROBES

CHAPTER B1

INTRODUCTION

Turbulent flows in non-circular ducts are commonly encountered in many engineering practice applications, among others, heat exchangers, air conditioning systems and rotary machinery. However, the need for refined flow control to improve equipment effectiveness, while maintaining or enhancing operation settings, has led to a renewed interest by the scientific community and a consequent research effort aiming at the understanding and characterization of these flows. Although there is a sizeable body of literature for this type of flow, where the most common configurations are triangular, square and rectangular cross-sections [1–4], it is apparent that many questions remain to be answered particularly the dependence of the flow structure and its interaction on pressure distribution and pressure loss.

The experimental data sets for the hydraulic resistance in non-circular conduits led to several friction coefficient correlations, which, as reviewed by He and Gotts [5], fall into three categories: the multiplier approach, the laminar length scale approach, and the characteristic length scale (l^*) approach. The characteristic length scale, which uses circular tube friction correlations for the study of flow through non-circular ducts, will be the methodology analyzed in the present work.

Due to the highly complex nature of turbulent flow in non-circular ducts, it should not be

expected that a single formulation for the characteristic length would be suitable for the representation of the experimental data associated with the full range of non-circular ducts [5,6]. Examples of different characteristic lengths are given by Bandopadhyay and Ambrose [6] for isosceles triangles, Ahmed and Brundrett [7] for equilateral triangles (and other regular polygons) and Jones [8] for rectangular ducts; further examples can be found in Duan et al. [9], who studied the pressure drop for turbulent flow in non-circular ducts used in engineering practice.

It should be noted that the friction correlations used for non-circular ducts are derived for circular pipes; consequently, they do not take into account the effect of secondary flows, which were first noticed by Nikuradse [10] for square and rectangular ducts. Ever since, the understanding of these secondary flows has attracted considerable interest and to this purpose both experimental and numerical approaches have been employed [3,4,11–14]. Gessner and Jones [15] described the secondary flows as a transverse mean current that interacts in a complex way with the axial mean stream along the duct yielding an increase of turbulence intensity. Similar conclusions were obtained by Rivas et al. [12], and Yao et al. [4], among others. Despite the velocities of the secondary flows being only a small fraction of the mean axial flow (1 to 3%), they have a noticeable effect on the isotachs patterns and transport of momentum, as reported by Schlichting [16], among others [2,4,12,15,17,18]. Even for wide rectangular ducts, where the secondary flow is commonly neglected, its effect should be taken into consideration, especially in the corner regions [19]. A comprehensive recent review for this particular topic was conducted by Rochlitz et al. [18].

For viscous internal flows, regardless the shape of the duct cross-section, the fluid velocity is assumed to go to zero at the walls; the layer near to the wall resists the motion of the adjacent layers and it slows them down gradually causing progressive thickening of the boundary layers. Thus, the velocity profile requires a certain length until it becomes fully developed, commonly called the entrance region (also known as entrance length, l_e).

A common simplification for the fully developed flow region is the assumption of uniform pressure over the cross-section. Being so, the relation between pressure gradient and wall shear stress (τ_w) is obtained through a force balance [e.g. 6].

Irwin probes are wall shear stress pressure probes developed by Irwin [20], and are used in many applications, e.g., in wind tunnel testing to estimate the wind velocity close to the ground level [20–22]. In previous work [23,24], these probes were used to measure the wall shear stress in two-dimensional models mimicking triangular piles. These experimental studies left unanswered a few questions about the suitability of the *Irwin* probes to determine the wall shear stress; the present work aims to further investigate this specific topic.

The *Irwin* sensors are simple in design, do not require alignment, as they are omnidirectional, and admit several closely spaced locations measurement. Additionally, they are very attractive due to their low cost, and easiness of construction and operation.

The numerical simulations performed in this work used the open source OpenFOAM [25] CFD toolbox (CFD: Computational Fluid Dynamics). Several reasons led to the choice of this code, such as no limitations for parallel computing and being open for adaptation and development, bringing great flexibility and suitability for the users, which is not the case of commercial CFD codes.

B1.1. GOAL

As mentioned in Part A, the aim of the present project is to study and simulate several configurations of sand piles. Besides the correlation with the measured erosion profiles (i.e., verify if erosion only occurs where the threshold condition, numerically predicted, is exceeded), the validation of the computationally predicted wall shear stress (τ_w) is performed using the *Irwin* probes measurements.

Given the importance of the model validation process, it became necessary to carry out a more in-depth study on the behavior of the *Irwin* probes. Thus, the main objective for Part B of the present work is:

- Assessment of the applicability of *Irwin* probes to measure the wall shear stress of fully developed, incompressible fluid flow under constant and variable pressure gradient conditions.

The path to reach the outlined goal comprises the following steps:

- Evaluation of the most suitable characteristic length scale (l^*) (hydraulic diameter (D_h), the square root of the cross-section area (\sqrt{A}) or the laminar equivalent diameter (D_L)), to calculate the friction coefficient using the analytical expression of Zigrang and Sylvester [26];
- Calibration of the *Irwin*-type probes for three representative cases, separately, by correlating the measured pressure difference in the probe (Δp_I) against the local wall shear stress (τ_w) values obtained using a *Preston* tube.

B1.2. INTRODUCTORY CONCEPTS

In engineering applications, it is quite common to consider fully developed flow characteristics

in non-circular ducts to be similar to those with circular cross-section [1,2,6,7,9]. Similarly, in this work the velocity distribution for turbulent flow along with the resistance law applied to circular pipes is used; hence, it is assumed that, regardless the shape, the cross-section is described by its hydraulic (or equivalent) diameter (D_h), given by:

$$D_h = 4 \frac{A}{P} \quad \text{(B1-1)}$$

where A [m²] is the cross-section area and P [m] is the wet perimeter. It should be noted that the equivalent diameter of a particular non-circular cross-section is not equal to the diameter of a circle with the same area [9]. However, the literature reports experimental data that do not correlate well when using the hydraulic diameter, indicating errors up to 30% [7,9,27]. This error is unacceptable for most engineering applications; therefore, new methodologies are sought to reduce the error of the friction coefficient in non-circular ducts [5,6,8,9,27,28].

According to Jones [8], the hydraulic diameter is not the appropriate dimension to use in the Reynolds number formulation, since it leads to a monotonic increase in the friction coefficient with the aspect ratio; therefore, the similarity between circular and rectangular ducts is seriously compromised. Moreover, in order to reduce the errors in the estimation of the friction coefficient, Jones [8] proposed a geometric function ($\phi^*(w/H)$) to relate ducts of rectangular cross-section to those of circular cross-section, as follows:

$$\phi^*(w/H) = \frac{2}{3} + \frac{11H}{24w} \left(2 - \frac{H}{w} \right) \quad \text{(B1-2)}$$

where H [m] is the height and w [m] is the width of the duct. Also, that author uses a Re number range between 10 and 103000, and proves empirically that this geometric function can be used in both laminar and turbulent flows.

In addition, Jones [8] defined a “laminar equivalent” diameter (D_L) given by Equation (B1-3), and it shows that this empirical parameter also leads to a good similarity between rectangular and circular ducts in turbulent flow.

$$D_L = \phi^* \left(\frac{w}{H} \right) D_h \quad \text{(B1-3)}$$

Duan et al. [9] also reported that the hydraulic diameter is not the suitable length scale to use in the definition of the Reynolds number to guarantee similitude between circular and non-circular ducts, and proposed a novel characteristic length scale, equal to the square root of the cross-sectional area (\sqrt{A}). This formulation guarantees that both the effect of the duct shape and the errors in estimating the pressure drop will be minimized. Furthermore, Duan et al. [9] found the procedure to be “applicable to most duct geometries”.

As already mentioned, the complexity of internal turbulent flow has hindered the development of physically-based relations to predict fluid resistance in circular pipes, which is the reason why

semi-empirical relations are often used. In this work it will be used the semi-empirical relation proposed by Zigrang and Sylvester [26] to predict the friction coefficient; this relation has the advantage over Colebrook's equation [29] of using an explicit approximation given by:

$$\frac{1}{\sqrt{c_f}} = -2.0 \log \left\{ \frac{\varepsilon/l^*}{3.7} - \frac{5.02}{Re_{l^*}} \log \left[\frac{\varepsilon/l^*}{3.7} - \frac{5.02}{Re_{l^*}} \log \left(\frac{\varepsilon/l^*}{3.7} + \frac{13}{Re_{l^*}} \right) \right] \right\} \quad (\text{B1-4})$$

where ε is the absolute roughness [m] and Re , the Reynolds number, defined here as follows:

$$Re = \frac{Ul^*}{\nu} \quad (\text{B1-5})$$

where U is the axial mean velocity [m s^{-1}], ν the kinematic viscosity of the fluid [$\text{m}^2 \text{s}^{-1}$] and l^* is the characteristic length scale [m], which is the diameter for circular ducts. Considering that this study aims to analyze turbulent flow in rectangular ducts, the friction coefficient is calculated using Equation (B1-4) with three different characteristic length scales (D_h , \sqrt{A} and D_L , respectively) for l^* . However, it is important to stress that Equation (B1-4) was derived for circular pipes; consequently, it does not take into account the effect of secondary flows.

B1.3. ENTRANCE REGION

The entrance length can be affected by different factors, such as fluid type and duct wall roughness [30]. However, it can be commonly approximated using correlations, such as the one suggested by White [31] for turbulent pipe flow, in which the only parameter that affects the entrance length is the Reynolds number, namely:

$$\frac{l_e}{D} \approx 4.4 Re^{\frac{1}{6}} \quad (\text{B1-6})$$

being D [m] the duct diameter; other authors express this parameter in terms of friction coefficient, e.g., Zagarola and Smits [32] or in terms of the number of diameters, e.g., Nikuradse [33] and Duan et al. [9], as:

$$l_e \approx 40D \quad (\text{B1-7})$$

Anselmet et al. [34] indicate for the entrance length a range between 30 and 40 diameters. Also, Hartnett et al. [1] reported that, for Reynolds number above 4000, the inlet region was less than 20 diameters.

It is well established that for fully developed flow the pressure gradient along the streamwise

direction is constant [31]. In the cases of variable longitudinal section, the pressure gradient can be favorable or adverse, depending on whether the duct is convergent or divergent, respectively.

In fully developed flow conditions, the pressure drop between two sections can be used to evaluate the friction coefficient [1]; therefore, the Darcy's friction factor (c_f) is computed as:

$$c_f = \frac{D_h \frac{\partial p}{\partial x}}{\frac{1}{2} \rho U^2} \quad (\text{B1-8})$$

where $\partial p / \partial x$ is the pressure gradient in the axial direction and D_h is the hydraulic diameter, as given by Equation (B1-1).

B1.4. WALL SHEAR STRESS

Assuming fully developed flow in ducts of constant cross section, the wall shear stress, τ_w , in a cross-section can be related to the pressure gradient, by assuming that τ_w has a uniform distribution, through a force balance given by:

$$\sum \vec{F} = 0 \gg \tau_w = -\frac{A}{P} \frac{dp}{dx} = -\frac{1}{4} D_h \frac{dp}{dx} \quad (\text{B1-9})$$

In the present study, the mean pressure drop measured in several cross-sections will be used to estimate τ_w using Equation (B1-9). The wall shear stress is related to the friction coefficient by:

$$\tau_w = \frac{1}{8} c_f \rho U^2 \quad (\text{B1-10})$$

In variable pressure gradients (favorable or adverse) situations, the wall shear stress varies along the duct, and in the present work is evaluated locally through measurements with *Preston* [35] tubes.

Ahmed and Brundrett [7] measured the wall shear velocity (u_*) at several locations along the duct and different Reynolds numbers, and observed that early in the development region, u_* becomes constant. By definition, the friction velocity is directly related to the wall shear stress, through Equation (A1-2).

CHAPTER B2

EXPERIMENTAL PROGRAM

The tests were carried out in a rectangular duct designed and built within the context of the present work. In this chapter, the experimental program is described, with particular emphasis on the characteristics of the cases studied. As already mentioned, it is intended to study the behavior of the *Irwin* probes in ducts with constant and variable section. The experimental apparatus used in these cases is the same, although with appropriate modifications, and it is presented in Section B2.1. The specific experimental parameters of each case are reported in Sections B4.1 and B5.1. For the constant section case, verifications were made to assure that the entrance length is sufficiently long to achieve fully developed flow in the test section, as it will be discussed in Section B2.2. The main features of the *Preston* tube and *Irwin* probe are described in Sections B2.3 and B2.4, respectively.

B2.1. APPARATUS

Figure B2-1 schematically depicts the experimental apparatus employed in the present work. A centrifugal fan was used to drive the airflow into the 5 meters long plywood rectangular duct, which has a constant width (w) of 0.12 m and wall thickness of 5 mm. The inner walls were sanded and measured with a contact profilometer, yielding an absolute roughness (ϵ) of the duct of approximately 0.005 mm. The duct has an initial flow development section followed by the actual test section; both sections have the same length (2.5 m). A hinge and a movable top wall permitted to study both constant (several aspect ratios - **AR**) and variable (convergent and divergent) section cases.

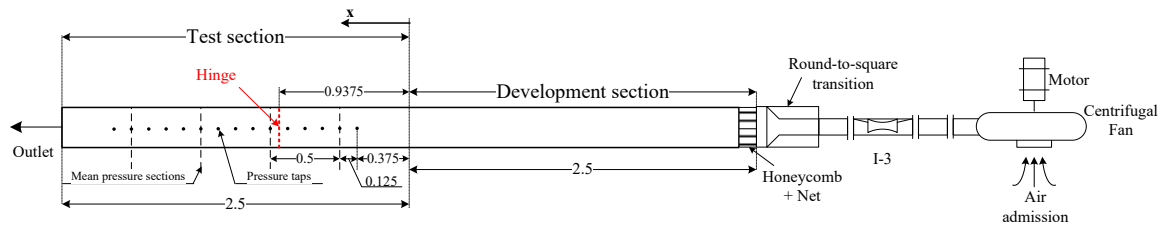


Figure B2-1: Schematic of experimental apparatus – top view (dimensions in meters).

Photographs with construction details of the apparatus are presented in Figure B2-2.



Figure B2-2: Experimental apparatus.

A round-to-square transition and a *Venturi* flowmeter were placed between the blower and the duct entrance. In the beginning of the development section, a honeycomb and a tight net were installed to reduce the effects of the fan by stabilizing the flow and to enhance the early onset

of fully developed flow in the test section. Fifteen pressure taps placed along the duct were initially considered in order to obtain four pressure-averaging locations (dashed lines in Figure B2-1). Four pressure taps, one on each sidewall, were used to determine the mean pressure in each cross-section; the values of the mean pressure for the different cross-sections are used in the calculation of the pressure gradient along the duct.

Both static pressure taps and *Irwin* sensors taps were connected to a 48 channel scanning valve, and the pressure was measured with a Multur pressure transducer with a range of ± 1000 Pa and accuracy of ± 0.5 Pa; the reference pressure is taken as equal to the atmospheric pressure. All tests were conducted at similar ambient conditions in what concerns temperature and humidity. A valve, positioned on the air admission section of the blower, was used to adjust the desired flow rate. Due to the sensitivity of the measuring equipment, only tests leading to values of wall static pressure above a certain threshold were considered; therefore, the Reynolds number range covered in the experiments was limited.

The measuring procedure was controlled by a personal computer-based platform, and after an initial period of operation, when the *Venturi* readings present no variation in time, the steady state condition was assumed. Sensitivity tests of acquisition time and rate were performed. The acquisition period selected was 15 seconds at each measuring station with a sampling rate of 50 Hz, since further increment of both parameters did not alter the mean results.

Prior to measurements, some pre-test visual checks, using smoke and wool yarn, were conducted to guarantee that the apparatus was leakage-free. All fixed joints were sealed with silicone; the joints adjacent to the top wall, which is not fixed to allow the change of the aspect ratio, and the slope, were sealed with duct tape.

B2.2. ENTRANCE LENGTH

The entrance length for the duct with the different aspect ratio cross-sections was estimated using Equation (B1-6) with D replaced by the three selected characteristic length scales. Since Re and l_e are directly proportional, only the larger values of Reynolds number were used in Equation (B1-6), as presented in Table B2-1, with results obtained using only the hydraulic diameter; the two other characteristic length scales (\sqrt{A} and D_L) lead to similar values.

Table B2-1: Entrance length for all cases.

Case	Maximum Re	l_e [m] (Equation (B1-6))		l_e/D_h	
		Critical	Actual	Critical	Actual
AR1	5.8×10^4	1.32	2.5	27.4	52.08
AR2	7.3×10^4	1.86	2.5	28.4	38.19
AR3	8.4×10^4	2.33	2.5	29.1	31.25
AR4	7.9×10^4	3.40	2.5	28.8	21.19

Close observation of Table B2-1 indicates that case **AR4** would require an entrance length greater than that of the apparatus; thus, to ascertain the existence of fully developed flow in the test section, the pressure along the duct was measured, and it was found that in all cases the pressure decreases linearly towards the outlet (Figure B4-3). The fully developed flow condition is essential in order to ensure a correct measurement by the *Irwin* probes [30].

Ahmed and Brundrett [7] report that at a streamwise distance beyond five hydraulic diameters away from the inlet fully developed wall shear stress does occur; while the core fluid to achieve full development requires a length an order of magnitude higher. Considering that τ_w is the parameter to be measured, the distance to achieve fully developed wall shear stress is satisfied for all cases (Table B2-1).

The study of the required entrance length to obtain fully developed flow in the present experimental apparatus was performed for the constant section cases. For the variable section cases, the same conditions were assumed.

B2.3. PRESTON TUBE

The pressure difference between the *Preston* [35] tube reading and the local static pressure (pressure tap) (Δp) is used to quantify the local wall shear stress (τ_w). The calibration of Patel [36], simplified by Bechert [37] later on, is used in the present work to compute τ_w as follows:

$$\tau^+ = [28.44 \Delta p^{+2} + (6.61 \times 10^{-6}) \Delta p^{+3.5}]^{\frac{1}{4}} \quad \text{(B2-1)}$$

The normalized quantities in Equation (B2-1) are defined as:

$$\Delta p^+ = \Delta p d_p^2 / \rho v^2 \quad \tau^+ = \tau_w d_p^2 / \rho v^2 \quad (\text{B2-2})$$

where d_p is the outside diameter of the *Preston* tube. Figure B2-3 presents the *Preston* tube used to perform the measurements and the respective placement.

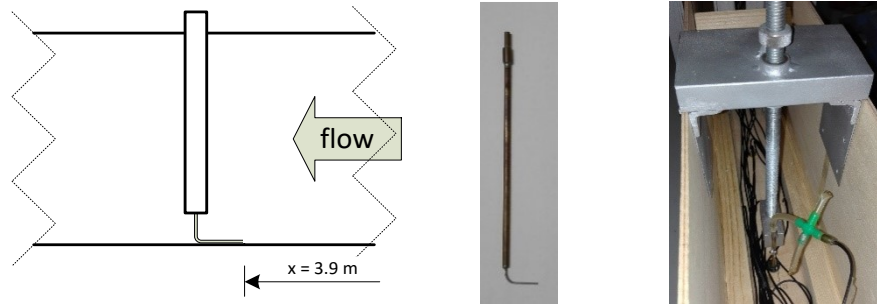


Figure B2-3: Placement of the used *Preston* tube.

B2.4. IRWIN PROBE

As already mentioned in Section A2.4.3.1, *Irwin* [20] probes are pressure sensors, and its calibration will be discussed in Sections B4.2.4.2 and B5.2.3. After calibration, the wall shear stress can be employed in Equation (B1-10) to calculate the friction coefficient (c_f). The *Irwin* probes are surface-mounted on the rectangular duct, with one of the taps flush with the surface and the other protruding it by 2 mm. In the development of such probes, *Irwin* [20] studied the influence of the degree of intrusion (i.e. the height of the protruding tube) in the calibration by testing different heights. Furthermore, Monteiro and Viegas [22] estimated the errors produced with *Irwin* probes in the measurement of wall shear stress in the presence of pressure gradients, and three different heights of the protruding tube were tested. These probes should be subjected to an adequate calibration [20–23], considering that they are usually manufactured with different dimensions.

The preliminary study of the pressure distribution along the duct aimed to give appropriate guidance on how to select the location for the *Irwin* probes. Thus, to evaluate the influence of the streamwise location of the *Irwin* probes, four equally spaced locations were selected for their positioning. The probes were placed along the centerline of both top and bottom walls; in this way, it will be possible to compare the data obtained for both walls. In addition, the influence of the transversal positioning was verified by mounting, on the top wall, three evenly-spaced (by 0.03 meters) sensors at the cross-section closest to the outlet (i.e., $x/L_{max}=0.72$ with $L_{max}=2.5$ m). The *Irwin* probes were located on positions of the test section that satisfy the

requirement of fully developed flow and midway cross-sections where the mean pressure was measured, as shown in Figure B2-4.

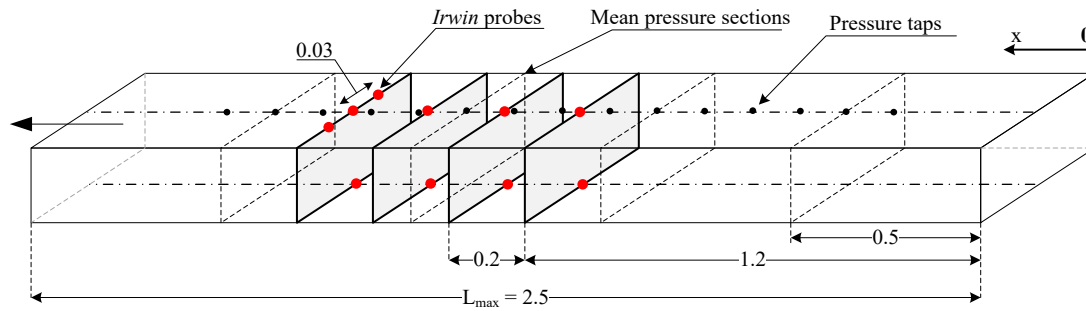


Figure B2-4: *Irwin* probes (red dots) positioning. Test section with mean pressure sections (dashed lines) and static pressure taps (black dots) (in addition, see Figure B2-1) (dimensions in meters).

CHAPTER B3

NUMERICAL SETUP

The numerical modeling was performed in this work by using primarily the open source OpenFOAM (OF) CFD toolbox, as already stated in Part A. In addition, several simulations were performed with ANSYS-CFX.

Due to the resemblance between the numerical setup of the constant and variable cross-section cases, in this chapter it will be presented only characteristics that are common to both cases. The computational domain is shown in Section B3.1; the mesh parameters and the structured meshes used in the mesh dependency study (Section B3.4) are discussed in Section B3.2. The solver, boundary conditions and remaining features of the case setup are presented in Section B3.3.

Although, as reported in Section B2.1, the experimental setup allows four different aspect ratios (**AR**) with constant cross-section [38], for the numerical simulations only the 1:2 case (**AR3**: $H = 0.06$ m) was considered.

B3.1. COMPUTATIONAL DOMAIN

Different computational domains were used (Figure B3-1), and due to the symmetry of the geometries under study, only a fraction of the physical domain is required to be simulated. Therefore, only a quarter, or a half, of the domain was modelled for the constant and variable section, respectively.

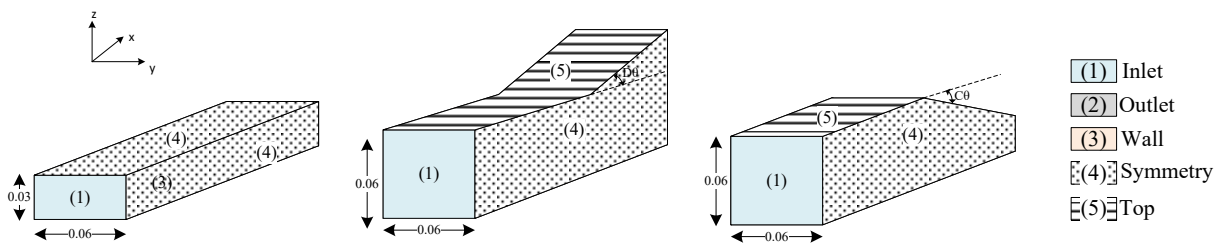


Figure B3-1: Computational domains (**left** – constant section duct; **center** – divergent duct; **right** – convergent duct).

As can be noted in Figure B3-1, the main differences between the cases under study are related to the top boundary. Beyond the geometry itself, in the constant duct the top boundary is modeled as a symmetry plane and in the variable section cases is assumed as a wall. All remain regions are similar.

B3.2. MESH PARAMETERS

The OpenFOAM *blockMesh* utility was used to generate several structured grids with increasing resolution to analyze the mesh dependency. For the cases of the rectangular duct with constant section, a dimensionless wall distance (y^+ - Equation (A3-4)) range of $0.5 < y^+ < 140$, was investigated. A simple grid expansion (*simpleGrading*) away from the walls was employed (as shown in Figure B3-2) with expansion factors varying between 1 (no expansion) and 1.15 (Table B3-1).

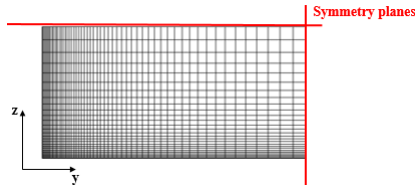


Figure B3-2: Typical mesh (M7) with *simpleGrading* for one-quarter of the cross-section (constant section case).

Table B3-1: Structured meshes characteristics.

Mesh	Cells			Expansion Factor			Elements	Iterations	Mean y^+
	x	y	z	x	y	z			
M1	201	12	6	1.008	1.000	1.000	14472	192	139.72
M2	201	20	10	1.008	1.000	1.000	40200	308	84.37
M3	201	24	12	1.008	1.018	1.038	57888	346	56.72
M4	201	33	16	1.008	1.035	1.076	106128	453	28.27
M5	201	43	21	1.008	1.044	1.094	181503	632	14.00
M6	201	70	34	1.008	1.051	1.109	478380	1460	2.41
M7	201	82	40	1.008	1.052	1.111	659280	1038	1.18
M8	347	75	37	1.004	1.071	1.151	962925	1030	0.53

After evaluating the overall performance of the several meshes studied in the case of the constant duct section (Section B3.4), no further mesh dependency test were carry out, and the chosen mesh, specifically the value of $y^+ \approx 1.2$, was used in the simulations performed in the rectangular duct with variable section cases.

B3.3. CASE SETUP

The standard solver *simpleFOAM* was employed, assuming steady state and incompressible conditions, to solve the RANS equations based on the finite-volume (FVM) discretization method. Numerical convergence was assumed satisfied when all the normalized residuals have a value lower than 1×10^{-5} . The $k-\omega$ SST (Shear Stress Transport) [39] turbulence model was used with the automatic near-wall treatment [40].

The boundary conditions at the inlet are, as follows: *zeroGradient* for pressure and *fixedValues* for the other properties; the turbulence intensity was considered 5% to match the experimental conditions. At the outlet, *zeroGradient* was assumed for all dependent variables, except pressure, which was set equal to experimental value (*fixedValue*). Walls were treated as smooth, with a no-slip condition. Symmetry conditions were imposed in the remaining boundaries, according the case under study, as shown in Figure B3-1. Similar conditions and identical mesh sizes were adopted for the ANSYS CFX simulations.

B3.4. MESH DEPENDENCY STUDY

Mesh dependency tests were performed to evaluate the behavior and sensitivity of the numerical tool to the increasing mesh resolution taking into consideration the flow type and the turbulence model used. Two test cases of OpenFOAM tutorials were chosen for this purpose, one case with laminar flow (cavity case) and the other one with the turbulence model $k-\omega$ SST (pitzDaily case). It can be noted in Figure B3-3 that in both cases, beyond a certain degree of refinement, the mean velocity results are not affected, yielding differences between the meshes lower than 1%; therefore, mesh independency was satisfied. Furthermore, the turbulence model $k-\omega$ SST is shown to be practically insensitive to the value of y^+ , since differences smaller than 4% were obtained within the entire range, $0.23 < y^+ < 65$, in line with the findings reported by Menter and Esch [40].

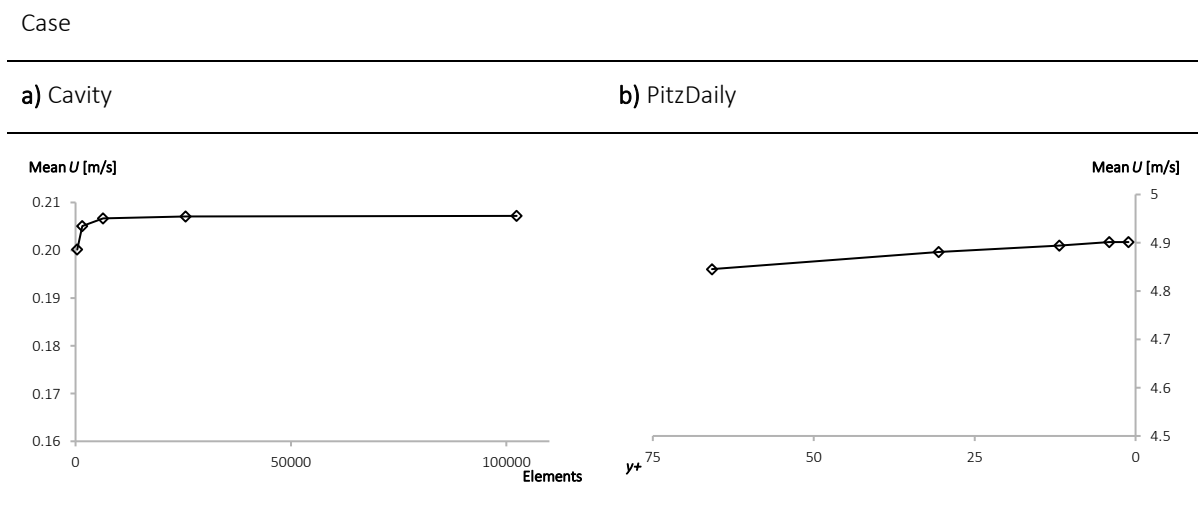


Figure B3-3 Mesh independency test - cross-section mean velocity. **a** cavity case; **b** pitzDaily case.

However, these results were only achieved for the properties way from the wall, like the cross-section mean velocity. When considering wall-bounded quantities, like the local wall shear stress, some discrepancies between the meshes were found. Similar behavior occurred in the performed tests for the present rectangular duct considering the meshes presented in Table B3-1.

As already mentioned, the $k-\omega$ SST turbulence model was used with the automatic near-wall treatment, which implies that the boundary layer is resolved in the fine grids (viscous sub-layer formulation – $y^+ < 5$) and modelled in the coarse grids (wall functions). Therefore, when performing mesh independency tests, besides the spatial discretization inaccuracy, the different wall treatment approaches also contributes to the errors; this can be observed when comparing the near wall velocity profile for the various meshes tested (Table B3-1) depicted in Figure B3-4.

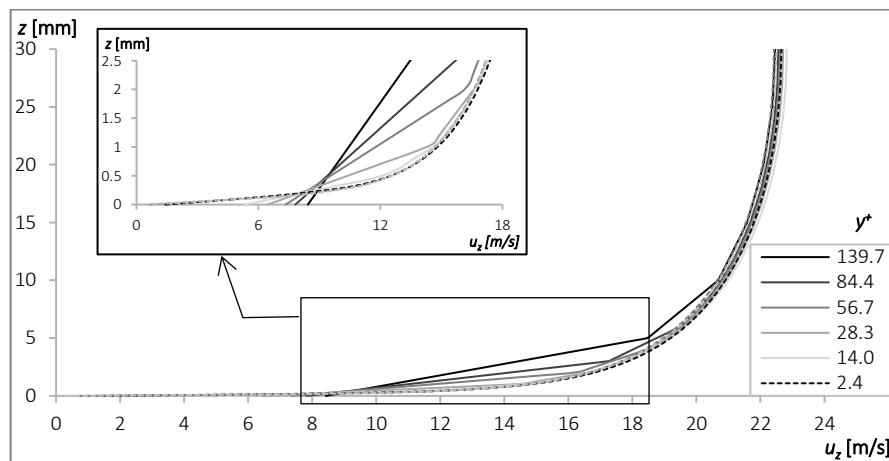


Figure B3-4 Mesh independency study - near wall vertical velocity profile.

To avoid this problem, typically the mesh independency study should be conducted within the y^+ validity range of a particular procedure. Since what is intended to evaluate are properties dependent on wall-bounded flow, namely the wall pressure distribution and the local wall shear stress, a viscous sub-layer formulation approach was used, i.e., a mesh with a $y^+ < 5$. The value of $y^+ \approx 1$, as suggested by the CFD community, is the best one to predict the wall-bounded quantities, especially when employing the $k-\omega$ SST turbulence model. Under the circumstances, the mesh 201x82x40 (M7 in Table B3-1) is used in the present work to conduct the model validation against the experimental results and, in the process, add further credibility to these computational results.

Furthermore, according to the selected near wall treatment, the applied boundary conditions must be chosen in accordance. A study on this subject was conducted, leading to the use of the boundary conditions already presented in Section B3.3.

CHAPTER B4

RECTANGULAR SECTION WITH CONSTANT SECTION

In order to meet the proposed goals presented in Section B1.1, a rectangular duct allowing different cross section configurations was used. In the present chapter, the constant section geometry is presented.

Since the main features of the test studies were already presented in Chapter B2 and Chapter B3, only the specific characteristics of the current case are presented in Section B4.1.

Both experimental tests and numerical simulations were performed, and the results are shown in Sections B4.2 and B4.3, respectively. Prior to the experimental tests, a repeatability and accuracy evaluation of the sensors employed was performed (Section B4.2.1). Regarding *Irwin* probes, an assessment of the variation along the duct and the calibration of the probes are discussed in Section B4.2.4. Along with the presentation of the numerical results, a discussion of the comparison against the experimental measurements is made. Finally, some conclusions are drawn with the aim to summarize the main findings of the present study case.

B4.1. CASE DESCRIPTION

With this case is intended to evaluate the potential of using *Irwin* [20] probes (Section B2.4) to measure the wall shear stress of fully developed, incompressible fluid flow in smooth-walled ducts of constant rectangular cross-section.

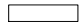
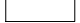


In addition, using the analytical expression of Zigrang and Sylvester [26] to calculate the friction coefficient, a comparative analysis with the experimental data will be performed to evaluate which is the most suitable characteristic length scale (l^*), whether the hydraulic diameter (D_h), the square root of the cross-section area (\sqrt{A}) or the laminar equivalent diameter (D_L).

The experimental setup consists of a rectangular duct equipped with static pressure taps and a set of *Irwin* probes, which were built specifically for the present study (Chapter B2).

A movable top wall permitted the height to be varied, and four different aspect ratios (**AR**) were considered, **AR1**=1:4.00, **AR2**=1:2.67, **AR3**=1:2.00 and **AR4**=1:1.03, as listed in Table B4-1.

The main geometric characteristics of the different configurations of the constant cross-section cases and the tested velocities, which were measured using the Venturi flow meter, are presented in Table B4-1.

Table B4-1: Main characteristics of the configurations with constant section.

Case					
Case		AR1	AR2	AR3	AR4
<i>Height [m]</i>		0.030	0.045	0.060	0.116
<i>Aspect Ratio (AR)</i>		1:4.00	1:2.67	1:2.00	1:1.03
<i>Characteristic length scale (l*)</i>	D_h [m]	0.048	0.065	0.080	0.118
	\sqrt{A} [m]	0.060	0.073	0.085	0.118
	D_L [m]	0.042	0.062	0.081	0.133
<i>U test range [m/s]</i>	<i>Min</i>	4.4	3.3	2.4	4.4
	<i>Max</i>	19.3	17.6	16.7	10.6

B4.2. EXPERIMENTAL RESULTS

The tests performed encompass primarily pressure measurements, both with static pressure taps and with *Irwin* probes distributed along the duct as shown in Figure B2-1 and Figure B2-4. In this section, the repeatability tests and the accuracy of the sensors are presented along with experimental results in the form of pressure and friction coefficients. The calibration of the *Irwin* probes is also reported. It should be noted that, in all figures, the value of $x = 0$ refers to the entrance of the test section (Figure B2-1).

B4.2.1. REPEATABILITY AND ACCURACY EVALUATION

In order to assess the repeatability of the measurements, as defined by VIM3: International Vocabulary of Metrology [41], for static pressure and *Irwin* probes pressure difference, five tests were conducted for each velocity. Due to the similarity of the obtained results for the four configurations and the volume of data to display, the outcome is only illustrated for the **AR4** case, considered here as representative of all other cases. The standard deviation of the measurements (σ) is normalized by the pressure (p) as (σ/p) , which is presented in Figure B4-1.

Measurements

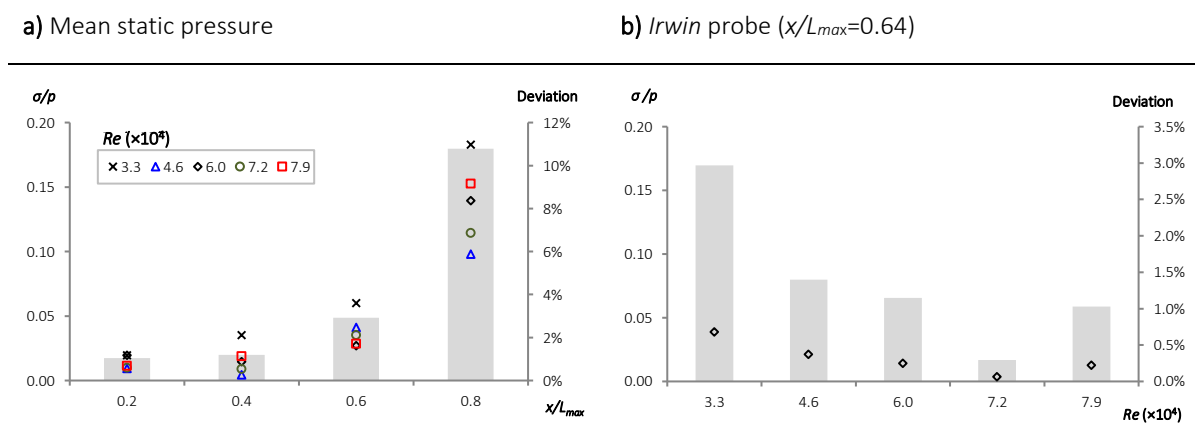


Figure B4-1: Normalized standard deviation (symbols – left vertical axle) and absolute deviation (bars – right vertical axle) of the repeatability tests: **a)** Mean static pressure and **b)** *Irwin* probe (Top face at $x/L_{max}=0.64$).

To allow an easier interpretation of the chart presented in Figure B4-1a), the normalized standard deviation is plotted against the distance normalized by the total length of the test section ($L_{max}=2.5$ m). The results presented in Figure B4-1a) are only for the cross-sections where the mean pressure was measured (Figure B2-4). Figure B4-1b) displays the results of the *Irwin* probe placed on the top face at $x/L_{max}=0.64$; similar results were observed for all the other *Irwin* probes. In both Figure B4-1a) and b), the gray bars represent the deviation (%), plotted on the right vertical axis.

By employing the repeatability data analysis methodology used by Ferreira and Fino [42], the calculated confidence interval is 95%, which is considered to be satisfactory for the purpose of the present study.

The mean deviation from the average yields for the static pressure a value approximately equal to 4% (for all Re), while for the *Irwin* probes, the mean deviation from the average pressure difference is 1.4%.

In the pressure taps the larger values of divergence (at $x/L_{max}=0.8$) can be explained by the fact that the pressure is low in the last section with values close to the pressure transducer sensitivity. Similar behavior occurred for the *Irwin* probes for the lower values of Re . Despite this particular limitation, in general, the measurements have good level of repeatability.

With regard to accuracy, the static pressure taps only depend on the accuracy of the pressure transducer (Multur), which, as mentioned before, has an accuracy of ± 0.5 Pa for a range of ± 1000 Pa. In the present study, the purpose is to determine the wall shear stress by measuring a pressure difference. To this effect, the pressure taps of each *Irwin* probe are connected to the pressure transducer; therefore, the accuracy of the *Irwin* probe and, specifically, of the measured pressure difference, depends primarily on the accuracy of the equipment Multur. The relation between the measured pressure difference in the probe and the wall shear stress is obtained by calibration, and it will be discussed in Section B4.2.4.2.

B4.2.2. PRESSURE COEFFICIENT DISTRIBUTION

Based on the static pressure measurements, the pressure coefficient was calculated by using Equation (A2-9). This procedure was employed in all four cases.

Due to the already mentioned limitation of the experimental setup, it was not possible to test the same range of Reynolds number for all aspect ratios configurations; notwithstanding, close examination of Figure B4-2 shows similar behavior for all cases within the comparable range.

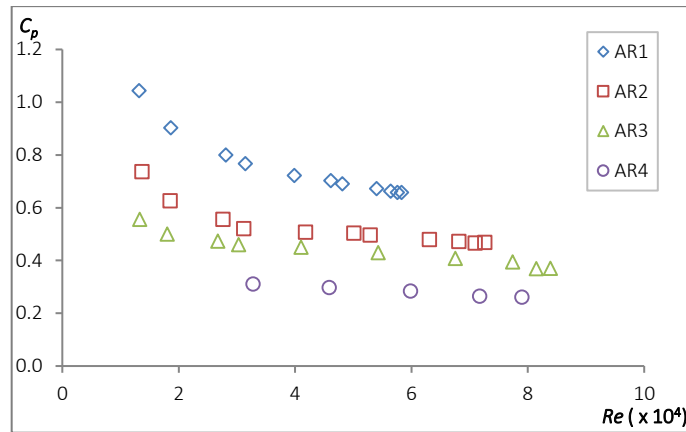


Figure B4-2: Influence of the Reynolds number on the pressure coefficient at $x/L_{max}=0.20$ (All cases).

By the observation of the trend of the curves in Figure B4-2, it can be expected Reynolds independency condition for the higher values.

The pressure coefficient distribution along the duct for cases **AR3** and **AR4** is presented in Figure B4-3.

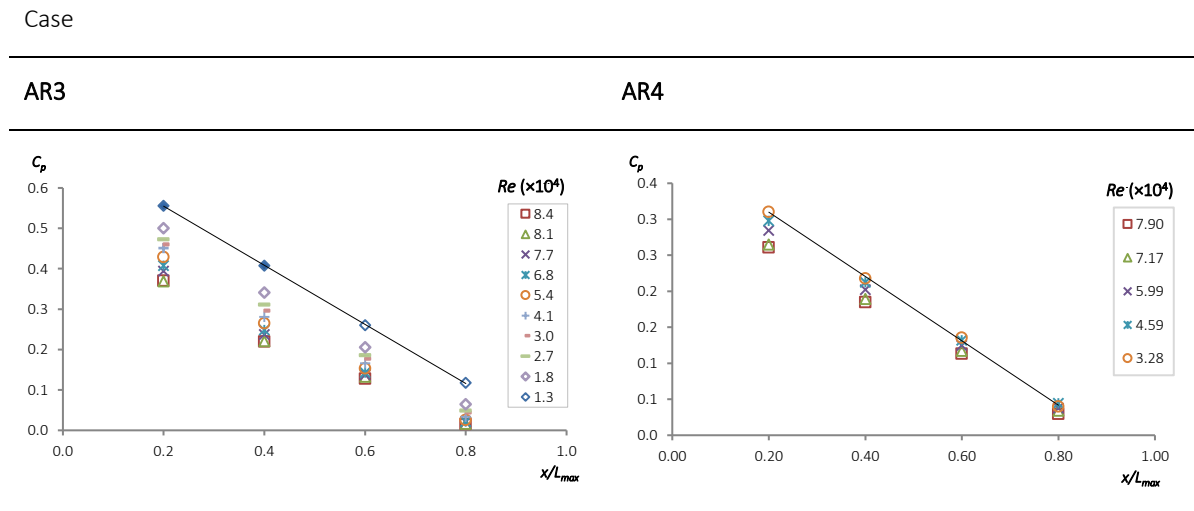


Figure B4-3: Pressure coefficient distribution along the streamwise direction of the duct for different values of Re . (Case **AR3** and Case **AR4**).

As already mentioned, in Figure B4-3 it can be seen that the pressure decreases linearly towards the duct exit independently of the Reynolds number, including case **AR4**, which requires an entrance length greater than that of the apparatus (Table B2-1). A linear trendline was added in both graphs of Figure B4-3 to facilitate this observation. Mean R-square coefficients of 99.42% (in the range of 99.00% to 99.99%) and 99.94% (in the range of 99.91% to 99.98%) were obtained for cases **AR3** and **AR4**, respectively.

In addition, the variation of the pressure coefficient with the Re number can be observed for each cross-section (x/L_{max}); their trend indicates that lower Re numbers yield higher pressure factors, which is in accordance with the findings of several authors, e.g., Rochlitz et al. [18].

B4.2.3. FRICTION COEFFICIENT DISTRIBUTION

In the fully developed region, the pressure gradient in the streamwise direction is constant, which can be confirmed by observing Figure B4-3. Thus, the difference between the mean pressures at the two most distant locations of the test section was used to calculate Darcy’s friction coefficient. The experimental results (obtained using Equation (B1-8)) are compared against the well-known empirical Blasius [43] equation (Equation (B4-1)), which is valid for steady, fully developed turbulent flow of an incompressible fluid through a closed, smooth circular pipe, in the Re range of 4×10^3 to 10^5 .

$$c_f = 4 \frac{0.0791}{Re^{\frac{1}{4}}} \tag{B4-1}$$

The experimental results are shown in Figure B4-4 against the Reynolds number considering the hydraulic diameter (D_h) as the characteristic length scale (l^*). Both axes are in logarithmic scales to facilitate the comparison.

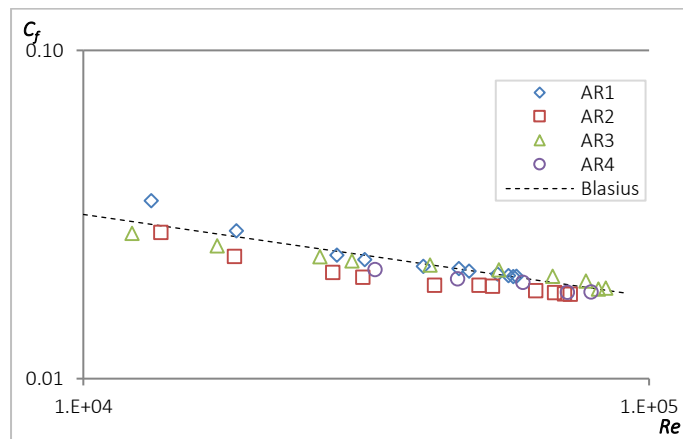


Figure B4-4: Comparison of the present experimental data against smooth circular tube predictions [43] – Equation (B4-1).

Independently of the aspect ratio and throughout the entire range of tested Re values, the experimental results agree well with the predicted results for smooth pipes (Blasius equation),

even when the hydraulic diameter is used as the characteristic length scale, contrary to statements made by several authors [7,9,27]. The very small value of the measured absolute roughness (Section B2.1) may contribute to this good agreement. In fact, according to the study performed by Zagarola and Smits [32], the inner walls of the duct used in the present work can be considered as smooth, even for the highest tested Re .

Hartnett et al. [1], Duan et al. [9], Mirmanto [44] and Sahar et al. [45] reported similar findings; however, many other authors do not favor using the hydraulic diameter when analyzing the data for rectangular ducts, as already mentioned (Section B1.2). Therefore, tests were performed to assess the influence of other characteristic length scales on the representation of the data. To this purpose, Figure B4-5 depicts a comparison of the experimental results of the friction coefficient (for all studied cases) with the predicted values obtained using Equation (B1-4), considering three different formulations for l^* , namely: the hydraulic diameter (D_h), the square root of the cross-section area (\sqrt{A}), and the laminar equivalent diameter (D_L).

Since the Reynolds number is dependent on the selected characteristic length, the velocity is normalized by its maximum mean value in the horizontal axis of Figure B4-5. To facilitate the visual comparison of the data, a margin of $\pm 5\%$ for the experimental data is presented, since that is the approximated overall mean deviation of the characteristic length scales (Table B4-2).

To quantify the differences in the data representation using the three characteristic length scales, the relative errors for the mean friction coefficient for all cases are calculated using Equation (B4-2) (analytical values calculated using Equation (B1-4)) and summarized in Table B4-2. It can be noted that in Figure B4-5 the cases **AR2** and **AR3** are those showing the lowest and the best fitting relative to the experimental data, respectively, as demonstrated by the values in Table B4-2.

$$error [\%] = \left| \frac{experimental - analytical_{l^*}}{experimental} \right| \times 100 \quad (B4-2)$$

Table B4-2: Mean relative errors for all cases (%).

Case	Equation (B1-4)		
	D_h	D_L	\sqrt{A}
AR1	2.87	3.87	7.41
AR2	9.12	10.52	6.45
AR3	3.32	3.30	3.36
AR4	4.76	2.17	4.75
Overall	5.02	4.97	5.49

Case

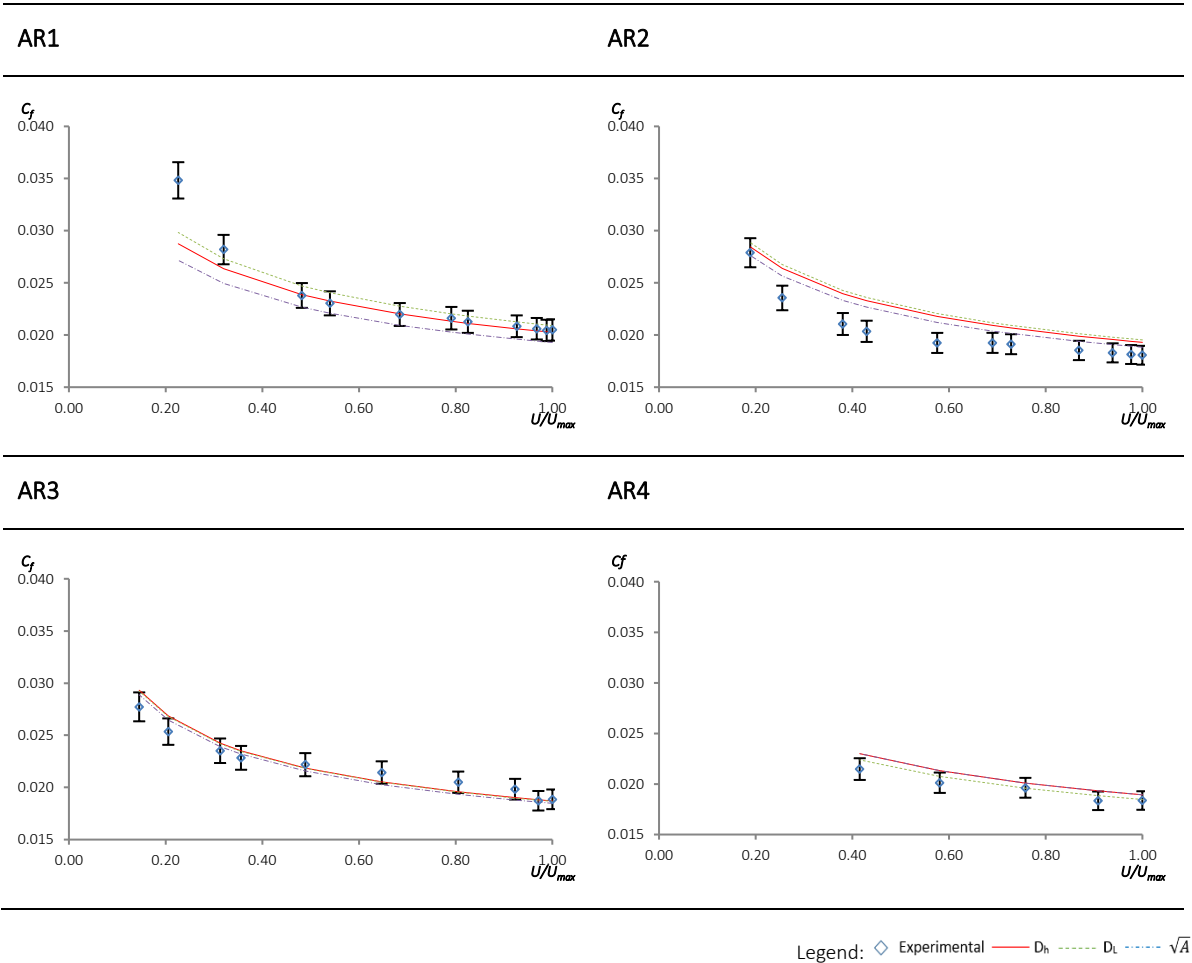


Figure B4-5: Assessment of the influence of the characteristic length scale on the friction coefficient; markers correspond to the experimental values and lines (legend) represent values obtained with a semi-empirical relation [26] – Equation (B1-4).

The present analysis is to a great extent inconclusive in what concerns the selection of the most appropriate characteristic length scale to represent the experimental data. On the basis of Figure B4-5 and Table B4-2, it can be stated that for higher aspect ratios the hydraulic diameter yields an adequate representation, while for the cross-section near the square shape, the best fitting was achieved using the laminar equivalent diameter. In addition, the square root of the cross-section area was well-suited for case **AR2**. Interestingly, case **AR3** presented similar results for the three characteristic length scales. Considering all cases, the three tested characteristic length scales present similar overall performance.

In view of these findings, the hydraulic diameter, which is commonly employed to compute the turbulent flow pressure drop in non-circular ducts, and in particular rectangular ducts, was selected as the characteristic length scale to be used in the present study.

Figure B4-5 also indicates that the friction factor is proportional to the aspect ratio, i.e., larger friction factors are associated to higher aspect ratios, which is in agreement with the observation of Hartnett et al. [1]. It should be noted that in rectangular ducts the secondary flow causes higher velocity gradients in the corner regions leading to the enhancement of the friction factor with increasing aspect ratios [1,17,18,46].

Gessner and Jones [15] and Yang [46], among others, concluded that secondary flow is the result of small differences in the opposing forces generated by static pressure gradients. Furthermore, Leutheusser [27] measured the static pressure distribution in both square and rectangular cross-section ducts, and attributed the observed pressure decrease towards the duct periphery to the existence of secondary flows. Similar results were obtained by Georgiou and Milidonis [47].

Therefore, as an attempt to reduce the weight of the secondary flow in the results, a mean pressure of all four walls of the cross-section was used; the location of the pressure taps was chosen to be in the centerline, i.e., as far away as possible from the corners.

Additionally, the local friction coefficient (at $x/L_{max} = 0.60$) was also determined through the *Preston* tube measurements (Equations (B2-1) and (B2-2)). The reported results were obtained for different velocities – the tested range is presented in Table B4-1. Figure B4-6 depicts the local friction coefficient dependence with Re .

The *Preston* measurements were only performed for case **AR3**, since these results will be used to evaluate the behavior of the flow under variable pressure gradient conditions in Chapter B5. The selected location for the *Preston* tube was based on a cross-section in which the mean static pressure was measured.

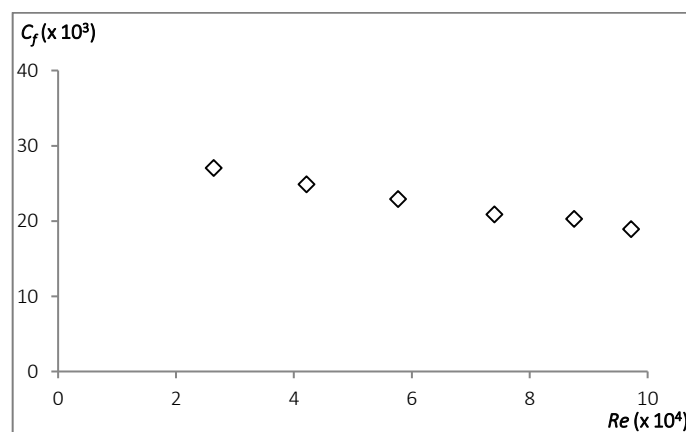


Figure B4-6: Influence of the Reynolds number on the local friction coefficient at $x/L_{max}=0.60$ (case **AR3**), obtained through *Preston* measurements.

The wall friction tends to a constant value as Re increases (Figure B4-6); there is evidence that with increasing values of Re , the Reynolds independence condition occurs in what concerns

the local friction coefficient. Several authors, like, Peysson et al. [28] reported similar findings.

B4.2.4. IRWIN PROBES

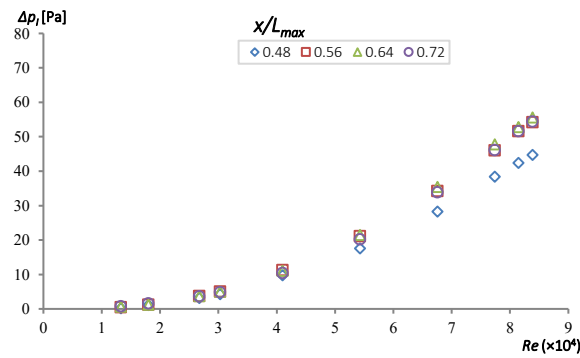
As stated before, ten *Irwin* probes were manufactured and some tests were performed to assess how the results change in the longitudinal and crosswise directions. After the positioning tests were completed, the calibration was performed using the wall shear stress values obtained through the measured mean pressure drop along the fully developed flow region as described in Section B1.4.

B4.2.4.1. VARIATION ALONG THE DUCT

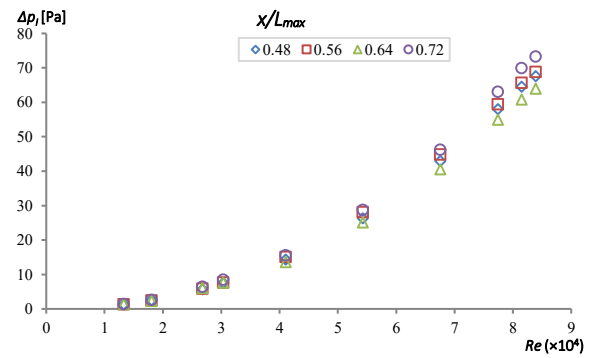
In view of the conclusions presented in Section B4.2.3 and of the similarity of the results obtained for the four configurations, the tests are only reported for the **AR3** case, which is taken as representative of all other cases.

The longitudinal and transversal positioning of the probes was assessed by placing them along the duct as shown in Figure B2-4. For different flow velocities, measurements of the pressure difference between two adjacent probe taps are reported in Figure B4-7. For the longitudinal positioning, the location of the sensors is represented by its normalized coordinate (x/L_{max}) in the test section. In what concerns the transversal measurements, they are taken for the probe located on the central longitudinal line and for the two probes located on the sides (30 mm from each other - Figure B2-4). For the cross-section at $x/L_{max} = 0.64$, it is also included the comparison between the measurements for the top and the bottom surfaces. In all graphs of Figure B4-7, the influence of the Reynolds number on the pressure difference can be noticed and, as expected, it augments with increasing values of Re .

a) Longitudinal distribution – Top face



b) Longitudinal distribution – Bottom face



c) Transversal distribution – Top face

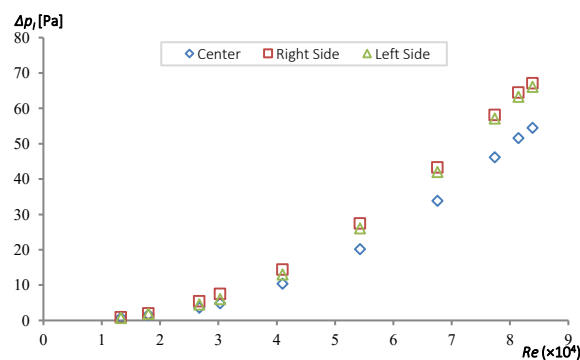
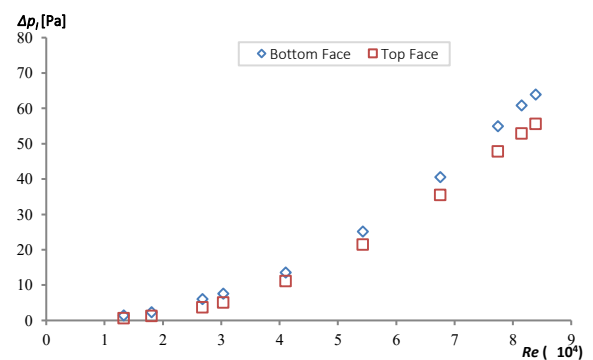
d) Top vs Bottom faces ($x/L_{max} = 0.64$)

Figure B4-7: Assessment of longitudinal placement (a) and b)), transversal placement (c)) and comparison between top and bottom faces (d)) on the pressure measurement by the Irwin probes.

The analysis for the transversal positioning reveals that both sides present similar results, which may indicate the flow symmetry. A significant difference between the central and the side values (around 22%) was observed, which can be likely justified by the proximity to the corners and consequent influence of the secondary flow. The secondary flow penetrates the corners and gets closer to the walls with increasing values of Re [2,15,17–19], which may explain the increase in the transversal discrepancies with increasing values of Re . Henceforth only the probes located in the centerline will be considered for the calibration, which is also where the pressure taps are placed.

In what concerns the analysis of the longitudinal distributions, the results are different between the top and bottom faces. On the top face, as the first probe (at $x/L_{max} = 0.48$) differs considerably from all the others; therefore, that probe will be excluded from calibration. A somewhat erratic behavior was observed on the bottom face, since the first two sensors (i.e., at $x/L_{max} = 0.48$ and 0.56) have analogous values, and then the third and fourth probes have lower and higher values, respectively, as shown in Figure B4-7d), which does not allow an obvious conclusion. The dynamic characteristics of the flow have the largest variation in the vicinity of the surface, making near-wall measurements rather challenging, in particular when

are used intrusive devices, which may affect the flow field itself. Moreover, despite the fact the probes were carefully manufactured, there is the possibility that each probe has a slightly different degree of intrusion into the flow.

By comparing the measurements taken at the top and bottom face for the same cross-section and different values of Re , the curves present similar trend; however, it is evident that the pressure difference is higher for the bottom face than that for the top one. This observation suggests that there is no symmetry of the flow over the cross-section; Melling and Whitelaw [2] mention a small unevenness in the flow, which reveals itself by the turbulence intensity contours. On the other hand, the conditions of top and bottom walls are not exactly the same, as the top wall has fifteen pressure taps against four on the bottom, which can influence the flow field, even with the taps perfectly levelled with the surface. In addition, as mentioned before, the sealing for the fixed and movable joints is different. The results for $x/L_{max} = 0.64$, which is the cross-section that presents the smallest differences between the bottom and top faces, are reported in Figure B4-7d).

The directional sensitivity of the probes was also tested, and, as expected, since they have a cylindrical geometry, the probes are omnidirectional, as reported by *Irwin* [20], with a mean deviation of the pressure difference lower than 2%.

After analyzing the results of the positioning tests, both probes located in the centerline at $x/L_{max} = 0.64$ (top and bottom faces) were those selected to perform the calibration.

B4.2.4.2. CALIBRATION OF THE PROBES

As already mentioned, it is common engineering practice to employ empirical methods to predict turbulent flow largely due to its complexity. As mentioned by Leutheusser [27], the fundamental principle of similitude permits the formulation of empirical relations through the fitting of a curve approximating the measured data points. This is the method used in the present work to obtain the calibration equation of the *Irwin* probes.

The calibration was conducted for each duct aspect ratio and bulk flow velocity by measuring the mean pressure difference between the two most distant test sections located at $x/L_{max} = 0.2$ and $x/L_{max} = 0.8$, respectively. The associated pressure gradient is used in Equation (B1-9) to determine the wall shear stress. The τ_w values are plotted against the pressure difference measured in the *Irwin* probes (Δp_I) as presented in Figure B4-8. The values displayed in Figure B4-8, taking into consideration the differences reported in Figure B4-7, correspond to both probes located at $x/L_{max} = 0.64$ at top and bottom faces, respectively, as discussed in Section B4.2.4.1

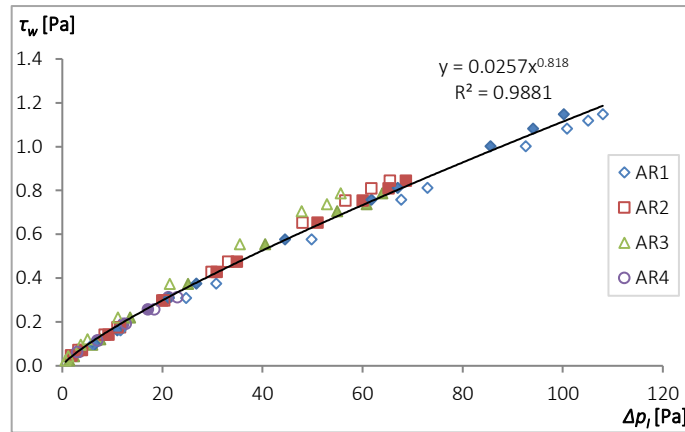


Figure B4-8: Calibration curve for the *Irwin* probes located at $x/L_{max} = 0.64$ (hollow markers correspond to top face and filled markers to the bottom face).

Figure B4-8 clearly shows that the results for all aspect ratios are quite similar; however, the top face values present higher scattering than those for the bottom face. The best fitting curve for all configurations and for both probes relating τ_w to Δp_I is a power function, as follows:

$$\tau_w = 0.0257 \times \Delta p_I^{0.818} \quad (\text{B4-3})$$

with a mean coefficient of determination (R^2) of 98.81%.

According to Irwin [20], although *Irwin* probes were initially designed to measure pedestrian-level winds, the sensor can also be used as an omnidirectional skin friction meter in conjunction with an appropriate calibration curve. Comparing the power law dependence of Equation (B4-3) with the exponent of around 0.9 proposed by Irwin [20], the values are similar.

In Figure B4-9 the values obtained by employing Equation (B1-9) are compared with those given by Equation (B4-3); it is apparent that the calibration curve fits well the measured values of the wall shear stress for all aspect ratios. The discrepancies are minimal for higher aspect ratios (**AR1** and **AR2**); the calibration curve tends to slightly underestimate the values for **AR3** and to overestimate the values of **AR4**. If the assumption of a uniform wall shear stress distribution around the cross-section perimeter is not considered, the overall mean relative error is evaluated to be less than 8%.

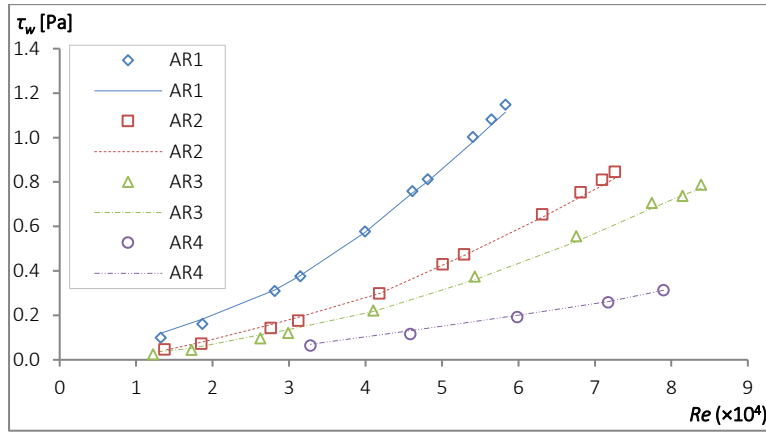


Figure B4-9: Comparison between experimental and correlated values of the wall shear stress; lines correspond to the calibration curve, Equation (B4-3), and markers were obtained with Equation (B1-9).

As mentioned in Section B4.2.3, *Preston* tube measurements of the local wall shear stress were performed at $x/L_{max} = 0.60$. Therefore, an *Irwin* probe was placed at the same location in order to carry out a more accurate calibration process.

For case **AR3**, the τ_w values, obtained using the *Preston* tube, are plotted, against the pressure difference measured by the *Irwin* probe (Δp_I), in Figure B4-10.

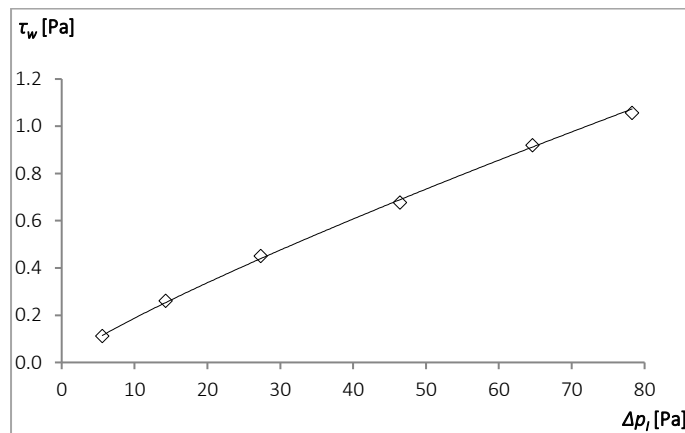


Figure B4-10: Calibration curve for the *Irwin* probe located at $x/L_{max} = 0.60$ using *Preston* tube measurements for case **AR3**.

The distribution presented in Figure B4-10 is correlated by the power function, as follows:

$$\tau_w = 0.0266 \times \Delta p_I^{0.8478} \tag{B4-4}$$

with a mean coefficient of determination (R^2) equal to 99.93%.

Figure B4-11 depicts the comparison of the local friction coefficient obtained through the measurements of the *Preston* tube (Equation (B2-1)) and the *Irwin* probe calibration (Equation

(B4-4)) for case **AR3**. As observed, there is good agreement between the two sets of measurements, with mean deviations lower than 2%.

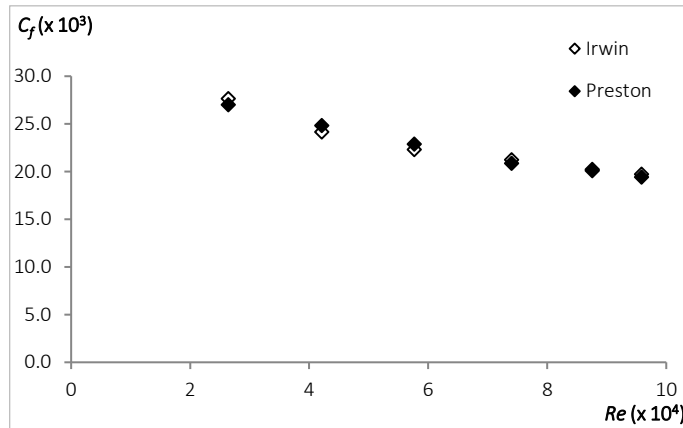


Figure B4-11: Comparison of the friction coefficient obtained through the measurements of the *Preston* tube (Equation (B2-2)) and the *Irwin* probe calibration curve (Equation (B4-4)) for case **AR3**.

Additionally, using only the *Irwin* probe placed in at $x/L_{max}=0.60$, the calibration curve (Equation (B4-5)) obtained employing the force balance in the test section was compared with the calibration curve using the *Preston* tube measurements (Equation (B4-4)). The two calibration curves are similar, as it can be noted in Figure B4-12, with a mean difference lower than 5%.

$$\tau_w = 0.0225 \times \Delta p_I^{0.9018} \tag{B4-5}$$

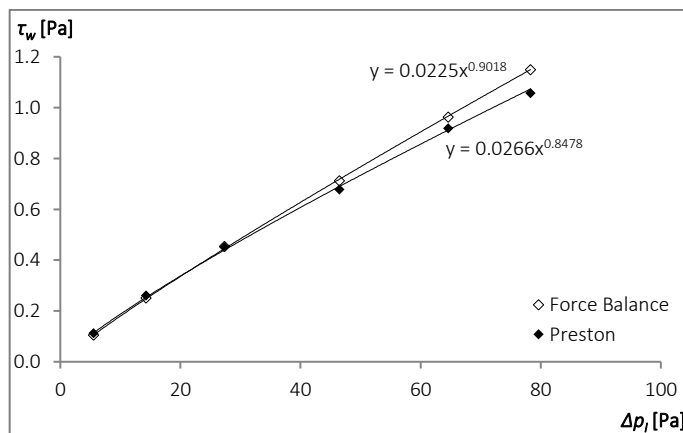


Figure B4-12: Comparison of the calibration curves for the *Irwin* probe ($x/L_{max}=0.60$) obtained using the *Preston* tube measurements (Equation (B4-4)) and the force balance for case **AR3** (Equation (B4-5)).

B4.3. NUMERICAL RESULTS

In the present work, the numerical results obtained with OpenFOAM are benchmarked against ANSYS CFX results, and compared against the experimental results. As mentioned in Chapter B3, only case **AR3** was considered to perform the numerical simulations.

In Section B3.4, a mesh dependency study was performed and was concluded that the M7 mesh (Table B3-1) is the most suitable to the present study. Therefore, the numerical results presented here are obtained using this mesh. Furthermore, the results presented in this section were obtained for the maximum velocity flow in the duct ($U_0=16.7$ m/s - Table B4-1).

B4.3.1. PRESSURE COEFFICIENT DISTRIBUTION

Figure B4-13 depicts the wall pressure distribution along the rectangular duct (experimental values just for the four averaging locations of mean pressure defined in Figure B2-1) with the predicted values by OpenFOAM and by CFX codes.

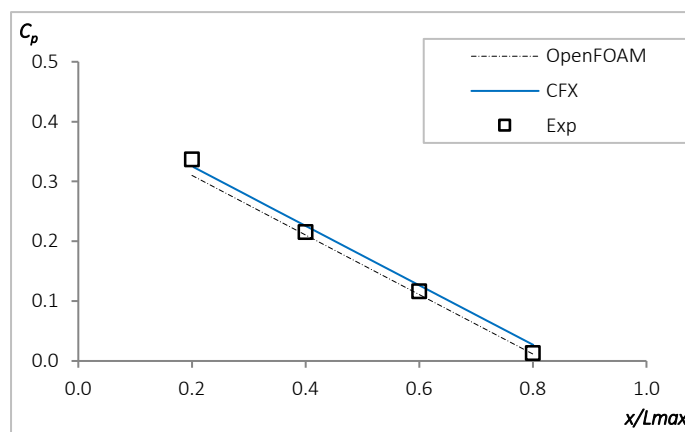


Figure B4-13: Comparison of the experimental wall pressure distribution along the rectangular duct (case **AR3**) with OpenFOAM and CFX predicted values ($U_0=16.7$ m/s).

It can be observed in Figure B4-13 that good agreement was observed in both predictions of OpenFOAM and CFX, being the deviation lower than 5%. However, it should be mentioned that, although the same conditions were adopted for both CFX and OpenFOAM simulations (in particular, computational domain, boundary conditions, and y^+), the calculation time and required number of iterations showed marked differences. To reach the converged solution,

the OF solution required 1038 iterations (Table B3-1), while CFX needed only 83. Regarding the calculation time, OF took about six hours, while CFX, required only 30 minutes. In spite of the fact that the mesh arrangement is different for these software packages as well as the residuals calculation procedure, the main factor for the calculation speed difference may be related to the solver algorithm: CFX uses a coupled solver, while OF adopts a segregated approach.

As mentioned, the numerical results were obtained for the maximum flow velocity ($U_{max}=16.7$ m/s). However, the velocity influence (Figure B4-14) was also analyzed for two other velocities, namely, 60% and 30% of the maximum velocity. Once again, the M7 mesh was used in the numerical simulations to predict the wall pressure distribution presented in Figure B4-14.

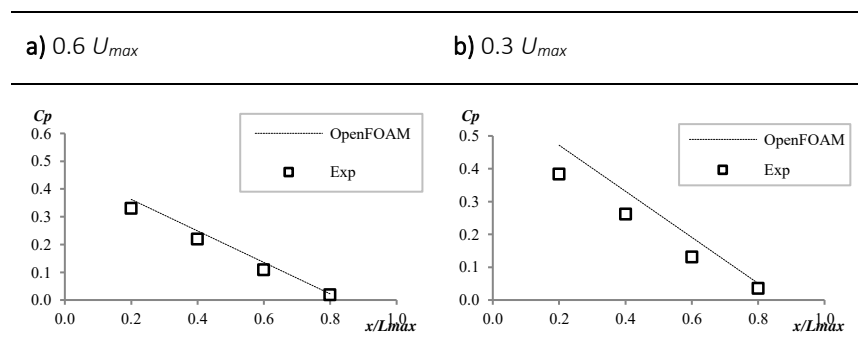


Figure B4-14: Wall pressure distribution. **a)** Velocity of $0.6 U_{max}$, **b)** Velocity of $0.3 U_{max}$.

In what concerns the wall pressure distribution, the results obtained with the velocity of $0.6 U_{max}$ are in better agreement with the experimental data than those for velocity of $0.3 U_{max}$, as reported in Figure B4-14. This can happen due to the fact that the measured pressure values for the velocity of $0.3 U_{max}$ are very low and close to the limit of the sensitivity range of the measuring equipment.

B4.3.2. FRICTION COEFFICIENT

In this section, the local friction coefficient (at $x/L_{max} = 0.60$), determined using the *Preston* tube measurements (Figure B4-6), is compared against the predicted values by OpenFOAM (OF) and CFX. Figure B4-15 depicts the local friction coefficient dependence with Re .

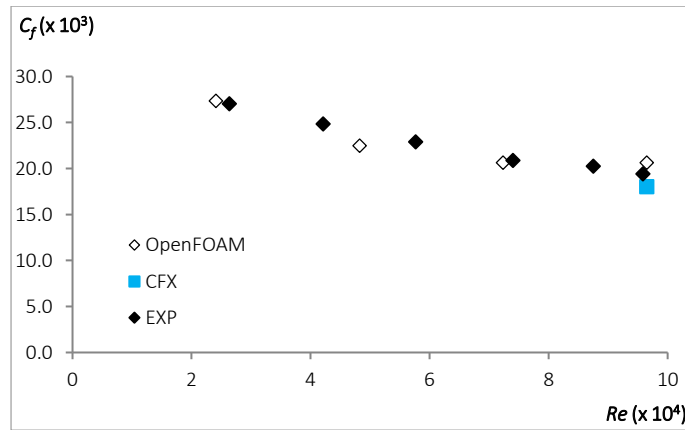


Figure B4-15: Influence of the *Reynolds* number on the friction coefficient. *Preston* measurements against predicted values using OpenFOAM and CFX (Case **AR3**).

Figure B4-15 allows to state that there is good agreement between the experimental results and the values predicted by OpenFOAM and CFX. Table B4-3 presents the local friction coefficient (at $x/L_{max} = 0.60$) predicted by OpenFOAM and by CFX, and respective deviations relatively to the *Preston* measurements, for the highest velocity tested.

Table B4-3: Local friction coefficient (at $x/L_{max} = 0.60$, for the maximum velocity - Table B4-1) predicted by OpenFOAM and by CFX and deviation relatively to *Preston* measurements.

Case	<i>Preston</i> (Equation. (B2-2))	OpenFOAM		CFX	
	$c_f (x10^3)$	$c_f (x10^3)$	Deviation (%)	$c_f (x10^3)$	Deviation (%)
AR3	19.42	20.64	6.27	18.00	7.31

The predictions obtained using OF and CFX, in comparison with the experimental values, deviate less than 7% and 8% respectively. Although Table B4-3 only presents the deviations for the higher velocity tested, it can be observed in Figure B4-15 that similar behavior is observed for the entire *Re* tested range.

The velocity influence in the friction coefficient was also investigated, and two velocities were tested, namely $0.3 U_{max}$ and $0.6 U_{max}$, with $U_{max}=16.7$ m/s. The M7 mesh (Table B3-1) is used in the simulations to predict the local wall shear stress.

Table B4-4 presents the local friction coefficient for both velocities; the deviation for both cases is less than 2%.

Table B4-4: Local friction coefficient ($c_f \times 10^3$) ($x/L_{max} = 0.56$) predicted by OpenFOAM and deviations from Preston measurements for two different velocities ($0.6 U_{max}$ and $0.3 U_{max}$).

Case	Preston measurements c_f ($\times 10^3$)	OpenFOAM c_f ($\times 10^3$)	Deviation (%)
$0.6 U_{max}$	21.51	21.95	1.97
$0.3 U_{max}$	27.17	27.67	1.80

B4.4. CONCLUDING REMARKS

An experimental apparatus was specifically designed and built to assess the applicability of *Irwin* probes to determine the wall shear stress of fully developed, incompressible fluid flow under constant pressure gradient conditions. Four different cross-sections were used with aspect ratios ranging from 1:1.03 to 1:4.00 and the experimental setup allows testing Reynolds number values between 10^4 and 9×10^4 .

Particular attention was given to assure the fully developed flow condition is satisfied in the test section, specifically in what concerns the length of the development section, which was analytically calculated and verified by the linear decrease of the pressure measured along the duct. Furthermore, the physical stabilization of the flow was also taken into consideration and a honeycomb and a tight net were used in the duct inlet.

Repeatability tests were performed for both static pressure taps and *Irwin* probes; the tests indicate a mean deviation equal to 4% and 1.4%, respectively. Both sensors present good level of repeatability with the *Irwin* probes overcoming the pressure taps. Regarding accuracy, *Irwin* probes provide a pressure difference; therefore, their accuracy depends on the pressure transducer, which has an accuracy of ± 0.5 Pa for a range of ± 1000 Pa. The relation between the pressure difference in the *Irwin* probe and the local wall shear stress is obtained by calibration.

The Darcy's friction coefficient was calculated based on the pressure drop in the test section for each aspect ratio and Reynolds number. The experimentally-derived data set was compared against the results for turbulent flow in smooth circular tubes and, regardless of the aspect ratio, and throughout the entire Re range tested, it shows similar trend to that of the circular tubes.

The assessment conducted to evaluate the influence of the characteristic length scale on the

representation of the friction factor revealed to be inconclusive, as the choice of the appropriate length scale appears to be dependent on the aspect ratio of the duct and the overall performance was similar in all tested scales. Thus, the hydraulic diameter was selected as the best-suited scale for the studied configurations, as commonly employed to compute the turbulent flow pressure drop in non-circular ducts.

Additionally, for case **AR3**, the local friction coefficient (at $x/L_{max} = 0.60$) was also determined through the *Preston* tube measurements. A clear evidence of the occurrence of the Reynolds independence condition was observed and supported by a square root fit of the local friction coefficient.

The calibration of the *Irwin* probes was analyzed in some detail. Their directional sensitivity was assessed along with the influence of the longitudinal and transversal positioning on the measurements. A possible explanation for the discrepancies may be related to the secondary flows arising on the duct corners.

Considering all tested aspect ratios, the entire range of Reynolds number and using a force balance to obtain the wall shear stress, the best calibration curve is a power function, with an overall mean relative error estimated to be less than 8%.

When the *Preston* tube measurements are considered in the calibration process, the best correlation between the pressure difference measured by the *Irwin* probe (Δp_I) and the local wall shear stress is also a power function, but with a mean deviation lower than 2%.

The numerical results obtained with OpenFOAM are benchmarked against ANSYS CFX results, and the two sets are compared against the experimental results. Only case **AR3** was considered to perform the numerical simulations.

Comparisons between numerically- and experimentally-derived pressure and friction coefficients were conducted to validate the numerical model and deviations below 7% were obtained.

Considering the obtained results of static pressure and from the *Preston* tube, it was concluded that *Irwin* probes are applicable to measure the local wall shear stress in turbulent incompressible flows through smooth rectangular ducts.

The Reynolds dependence was also studied; besides U_{max} ($U_{max}=16.7$ m/s), two additional velocities were considered, namely, $0.6U_{max}$ and $0.3U_{max}$. The difference between predictions and experimental data for the wall pressure distribution increased for the lower velocity. However, for both cases, the difference between predicted and experimental local wall shear stress was lower than 2%.

CHAPTER B5

RECTANGULAR DUCT WITH VARIABLE SECTION

The present chapter aims to conduct the assessment of the applicability of *Irwin* probes to measure the wall shear stress of fully developed, incompressible fluid flow under variable pressure gradient conditions; being so, the variable section geometry is discussed, namely, convergent and divergent longitudinal sections.

Since the features of the test studies were already presented in Chapter B2 and Chapter B3, only the specific characteristics of the current cases are presented in Section B5.1.

Both experimental tests and numerical simulations were performed, and the obtained results are compared and discussed in Section B5.2. As benchmark, these results are also confronted with the horizontal top wall (constant cross-section) case (Chapter B4). The calibration of the *Irwin* probes is discussed in Section B5.2.3.

Finally, some conclusions are drawn summarizing the main findings of the present study case.

B5.1. CASE DESCRIPTION

The experimental apparatus versatility (Section B2.1) allows the study of both constant and variable (convergent and divergent) section configurations. After the study performed in Chapter B4, only **AR3** case ($H = 0.06$ m) was considered in this chapter.

Figure B5-1 depicts the two different cases considered here, the convergent longitudinal section with 1° slope (**C1**) and divergent longitudinal section with 1° slope (**D1**). As benchmark, these results are also compared with the horizontal (**H**) top wall (constant cross-section) case.

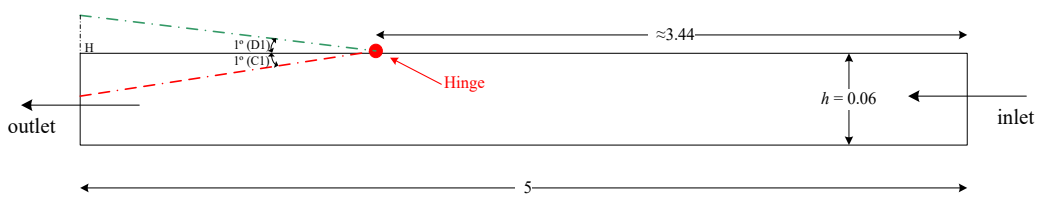


Figure B5-1: Schematic of experimental apparatus – Side View (dimensions in meters).

The main characteristics of the different configurations tested (including the constant cross-section case) are summarized in Table B5-1. Apart from the cross-section geometry, the experimental procedure and the numerical simulations performed are similar to those presented in Chapter B4. In Table B5-1, the Reynolds numbers are obtained with Equation (B1-5), using the hydraulic diameter (D_h) as characteristic length scale and the velocity measured at the entrance of the duct using the *Venturi* flow meter, and, in cases **C1** and **D1**, is considered the total height of the duct ($H = 0.06$ m).

Table B5-1: Main characteristics of the tested configurations (constant and variables sections).

Case		H	C1	D1
Type		Horizontal	Convergent	Divergent
Slope angle (°)		0	1.0	1.0
U (m/s)	test range			
	Min	4.8	4.1	4.9
	Max	19.2	16.7	19.8
Re ($\times 10^4$)	test range			
	Min	2.41	2.08	2.48
	Max	9.65	8.43	9.95

B5.2. RESULTS AND DISCUSSION

Likewise the configurations of constant cross-section, the tests performed cover mainly pressure measurements, using *Irwin* probes, the *Preston* tube and also static pressure taps distributed along the duct as mentioned in Chapter B2.

In this section, the pressure (c_p) and friction (c_f) coefficients predicted by OpenFOAM (OF) and CFX are compared against the experimental results (measured in the pressure taps and by *Preston* tubes, respectively) in order to validate the numerical results. In addition, the calibration of *Irwin* probes is discussed.

Similarly to Chapter B4, in the following figures, the value of $x = 0$ refers to the entrance of the test section and x/L_{max} refers to the distance (x) normalized by L_{max} , which is the length of the test section, $L_{max} = 2.5$ m (Figure B2-1).

B5.2.1. PRESSURE COEFFICIENT DISTRIBUTION

The pressure distribution along the mean pressure sections of the duct is discussed in this section. The results are reported for the maximum flow velocity in the duct for each case (Table B5-1).

The comparison between the experimental measurements (markers) and the values predicted by OpenFOAM (OF) and by CFX is depicted in Figure B5-2.

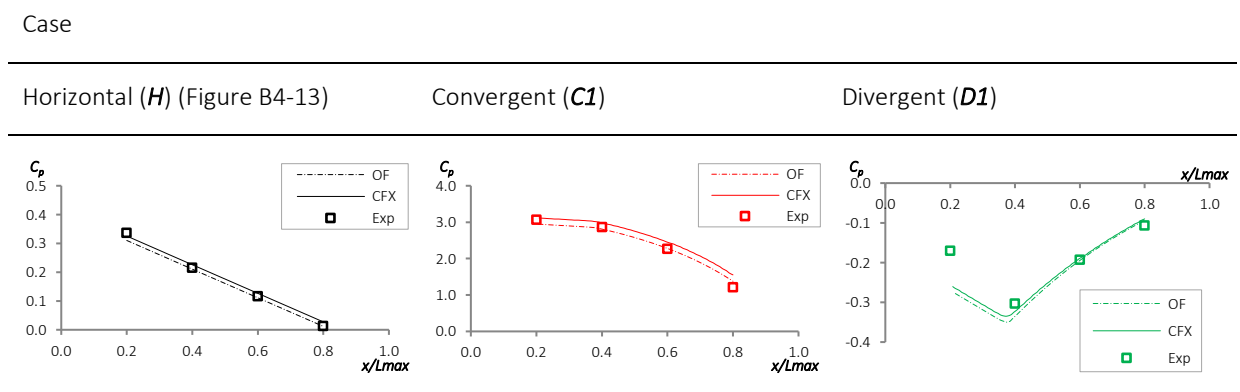


Figure B5-2: Experimental pressure coefficient distribution against predicted values by OpenFOAM and by CFX.

Figure B5-2 indicates good agreement between the experimental and predicted pressure

coefficient. For the horizontal (Figure B4-13), convergent and divergent cases, the deviation values are less than 5%, 2% and 20%, respectively. In the latter, if only the divergent longitudinal section is considered ($x/L_{max} > 0.4$), the mean deviation drops to 8%. Similar deviation values were obtained when comparing the CFX predictions against the experimental values, being the exception the case **C1**, with a deviation of 5%.

B5.2.2. FRICTION COEFFICIENT DISTRIBUTION

In this section, the local friction coefficient (at $x/L_{max} = 0.60$) obtained using the *Preston* tube measurements is compared against the predicted values by OpenFOAM (OF) and CFX.

The influence of the Reynolds number on the friction coefficient is depicted in Figure B5-3.

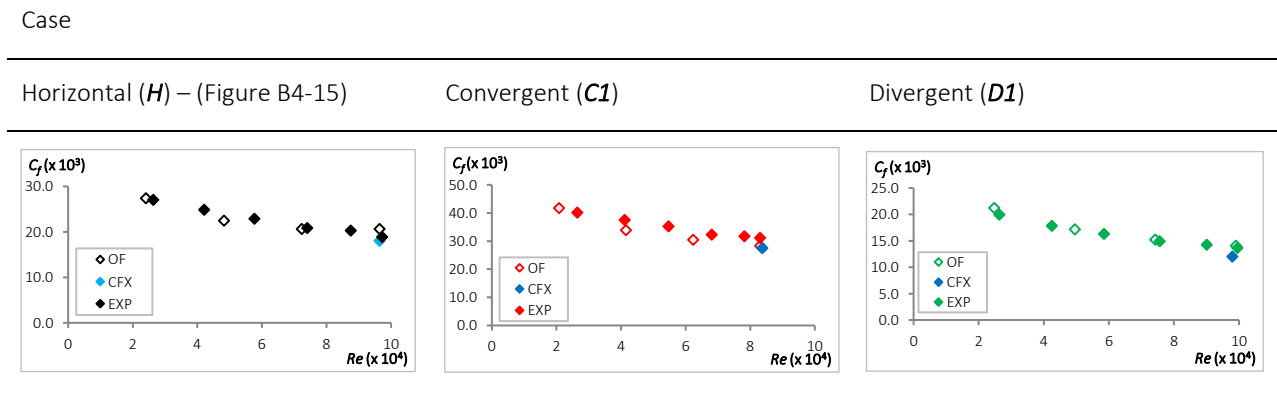


Figure B5-3: Influence of the Reynolds number on the friction coefficient. Preston measurements against predicted values using OpenFOAM and CFX and a power function.

It can be observed in Figure B5-3 that, regardless the configurations, the wall friction tends to a constant value as Re increases, evidencing a Reynolds independency situation in what concerns the local friction coefficient.

Furthermore, Figure B5-3 allows to state that there is a good agreement between the experimental results and the values predicted by OpenFOAM and CFX. Table B5-2 presents local friction coefficient (at $x/L_{max} = 0.60$) predicted by OpenFOAM and by CFX, and respective deviations relatively to the *Preston* measurements, for the highest velocity tested (Table B5-1).

Table B5-2: Local friction coefficient (at $x/L_{max} = 0.60$, and for the maximum velocity - Table B5-1) predicted by OpenFOAM and by CFX and deviation relatively to *Preston* measurements.

Case	<i>Preston</i> (Equation (B2-2))	OpenFOAM		CFX	
	$c_f (x10^3)$	$c_f (x10^3)$	Deviation (%)	$c_f (x10^3)$	Deviation (%)
H	19.42	20.64	6.27	18.00	7.31
C1	31.09	28.29	8.99	27.43	11.76
D1	13.67	14.08	3.02	12.03	11.95

The predictions, obtained using OF and CFX, comparatively to the experimental values, deviate less than 9% and 12%, respectively. Although Table B5-2 only presents the deviations for the higher velocity tested, it can be observed in Figure B5-3 that similar behavior is observed for the entire Re range. However, some caution is required in these comparisons, considering that *Preston* tubes in the presence of pressure gradients have severe limitations. In fact, Patel [36] reports that in favorable and adverse pressure gradients the *Preston* tube tends to overestimate the skin friction, as observed in Table B5-2. Using the interval of the parameter Δ (severity of the pressure gradient - $\Delta = \frac{v}{\rho u_*^3} \frac{dp}{dx}$) proposed by Patel [36], the prescribed maximum error is 6% and 3%, for the convergent and divergent cases, respectively, which may explain partially the measured deviations between experimental and predicted values.

B5.2.3. IRWIN PROBES - CALIBRATION

Although different configurations of the cross-section are used in Chapter B5, the empirical method used to perform the calibration of the *Irwin* probes is similar to the one described in Section B4.2.4.2. Since the horizontal top wall case (**H**), is used as a benchmark for the variable cross-section cases, the location of the *Preston* tube and *Irwin* probe, is the same as indicated in Section B4.2.4.2 (at $x/L_{max}=0.6$).

Due to the flow structure under variable pressure gradients, in this section, the pressure difference measured by the *Irwin* probe (Δp_I) is plotted only against the local wall shear stress measured by the *Preston* tube (Equations (B2-1) and (B2-2)), as illustrated in Figure B5-4. Those distributions can be correlated by power functions, as presented in Table B5-3 along with the respective R-square coefficients.

Case

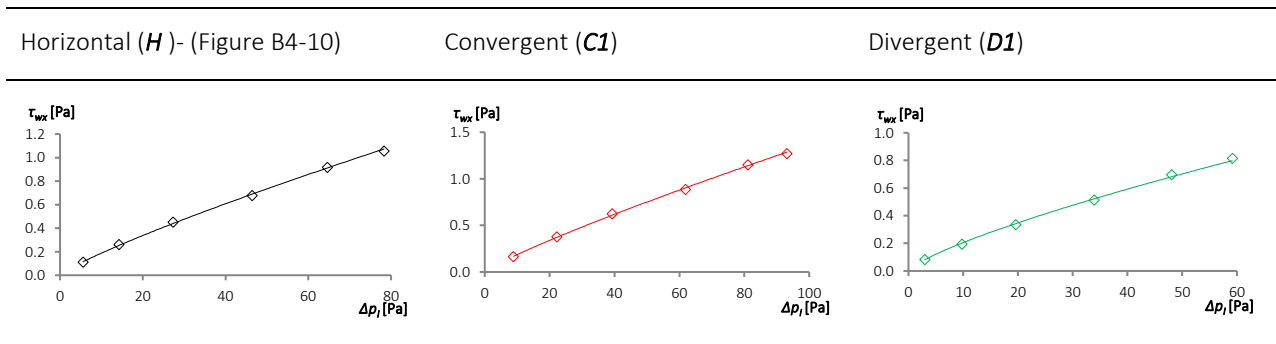


Figure B5-4: Calibration curve for the *Irwin* probe located at $x/L_{max} = 0.60$.

Table B5-3: Calibration curves, and respective R-square coefficient, for the *Irwin* probe located at $x/L_{max} = 0.60$.

Case	Calibration curve	R-square coefficient (%)
<i>H</i>	$\tau_w = 0.0266 \Delta p_I^{0.8478}$	99.93
<i>C1</i>	$\tau_w = 0.0254 \Delta p_I^{0.8656}$	99.95
<i>D1</i>	$\tau_w = 0.0354 \Delta p_I^{0.7637}$	99.88

Although three different calibration curves were obtained, one for each case, the power functions presented in Table B5-3 are similar. Comparing the curves in the tested range of *Irwin* probe pressure difference (Δp_I) in each case, the similarity becomes even more evident, as can be observed in Figure B5-5. Therefore, one single calibration curve can be employed regardless the case, being the curve obtained for the horizontal case, ($\tau_w = 0.0266 \Delta p_I^{0.8478}$), the one with the best overall results.

In order to evaluate the limitations of the use of one single calibration curve to all cases, a wider range of *Irwin* probe pressure difference (Δp_I) was employed, and, as shown in Figure B5-5, increasing Δp_I higher discrepancies between the various curves arise, being more evident in the divergent case. Considering that the curves presented in Table B5-3 remain constant, some caution is advised when using a single calibration curve, especially under adverse pressure gradients, since for values of Δp_I higher than 100 Pa deviation values greater than 10% were observed.

Irwin probe pressure difference (Δp_i) range

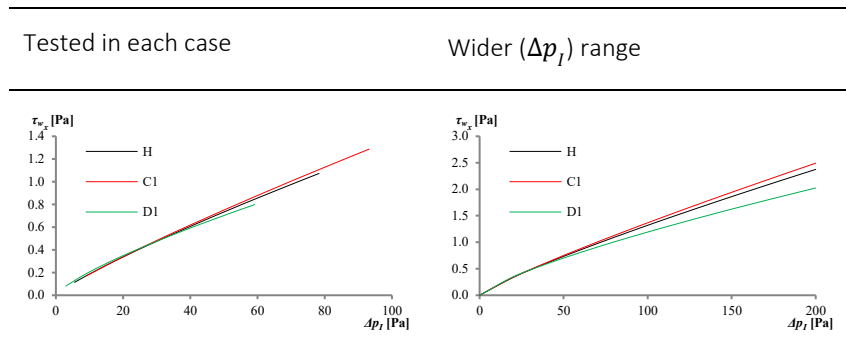


Figure B5-5: Comparison of the calibration curves (Table B5-3) for the *Irwin* probe located at $x/L_{max} = 0.60$. Two different ranges of *Irwin* probe pressure difference (Δp_i): tested range in each case (left) and wider range (right).

Figure B5-6 depicts the comparison of the local friction coefficient obtained through the measurements of the *Preston* tube and the *Irwin* probe calibration for the three cases (Table B5-3). As expected, based on adequate calibration, good agreement between the two sets of measurements is obtained, with mean deviations lower than 3% for the three configurations.

Case

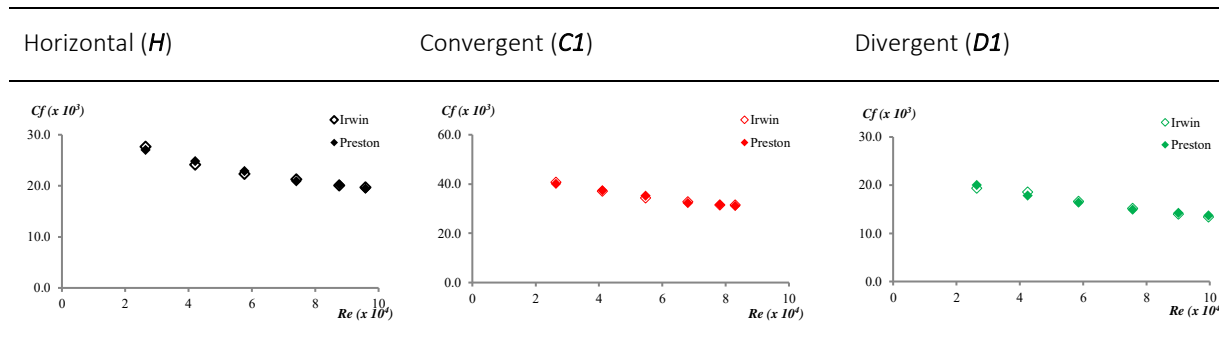


Figure B5-6: Comparison of the friction coefficient obtained through the *Preston* tube and the *Irwin* probe.

B5.3. CONCLUDING REMARKS

A plywood duct with a rectangular cross-section of 0.12 m width and a length of 5 m was used to perform the experimental tests. Three duct configurations were considered in this study: the constant cross-section with an aspect ratio of $AR=1:2$ (horizontal (*H*) top wall), the convergent longitudinal section with one degree slope (*C1*), and the divergent longitudinal section with one

degree slope (**D1**). The Reynolds number tested range from 2×10^4 to 10^5 . The local wall shear stress (τ_w) was obtained using the *Preston* tube measurements.

The numerical simulations were mainly conducted with OpenFOAM toolbox. Additional calculations were performed with ANSYS-CFX for comparison. Similar meshes to the constant cross-section case were used, and with y^+ approximately equal to 1.

The comparison between OpenFOAM predicted and experimentally-derived values, respectively, for pressure and friction coefficient with the aim of validating the numerical model yields good agreement; the deviations are less than 8% demonstrating in this way that the numerical model offers considerable promise as a numerical tool.

The calibration of the *Irwin* probes is discussed in some detail. For all cases, the calibration relation encompasses a power function. Although three different calibration curves were obtained, one for each duct configuration, the obtained power functions are quite similar, being the deviation from each other lower than 5% in the tested range of *Irwin* probe pressure difference (Δp_I). Thus, one single calibration curve can be employed regardless the case, being the curve obtained for the horizontal case the one with the best overall results. However, considering that the obtained calibration curves remain constant outside the tested domain, some caution is advised in what concerns the use of a single calibration curve particularly in the presence of adverse pressure gradients, since values of Δp_I higher than 100 Pa may lead to deviation values greater than 10%.

Comparison for the local friction coefficient obtained using the measurements of the *Preston* tube and the calibrated *Irwin* probe, respectively, indicates good agreement with mean deviation values less than 3% for all cases.

CHAPTER B6

CONCLUSIONS

The present study is expected to make a contribution toward the evaluation of the engineering usability of *Irwin* probes to measure the wall shear stress of fully developed, incompressible fluid flow under constant and variable pressure gradient conditions. The preference for these probes lies with their simplicity, low-cost, easy manufacturing and operation, and widespread use by many researchers.

A plywood duct with a rectangular cross-section of 0.12 m width and a length of 5 m was used to perform the experimental tests. Six duct configurations were considered in this study: the constant cross-section with four different aspect ratios (**AR1**=1:4.00, **AR2**=1:2.67, **AR3**=1:2.00 and **AR4**=1:1.03), the convergent longitudinal section with one degree slope (**C1**), and the divergent longitudinal section with one degree slope (**D1**). The Reynolds numbers tested range from 10^4 to 10^5 . The local wall shear stress (τ_w) was obtained through (when applicable, i.e., rectangular duct with constant cross-section) the force balance between two cross-sections and also by the *Preston* tube measurements.

Prior to the actual measurements, some tests were performed in order to assure the fully developed flow condition in the test section, specifically in what concerns the length of the development section, and the repeatability and accuracy of the employed sensors. Both static

pressure taps and *Irwin* probes present good level of repeatability with the *Irwin* probes overcoming the pressure taps.

The assessment conducted to evaluate the influence of the characteristic length scale on the representation of the friction factor lead to the selection of the hydraulic diameter as the best-suited scale for the studied configurations, as commonly employed to compute the turbulent flow pressure drop in non-circular ducts.

The calibration of the *Irwin* probes was analyzed in some detail. For all cases, the calibration curve encompasses a power function. In the constant cross-section case, when the *Preston* tube measurements are considered in the calibration process, instead of the wall shear stress obtained through a force balance, better results are achieved with a mean deviation between the two calibration curves lower than 5%.

For the case **AR3**, when compared with the variable cross-section cases, although three different calibration curves were obtained, one for each case, the power functions are quite similar. Thus, one single calibration curve can be employed, being the horizontal case curve, the one with the best overall results. Comparison for the local friction coefficient obtained using the measurements of the *Preston* tube and the calibrated *Irwin* probe, respectively, indicates good agreement with mean deviations less than 3% for all cases.

The numerical simulations were conducted with the OpenFOAM, and also with ANSYS-CFX for comparison. A range of y^+ from 0.5 to around 140 was used to perform the mesh dependency study in OpenFOAM. A viscous sub-layer formulation was the approach selected with $y^+ \approx 1$ for the mesh based on CFD best practice, which indicates that with the $k-\omega$ SST turbulence model it is the appropriate value to predict the wall-bounded quantities.

The comparison between OpenFOAM predicted and experimentally-derived values, respectively, for pressure and friction coefficient with the aim of validating the numerical model yields good agreement; the deviations are less than 8% demonstrating in this way that the numerical model offers considerable promise as a numerical tool.

REFERENCES

- [1] Hartnett, J. P., Koh, J. C. Y., and McComas, S. T., 1962, "A Comparison of Predicted and Measured Friction Factors for Turbulent Flow Through Rectangular Ducts," *J. Heat Transfer*, **84**(1), p. 82.
- [2] Melling, A., and Whitelaw, J. H., 1976, "Turbulent Flow in a Rectangular Duct," *J. Fluid Mech.*, **78**(2), p. 289.
- [3] Rokni, M., Olsson, C., and Sundén, B., 1998, "Numerical and Experimental Investigation of Turbulent Flow in a Rectangular Duct," *Int. J. Numer. Methods Fluids*, **28**(2), pp. 225–242.
- [4] Yao, J., Zhao, Y., and Fairweather, M., 2015, "Numerical Simulation of Turbulent Flow through a Straight Square Duct," *Appl. Therm. Eng.*, **91**, pp. 800–811.
- [5] He, S., and Gotts, J. A., 2005, "Calculation of Friction Coefficients for Noncircular Channels," *ASME J. Fluids Eng.*, **126**(6), pp. 1033–1038.
- [6] Bandopadhyay, P. C., and Ambrose, C. W., 1980, "A Generalised Length Dimension for Non-Circular Ducts," *Lett. Heat Mass Transf.*, **7**(5), pp. 323–328.
- [7] Ahmed, S., and Brundrett, E., 1971, "Turbulent Flow in Non-Circular Ducts. Part 1," *Int. J. Heat Mass Transf.*, **14**(3), pp. 365–375.
- [8] Jones, O. C., 1976, "An Improvement in the Calculation of Turbulent Friction in Rectangular Ducts," *ASME J. Fluids Eng.*, **98**(2), p. 173.
- [9] Duan, Z., Yovanovich, M. M., and Muzychka, Y. S., 2012, "Pressure Drop for Fully Developed Turbulent Flow in Circular and Noncircular Ducts," *ASME J. Fluids Eng.*, **134**(6), p. 61201.
- [10] Nikuradse, J., 1926, *Untersuchung Über Die Geschwindigkeitsverteilung in Turbulenten Strömungen. Mit 51 Abb. Und 16 Zahlentafeln. Forschungsarbeiten Auf Dem Gebiete Des*

Ingenieurwesens. Heft 281, VDI-Verlag G. m. b. H., Berlin, Germany.

- [11] Maeda, N., Hirota, M., and Fujita, H., 2005, "Turbulent Flow in a Rectangular Duct with a Smooth-to-Rough Step Change in Surface Roughness," *Energy*, **30**(2–4 SPEC. ISS.), pp. 129–148.
- [12] Rivas, G., Garcia, E., and Assato, M., 2008, "Turbulent Flow Simulations in a Square-Duct Using Non Linear and Reynolds Stress Models," *Anais Do 14^o Encontro de Iniciação Científica E Pós-Graduação Do ITA – XIV ENCITA / 2008*.
- [13] Uruba, V., Hladík, O., and Jonáš, P., 2011, "Dynamics of Secondary Flow in Rectangular Channel," *Colloq. Fluid Dyn. 2011*, Inst. Thermomechanics AS CR, (April 2016), pp. 1–7.
- [14] Vinuesa, R., Schlatter, P., and Nagib, H. M., 2015, "Characterization of the Secondary Flow in Turbulent Rectangular Ducts With Varying Aspect Ratio," *Int. Symp. Turbul. Shear Flow Phenom.*, (January), pp. 3–8.
- [15] Gessner, F. B., and Jones, J. B., 1965, "On Some Aspects of Fully-Developed Turbulent Flow I N Rectangular Channels," *J. Fluid Mech.*, **23**(4), p. 689.
- [16] Schlichting, H., 1979, *Boundary Layer Theory*, McGraw-Hill Book Company, New York.
- [17] Pinelli, A., Uhlmann, M., Sekimoto, A., and Kawahara, G., 2010, "Reynolds Number Dependence of Mean Flow Structure in Square Duct Turbulence," *J. Fluid Mech.*, **644**, pp. 107–122.
- [18] Rochlitz, H., Scholz, P., and Fuchs, T., 2015, "The Flow Field in a High Aspect Ratio Cooling Duct with and without One Heated Wall," *Exp. Fluids*, **56**(12), pp. 1–13.
- [19] Brundrett, E., and Baines, W. D., 1964, "The Production and Diffusion of Vorticity in Duct Flow," *J. Fluid Mech.*, **19**(3), p. 375.
- [20] Irwin, H. P. A. H., 1981, "A Simple Omnidirectional Sensor for Wind-Tunnel Studies of Pedestrian-Level Winds," *J. Wind Eng. Ind. Aerodyn.*, **7**(3), pp. 219–239.
- [21] Ferreira, A. D., Silva, M. C. G., Viegas, D. X., and Lopes, A. M. G., 1991, "Wind Tunnel Simulation of the Flow around Two-Dimensional Hills," *J. Wind Eng. Ind. Aerodyn.*, **38**(2–3), pp. 109–122.
- [22] Monteiro, J. P., and Viegas, D. X., 1996, "On the Use of Irwin and Preston Wall Shear Stress Probes in Turbulent Incompressible Flows with Pressure Gradients," *J. Wind Eng. Ind. Aerodyn.*, **64**(1), pp. 15–29.
- [23] Faria, R., Ferreira, A. D., Sismeiro, J. L., Mendes, J. C. F., and Sousa, A. C. M., 2011, "Wind Tunnel and Computational Study of the Stoss Slope Effect on the Aeolian Erosion of Transverse Sand Dunes," *Aeolian Res.*, **3**(3), pp. 303–314.
- [24] Ferreira, A. D., Pinheiro, S. R., and Francisco, S. C., 2013, "Experimental and Numerical Study on the Shear Velocity Distribution along One or Two Dunes in Tandem," *Environ. Fluid Mech.*, **13**(6), pp. 557–570.
- [25] "The Open Source CFD Toolbox - OpenFOAM" [Online]. Available: <https://www.openfoam.com/>.
- [26] Zigrang, D. J., and Sylvester, N. D., 1982, "Explicit Approximations to the Solution of Colebrook's Friction Factor Equation," *AIChE J.*, **28**(3), pp. 514–515.

- [27] H. J. Leutheusser, 1963, "Turbulent Flow in Rectangular Ducts," ASCE, J. Hydraul. Div., **89**(HY3), p. 19.
- [28] Peysson, Y., Ouriemi, M., Medale, M., Aussillous, P., and Guazzelli, É., 2009, "Threshold for Sediment Erosion in Pipe Flow," *Int. J. Multiph. Flow*, **35**(6), pp. 597–600.
- [29] Colebrook, C. F., 1939, "Turbulent Flow in Pipes, with Particular References to the Transition Region Between the Smooth and Rough Pipe Laws," *J. Inst. Civ. Eng.*, **11**(October 1939), pp. 133–156.
- [30] Tongpun, P., Bumrunghthaichaichan, E., and Wattananusorn, S., 2014, "Investigation of Entrance Length in Circular and Noncircular Conduits by Computational Fluid Dynamics Simulation," *Songklanakarin J. Sci. Technol.*, **36**(4), pp. 471–475.
- [31] White, F., 1999, *Fluid Mechanics*, McGraw-Hill Book Company, New York.
- [32] Zagarola, M. V., and Smits, A. J., 1998, "Mean-Flow Scaling of Turbulent Pipe Flow," *J. Fluid Mech.*, **373**, pp. 33–79.
- [33] Nikuradse, J., 1932, "Gesetzmäßigkeiten Der Turbulenten Strömung in Glatten Rohren," *Forsch. auf dem Gebiet des Ingenieurwesens*, **3**, pp. 1–36.
- [34] Anselmet, F., Ternat, F., Amielh, M., Boiron, O., Boyer, P., and Pietri, L., 2009, "Axial Development of the Mean Flow in the Entrance Region of Turbulent Pipe and Duct Flows," *Comptes Rendus - Mec.*, **337**(8), pp. 573–584.
- [35] Preston, J. H., 1954, "The Determination of Turbulent Skin Friction by Means of Pitot Tubes," *J. R. Aeronaut. Soc.*, **58**(518), pp. 109–121.
- [36] Patel, V. C., 1965, "Calibration of the Preston Tube and Limitations on Its Use in Pressure Gradients," *J. Fluid Mech.*, **23**(1), p. 185.
- [37] Bechert, D. W., 1996, "Calibration of Preston Tubes," *AIAA J.*, **34**(1), pp. 205–206.
- [38] Faria, R., Ferreira, A. D., Lopes, A. M. G., and Sousa, A. C. M., 2016, "On the Use of Irwin Probes to Measure Wall Shear Stress in Rectangular Ducts of Constant Section," *CYTEF2016 - Proc. - Adv. Refrig. Sci. Technol. - VIII*, p. 9.
- [39] Menter, F. R., 1994, "Two-Equation Eddy-Viscosity Turbulence Models for Engineering Applications," *AIAA J.*, **32**(8), pp. 1598–1605.
- [40] Menter, F. R., and Esch, T., 2001, "Elements of Industrial Heat Transfer Predictions," *16th Brazilian Congress of Mechanical Engineering (COBEM)*, pp. 117–127.
- [41] JCGM, 2012, *International Vocabulary of Metrology – Basic and General Concepts and Associated Terms (VIM - 3rd Ed.)*.
- [42] Ferreira, A. D., and Fino, M. R. M., 2012, "A Wind Tunnel Study of Wind Erosion and Profile Reshaping of Transverse Sand Piles in Tandem," *Geomorphology*, **139–140**, pp. 230–241.
- [43] Blasius, H., 1911, "The Law of Similarity Applied to Friction Phenomena," (in Ger. *Phys. Zeitschrift*, **12**, p. 1175.
- [44] Mirmanto, 2013, "Developing Flow Pressure Drop and Friction Factor of Water in Copper Microchannels," *J. Mech. Eng. Autom.*, **3**, pp. 641–649.
- [45] Sahar, A. M., Özdemir, M. R., Fayyadh, E. M., Wissink, J., Mahmoud, M. M., and

- Karayiannis, T. G., 2016, "Single Phase Flow Pressure Drop and Heat Transfer in Rectangular Metallic Microchannels," *Appl. Therm. Eng.*, **93**, pp. 1324–1336.
- [46] Yang, S.-Q., 2009, "Mechanism for Initiating Secondary Currents in Channel Flows," *Can. J. Civ. Eng.*, **36**(9), pp. 1506–1516.
- [47] Georgiou, D. P., and Milidonis, K. F., 2014, "The Static Pressure Field as a Driving Mechanism for the Streamwise Corner Flow in the Presence of an Inclined Transverse Plane," *Exp. Fluids*, **55**(3), p. 1694.

CLOSURE

This is the closing chapter of the present thesis. Due to the reasons mentioned in the Introduction, it was necessary to divide it into two parts, namely, *Part A - Numerical and experimental study of granular piles when subjected to wind erosion*; and *Part B – Calibration of Irwin probes*. For the sake of completeness and clarity, both of them include several chapters, which are organized to give a coherent description of the goals of each part and how they contribute to the objectives of the present project.

Part B is essentially designed to confer further confidence to the data employed in the model validation conducted in Part A; therefore, each part has its own goals, which are different, but complementary.

Notwithstanding that the final remarks were already presented in the end of each part, in the next sections it is intended to sum up the achievements of the present work, as well as, giving suggestions and recommendations for future work.

MAIN ACHIEVEMENTS

The original proposal of the present thesis is the assessment of the interaction between the airflow and granular material 3D oblong piles for various wind velocities and incidence angles. The study was carried out from two points of view, namely: a) the impact of the obstacle in the airflow characteristics, considering the oblong pile and its surroundings; and b) the behavior of the oblong pile when subjected to wind erosion, in what concerns the deformation of the free-surface, as well as, the sand emission rate. The performance of the sand piles was assessed based on the experimental results obtained in tests conducted in a wind tunnel facility, and on predictions of numerical simulations using the open source CFD code OpenFOAM.

As already stated, the prediction of phenomena associated with wind erosion can prevent or mitigate major threats related to transportation safety, air quality or even climate changes. Furthermore, at industrial level, in particular for coal-fired power plants, the understanding of the interaction between the wind and the stockpiles is critical, not only from the economic point of view, but also in environmental terms.

Therefore, the knowledge and understanding of the airflow over and around stockpiles, as well as, its interaction and consequent particle emissions rate is of major importance; and the present work aims to contribute to the accuracy of the wind erosion prediction methodology.

The interaction between the wind flow and triangular piles, with several slope angles and two different crest heights, was also assessed considering the distribution of pressure and friction coefficients, as well as the free-surface deformation. The behavior of the stoss side of the models was similar to all cases, being the measured pressure coefficient related to the slope angle. In the recirculation zone, i.e., in the leeward side, nearly uniform pressure coefficient was registered for all tested configurations. The wall shear stress was measured in the windward face of the piles, and, independent of the slope, its value increased towards the crest of the pile and the range of its values was similar

The free-surface deformation for 2D triangular sandy piles was recorded and the erosion profiles correlate well with the obtained friction velocity. Erosion occurs mainly where the shear stress exceeded the threshold condition. The influence of the slope angle over the computed sand emission rate was investigated, and the increase of the configuration slope yielded the erosion rate to be reduced and the erosion time necessary to achieve the maximum flux rate to increase.

The numerical model predictions were benchmarked against the triangular piles experimental results and good agreement was obtained, in particular for the friction coefficient distribution. In what concerns the pressure coefficient, the best agreement was found between the foothill and half-length of the windward surface, although the trend between predictions and experiments for the leeward side was similar, the magnitude of the predicted pressure

coefficient was around two times higher than that determined experimentally.

For tests and simulations performed, regardless the quantity (pressure or wall shear stress), it was evident the occurrence of the Reynolds number independency condition.

The flow topology was investigated, and it was observed that, for the initial profile and despite the height of the pile crest remained nearly constant, the size of the recirculation zone grew with the increase of the upwind slope angle. In addition, for a given configuration, as the erosion progresses, the recirculation zone decreases due to the flattening of the free surface profile, causing a major modification of the flow topology in the wake.

The usability of the dust scheme of Shao [15] to model sand emission flux, as well as, the appropriate saltation model to be used were assessed. It was demonstrated that regardless of the saltation model that the Shao's model calibration procedure to estimate the normal sand flux is valid, when the adequate model empirical coefficient is used. However, these coefficients values are specific to the saltation model selected and slope angle.

A new device that allows oblong piles to form naturally in a wind tunnel facility was designed and built. After several tests, it was considered that the projected device was capable of guaranteeing the shape and dimensions of the piles.

The free-surface deformation evolution of oblong piles was studied taking into consideration the influence of the undisturbed wind velocity and of the wind incidence angle. The erosion process was gradual and the most significant modifications in the shape occurred in the initial time instants. Independently of the wind incidence angle, similar behavior was observed for both tested velocities ($U_0=9.1$ m/s and $U_0=9.9$ m/s); however, the erosion and the extension of the piles downstream the limit edge were more accentuated for the higher velocity ($U_0=9.9$ m/s).

Two different wind incidence angles ($\beta = 60^\circ$ and $\beta = 90^\circ$) were studied, and its influence was evident, namely, in the height isolines and extension of the piles. For $\beta = 90^\circ$, although eroding during the course of the tests, the crest was the last feature to disappear, receding over time and tending to a V-shape relative to the symmetry plane of the pile. Whereas for $\beta = 60^\circ$, the crest tends to a peak in the region further downstream of the pile, and it was observed further erosion and alteration of the initial contour of the pile on the first zone subjected to the incoming flow. Furthermore, the erosion of the piles was more intense for the cases with $\beta = 60^\circ$ and the extension of the piles downstream was more evident for $\beta = 90^\circ$.

Considering that the sand emission rate was computed based on erosion profiles, similar conclusions are expected. The influence of the undisturbed wind velocity and incidence angle was also investigated. Regardless the wind incidence angle, higher erosion fluxes were registered for $U_0=9.9$ m/s; similar trend was observed for the experimental tests. In what concerns the deposition fluxes, no specific trend was observed; however higher values were obtained for $\beta = 60^\circ$, in particular for the initial time, which can be explained by the particles

that roll along the leeward face of the pile (creeping) and get trapped at the foot of the pile due to the flow topology in the wake of the piles.

The flow topology over and around the piles was verified against oil-film visualization tests and numerical results from other authors, who used Fluent, as well as against the experimental measurements carried out within the context of the present project; both incidence angles and velocities were also considered.

The wall flow topology was numerically investigated and high friction zones were identified as potential particles emissions regions. For both wind incidence angles, minor differences were observed between the tested velocities ($U_0=9.1$ m/s and $U_0=9.9$ m/s). On the other hand, the influence of β was quite evident in the disturbance of the flow downstream the pile and areas of high friction. Symmetrical behavior downstream of the pile (with two distinct zones) and lower wall shear stress were observed for $\beta = 90^\circ$; whereas for $\beta = 60^\circ$ the higher wall shear stress was attained downstream the pile, extending into the wake zone.

The flow features around the piles, namely, 3D streamlines over the piles and 2D plots of streamlines, vectors field and wall shear stress profile over a vertical plane downward the pile were analyzed; this was an important step toward the understanding of the phenomena intervening in the wind erosion of stockpiles and its surroundings.

Significant influence of the wind incidence angle was noticed in the vortical structures formed in the wake zone. Two major counter-rotating vortices were observed in both cases ($\beta = 60^\circ$ and $\beta = 90^\circ$); however, for $\beta = 90^\circ$ the vortices were symmetrical with the rotation axis initially perpendicular to the ground and then curved by the main flow passing over the crest of the pile, while for $\beta = 60^\circ$, the rotation of one of the vortices was stronger than that of the other one and its axis was oriented toward the main flow direction.

For the oblong piles, the OpenFOAM predictions agree well with those using Fluent and they present good correlation with the experimental erosion profiles. This observation gives high confidence about the numerical model and it is another step supporting the usability of OpenFOAM in this field of research.

In addition, the study makes an important contribution toward the assessment of the engineering capability of *Irwin* probes to measure the wall shear stress of fully developed, incompressible fluid flow under constant and variable pressure gradient conditions. These sensors were used to obtain the experimental data employed to validate the OpenFOAM model for triangular piles.

The flow fully developed condition was guaranteed by verifying the linear constant pressure drop along the test section; good level of repeatability was obtained for the *Irwin* probes.

The influence of the characteristic length scale on the representation of the friction factor for rectangular sections was evaluated, and the hydraulic diameter was the best-suited scale for these configurations, this approach is commonly followed for non-circular ducts.

The calibration of the *Irwin* probes was analyzed in some detail, and an empirical method was used, which consists in the fitting a curve approximating the measured data points. Two approaches were employed to obtain the wall shear stress: a force balance (only for the constant cross-section) and *Preston* tube measurements, being the difference between the correlations obtained with the two approaches less than 5%.

In addition to constant cross-section experiments, both favorable and adverse pressure gradient conditions were evaluated in the calibration of the *Irwin* probes. For the constant and variable cross-section cases, the calibration curve encompassed a power function. Although three different calibration curves were obtained, the power functions were similar. Therefore, for the tested range of pressure difference, a single calibration curve can be employed, with the one for the constant cross-section case showing the best overall results. For all configurations, the deviation between the *Preston* and the calibrated *Irwin* probe measurements was less than 3%.

For the numerical simulations performed for the duct with rectangular cross-section, it was conducted a mesh dependency study, which demonstrated the validity of a viscous sub-layer formulation. The selected turbulence model was the $k-\omega$ SST with $y^+ \approx 1$. The validation of the numerical model was performed through the comparison between OpenFOAM predicted and experimentally-derived values for pressure and friction coefficients. Good agreement was achieved with deviation values lower than 8%, in this way, giving further confidence to the use of the numerical model.

RECOMMENDATIONS FOR FUTURE WORK

During the development of the present study, it came across several issues, which, although not within the scope of the work, raised pertinent questions that were left unanswered. Due to different reasons, including time management and constraints, there are several tests and simulations that were not performed. Consequently, in this section, suggestions, and recommendations for future work are given.

In what concerns the erosion tests, it would be interesting to build the sand piles, no matter its configuration, over a flat bed of sand, in order to evaluate the interaction between the surroundings of the piles and the piles themselves. In this way, it would be possible to study the contribution of the environment to the evolution of the free-surface deformation. In addition, the use of enhanced visualization techniques, such as laser sheets and high-resolution video, to allow, for instance, the observation of the particles trajectories and vortical structures would be an important contribution to further understanding of the intervening phenomena

and to validation data of numerical models.

In the present work, two different pile configurations and one type of granular material were used; however, it is important to note that further work will need to be done to evaluate the applicability and generality of the present approach to other saltating grain dimensions, configurations and scales.

A numerical tool that can use CFD technology associated with a method capable to model the topographical changes of a granular free surface is of great importance in order to be able to assess the wind field and associated phenomena at a given location. This numerical tool would allow the simultaneous evaluation of the feedback mechanism between the ground and the wind field. Therefore, the development of this tool should be considered a priority in future in this field of research.

In what concerns the rectangular duct, although the occurrence of secondary flow has been reported in the past few years, it deserves further investigation to fully characterize this type of flow and, consequently, to evaluate its influence on the measurements with *Irwin* probes.